Thesis Advisor: Professor Robert P. Kirshner Andrew Samuel Friedman

Infrared Light Curves of Type Ia Supernovae

Abstract

This thesis presents the CfAIR2 data set, which includes over 4000 near-Infrared (NIR) JHK_s-band measurements of 104 Type Ia Supernovae (SN Ia) observed from 2005-2011 using PAIRITEL, the 1.3-m Peters Automated InfraRed Imaging TELescope at the Fred Lawrence Whipple Observatory (FLWO) on Mount Hopkins, Arizona. While the discovery of dark energy and most subsequent supernova cosmology has been performed using optical and Ultraviolet wavelength observations of SN Ia, a growing body of evidence suggests that NIR SN Ia observations will be crucial for future cosmological studies. Whereas SN Ia observed at optical wavelengths have been shown to be excellent *standardizeable* candles, using empirical correlations between luminosity, light curve shape, and color, the CfAIR2 data set strengthens the evidence that SN Ia at NIR wavelengths are essentially *standard* candles, even without correction for light-curve shape or for reddening. CfAIR2 was obtained as part of the CfA Supernova Program, an ongoing multi-wavelength follow-up effort at FLWO designed to observe high-quality, densely sampled light curves and spectra of hundreds of low-redshift SN Ia. CfAIR2 is the largest homogeneously observed and processed NIR data set of its kind to date, nearly tripling the number of individual JHK_s band observations and nearly doubling the set of SN Ia with published NIR light curves in the literature. Matched only by the recently published Carnegie Supernova Project sample, CfAIR2 complements the large and growing set of low-redshift optical and NIR SN Ia observations obtained

by the CfA and other programs, making this data set a unique and particularly valuable local universe anchor for future supernova cosmology.

Contents

List of Figures

List of Tables

For my Parents, Family, and

For the love of my life, Kristen.

Acknowledgments

I have pursued PhD research in observational astronomy and cosmology under the supervision of my thesis advisor, Robert P. Kirshner, Clowes Professor of Science in the Harvard University Department of Astronomy. My PhD thesis work is entitled *"Infrared Light Curves of Type Ia Supernovae"*. It has been a privilege working with Professor Kirshner, who has been both a wonderful and patient advisor and an extremely compassionate human being who has supported me through difficult circumstances in the course of the PhD program. Beyond being an excellent thesis supervisor and mentor, as one of the leading founders of the field of supernova cosmology — who just barely missed out on winning the 2011 Physics Nobel Prize for his work — there is a fundamental sense in which he is responsible for making my both my thesis — and the entire field I work in — possible.

Many other scientific colleagues and collaborators that helped me complete the thesis, but I single out two additional major academic mentors and advisers here. I have also been fortunate work closely with Dr. Joshua Bloom, now a Professor in the Department of Astronomy at UC Berkeley, starting in my early years of graduate school when he was a postdoctoral Junior Fellow at Harvard and the CfA. Professor Bloom advised me on my research exam project on Gamma-Ray Burst energetics and cosmology prior to selecting my thesis project (Friedman Bloom 2005b,a). He is also largely responsible for my thesis project itself, since he led the team that roboticized the PAIRITEL 1.3-m telescope — which has provided the bulk of the data presented in my thesis — and gave me the amazing opportunity to use it extensively in its early years and beyond.

More recently, I have also found an excellent mentor in Dr. Michael Wood-Vasey, now a Professor in the Department of Astronomy & Astrophysics at the University of Pittsburgh, also starting when he was a postdoctoral fellow at the CfA. His expertise in supernova data analysis, photometry, and cosmology and his continued willingness to serve as a sounding board for my persistent technical questions has played a significant role in the completion of my thesis (Wood-Vasey & Friedman et al. 2008, Friedman et al. 2012 in preparation). Despite his incredibly busy schedule, and his presence at another university, he has made the time to discuss my progress and setbacks over the phone with me almost every week in the past year. His help and support have been especially crucial in these final days as I approach the endgame of what has been nearly a 7-year project.

I would also like to thank many other colleagues and collaborators at the CfA. First off, I would like to thank Dr. Kaisey Mandel, now a Postdoctoral Fellow in the Cosmology and Astrostatistics Group at Imperial College, London, who is responsible for teaching me a great deal about statistical methods in astronomy, which are only growing in application and importance. I am by no means an expert in astrostatistics, but what I have learned, I have learned from Kaisey and thanks to him I am now sufficiently conversant in the discipline to work more productively with astrostatisticians moving forward. Kaisey is also the architect of a set of impressive tools that he has used to analyze a subset of my thesis data along with other optical and infrared Type Ia supernova data in the literature. His computational techniques are, in my opinion, the best tools available to make scientific inferences using multi-wavelength SN Ia data from my thesis and elsewhere. In an astronomical collaboration, observers and data gatherers like myself and statistical data analysts

like Kaisey each play vital roles, both of which are necessary for achieving our shared scientific goals. However, without his help, the utility of my thesis data as a means toward answering our key scientific questions would not yet have been realized.

Pete Challis, a longtime research astronomer at the CfA working with Prof. Bob Kirshner, has been the glue that has held our Supernova group together for close to two decades. While graduate students and postdocs come and go, he serves as the institutional memory of our group, keeping track of technical skills and data sets that would otherwise be lost in the whirlwind stream of new data that pours in much to fast for all of us to process and analyze. Pete has also been a huge help to me personally, managing the PAIRITEL observational queue at times when I was unable, sometimes for long stretches. I have benefitted greatly from his expertise in optical photometry, spectroscopy and observational astronomy over the years.

Howie Marion, a relatively recent addition to our supernova research group, arrived as a postdoc not quite two years ago. Over a year ago, as I prepared for the home stretch of the thesis finishing process, Howie took over the day-to-day management of the PAIRITEL observational queue. While robotic telescopes have many advantages over traditional telescopes, they still require a great deal of energy and effort to manage, which can amount to several hours a day depending on how diligent and flexible you can be. Maryam Modjaz was originally in charge the SN project, managing the PAIRITEL queue heroically for several years until I took over sometime in 2007. When Howie took on this task in 2011, it finally freed me up to focus more intensely on getting the data and thesis itself into shape. After manning the helm of the PAIRITEL queue for nearly five years, Howie spared me from being drowned by the constant deluge of acquiring, managing, and processing

new data that never ceases as long as the telescope is functioning. Supernovae, it turns out, rarely decide to stop exploding merely for our convenience. Since my efforts have focused primarily on infrared photometry, it has been wonderful to draw upon Howie's expertise in infrared supernova spectroscopy, complementing the optical spectroscopic expertise of former and current CfA postdocs Stephane Blondin, Ryan Foley, along with spectroscopic gurus Bob Kirshner, Pete Challis, and Tom Matheson (now at NOAO), amongst others, whose pioneering efforts have make the CfA arguably the world's leading center for optical supernova spectroscopy.

I would also like to thank many other colleagues and collaborators at UC Berkeley, which jointly became the institutional center of PAIRITEL with Harvard after Josh Bloom joined the Astronomy faculty at Berkeley in 2006. The code to turn the telescope data into mosaicked images suitable for photometry was initially developed at Berkeley, in varying stages, by Josh Bloom, Cullen Blake, Dan Starr, and Chris Klein, all of whom have been extremely helpful with the many questions I have had regarding the technical intricacies of the PAIRITEL project, especially in regard to the software tools they developed. Cullen Blake, now an NSF Astronomy postdoctoral fellow at Princeton, wrote the first generation of the PAIRITEL mosaic code and many of the other software tools that help PAIRITEL to function and was a huge help, especially in the early days of the project. Dan Starr wrote the second generation mosaic code, and has been the go-to-guy for any questions related to the day-to-day operations of PAIRITEL and the software underlying the observing queue. Chris Klein, who wrote the third generation PAIRITEL mosaic code, was very patient with me as I grilled him on its inner workings, which was especially important since I began my inquiries relatively inexperienced with python, the

programming language in which he wrote it. Adam Miller and Adam Morgan have been involved in other PAIRITEL projects at Berkeley which have some overlap with objects observed by the SN project. In this role, the two Adams have been very helpful in coordinating with Pete, Howie, and myself to appropriately identify which observations belong under which project and add them to the queue as needed.

When we determined that we needed to add a few new features to Chris Klein's pipeline 3.0 version of the mosaic code that were mainly of interest to the PAIRITEL SN project, it made the most sense for me to develop, test, and implement the code. This involved the painstaking installation of all the dependent software on our local machines at the CfA, a task which I would have had a great deal of trouble performing without the help of Bill Wyatt, an experienced Smithsonian Astrophysical Observatory research scientist in the Optical and Infrared Division at the CfA. Bill's computational and system administration expertise was instrumental in helping me implement a functioning, automated, local version of the upgraded pipeline3.6 code for making Infrared mosaic images here at the CfA. Chris Klein and Dan Starr were extremely helpful in this process, always willing to explain to me the many facets of the mosaic pipeline as I struggled to adapt and upgrade Chris Klein's thousands of lines of python code. While difficult, this proved to be much easier than starting from scratch on a project that Chris took several dedicated years to write. In addition, the task helped me learn a great deal of the python programming language, which is becoming the tool of choice for many modern astronomers and astrophysicists, as many of us transition from using IDL, Interactive Data Language, an excellent (but expensive!) astronomical programming language that has been long entrenched as the flagship code of NASA and most astronomical institutions.

Several Optical supernova astronomy colleagues have been a great help to me as well. Gautham Narayan has been the resident expert in the intricacies of the photometry pipeline used both for optical low and high redshift supernova light curves at the CfA. Originally developed by Armin Rest and collaborators for the ESSENCE and SuperMacho projects, we adapted Armin's photometry pipeline for Infrared observations with the help of Michael Wood-Vasey, Maryam Modjaz, and myself. Dr. Malcolm Hicken — who has been responsible for the optical counterparts to the Infrared observations I have been managing — has been a huge help to me in providing a model for how I should proceed, since he preceded me as a PhD student working with Bob Kirshner. Since both Malcolm and the optical data have always been a little ahead of myself and the notoriously difficult Infrared data, I have benefitted tremendously from being able to follow in the footsteps that Malcolm provided, both in terms of the organization and writing of scientific papers and sharing his work for things which were equally relevant to the PAIRITEL Infrared data. Overall, Malcolm has been a helpful and knowledgeable colleague in regard to my many photometry questions over the years.

In addition, I would be remiss to thank all of the people at the Fred Lawrence Whipple Observatory at Mount Hopkins, Arizona where the PAIRITEL 1.3-meter telescope is physically located. Especially since I have never had the pleasure — or even been required — to actually visit PAIRITEL in person, I must give extra thanks and emphasize that the support staff at Mount Hopkins are the people who actually fix the telescope when it breaks, refill the cryogenic helium dewar, and deal with anything from the telescope motor getting stuck to lightening strikes. We've had the dome control electronics fail and had the telescope and camera get rained

on when the dome failed to close. We've had our server compromised by hackers who probably had no idea what PAIRITEL did other than that it was hosted on a server with a university's name on it. Although I sometimes helped identify these problems as they occurred, they all had to be solved by people at Berkeley or on the ground at Mount Hopkins who could physically pull the plugs, close the dome, and keep the telescope and its instrumental infrastructure safe and dry. Furthermore, while I have been fortunate to use the robotic telescope as a remote observer, trading the inconveniences of travel for the relative comfort (or discomfort?) of my office chair, it is the people on the ground who actually make possible the use of PAIRITEL as a scientific instrument. These include the FLWO director Emilio Falco, FLWO engineering staff guru Wayne Peters, who has personally fixed a broken PAIRITEL dozens of times, as well as FLWO regular optical observers Michael Calkins, Perry Berlind and others who are often on call to leave their optical post to help PAIRITEL with time sensitive problems like closing the dome or dealing with an emergency when the robotic automation has failed. I owe thanks to many other regular observers and support staff at the FLWO 1.5-meter or 1.2-meter telescopes that have been there as backup for PAIRITEL when needed.

In the early days of PAIRITEL, CfA/SAO scientists Andy Szentgyorgi and Nelson Caldwell were also instrumental in working with Josh Bloom and the folks at Mount Hopkins to make the robotization of PAIRITEL a reality. Further back in time, I have to thank Mike Skrutskie, along with the late — and dearly missed — John Huchra, and everyone else (too many to mention; see Skrutskie et al. 2006; Cutri et al. 2003) involved in the landmark 2 Micron All Sky Survey (2MASS) project, who eventually bequeathed to us the 2MASS north telescope and the 2MASS

south infrared camera that eventually became PAIRITEL. More specifically, the PAIRITEL infrared camera has been on indefinite loan from Prof. Mike Skrutskie at the University of Virginia, who led the team that developed the camera for 2MASS. Without the years of hard work from everyone at 2MASS, PAIRITEL would not have existed, and would certainly not have detected any infrared photons.

In the Astronomy department at Harvard, I also would like to thank my thesis committee, which has evolved considerably over the years. Members that have served and attended at least one thesis advisory committee meeting have included Professors Ramesh Narayan, Lars Hernquist, Chris Stubbs, and John Huchra, who sadly passed away unexpectedly in 2011. In light of the tragedy, Prof. Daniel Eisenstein graciously agreed to take Prof. Huchra's place on the committee. Due to the sabbatical schedules of Professors Stubbs and Hernquist, newer Professors Edo Berger and Alicia Soderberg also kindly agreed to served on my committee at fairly short notice. With scheduling a nearly intractable problem for several months prior to the defense, this was something I greatly appreciated. Along with my advisor, Prof. Bob Kirshner, and Prof. Michael Wood-Vasey as my outside member from the University of Pittsburgh, I was somehow able to round up a reasonable and fair-minded five person committee at a single space-time point and successfully defend the thesis, thanks in no small part to the added presence of Professors Eisenstein, Berger, and Soderberg.

For my earlier research exam project, which I undertook in my first few years of graduate school, Professor Ramesh Narayan advised me on a project involving Gamma-Ray burst explosions. When it became clear that my interests and inclinations were more focused on cosmology than astrophysical theory, Ramesh

was very supportive of letting me redirect the project under the supervision of Josh Bloom, who became my de-facto research exam advisor as a postdoc. This resulted in my first lead author paper which reinforced our understanding of the difficulty of trying to turn GRBs into standard candles for cosmology and eventually turned me back toward Type Ia supernova astronomy, to deal with standard candles that were considerably more well understood (at least empirically) and considerably more cosmologically promising.

I say that I turned back to supernova astronomy for my thesis because this was, in fact, what I had worked on as an undergraduate in Physics and Astronomy at UC Berkeley working with Prof. Alex Filippenko. Alex was a fantastic mentor and advisor, giving me the chance to get involved in the supernova search efforts at Berkeley starting shortly after the time of the seminal 1998 discovery of the acceleration of the expansion of the universe that would eventually win the 2011 Physics Nobel prize. As one of the most inspiring teachers I have ever known, Alex was an influential role model for me, undoubtedly helping encourage me to pursue a career where teaching is an integral part. As an undergraduate teaching assistant for Astro 10, Alex's introductory astronomy course, I had the chance to help teach a class with over 850 students, easily the most popular class on a large campus. This gave me the chance both to experience how effective a course like that could be at reaching a very large audience, and to be recognized on campus by hundreds of students that I had never actually met.

My day-to-day advisor for my undergraduate thesis project was Dr. Weidong Li, who Alex wisely hired to be the architect of the impressive Lick Observatory Supernova Search, which has been the world's most successful nearby supernova

search and discovery engine to date. Weidong was a kind and patient mentor, helping me learn the basics of image detection and supernova photometry, and giving me and the team of dedicated image checking undergrads the chance to help his software discover supernova of our own. I was fortunate to discover 7 supernovae as an undergrad — a fact which had the expected effect on my parents — but none of this would have been possible without the amazing efforts of Weidong, who transformed the entire field of supernova discovery. Sadly, Weidong passed away earlier this year, shocking the Berkeley and supernova astronomy communities, and leaving an indelible impression on me personally. I would like to dedicate this graduate thesis, in part, to honor of the memory of Weidong Li who I will alway be indebted to as the primary technical mentor for my undergraduate thesis. He will be greatly missed.

I would also like to thank other teachers and notable undergraduate mentors at Berkeley including Prof. James Graham (now at the University of Toronto) and Prof. Nate McCrady (now at the University of Montana), who led the Astro Lab course, which was the most challenging and transformative academic experience of my life. I have yet to experience anything like it since then in graduate school and it was undoubtedly crucial in helping me decide to continue the path into astronomy. I would also be remiss if I failed to thank Professor Frank Shu, who taught Astro 7AB for astro majors and gave me my first experience of rigorous mathematical astrophysics. Bill Holzapfel, who taught me high energy astrophysics and general relativity, was a great person to bounce crazy ideas off of, and I appreciate his willingness to still write me letters of recommendation for grad school despite my sometimes unbridled speculative tendencies. I would also like to thank my

undergraduate Physics advisor Richard Muller, who helped me figure out how to balance the double major of Physics and Astrophysics without spending the Hubble time in school.

Back to graduate school, I also want to thank many of the Harvard astronomy faculty who I was fortunate to have as professors for graduate courses, including Ramesh Narayan, George Rybicki, Dimitar Sasselov, Krysztof Stanek, Lars Hernquist, Avi Loeb, Matias Zaldariagga, and Harvard Physics professor Andy Strominger. I would also like to thank Bob Kirshner and Dave Charbonneau for the opportunity to be a teaching assistant for their courses (twice for Bob!). Other astronomy faculty including former CfA directory Irwin Shapiro and former Astronomy department chair Jim Moran have been extremely supportive and helpful to me over the years, in addition to constantly trying to improve the department to better support its students.

The Astronomy department administrators at the CfA including Jean Collins, Peg Herlihy, and more recently, Donna Adams, also deserve a great deal of thanks for all of their help and support. They serve as the glue that holds the department together and their warmth, kindness, and empathy has been a welcome beacon in an intense academic environment which can often lack the kind of human consideration that they have consistently shown both to all of my fellow graduate students and to me personally. As a graduate student, one gets the sense that Jean and Peg have always viewed us, in some sense, as their extended family. Their presence has provided a wonderful support network in what could otherwise be somewhat of an impersonal and sterile working environment.

However, no group deserves more credit for making the department feel like a family than my fellow graduate students, who have truly made this a wonderful place to live and work for what would otherwise have seemed like far too long. Bonding through shared suffering, struggle, and our many successes has helped me make a great number of close and lifelong friends in graduate school. For helping make what could easily have been an alienating and isolating experience livable, I would like to thank (in no particular order) my friends and fellow Astro graduate students including: Kamson Lai, Xavier Koenig, Ryan Hickox, Christopher Night, Shinae Park, Slavko Bogdanov, Deborah Freedman, Jonathan Devor, Jonathan Foster, Kaisey Mandel, Malcolm Hicken, Gautham Narayan, Diego Munoz, Laura Blecha, Gurtina Besla, Meredith Hughes, Sarah Ballard, Robert Harris, Nick Stone, Joshua Suresh, Rebekah Dawson, Sarah Rugheimer, and many others. I would also like to thank the many friends I have made at Harvard outside the Astronomy department through the Graduate Residence Halls, Dudley House, and in the greater Cambridge/Boston area. Although they are too numerous to mention individually here, a community of friends is ultimately what makes a place feel like home.

On a somewhat more formal note, while grad school may be free for us, somebody has to pay for us to do science, so I would like to extend a great thanks to the several institutions and national funding agencies who made my thesis work possible. These include the National Science Foundation, who kindly awarded me a NSF Graduate Research Fellowship from 2003-2006, and the National Aeronautics and Space Administration, who awarded me a NASA Graduate Research Program Fellowship from 2006-2009. In the absence of external funding, I was very fortunate to receive institutional support from the Harvard-Smithsonian Center for

Astrophysics under the leadership of Directors Irwin Shapiro and Charles Alcock, along with NSF grant support from my Advisor, Prof. Robert Kirshner. I also would like to than the Astronomy department for its very generous yearly travel grants, the Loomis fund for its one-time research fund grant for graduate students, and the Harvard Astronomy department for the well received "laptop grant", who's name indicates that it was earmarked for something clearly essential to modern astronomical research. I would also like to thank the Harvard Graduate Student council, which supported two of my applications to for conference grants, to help supplement the support from the Astronomy department when needed.

Much of my thesis relies on the hard work of the greater astronomical community. I would like to specifically thank the Carnegie Supernova Project, our ostensible competitors (but really our supernova-interested friends and colleagues) for providing a great example to follow and challenging us to produce our best work at the CfA with PAIRITEL. In addition, I would like to thank the High-Z team and the Supernova Cosmology Project for lighting the spark back in 1998 (and before) that turned the field of supernova cosmology into the exciting and active cutting edge field that I have the privilege of working in today. I would also like to thank the greater community for producing and sharing many of the open source software tools in IDL, python, C and other languages that have been indispensable for my thesis project including DoPHOT, SExtractor, SWarp, HOTPANTS (yes, I know), and Astrometry.net, to name a few of those too numerous to properly cite or mention here (see **References** at the end of the thesis). I would also like to thank CfA folks like Doug Mink and Bill Joye for building astronomical utilities like WCS Tools and SAOimage ds9 that so many of us rely on daily as well as Tom Aldcroft and the

astropython community for continuing to build python into the tool of choice for modern astronomers, although I admit a love for most things about IDL and its magic plotting and visualization tools aside for the cost of its licenses!

Many other thanks go out to the people behind the scenes who make everything I have done for this thesis possible. This especially pertains to those who maintain and support the computational infrastructure that I and other astronomical researchers rely on to do essentially everything we do in astronomical research today. I'd like to thank all the people at the Harvard CfA Computation Facility for ensuring that we had working internet connections and beginning to support the Astronomy Mac revolution in addition to the standard unix, Linux, and Sun machines that today's Macs built their backbones on. I'd like to thank Matt Phelps and the administrators of the CfA Hydra cluster, whose computational infrastructure allowed us to run our photometry pipeline for our first PAIRITEL data release back in 2008. Finally, I'd like to thank the staff at the Harvard Odyssey cluster, especially Dr. James Cuff and Dr. Paul Edmon, who have truly enabled us to employ high performance computation to effectively parallelize our photometry pipeline, turning what was a month long computation as recently as 3 years ago into something we can re-run essentially overnight.

I would also like to thank my future colleagues at the Massachusetts Institute of Technology, including Professors David Kaiser, Alan Guth, and Max Tegmark, each of whom supported different incarnations of my NSF Astronomy, NSF STS and other postdoctoral fellowship applications. Finding out that you have a postdoc is the surest way to light a fire under one's office chair aimed at thesis completion and it was a huge relief to know that I would have somewhere to go when the thesis

itself had been finally laid to rest. I am looking forward toward to the submission of the paper accompanying this thesis, and to exploring my new postdoc project, both with great and long awaited anticipation.

And last, but not least, I'd like to thank my parents, Richard and Randee Friedman for their unending and unconditional love and support through what has been a long a difficult process for me. I got really lucky in the parent lottery and I can't imagine having grown up in a situation any better than my actual life. They gave me an amazing world to grow up in and made it possible for me to reach for the stars. I'd also like to thank my brother Barry Friedman for always being there for me to talk to about anything, riffing for five minute snippets or hours at a time about everything from the serious to the ridiculous, always making each other laugh.

And finally, I'd like to thank my fiancee, Kristen Keerma (soon to be Kristen Friedman!), who this thesis is dedicated to. You are the love of my life and you finally made it possible for me finish a project that has been hanging over my head for as long as I can remember. I love you so much and I look forward to the next, thankfully thesis free, chapters of our life together.

Grant and Institutional Support Acknowledgements

The Peters Automated Infrared Imaging Telescope (PAIRITEL) is operated by the Smithsonian Astrophysical Observatory (SAO) and was made possible by a grant from the Harvard University Milton Fund, the camera loan from the University of Virginia, and the continued support of the SAO and UC Berkeley. Partial support for PAIRITEL operations and this work comes from National Aernonautics and Space Administration (NASA) grant NNG06GH50G ("PAIRITEL: Infrared Follow-up for Swift Transients"). PAIRITEL support and processing is conducted under the auspices of a DOE SciDAC grant (DE-FC02-06ER41453), which provides support to J.S.B.'s group. J.S.B. thanks the Sloan Research Fellowship for partial support.

We gratefully made use of the NASA/IPAC Extragalactic Database (NED). THE NASA/IPAC EXTRAGALACTIC DATABASE (NED) IS OPERATED BY THE JET PROPULSION LABORATORY, CALIFORNIA INSTITUTE OF TECHNOLOGY, UNDER CONTRACT WITH THE NATIONAL AERONAUTICS AND SPACE ADMINISTRATION. This publication makes use of data products from the 2MASS Survey, funded by NASA and the US National Science Foundation (NSF). IAUC/CBET were useful. M.W.V. is funded by a grant from the US National Science Foundation (AST-057475). A.S.F. acknowledges support from an NSF Graduate Research Fellowship and a NASA Graduate Research Program Fellowship. M. M. acknowledges support in part from a Miller Research Fellowship. A.S.F, R.P.K, M.M., and S.B. thank the Kavli Institute for Theoretical Physics, which is supported by the NSF through grant PHY05-51164. The CfA Supernova

Program is supported in part by NSF Grant AST 06-06772. C.B. acknowledges support from the Harvard Origins of Life Initiative. The computations in this thesis were run on machines supported by the Harvard Astronomy Computation Facility including the CfA Hydra cluster and machines supported by the Optical and Infrared Astronomy Division of the Harvard-Smithsonian Center for Astrophysics. Other crucial computations were performed on the Harvard Odyssey cluster, supported by the FAS Science Division Research Computing Group at Harvard University.

Chapter 1

Introduction: Infrared Light Curves of Type Ia Supernovae

"CfAIR2: 104 Type Ia Supernova Near-Infrared Light Curves from PAIRITEL", Andrew S. Friedman, W. Michael Wood-Vasey, Peter Challis, Kaisey S. Mandel, G.H. "Howie" Marion, Gautham Narayan, Malcolm Hicken, Ryan Foley, Joshua S. Bloom, Chris Klein, Dan L. Starr, Adam Miller, Adam Morgan, Armin Rest, Maryam Modjaz, Cullen H. Blake, Stéphane Blondin, Emilio E. Falco, William. F. Wyatt and Robert P. Kirshner, 2012, to be submitted to *The Astrophysical Journal*

Abstract

With the aid of a NSF Graduate Research Fellowship from 2003-2006, a NASA Graduate Student Research Program Fellowship from 2006-2009, and continued support from the Harvard-Smithsonian Center for Astrophysics (CfA), I have pursued PhD research in observational astronomy and cosmology under the supervision of my thesis advisor, Robert P. Kirshner, Clowes Professor of Science in the Harvard University Department of Astronomy. My PhD thesis work is entitled *"Infrared Light Curves of Type Ia Supernovae"*.

While the discovery of dark energy and most subsequent supernova cosmology has been performed using optical wavelength SN Ia observations, a strong and growing body of evidence suggests that SN Ia observations at rest-frame Near-Infrared (NIR) wavelengths are superior to those at optical and Ultraviolet (UV) wavelengths for future cosmological studies, yielding more accurate and more precise distance estimates to SN Ia host galaxies than optical data alone. While SN Ia observed at optical wavelengths have been shown to be excellent *standardizeable* candles, using a variety of sophisticated methods correlating luminosity with light curve (LC) shape and color, recent work — including the work presented in this thesis — demonstrates that SN Ia are essentially *standard* candles at NIR wavelengths, even without correction for light-curve shape or reddening. Many of the systematic uncertainties of and discrepancies between many of the most prominent optical LC fitting and distance estimation methods are largely obviated with the incorporation of NIR data. Overall, systematic distance errors from uncertain dust estimates and intrinsic variability of un-reddened SN Ia colors are the major outstanding problems

with using SN Ia for precise cosmological measurements of dark energy with optical data alone. In comparison to SN Ia observed at optical wavelengths, NIR SN Ia are both better standard candles and relatively immune to the effects of extinction and reddening by dust. The most promising route toward understanding the dust in other galaxies and mitigating systematic distance errors thus comes from NIR observations. Because the addition of NIR SN Ia data can lead to more precise and more accurate galaxy distance measurements — and more accurate dark energy measurements — than optical data alone, my colleagues and I hope that my thesis data will ultimately play a small but significant part in helping to elucidate the mystery of dark energy.

At the CfA, we have been pioneers in this field, developing the most effective ways to obtain NIR observations and novel techniques to combine NIR and optical samples to determine increasingly precise and accurate distances to SN Ia host galaxies. Two thesis projects — including my own — have grown out of this unique, cutting edge work with NIR SN Ia data under the supervision of Professor Kirshner as part of the CfA Supernova Group. Our research efforts in NIR observations, photometry, and data reduction have been led by myself and Professor Michael Wood-Vasey[1] (Wood-Vasey & Friedman et al. 2008, Friedman et al. 2012 *in preparation*), helping to confirm that SN Ia are excellent standard candles in the NIR, especially in the rest-frame H-band, where they are ~ 5 times less sensitive to extinction from dust than in the optical V-band. Our work emphasizing the intrinsically standard and relatively dust insensitive nature of NIR SN Ia has further

[1]Professor Michael Wood-Vasey is now a faculty member of the Department of Astronomy & Astrophysics at the University of Pittsburgh

promoted the rest-frame NIR as a promising wavelength range for future space based cosmological studies of SN Ia and dark energy, where reducing the systematic uncertainties from dust extinction and intrinsic color variation becomes more important than simply increasing the statistical power of the sample by observing additional SN Ia (e.g. Gehrels 2010; Beaulieu et al. 2010; Astier et al. 2011). In addition, for his PhD thesis as a member of the CfA Supernova Group, Dr. Kaisey Mandel[2] has spearheaded the development of novel sophisticated statistical methods to mathematically model NIR LCs within a Hierarchical Bayesian framework (Mandel et al. 2009) and to combine NIR and optical SN Ia LCs to obtain estimates of extinction by dust and distances to the SN Ia host galaxies that are more precise and more accurate than with optical data alone (Mandel et al. 2011).

The primary scientific goal of my thesis has been to obtain and present a high quality low-redshift data set of NIR SN Ia observations. This thesis presents the CfAIR2 data set, which includes 104 Near-Infrared JHK_s-band light curves of SN Ia observed through the CfA Supernova Program from 2005–2011 with the PAIRITEL 1.3-m telescope at the Fred Lawrence Whipple Observatory at Mount Hopkins, Arizona. Out of the 122 SN Ia observed by PAIRITEL from 2005-2011 (not all of which are presented in CfAIR2), 58 (48%) have NIR observations before $t_{B\mathrm{max}}$, while 34 (28%) have observations at least 5 days before $t_{B\mathrm{max}}$. These fractions of early time observations are comparable to similar SN Ia follow-up work by the CSP (Contreras et al. 2010; Stritzinger et al. 2011). The 4269 individual data points in this sample represent the largest homogeneously observed and reduced set of

[2]Dr. Kaisey Mandel is now a Postdoctoral Fellow in the Cosmology and Astrostatistics Group at Imperial College, London

NIR SN Ia observations to date, nearly doubling the number of objects and nearly tripling the number of individual JHK_s band photometric observations of SN Ia in the literature. The NIR JHK_s observations are part of a systematic program at the CfA of supernova observations that includes dense sampling of optical supernova spectra and concurrent $UBVRIr'i'$ optical photometry. This work is a new report on the NIR SN Ia data from PAIRITEL following a previously published subset of of my thesis data set including 21 JHK_s SN Ia LCs (Wood-Vasey & Friedman et al. 2008).

Sections of this thesis will become a paper releasing the full CfAIR2 data set, entitled *"CfAIR2: 104 Type Ia Supernova Near-Infrared Light Curves from PAIRITEL"*, to be submitted to *The Astrophysical Journal* (Friedman et al. 2012 *in preparation*).

The Introduction to this thesis (§1) is organized as follows. In §1.1 we provide background on the use of SN Ia for cosmology and describe the fundamental role of SN Ia in the surprising and mysterious discovery of dark energy now thought to be causing the acceleration of the expansion of the universe. In §1.2, we briefly review the cosmological results obtained from high redshift optical SN Ia observations. In §1.3, we present a broad overview of the scientific motivations underlying this thesis project, highlighting the distinct advantages of newer NIR observations over traditional optical observations of SN Ia, based on work which includes results derived from a previously published subset of my thesis data (Wood-Vasey & Friedman et al. 2008; Mandel, Wood-Vasey, Friedman, & Kirshner 2009; Mandel et al. 2011). In §1.5, we outline the organization of the remainder of the thesis.

1.1 SN Ia Cosmology, Dark Energy, & Cosmic Acceleration

Observational cosmology has undergone a renaissance in the past decade, largely due to the surprising 1998 discovery of the acceleration of the expansion of the universe and the inference of the existence of the dark energy thought to be causing cosmic acceleration. Just over a decade ago, two teams of observational astronomers — the High-Z team and the Supernova Cosmology Project — presented the first evidence for cosmic acceleration based on optical observations of exploding white dwarf stars in distant galaxies called Type Ia Supernovae (Riess et al. 1998; Schmidt et al. 1998; Perlmutter et al. 1999). The primary observational evidence for cosmic acceleration came from the discovery that many distant SN Ia are significantly dimmer — and thus more distant — than would have been expected if the universe was currently expanding at a constant velocity or decelerating. In the decade plus since the discovery, SN Ia have further proven to be excellent tools for measuring galactic distances and constraining cosmic expansion history. SN Ia cosmology has grown into a cottage industry driving the field of observational cosmology and is now the most mature astrophysical technique we have to elucidate the mysterious nature of dark energy, the discovery of which recently won the 2011 Nobel Prize in Physics for Saul Perlmutter, Adam Riess, and Brian Schmidt, who all have ties to Harvard. Saul Perlmutter was a Harvard undergraduate while Brian Schmidt and Adam Riess were both Harvard Astronomy PhD students supervised by Professor Kirshner in the early 1990s. In addition to training some of the most prominent members of the SN Ia research community, Professor Kirshner is widely regarded

as the founder of the field of supernova cosmology. His efforts to establish the observational programs to discover and follow-up both high and low-redshift SN Ia laid the groundwork for cosmology to finally become a precision science, and played a decisive role in the discovery of dark energy. See Kirshner 2004 for an engaging popular account of the discovery of cosmic acceleration with SN Ia, while Kirshner 2010 and Goobar & Leibundgut 2011 present more recent technical reviews of the current state of cosmology with SN Ia. Here we present a brief review of the basic methods underlying cosmology with SN Ia.

In an expanding universe described by the Friedmann-Lemaitre-Robertson-Walker (FLRW) metric of Einstein's theory of general relativity, the redshift z of an astronomical object quantifies that the light from the object has been stretched in wavelength by a factor of $1 + z$ by cosmic expansion during the time between its emission by the source and its detection at our telescopes. In practice, we measure the redshift z for a SN Ia by observing it (or its host galaxy) through a spectrograph, and looking for sets of characteristic spectral features in the observed spectrum that have been shifted in wavelength by an amount $1 + z$ compared to their laboratory measured values. The redshift z of an object like a galaxy — or a supernova within that galaxy — is a monotonically increasing function of its distance d_L from Earth and, in the nearby universe, z is directly proportional to its recessional velocity v radially away from us due to the expansion of the universe. For $z << 1$, this is codified by the Hubble Law given by:

$$d_L(z << 1) \approx cz/H_o \tag{1.1}$$

where c is the speed of light and H_o is the Hubble Constant which quantifies the

current expansion rate at the present epoch. H_o is constant in space at a given cosmic epoch but varies in time over cosmic history (See Equation 13 of Goobar & Leibundgut 2011). The best measured current value of the present day Hubble Constant is $H_o = 74.2 \pm 3.6$ km s^{-1} Mpc^{-1}(Riess et al. 2011). For any redshift, including $z \gtrsim 1$, the distance-redshift relation $d_L(z, \vec{\Omega})$ is given by Equations 10–14 of Goobar & Leibundgut 2011, where $\vec{\Omega}$ is a vector of parameters describing the cosmological model corresponding to a particular expansion history. Typically, FLRW models are parameterized by a parameter vector $\vec{\Omega} = (\Omega_{\rm M}, \Omega_\Lambda, w)$, where $\Omega_{\rm M}$ is the cosmic matter density fraction, Ω_Λ is the dark energy density fraction, and $w = P/(\rho c^2)$ is the equation of state parameter describing dark energy.

The fundamental cosmological technique used to measure cosmic expansion history with SN Ia involves the construction of a Hubble diagram, where we compare the differences between the estimated luminosity distances for a set of SN Ia with measured spectroscopic redshifts to the theoretical $d_L(z, \vec{\Omega})$ relation defined for a given cosmological expansion history. This can be used to test whether a given cosmological model is consistent with the data or to estimate the parameters $\vec{\Omega}$ and uncertainties of that model under the assumption that the model is correct. At low redshifts $z \lesssim 0.1$, all FLRW cosmological models yield a luminosity distance given by the Hubble Law (Equation 1.1) independent of the cosmological parameters $\vec{\Omega}$. As such, low redshift SN Ia data alone can not be used to estimate cosmological parameters $\vec{\Omega}$ or test individual cosmological models. Rather a low-z SN Ia data set serves as the local linchpin to measure and characterize the properties of SN Ia in the nearby universe, in order to calibrate cosmological inferences made using high-z SN Ia data sets, which require the anchoring properties of the low-z sample

to yield accurate and precise cosmological measurements. Since this thesis presents an entirely low-z SN Ia data set and is not directly concerned with cosmological parameter estimation, we refer the reader to a standard cosmology textbook for a full derivation of the $d_L(z, \vec{\Omega})$ relation for a given cosmology (Weinberg 2008). Also see Davis & Lineweaver 2004 for an excellent technical review of the many cosmological misconceptions surrounding the idea of an expanding universe.

Constructing a cosmologically useful SN Ia Hubble diagram requires the estimation of accurate luminosity distances to the SN Ia host galaxies. Unlike the redshift z, which is measured directly from the observed SN Ia spectrum, the luminosity distance d_L is not measured directly but indirectly inferred from measurements of the apparent brightness of the SN Ia. This indirect inference uses a complex model based on detailed background information from other astrophysical measurements and includes many subtle steps in order to link the observed apparent brightness to the inferred intrinsic luminosity and luminosity distance (e.g. Jha et al. 2007; Mandel et al. 2011). However, accurate and precise distance measurements to SN Ia host galaxies are ultimately possible with such a procedure because SN Ia are approximately "standard candles": astrophysical objects with roughly standard intrinsic luminosities.

Although the unambiguous identification of individual SN Ia progenitor star systems remains a major unsolved astrophysical problem, strong evidence supports the idea that SN Ia result from thermonuclear disruptions of white dwarf stars in binary systems which explode at a mass near the Chandrasekhar mass limit ($M_{\rm ch}$) of 1.4 solar masses (See Maoz & Mannucci 2011 for a review). To zeroth order, in an idealized scenario, if SN Ia explosions arise from progenitors of similar masses

($\sim 1.4 M_{\odot}$) and use similar amounts of thermonuclear fuel, we might theoretically expect them to emit roughly standard amounts of intrinsic energy and thus have similar intrinsic luminosities. If one knows the intrinsic luminosity L of the standard candle relative to a standardized source measured in a galaxy in the very nearby universe (e.g. Cepheid variable stars), one can estimate the relative distance to the SN Ia by measuring the apparent brightness F and using the cosmological version of the inverse square law for the dimming of light from distant sources, $F = L/(4\pi d_L^2(z, \vec{\Omega}))$, where the luminosity distance d_L is a function of the redshift z and cosmological parameters $\vec{\Omega}$ (see Eqs. 10–14 of Goobar & Leibundgut 2011).

In reality, SN Ia empirically display a peak luminosity distribution that is not perfectly standard, but is moderately well-determined to within a width of roughly a factor of three in luminosity from the intrinsically brightest, slowly declining objects (e.g. SN 1991T; Filippenko et al. 1992a; Phillips et al. 1992) to the intrinsically faintest, fastest declining objects (e.g. SN 1991bg; Filippenko et al. 1992b; Leibundgut et al. 1993). SN 1991T-like and SN 1991bg-like objects comprise roughly 9% and 15% respectively of the SN Ia population discovered in practice by the Lick Observatory Supernova Search (Li et al. 2000; Filippenko et al. 2001; Filippenko 2005; Leaman et al. 2011), the world's premier volume-limited optical survey (Li et al. 2011a)[3]. Other intrinsically faint peculiar SN Ia that evolve rapidly include prototypical objects like SN 2002cx (Li et al. 2003), with more recent

[3]I had to the good fortune to work on the Lick Observatory Supernova Search as an undergrad at UC, Berkeley working with Alex Filippenko and Weidong Li. I was part of an undergraduate team of image checkers supplementing the evolving supernova detection software and I was fortunate to discover 7 supernovae as an undergraduate: SN 1999bh (Li et al. 2000), SN 1999bx (Friedman & Li 1999), SN 1999ej (Friedman et al. 1999a), SN 1999gb (Friedman et al. 1999b), SN 2000fa (Friedman et al. 2000), SN 2001L (Friedman et al. 2001a), SN 2001ae (Friedman et al. 2001b).

examples including SN 2005hk (Phillips et al. 2007) and SN 2008ha (Foley et al. 2009a). These extremely peculiar SN 2002cx-like SN Ia may comprise $\sim 5-10\%$ of the SN Ia sample (Foley et al. 2009a; Li et al. 2011a). Non-standard SN Ia thus account for at $\sim 30\%$ of all SN Ia in a volume-limited sample observed at optical wavelengths (Li et al. 2011b). Also see Phillips 2011 for a review of peculiar SN Ia properties at Near-Infrared wavelengths.

In addition, a strong body of evidence suggests that nature may allow at least two prominent paths to producing SN Ia including, the single degenerate scenario, where a white dwarf star made of degenerate matter accretes mass from its main sequence binary companion until reaching $\sim M_{\rm ch}$, and the double degenerate scenario, where a pair of binary white dwarf stars, each initially with mass $< 1.4 M_{\odot}$, merge after orbital decay from release of gravitational radiation (Maoz & Mannucci 2011). In the latter case, a total explosion mass greater than $1.4 M_{\odot}$ may be possible, as discussed in analyses of several recently observed over-luminous SN Ia regarded as potentially Super-Chandrasekhar mass candidates (e.g. SN 2006gz: Hicken et al. 2007, SN 2007if: Scalzo et al. 2010; SN 2009dc: Taubenberger et al. 2011), although the increased intrinsic luminosity of these explosions may be due to other causes and not necessarily due to a greater than Chandrasekhar mass white dwarf merger.

Even after excluding the peculiar SN Ia, which are important to limit from contaminating cosmological studies, the remaining normal $\sim 70\%$ of discovered SN Ia do not have a perfectly narrow luminosity distribution. Because SN Ia do exhibit subtle intrinsic luminosity variation, in lieu of a detailed physical understanding of this process, we use several well studied empirical correlations to account for the fact that SN Ia are not perfect standard candles (e.g. Phillips 1993; Riess et al. 1996;

Perlmutter et al. 1997; Jha et al. 2007). These include correlations between the peak luminosity and shape of the light curve (the brightness of the SN over time), and correlations between the peak brightness and SN colors (brightness differences at different wavelengths), which are used to standardize the observed SN Ia brightness. These form a well studied set of distance-independent clues that allow us to estimate the distance by measuring the SN Ia light curve and colors. As such, SN Ia are more accurately called *standardizeable* candles.

In the decade since the initial discovery of cosmic acceleration with SN Ia, several independent techniques have confirmed the now standard ΛCDM cosmological model (see Frieman et al. 2008a for a review). In the standard ΛCDM model, the dark energy is described by Einstein's cosmological constant Λ, where the energy density of the universe is comprised of roughly 4% normal baryonic matter (protons and neutrons that make up ordinary atoms), 20% dark matter (mass that does not emit light but interacts gravitationally with luminous baryonic matter), and 76% dark energy (a mysterious cosmic anti-gravitational force that results in the acceleration of the expansion of the universe). This is equivalent to a standard cosmological parameter set $\vec{\Omega} = (\Omega_{\rm M}, \Omega_\Lambda, w) = (0.24, 0.76, -1)$, where the matter density is the sum of the contributions from dark matter (Ω_{DM}) and normal baryonic matter (Ω_b), $\Omega_{\rm M} = \Omega_{DM} + \Omega_b = 0.20 + 0.04 = 0.24$, and where $w = -1$ is the equation of state parameter parameterizing the ratio of pressure to density for Einstein's cosmological constant, $\Lambda = (3H_o^2)/(\Omega_\Lambda c^2)$.

Independent cosmological approaches that have provided complementary evidence supporting the SN Ia results include studies of the Large Scale Structure of galaxies with the Sloan Digital Sky Survey (Tegmark et al. 2004), Baryon Acoustic

Oscillations (BAO; Eisenstein et al. 2005), the Integrated Sachs-Wolf effect (ISW; Giannantonio et al. 2008), X-ray cluster distances (Allen et al. 2008), and — arguably of the greatest importance next to SN Ia — space based observations of the Cosmic Microwave Background radiation with the Wilkinson Microwave Anisotropy Probe (WMAP3: Spergel et al. 2007; WMAP5: Dunkley et al. 2009; WMAP7: Larson et al. 2011). All of these — and numerous other independent cosmological techniques — have further confirmed the SN Ia results (See Frieman et al. 2008a for a review). Although many other cosmological techniques are concordant with the SN Ia results, standard candle cosmology with the distance-redshift relation is the best method that *directly* probes the effects of dark energy. For example, the CMB measurements do not measure Ω_Λ directly, but rather $\Omega = \Omega_M + \Omega_\Lambda$, the total mass-energy density, which measures the global geometry and curvature of the universe[4]. While many outstanding problems remain, SN Ia cosmology is both the first and still the best tested cosmological method providing evidence for dark energy. Still, if the astrophysical community had not reached a consensus on the existence of cosmic acceleration through a host of independent techniques yielding results concordant to and consistent with the SN Ia studies, it is safe to say that the 2011 Physics Nobel prize would not have been awarded to the lead authors of the seminal dark energy discovery papers based on the SN Ia results alone (e.g. Riess et al. 1998; Schmidt et al. 1998; Perlmutter et al. 1999).

Although the astrophysical community has provided strong evidence that dark energy causes cosmic acceleration and that dark matter plays a crucial role in the

[4]A FLRW universe can take on one of 3 geometrical configurations depending on the value of Ω: ($\Omega < 1$) open, Hyperbolic saddle-shaped geometry with negative curvature, ($\Omega = 1$) flat, Euclidean geometry with zero curvature, or ($\Omega > 1$) closed, Spherical geometry with positive curvature.

formation of galaxies and galaxy clusters, in each case, the label "dark" merely represents our ignorance. Even in this era of so-called "precision cosmology" we do not understand the physics of over 95% of the observable universe. While the nature of dark matter is still unknown, the unknown physical basis of dark energy is arguably the biggest mystery in modern theoretical physics. In the simplest picture, dark energy is due to a cosmological constant Λ, which is interpreted as a form of "vacuum energy" arising from the quantum mechanical properties of seemingly empty space. In this picture, Λ provides a negative pressure anti-gravitational force that operates over the entire cosmos, causing the expansion of space to accelerate and the average distance between galaxy clusters to increase exponentially. Unfortunately, observational support for dark energy has presented a thus far insurmountable challenge to theoretical physics. Our best fundamental theory of elementary particles, the standard model of particle physics, predicts a "natural" value for Λ that is at least 10^{60} and as many as 10^{120} times larger than the observed value (Weinberg 1989), perhaps the most numerically discrepant prediction in the recent history of science. This "Cosmological Constant Problem" remains one of the most vexing issues in all of theoretical physics. The discovery of dark energy has thus challenged the astrophysics community to reconsider how predictions are extracted from our best physical and cosmological theories. Next generation experiments hope to reveal whether dark energy is a cosmological constant or some other phenomenon, which may vary in time over cosmic history. More than arguably any other factor, the fundamental enigma of dark energy is the driving force motivating the efforts of supernova cosmology community.

1.2 Cosmology With Optical/UV SN Ia Data

Type Ia supernovae observed at optical and ultraviolet wavelengths in the rest frame have played a leading role in extragalactic astronomy and cosmology in the past decade (See Goobar & Leibundgut 2011 for a review). SN Ia have been the key to measuring the Hubble constant (Freedman et al. 2001; Jha et al. 1999; Riess et al. 2005, 2011) and demonstrating cosmic acceleration (Riess et al. 1998; Schmidt et al. 1998; Perlmutter et al. 1999). These discoveries rest on a foundation of photometric and spectroscopic similarities between high and low redshift SN Ia (Hamuy et al. 1996; Riess et al. 1999; Goldhaber et al. 2001; Hook et al. 2005; Blondin et al. 2006; Jha et al. 2006; Conley et al. 2006; Garavini et al. 2007; Garg et al. 2007; Bronder et al. 2007; Foley et al. 2008, 2009b; Ellis et al. 2008). The accelerating universe result has been confirmed out to redshift $z \sim 1$ (Tonry et al. 2003; Knop et al. 2003; Barris et al. 2004; Kowalski et al. 2008; Amanullah et al. 2010). The turnover to the matter-dominated era and the corresponding decelerating expansion at $z > 1$ has been seen by space-based work from *HST* (Riess et al. 2007; Amanullah et al. 2010).

Several current ground based projects including: ESSENCE (Equation of State: SupErNovae trace Cosmic Expansion; Krisciunas et al. 2005b; Miknaitis et al. 2007; Wood-Vasey et al. 2007, Narayan et al. 2012 *in preparation*), SNLS (SuperNova Legacy Survey; Astier et al. 2006; Guy et al. 2007; Kilbinger et al. 2009; Guy et al. 2010; Conley et al. 2011), SDSS-II (Sloan Digital Sky Survey II Supernova Project; Kessler et al. 2009), CSP (Carnegie Supernova Project; Freedman et al. 2009), and the CfA (Harvard-Smithsonian Center for Astrophysics; Hicken et al. 2009a) seek to constrain the nature of the dark energy responsible for cosmic acceleration

by measuring the equation-of-state parameter w with large, homogeneous samples of SN Ia. The quantity and quality of SN Ia observations have finally made it possible to begin testing non-standard cosmological models (e.g. Davis et al. 2007; Sollerman et al. 2009), work which provides a solid counter example to the main — and eminently reasonable — critique of Gopal Vishwakarma & Narlikar 2010 that most SN Ia cosmology is concerned with parameter estimation for an assumed cosmological model (e.g. the Λ-CDM concordance model with cold dark matter and cosmological constant) rather than testing whether a given cosmological model is supported by the data. This critique applies to many papers which compile the available SN Ia low and high-z data sets and assume the standard Λ-CDM concordance model in order to estimate its cosmological parameters $\vec{\Omega}$ more precisely than with previous, smaller samples, or combine the SN Ia results with those from other cosmological techniques (Astier et al. 2006; Kowalski et al. 2008; Guy et al. 2010; Amanullah et al. 2010; Lampeitl et al. 2010). High-z cosmological results all rely upon combining their data with the available low-redshift samples (see §2.1–2.2), with some recent example compilations whimsically named chronicling the continued growth of the high and low-redshift SN Ia data sets, including the Union1: Kowalski et al. 2008 (307 SN Ia), Constitution: Hicken et al. 2009a (397 SN Ia), and Union2: Amanullah et al. 2010 (557 SN Ia) data sets. The CSP have also combined their high-z and low-z optical data sets to produce the first published Hubble diagram using optical I-band observations of SN Ia out to $z \sim 0.7$ (Freedman et al. 2009).

While future studies will have the statistical and systematic power to probe the time variation of dark energy (e.g. $\dot{w}$), searching for evidence of a cosmological model inconsistent with a cosmological constant, our best current high-z data sets,

including ESSENCE, SNLS, SDSS-II, CSP, and studies with HST are all consistent with dark energy described by a cosmological constant, where $w = -1.0$, to better than 0.1 (e.g. 10% uncertainty). However, the dark energy is not necessarily due to the cosmological constant, and finding out what it really is constitutes the principal task for future precise distance-measuring techniques as described by the Report of the Dark Energy Task Force (Albrecht et al. 2006), which emphasized the scientific merit of studies which seek to narrow down the uncertainty contours in the w–$\Omega_{\rm M}$ plane and constrain $\dot{w}$, the time variation of w. Several ongoing or near-term experiments which will all contribute to this goal include ground based projects like the Dark Energy Survey, PanStarrs, and LSST (the Large Synoptic Survey Telescope)[5], along with space experiments including WFIRST (Wide-Field Infrared Survey Telescope; a candidate for the NASA/DOE Joint Dark Energy Mission; JDEM Gehrels 2010), the European Space Agency's EUCLID mission (Beaulieu et al. 2010), and the NASA James Webb Space Telescope (Clampin 2011). See Wood-Vasey 2010 for a review of the future plans and prospects for SN Ia cosmology and dark energy studies.

1.3 Cosmological Advantages of NIR SN Ia

While SN Ia observed at optical wavelengths have been shown to be excellent *standardizeable* candles, using empirical correlations between luminosity, light curve (LC) shape, and color, a growing body of evidence suggests that SN Ia are essentially

[5]Dark Energy Survey: `http://www.darkenergysurvey.org/`
PanStarrs: `http://pan-starrs.ifa.hawaii.edu/public/`
LSST: `http://www.lsst.org/lsst/`

standard candles at NIR wavelengths, even without correction for light-curve shape or reddening (Elias et al. 1985; Meikle 2000; Krisciunas et al. 2004a; Wood-Vasey et al. 2008; Mandel et al. 2009; Folatelli et al. 2010; Mandel et al. 2011; Burns et al. 2011; Friedman et al. 2012 *in preparation*). Furthermore, since longer wavelength NIR light (JHK_s-bands) is $\sim$ 2-12 times less likely to be absorbed or scattered by dust than shorter wavelength optical light ($BVRI$-bands), NIR observations are less sensitive to extinction from dust in the host galaxy of the supernova (Cardelli et al. 1989), which causes the supernova to appear dimmer and farther away than it really is, leading to systematic overestimates of the distance to the galaxy. NIR data is particularly valuable because adding it to optical data helps disentangle one of the most troubling sources of systematic error affecting SN Ia cosmological distance measurements, the confounding effects of dust dimming and intrinsic color variation (e.g Conley et al. 2007; Wood-Vasey et al. 2007). The effect of dust in the SN Ia host galaxy is both to absorb or scatter the light away from the line of sight and produce dimming (extinction), and to preferentially absorb or scatter shorter wavelength "bluer" light, leading to more long wavelength light and a "redder" color compared to what would be observed in the absence of dust (reddening). SN Ia intrinsic colors for objects suffering little reddening do show some intrinsic variation as a function of phase and bandpass (e.g Phillips et al. 1999; Krisciunas et al. 2004b, 2007; Mandel et al. 2011). When we observe a SN Ia with a redder than average color, it is initially ambiguous whether the observed color is a result of reddening by dust or because the object was *intrinsically* red. Because NIR data is relatively immune to the effects of dust compared to optical data, including it allows us to help break this degeneracy between dust extinction and intrinsic color variation.

Accurate and precise distance measurements underpin the construction of the SN Ia Hubble diagram, the fundamental cosmological technique used to measure cosmic expansion history by comparing the measured luminosity distance-redshift relation for a set of objects to the theoretical relation for a given expansion history (See §1.1). With current LC fitting techniques, systematic distance errors from uncertain dust estimates and intrinsic color variation are arguably the most important outstanding problems with generating SN Ia Hubble diagrams for precise cosmological measurements of dark energy with optical data alone (Conley et al. 2007; Wood-Vasey et al. 2007). In addition, some of the major LC fitting methods (e.g. MLCS: Jha et al. 2007 and SALT: Guy et al. 2005; Astier et al. 2006; Guy et al. 2007) do not always give consistent distance estimates for individual objects or consistent cosmological results when applied to the same SN Ia data sets (Kessler et al. 2009). This disagreement is a complex result stemming from differing input assumptions of the methods, most notably in the way the LC fitters model the combination of extinction and reddening by dust and reddening from intrinsic variation of SN Ia colors. Thankfully the inclusion of NIR data helps to break the degeneracy between reddening and intrinsic color and ensure that the distance estimates will be less sensitive to the model assumptions of individual LC fitters, as already demonstrated using a subset of my thesis data (Mandel et al. 2011). Overall, the published subset of my thesis data has already helped confirm and strengthen the claim that SN Ia are more standard in NIR luminosity than at optical wavelengths, less sensitive to dimming by host galaxy dust, and crucial to reducing systematic galaxy distance errors due to the degeneracy between intrinsic supernova color variation and reddening of light by dust, arguably the most dominant source of

systematic error in SN Ia cosmology (Wood-Vasey & Friedman et al. 2008; Mandel, Wood-Vasey, Friedman, & Kirshner 2009; Mandel et al. 2011).

1.4 Previous Results with NIR SN Ia

Cosmological results from SN Ia have historically been based on measurements of optical emission in the SN rest frame, but recent work suggests that SN Ia may be superior standard candles and distance indicators in the NIR, with a narrow distribution of peak JHK_s magnitudes and 4–9 times less sensitivity to reddening than from optical V-band data alone (Meikle 2000; Krisciunas et al. 2004a, 2007; Wood-Vasey et al. 2008; Mandel et al. 2009, 2011). Following a compilation studying the NIR properties of the extant published set of SN Ia by Meikle 2000, pioneering work by Krisciunas et al. (2004a) demonstrated that SN Ia have a narrow range of luminosity in JHK_s at the time of B-band maximum light ($t_{B\mathrm{max}}$) with smaller scatter than the B and V bands. Krisciunas et al. (2004a) found no correlation between optical light-curve shape and intrinsic IR luminosity. For a sample of 16 SN Ia observed in NIR bands, Krisciunas et al. (2004a) found a RMS of $\sigma_J = 0.14$, $\sigma_H = 0.18$, and $\sigma_{K_s} = 0.12$ mag. The NIR behavior is a sharp contrast to optical light curves, where a variety of ingenious methods are used to reduced the scatter in distance estimates: the $\Delta m_{15}(B)$ method (Phillips 1993; Hamuy et al. 1996; Phillips et al. 1999; Prieto et al. 2006), the multicolor light-curve shape method (MLCS; Riess et al. 1996, 1998; Jha et al. 2006, 2007), the "stretch" method (Perlmutter et al. 1997; Goldhaber et al. 2001), the Bayesian Adapted Template Match method (BATM; Tonry et al. 2003), the color-magnitude intercept calibration method

(CMAGIC; Wang et al. 2003), the spectral adaptive template method (SALT; Guy et al. 2005; Astier et al. 2006; Guy et al. 2007), and (SiFTO; Conley et al. 2008), to name a few. As a result, unlike optical Type Ia SN, which are *standardizable* candles — after a great deal of effort — NIR SN Ia appear to be essentially *standard* candles at the $\sim$ 0.15–0.2 mag level or better, depending on the filter (Krisciunas et al. 2004a, 2005a; Wood-Vasey et al. 2008; Mandel et al. 2009, 2011; Folatelli et al. 2010; Burns et al. 2011; Phillips 2011).

While the Krisciunas et al. (2004a) result was determined from a small, inhomogeneous sample of 16 light curves, in WV08, we presented 1087 JHK_s photometric observations of 21 SN Ia, the largest homogeneous low-z training set at the time of its publication, doubling the published sample of objects, and tripling the number of published photometric observations at the time. This NIR data from WV08 and the literature strengthened the evidence that SN Ia are excellent NIR standard candles, especially in the H-band, where distances have an intrinsic RMS of 0.15–0.16 mag, *without applying any light curve shape corrections*, comparable to the scatter in optical data corrected for light curve shape. However, in WV08 we suggested that light curve shape variation, especially in the J-band, might provide additional information for correcting NIR LCs and improving distance determinations. Using a novel hierarchical Bayesian framework, using NIR only data and a model accounting for variations in the J-band LC shape, Mandel et al. 2009 (hereafter M09) further constrain the marginal variances of the NIR peak absolute magnitudes to 0.17 ± 0.03, 0.11 ± 0.03, and 0.19 ± 0.04, for the JHK_s bands, respectively (See Fig. 9 of M09). In particular, variance in the peak H-band absolute magnitudes of 0.11 mag is smaller than in any known method using only optical

data. Recent work by Kattner et al. 2012 analyzing 27 CSP NIR LCs also finds evidence for a non-zero decline rate relation between the peak absolute JH-maxima (and perhaps the Y-band maximum) to the decline rate parameter Δm_{15} (Phillips 1993). This augments the results of Mandel et al. 2009 who also find variation in the intrinsic J-band LC shape which correlates with intrinsic NIR luminosity.

Furthermore, previous work has suggested that the systematic distance errors due to dust extinction, which currently dominate cosmology systematics, are reduced by a factor of $\sim 2-3$ relative to the optical by including NIR data (Krisciunas et al. 2007). To investigate this with modern data sets Mandel et al. 2011 (hereafter M11) present a sophisticated hierarchical Bayesian model and implement the novel BayeSN Markov Chain Monte Carlo computational method to estimate distances (see Fig. 16 of M11) and dust properties (see Fig. 3 of M11) of SN Ia using optical and NIR light curve data, further improving reddening estimates and distance errors (see Figs 17-18 of M11). This approach has inspired further work using Hierarchical Bayesian modeling to constrain cosmological parameters with SN Ia (March et al. 2011, Mandel et al. 2012 *in preparation*). After correcting for NIR LC shape and reddening, M11 also find a minuscule RMS dispersion of ~ 0.11 mag ($\sim 5\%$ in distance) in the combined NIR and optical SN Ia low-z Hubble diagram, compared to ~ 0.15 mag ($\sim 7\%$ in distance) with optical data alone using BayeSN. This is equivalent to a $\sim 60\%$ improvement in the predictive precision (the inverse variance)[6] of individual distance estimates by including JHK_s NIR data compared to optical $BVRI$ data alone using BayeSN. The BayeSN method of M11 models the

[6]The inverse variance of 0.11 mag and 0.15 mag is given by $(0.11/0.15)^2 = 0.55 \sim 60\%$, or a factor of $(0.15/0.11)^2 = 1.85$.

full covariance structure of the observed data set, exploiting multiple informative correlations between light curve properties across all available bandpasses and phases to standardize SN Ia distances. Previous methods using only optical data did not incorporate all the available information in this way. For example, the MLCS method of Jha et al. 2007 found an intrinsic RMS Hubble diagram dispersion of ~ 0.18 mag ($\sim 8\%$ in distance) from optical SN Ia data alone, considerably worse than the 0.15 mag found with BayeSN by M11 using only optical data. In other words, BayeSN provides distances estimates with a predictive precision a factor of ~ 1.4 times better $[(0.18/0.15)^2]$ than MLCS using comparable optical only data sets, whereas BayeSN provides distance estimates with a predictive precision a factor of ~ 2.7 times better $[(0.18/0.11)^2]$ than MLCS by also including NIR data. Following M11, Mandel et al. 2012 *in preparation* will present a refined method for estimating extinction and dust properties for SN Ia with optical and NIR data, including a subset of the additional 104 new NIR SN Ia LCs in CfAIR2 (see §6.3.2).

Furthermore, most previous analyses naively assume that dust in SN Ia host galaxies has similar properties to dust in the Milky Way galaxy ($R_V = 3.1$), a simplifying assumption that introduces additional systematic errors into our distance estimates (Mandel et al. 2009, 2011). Adding NIR to optical SN Ia data allows a much improved simultaneous determination of the host galaxy optical extinction (A_V) and the slope of the dust law (R_V) which characterizes the properties of the dust in each SN Ia host galaxy. The addition of NIR data also helps reduce the sensitivity to the non-trivial assumptions used to model the dust, for example, assuming the same R_V for all SN Ia or assuming R_V is correlated with A_V. Independent R_V and A_V estimates for each object further allows us to constrain the extinction and dust

properties of the SN Ia parent population with the most comprehensive data set to date (Mandel et al. 2011, Friedman et al. 2012 *in preparation*). Uncertainty in our knowledge of the *a priori* host galaxy dust and extinction distributions is a major obstacle to obtaining consistent dark energy constraints with different SN Ia cosmological analysis methods (Jha et al. 2007; Conley et al. 2007; Guy et al. 2007; Wood-Vasey et al. 2007; Hicken et al. 2009a; Kessler et al. 2009).

These results have been further confirmed in recent analyses by the CSP (Folatelli et al. 2010; Burns et al. 2011; Phillips 2011), including published CSP data (Phillips et al. 2007; Taubenberger et al. 2008; Schweizer et al. 2008; Contreras et al. 2010; Stritzinger et al. 2011; Taubenberger et al. 2011), along with results including some currently unpublished CSP data discussed by Phillips 2011. Folatelli et al. (2010) study the effects of including NIR data to help measure host galaxy dust properties and extinction, finding evidence for different host galaxy dust properties for the most highly reddened SN Ia which yield estimates of $R_V \sim 1$–2, as opposed to $R_V \approx 3.2$ for SN Ia with moderate to little extinction, the latter of which is very close to the standard $R_V = 3.1$ value found for average lines of sight through dust in the Milky Way galaxy (Cardelli et al. 1989). M11 also find evidence for a similar trend, specifically modeling and testing for a potential correlation between A_V and R_V, finding strong evidence for a linear trend where R_V decreases for greater A_V, and evidence for $R_V \approx 1.7$ for SN Ia with $A_V \gtrsim 1$ and $R_V \sim 2.4$–2.9 for $A_V \lesssim 0.4$. Both the Folatelli et al. (2010) and M11 studies suggest that the most highly reddened SN Ia may be affected by a different kind of dust, for example circumstellar dust local to the supernova explosion, which has been suggested based on other observational and theoretical work (Wang 2005; Patat et al. 2007; Goobar

2008; Wang et al. 2008, 2009a).

Burns et al. (2011) present SNooPy (SuperNova e Object-Oriented Python LC fitting method used by the CSP to fit the LCs of and derive distance estimates using Optical and NIR SN Ia data in order to produce Hubble diagrams. Following up on the Folatelli et al. (2010) and Burns et al. (2011) studies and unpublished work in progress, Phillips (2011) report intrinsic Hubble diagram dispersions of 0.19, 0.20, and 0.23 mag in YJH, respectively without correcting for host galaxy reddening or NIR LC shape, while they find a marginal improvement with dispersion of 0.17, 0.16, and 0.20 mag in YJH, respectively after correcting for NIR host galaxy reddening and accounting for variations in NIR LC shape. The smaller dispersion of 0.11 mag found by M11 is derived from the fact that the Hierarchical Bayesian approach fits *all* optical and NIR data simultaneously, coherently modeling covariances between absolute magnitude, light curve shape, and color across different bandpasses and between all epochs. Since the Hubble diagram dispersion in the nearby data set is significantly affected by peculiar velocities, the true precision of SN Ia distances with NIR and optical data may be as small as $\sim 3\% - 4\%$, to be measured with future data for more distant SN Ia in galaxies well into the Hubble flow at $z \gtrsim 0.1$. The CSP light curve fitting SNooPy package (Burns et al. 2011) also uses all the available $uBVgriYJH$ data to generate their Hubble diagram, finding a combined Hubble diagram statistical dispersion of 0.06 mag due to measurement error only, which excludes the systematic uncertainties due to peculiar velocities, the error on H_0, errors on calibration parameters of their model, intrinsic SN Ia scatter, and uncertainties due to K-corrections. The M11 dispersion of 0.11 mag includes all known sources of statistical and systematic uncertainty. Combining the CfAIR2 data

set with future high-redshift NIR SN Ia data will reveal the full potential of NIR SN Ia observations as cosmological distance indicators and probes of dark energy.

1.5 Organization of Thesis

This thesis is organized as follows. In §2, we situate the extensive low-redshift NIR data set presented in this thesis with the growing sample of optical (§2.1) and NIR (§2.2) observations of SN Ia in the nearby universe. In §2.5, we describe the characteristics and observing capabilities of PAIRITEL along with our observing strategy for following up SN Ia in JHK_s (§2.6). In §3 we outline the data reduction process for our image creation and photometry pipelines, including mosaic creation, sky subtraction, host galaxy subtraction, our approach to screening out bad images, and our computational infrastructure. In §4, we present tests of the CfAIR2 photometry with PAIRITEL, with particular emphasis on internal calibration with 2MASS field star photometry (§4.1), tests for potential systematic photometric errors (§4.2), and external consistency checks of photometry for objects observed both by PAIRITEL and the CSP (§4.3). In §4.4, we present our final, galaxy subtracted photometry for the CfAIR2 data set. A limited analysis of the properties of the observed data is discussed in §5. Conclusions, previous results, and suggestions for future work are summarized in §6. An appendix of additional mathematical and other details is presented in §7.4.

Chapter 2

Observations

Observations

In §2, we situate the extensive low-redshift CfAIR2 NIR data set presented in this thesis with the growing sample of optical (§2.1) and NIR (§2.2) observations of SN Ia in the nearby universe. In §2.3 we review the current subset of SN Ia with *both* optical and NIR data in this thesis and in the Literature. In §2.4, we discuss the observational campaign we have conduced at the CfA with PAIRITEL to obtain the CfAIR2 NIR SN Ia data set. In §2.5, we further describe the characteristics and observing capabilities of PAIRITEL. In §2.6, we detail our observing strategy for following up SN Ia in JHK_s with PAIRITEL.

2.1 Low-z Optical Light Curves of SN Ia

High redshift SN Ia cosmology rests on a foundation of high quality optical LCs for hundreds of SN Ia in the nearby universe ($z < 0.10$). Pioneering efforts to obtain a significant low-redshift sample were undertaken by Hamuy et al. 1996, who presented LCs for 29 $BVRI$ SN Ia. The Hamuy et al. 1996 local SN Ia sample was the nearby universe anchor used by both the High-Z Team and the Supernova Cosmology Project to discover cosmic acceleration (Riess et al. 1998; Schmidt et al. 1998; Perlmutter et al. 1999). At the Harvard-Smithsonian Center for Astrophysics, the CfA supernova group has continued to dramatically augment the low-z SN Ia sample over the last decade, publishing 22 additional $BVRI$ LCs (CfA1; Riess et al. 1999), 44 $UBVRI$ LCs (CfA2; Jha et al. 2006), and $UBVRIr'i'$ LCs for another 185 objects (CfA3; Hicken et al. 2009b), with additional information published in

Malcolm Hicken's Harvard Astronomy PhD thesis supervised by Professor Robert P. Kirshner (Hicken 2009). In addition, 93 new $UBVRIr'i'$ SN Ia LCs are forthcoming in the more recent CfA4 sample (Hicken et al. 2012 *in preparation*). The combined CfA nearby optical sample of 344 LCs provides the most comprehensive optical data set of its kind to date.

Other notable work producing significant low-z optical data sets include the Lick Observatory Supernova Search (LOSS; Li et al. 2000; Filippenko et al. 2001; Filippenko 2005; Leaman et al. 2011) run through the University of California, Berkeley which recently published $BVRI$ LCs for 165 SN Ia observed over the decade spanning 1998–2008 (Ganeshalingam et al. 2010). At intermediate redshifts ($0.05 < z < 0.35$), the most prominent optical sample of ~ 500 $ugriz$ LCs for spectroscopically confirmed SN Ia comes from the Sloan Digital Sky Survey-II Supernova Survey (SDSS-II; Frieman et al. 2008b). In addition, the Carnegie Supernova Project (CSP; Freedman 2005; Hamuy et al. 2006) has recently published optical $uBgVri$ observations for 35 low-redshift SN Ia (CSP1; Contreras et al. 2010) followed by 50 additional objects (CSP2; Stritzinger et al. 2011) with 5 objects presented elsewhere (SN 2005hk: Phillips et al. 2007, SN 2005bl: Taubenberger et al. 2008, SN 2007sr: Schweizer et al. 2008, SN 2006dd: Stritzinger et al. 2010, and SN 2009dc: Taubenberger et al. 2011, for a total of 88 unique SN Ia observed in the optical bands from 2005–2009[1].

[1]Optical data for SN 2005bl is published in both Taubenberger et al. 2008 and Contreras et al. 2010 so to avoid counting it twice if we exclude it from the 35 objects from Contreras et al. 2010, yielding 34 objects. SN 2009dc is listed as one of the 50 objects in Stritzinger et al. 2011, but its data is actually published in Taubenberger et al. 2011, yielding 49 objects. Including 5 other unique CSP objects (SN 2005hk, SN 2005bl, SN 2007sr, SN 2006dd, and SN 2009dc), this yields 34+49+5=88 total unique CSP SN Ia with optical data as of February 2012.

2.2 Low-z NIR Light Curves of SN Ia

Technological advances in Infrared detector technology have only recently made it possible to obtain high quality NIR photometry for large numbers of SN Ia. In particular, Phillips 2011 provides an excellent recent review of the cosmological and astrophysical results derived from NIR SN Ia observations made over the past 30 years. Early NIR observations of SN Ia were made by Kirshner et al. (1973); Elias et al. (1981, 1985); Frogel et al. (1987), and were particularly challenging due to the limited technology of the time which consisted primarily of single element photon detectors, as opposed to today's digital Infrared arrays with tens or hundreds of thousands of pixels each with dramatically increased detection sensitivity. In addition, the flux contrast between the host galaxy and the SN Ia is typically much smaller in the NIR than at optical wavelengths, making high signal-to-noise observations possible for only the brightest objects in the NIR with detectors available in the 1970s and 1980s. Elias et al. 1985 was both the first work to present a NIR SN Ia Hubble diagram for 6 SN Ia and to use the modern Type Ia nomenclature instead of Type I to distinguish between Type Ia and Type Ib supernovae, which we now believe are core collapse supernovae for stars having lost their outer Hydrogen envelopes (Phillips 2011).

In the late 1990s and early 2000s, Panoramic NIR Arrays finally made it possible to obtain NIR photometry comparable in quantity and quality to optical photometry for nearby SN Ia. The first early-time NIR photometry with modern NIR detectors observed before $t_{B\mathrm{max}}$ (the time of maximum light in the optical B-band) was presented for sn1998bu (Jha et al. 1999; Hernandez et al. 2000).

Since the first peak in the JHK_s-band occurs $\sim$ 3–5 days *before* $t_{B\max}$ (see §5.2.1), depending on the filter, SN Ia must generally be discovered by optical searches at least $\sim$ 5–8 days before $t_{B\max}$ in order to be observed before the NIR maximum, an issue which remains relevant even with modern robotic NIR telescopes (See §2.6). The most comprehensive and pioneering early program to systematically obtain NIR SN Ia photometry was performed in the early 2000s at the Las Campanas Observatory (LCO) in Chile, spearheaded by the work of Krisciunas et al. (2000, 2001, 2003, 2004b,c). Following a compilation studying the NIR properties of the extant published set of SN Ia by Meikle 2000, Krisciunas et al. (2004a) presented the largest Hubble diagram of its kind to date, including 16 SN Ia. Before the first publication of 21 NIR LCs observed by the CfA with PAIRITEL (Wood-Vasey et al. 2007), a handful of other more recent NIR observations, usually for individual or small numbers of SN Ia of particular interest were presented in Krisciunas et al. (2005a, 2006, 2007); Phillips et al. (2006); Pastorello et al. (2007b,a); Stritzinger & Sollerman (2007); Elias-Rosa et al. (2006, 2008); Phillips et al. (2007).

While several hundred nearby SN Ia have been observed at optical wavelengths, there are currently only $\sim$ 120 nearby SN Ia with published NIR observations (Phillips 2011), 21 of which we presented in Wood-Vasey et al. 2008. A fairly comprehensive list of published NIR $YJHK_s$ light curves and compilations using data from modern NIR detectors, including the newest CSP data sets is listed here (Jha et al. 1999; Hernandez et al. 2000; Valentini et al. 2003; Candia et al. 2003; Krisciunas et al. 2000, 2001, 2003, 2004b,c, 2005a, 2006, 2007, 2009; Phillips et al. 2006; Pastorello et al. 2007b,a; Stritzinger & Sollerman 2007; Elias-Rosa et al. 2006, 2008; Phillips et al. 2007; Wood-Vasey et al. 2008; Taubenberger et al.

2008; Schweizer et al. 2008; Contreras et al. 2010; Stritzinger et al. 2010, 2011; Taubenberger et al. 2011).

With the advent in 2005 of CfA observations with PAIRITEL and NIR observations by the CSP, it has finally become possible to compile a low-z NIR sample consisting of hundreds of SN Ia, not yet matching the current optical sample, but significant in its own right. Current work from the CfA Supernova Program uses observations from the robotic 1.3-m Peters Automated Imaging TELescope (PAIRITEL; Bloom et al. 2006) at Mount Hopkins, Arizona. Similar work is underway by the CSP using observations at the Las Campanas Observatory in La Serena, Chile with the 1.0-m Swope telescope and the 2.5-m du Pont telescope (Freedman 2005; Hamuy et al. 2006; see Table 2.1). At the CfA, we have obtained observations of 122 SN Ia at NIR JHK_s wavelengths with PAIRITEL since 2005. 104 of these objects will be presented in Friedman et al. 2012 *in preparation*, comprising the CfAIR2 data set, including 83 new SN Ia LCs and revised photometry for the 21 WV08 SN Ia. After publication of CfAIR2, essentially half of the objects in the published sample of $\sim$ 220 LCs will come from the CfAIR2 data set, with CfAIR2 contributing nearly triple the number of individual published SN Ia photometric observations in JHK_s from all other studies combined and considerably augmenting the published sample of K_s-band observations by a factor of $\sim$ 10. The dramatic contribution to both the extant quantity and quality of NIR SN Ia data constitutes the primary scientific contribution of this thesis.

The CfAIR2 northern hemisphere NIR observations are matched only by the comparable, excellent quality southern hemisphere NIR set acquired by the CSP. Published CSP $YJHK_s$ data includes 74 SN Ia LCs, including 25 from Contreras

et al. 2010, 45 from Stritzinger et al. 2011 and 4 SN Ia of particular interest with NIR observations presented in separate work (SN 2005hk: Phillips et al. 2007, SN 2007sr: Schweizer et al. 2008, SN 2006dd: Stritzinger et al. 2010, SN 2009dc: Taubenberger et al. 2011). Both the CfAIR2 and CSP NIR SN Ia data sets will form the benchmark low-redshift training sets that will help us to establish priors on the distribution of intrinsic SN Ia properties in order to anchor future cosmological use of SN Ia in the NIR (see §6.3.3). The prospect of increasingly large, homogeneous data sets and progress in modeling SN Ia NIR light curves (Kasen 2006) raise hopes that SN Ia, especially in the rest-frame YH bands, can be developed into the most precise and accurate of cosmological distance probes.

While the CfAIR2 data set presents more SN Ia LCs than the CSP data set (104 vs. 74), and includes $\sim$ 3–4 times the number of individual NIR observations than the CSP data set, the CSP photometric uncertainties are typically $\sim 2-3$ times smaller than the photometric uncertainties of the CfAIR2 data (See Table 2.2). With better seeing at LCO vs. FLWO, a better, higher resolution camera on the Swope 1.0-m telescope compared to the old 2MASS south camera on the PAIRITEL-1.3m telescope, and CSP host galaxy template images taken with the 2.5-m du Pont telescope compared to CfAIR2 undersampled template images taken with the 1.3-m PAIRITEL, the CSP NIR photometric precision is generally a factor of $\sim 2-3$ better than PAIRITEL, with typical photometric uncertainties of $\sim$ 0.01–0.03 mag for CSP and $\sim 0.02-0.10$ mag for PAIRITEL (See Table 2.1). As such, what the CSP lacks in quantity compared to CfAIR2, it makes up for in quality. However, one significant advantage of PAIRITEL compared to the CSP NIR observations with the Swope 1.0-m and duPont 2.5-m telescopes, is that the PAIRITEL natural system

photometry is already on the standard 2MASS JHK_s system by virtue of using the former 2MASS northern telescope and 2MASS southern camera. This obviates the need for S-corrections to transform PAIRITEL NIR data to the standard 2MASS JHK_s bands. Since the current spectral NIR sample of SN Ia is still quite limited (Hsiao et al. 2007; Marion et al. 2009) S-corrections to convert other passbands to 2MASS JHK_s based on highly uncertain NIR SN Ia SEDs (e.g. Stritzinger et al. 2002) would result in an additional source of systematic uncertainty which does not affect PAIRITEL data. Overall, the PAIRITEL and CSP data sets are quite complementary, observing mostly different objects and with different frequencies of observations taken in individual NIR bandpasses. Whereas the CfAIR2 PAIRITEL data include comparable numbers of JH observations, with fewer K_s observations that meet our image quality standards (See §3.3), CSP NIR observations primarily use the YJH filters with comparatively little data in the K_s-band. As such, the CSP Y-band observations form a unique data set unmatched elsewhere, including the CfA, which do not have Y-band filters on telescopes at FLWO. Conversely, CfAIR2 presents a significantly larger K_s-band data set than the CSP observations in that bandpass. In more detail, the combined CSP NIR data for 74 SN Ia includes 826, 739, 674, and 103 LC epochs in $YJHK_s$, respectively, for a total of 2365 individual NIR photometric observations in $YJHK_s$ (See Table 2.2). The CfAIR2 data set includes 1583, 1514, and 1172 LC epochs in JHK_s, respectively for a total of 4269 individual NIR photometric observations JHK_s (See Table 2.2). The CfAIR2 and CSP NIR data sets also contain concurrent overlapping photometry for 19 SN Ia which we present in §4.3.2.

Table 2.1: PAIRITEL and CSP Instrument Specifications

Project	Telescope	Mirror Diameter	Camera	Pixel Size	FOV	Image FWHM	Under -sampled	Refs[a]
CfAIR2	PAIRITEL	1.3-m	2MASS South	2.0 ″	8.53′	$\sim 2.5 - 3.0''$	Yes	1,2
CSP	Swope	1.0-m	RetroCam	0.54 ″	3.4′	$\sim 1.0 - 2.0''$	No	3,4
CSP	duPont	2.5-m	WIRC	0.196 ″	3.3′	$\sim 0.5 - 0.8''$	No	3,4

[a] (1) Skrutskie et al. 2006; (2) Wood-Vasey et al. 2008; (3) Hamuy et al. 2006; (4) Contreras et al. 2010

Table 2.2: PAIRITEL and CSP NIR Data Census

Project	SN Ia[a]	NIR[b]	Y^b	J^b	H^b	${K_s}^b$	σ [mag][c]
CfAIR2	104	4269	0	1583	1514	1172	$\sim 0.02 - 0.10$
CSP	74	2365	826	739	674	103	$\sim 0.01 - 0.03$

(*a*) Number of SN Ia with NIR YJH or K_s observations in CfAIR2 (Friedman et al. 2012 *in preparation*) or CSP (Contreras et al. 2010; Stritzinger et al. 2011; Phillips et al. 2007; Schweizer et al. 2008; Taubenberger et al. 2011; Stritzinger et al. 2010); (*b*) Number of epochs of photometry.; (*c*) Typical SN photometric magnitude uncertainties.

2.3 Low-z SN Ia with Optical & NIR Observations

344 SN Ia have been optically observed at the CfA since 1998, including the CfA1 (Riess et al. 1999; 22 SN Ia), CfA2 (Jha et al. 2006; 44 SN Ia), CfA3 (Hicken 2009; Hicken et al. 2009a,b; 185 SN Ia), and CfA4 (Hicken et al. 2012 *in preparation*; 93 SN Ia) data sets. 139 SN Ia LCs, including the 66 SN Ia observed in the CfA1/CfA2 samples and the first 73 SN Ia in the CfA3 sample pre-date the first PAIRITEL observations, which began shortly after the PAIRITEL Supernova Program became active in January 2005 (See §2.5). We thus could not obtain PAIRITEL NIR observations for all 344 SN Ia optically observed at the CfA in the past 13 years. However, of the 205 optical SN Ia LCs obtained by the CfA since 2005 (112 CfA3 SN Ia and all 93 CfA4 SN Ia), 108 SN Ia also have PAIRITEL observations.

Similarly, of the 122 nearby SN Ia observed by PAIRITEL since 2005, 108 have complementary CfA optical light curves along with 4 SN Ia observed by other groups (SN 2005cc, SN F20080514-002: KAIT; Ganeshalingam et al. 2010) and (SN 2005bl, SN 2005bo: CSP; Contreras et al. 2010 and KAIT; Ganeshalingam et al. 2010). All told, of the 122 PAIRITEL LCs, complementary optical data exists for 112 SN Ia. Overall, of the 200 SN Ia from the literature and CfAIR2 with NIR data, 191 have existing optical data from the CfA, CSP, or KAIT/LOSS, or other groups.

2.4 CfA NIR SN Ia Observations with PAIRITEL

The ongoing project that produced my thesis data set began in 2005 and has continued to build a large, homogeneous, data set of SN Ia observations at NIR wavelengths. Our NIR photometric data is obtained primarily through PAIRITEL, the f/13.5 1.3-meter Peters Automated Infrared Imaging TELescope at the Fred Lawrence Whipple Observatory (FLWO) on Mount Hopkins, Arizona (Bloom et al. 2006). The CfAIR2 data set presented in this paper includes 4269 JHK_s-band photometric measurements[2] of 104 nearby SN Ia obtained from 2005 to 2011 using the f/13.5 1.3-m PAIRITEL (See Table 2.3 and Table 4.3). CfAIR2 includes

[2]Astronomical images with modern telescopes are recorded with electronic detectors instead of photographic film or plates. Detectors include charge coupled devices (CCD) for optical observations or similar Infrared Array detectors for Near-Infrared observations. Photometry is the measurement of the brightness of astronomical objects from those images observed through a particular filter or bandpass that only allows the transmission a wavelength dependent fraction of light over a specific range of wavelengths. By performing photometry on a time-series of images, we compile a sequence of brightness measurements of the object that we call its light curve for that band. NIR light is comprised of photons with wavelengths in the range of 0.7–5 microns, slightly longer than for optical light with visible wavelengths of 0.4–0.7 microns. Standard NIR filters in astronomy include the 2MASS JHK_s band filters with central wavelengths of 1.25, 1.65 and 2.17 microns, respectively (Skrutskie et al. 2006).

improved photometry for the subset of 21 SN Ia presented in Wood-Vasey et al. 2008 (hereafter WV08), including additional observations not published in WV08 for the same SN Ia, all processed homogeneously using an upgraded mosaic and photometry pipeline (See §3). PAIRITEL data for 18 additional SN Ia are not included in CfAIR2 because we either have yet to obtain host galaxy template observations or have not achieved the desired photometric accuracy and precision (See §4). Table 2.3 presents the general properties of the 104 CfAIR2 SN Ia, including the IAUC SN Name, the epoch 2000 celestial coordinates, the name and morphology of the Host Galaxy (where available), the heliocentric redshift $z_{\rm helio}$, along with the optical discovery references.

Overall, since 2005, we have observed 172 SN of all types with PAIRITEL. In addition to the 122 observed SN Ia, we have also obtained extensive NIR observations of 49 SN of other types, including, 27 SN Ib/c, 20 SN II, and 2 SN of unknown type (See Table 2.4). The first published PAIRITEL supernova observations were of the unusual core-collapse object SN 2005bf (Tominaga et al. 2005). Other PAIRITEL publications for individual core collapse supernovae of interest include the Type Ic SN 2006aj associated with GRB 060218 (Kocevski et al. 2007; also see Modjaz et al. 2006), the peculiar SN Ib/c core collapse object SN 2006jc (Modjaz 2007), and the Type Ib SN 2008D associated with the *Swift* X-ray transient XRT 080109 (Modjaz et al. 2009). PAIRITEL observations published for individual SN Ia of interest include the normal SN Ia SN 2005cf (Wang et al. 2009b) and the peculiar SN Ia SN 2008ha (Foley et al. 2009a). We published a compilation of 21 NIR SN Ia LCs in Wood-Vasey et al. (2008), which were analyzed with other available low-z Optical and NIR data sets (Mandel et al. 2009, 2011). CfAIR2 presents revised

photometry for these 21 objects (with the exception of SN 2005cf). Most recently, we submitted for publication PAIRITEL NIR data for the Type IIb SN 2011dh in M51 (Marion et al. 2012 *in preparation*). A subset of the SN Ib/c observed by PAIRITEL was presented in Maryam Modjaz's[3] PhD thesis supervised by Professor Kirshner (Modjaz 2007). PAIRITEL NIR Photometry compilations for supernova types other than SN Ia will be published in forthcoming work including SN Ib/c (Modjaz et al. 2012 *in preparation*) and SN II (Marion et al. 2012 *in preparation*).

PAIRITEL NIR photometry is a crucial component of the extensive multi-wavelength supernova effort at the CfA. The PAIRITEL SN Project is the NIR branch of the CfA Supernova Program maintained with support from the CfA, the Smithsonian Astrophysical Observatory (SAO), FLWO, and the University of California, Berkeley (UCB). This ongoing project aims to follow-up nearby supernovae as they are discovered and obtain well sampled, high signal-to-noise NIR LCs of hundreds of nearby, low-redshift SN in JHK_s. At the CfA we routinely obtain extensive complementary optical data sets for these objects using other telescopes and instruments at FLWO and elsewhere. Whenever possible, PAIRITEL NIR data are observed in conjunction with contemporaneous optical photometry at the FLWO 1.2-m, optical spectroscopy at the 1.5-m Tillinghast telescope with the FAST spectrograph, and with late time spectroscopy at the MMT (Matheson et al. 2008; Hicken 2009; Hicken et al. 2009b, Hicken et al. 2012 *in preparation*). By obtaining concurrent optical photometry and spectroscopy for many objects observed with PAIRITEL, we considerably increase the value of the CfAIR2 data set.

[3]Dr. Maryam Modjaz is now an Assistant Professor in Astrophysics at the Center for Cosmology and Particle Physics of the NYU Physics department.

We also frequently collaborate with other teams including *Swift*, Pan-STARRS, and HST to follow-up specific SN of all types. For interesting SN Ia, we also occasionally coordinate PAIRITEL JHK_s photometry with NIR spectroscopy using the SpeX instrument on the NASA Infrared Telescope Facility (IRTF) 3.0-m telescope on Mauna Kea, Hawaii (See Marion et al. 2009; Marion & collaborators 2011). In support of my thesis project, I have authored or been a member on several successful telescope proposals designed to maintain and expand programs to observe nearby SN Ia with ground-based Infrared telescopes photometrically with PAIRITEL and spectroscopically with IRTF. Coordinated PAIRITEL photometry and NIR spectroscopy with other instruments can be used to test physical models of SN Ia (e.g. Kasen 2006), and look for NIR spectral features that correlate with SN Ia luminosity, helping to better standardize SN Ia as cosmological distance indicators, similar to what has already been demonstrated with optical spectra (Bailey et al. 2009; Blondin et al. 2011).

Table 2.3:: General Properties of 122 PAIRITEL SN Ia

SN[a]	RA[b]	DEC[b]	Host[c]	Morphology[d]	$z_{\rm helio}$[e]	Discovery[c]	Discovery Group[f]
05ao	266.20653	61.90786	NGC 6462	SABbc	0.0384	CBET 115	POSS
05ak	220.13320	3.50999	Anon	···	0.0274	CBET 110	POSS
05bl	181.05098	20.40683	NGC 4070	E	0.0241	IAUC 8512	LOSS; POSS
05bo	192.42099	-11.09663	NGC 4708	SA(r)ab pec?	0.0137	CBET 141	POSS
05cc	209.27019	41.84477	NGC 5383	(R')SB(rs)b:pec	0.0076	CBET 154	POSS
05cf	230.38906	-7.44874	MCG -01-39-3	S0 pec	0.0065	CBET 158	LOSS
05ch	215.52815	1.99316	Anon	···	0.0270	CBET 166	ROTSE-III
05el	77.95316	5.19417	NGC 1819	SB0	0.0149	CBET 233	LOSS
05eq	47.20575	-7.03332	MCG -01-9-6	SB(rs)cd?	0.0290	IAUC 8608	LOSS
05eu	36.93011	28.17698	Anon	···	0.0341	CBET 242	LOSS
05hf	21.77516	19.11660	Anon	···	0.0431	IAUC 8622	ROTSE-III
05hk	6.96187	-1.19819	UGC 272	SAB(s)d	0.0130	IAUC 8625	SDSS-II; LOSS
05iq	359.63517	-18.70914	MCG -03-1-8	Sa	0.0340	IAUC 8628	LOSS
05ke	53.76810	-24.94412	NGC 1371	(R')SAB(r'l)a	0.0049	IAUC 8630	LOSS
05ls	43.56630	42.72480	MCG +07-7-1	Spiral	0.0211	IAUC 8643	Armstrong
05mc	126.77605	21.64609	UGC 4414	(R')SB0/a(s)	0.0252	CBET 331	THCA
05na	105.40287	14.13304	UGC 3634	SB(r)a	0.0263	CBET 350	POSS
06D	193.14111	-9.77519	MCG -01-33-34	SAB(s)ab pec?	0.0086	CBET 362	BRASS
06E	208.36880	5.20619	NGC 5338	SB0	0.0027	CBET 363	POSS; LOSS; CROSS
06N	92.13021	64.72362	MCG +11-8-12	···	0.0143	CBET 375	Armstrong
06X	185.72471	15.80888	NGC 4321	SAB(s)bc	0.0053	IAUC 8667	Suzuki; CROSS
06ac	190.43708	35.06872	NGC 4619	SB(r)b pec?	0.0231	IAUC 8669	LOSS
06ax	171.01434	-12.29156	NGC 3663	SA(rs)bc pec	0.0167	CBET 435	LOSS
06az	183.06059	56.17957	NGC 4172	S?	0.0309	IAUC 8691	POSS
06bq	279.99460	39.98217	NGC 6685	S0-	0.0219	CBET 479	POSS
06cp	184.81198	22.42723	UGC 7357	SAB(s)c	0.0223	CBET 524	LOSS
06cz	222.15254	-4.74193	MCG -01-38-2	SA(s)cd?	0.0418	IAUC 8721	LOSS
06gr	338.09445	30.82871	UGC 12071	SBb	0.0346	CBET 638	LOSS
06is	79.39300	-23.78120	Anon	···	0.0314	CBET 659	LOSS
06le	75.17457	62.25525	UGC 3218	SAb	0.0174	CBET 700	LOSS
06lf	69.62286	44.03379	UGC 3108	S?	0.0132	CBET 704	LOSS
06mq	121.55157	-27.56262	ESO 494-G26	SAB(s)b pec	0.0032	CBET 721	LOSS
07S	150.13010	4.40702	UGC 5378	Sb	0.0139	CBET 825	POSS
07bj	245.54405	-1.51428	NGC 6172	E+	0.0167	CBET 930	POSS

(a) Non-IAUC SN Name abbreviations in **bold**: **snf02**=snf20080514-002, **snf00**=snf20080522-000, **snf01**=snf20080522-011, **psb26**=snpsb26, **10bjs**=snPTF10bjs, **10icb**=snPTF10icb

(b) SN RA, DEC positions [in decimal degrees] are best fit SN centroid positions appropriate for forced photometry (e.g. DoPHOT) at fixed coordinates (see §4.2.5, §7.2).

(c) Host Galaxy Names, discovery references, and discovery group/individual credits from IAUC List of Supernovae: http://www.cbat.eps.harvard.edu/lists/Supernovae.html. (+ ≡ et al.).

(d) Host galaxy morphologies taken from the NASA/IPAC Extragalactic Database (NED; http://ned.ipac.caltech.edu/) where available. Anonymous host galaxies in NED (Anon) or hosts with unknown morphologies are denoted by ···

(e) Heliocentric redshifts $z_{\rm helio}$ are from NED. Otherwise, redshifts are from CfA optical spectra or IAUC/ATEL/CBET discovery references.

(f) References/URLs: LOSS: Lick Observatory Supernova Search (see Li et al. 2000; Filippenko 2005, and references therein); Tenagra II (`http://www.tenagraobservatories.com/Discoveries.htm`); ROTSE-III (Quimby 2006); POSS: Puckett Observatory Supernova Search (`http://www.cometwatch.com/search.html`); BRASS: (`http://brass.astrodatabase.net`); SDSS-II: Sloan Digital Sky Survey II (Frieman et al. 2008b); CSS: Catalina Sky Survey (`http://www.lpl.arizona.edu/css/`); SNF: Nearby Supernova Factory (`http://snfactory.lbl.gov/`); CHASE: CHilean Automatic Supernova sEarch (`http://www.das.uchile.cl/proyectoCHASE/`); CRTS: Catalina Real-Time Transient Survey (`http://crts.caltech.edu/`); Itagaki (`http://www.k-itagaki.jp/`); Boles: Coddenham Astronomical Observatory, U.K. (`http://www.coddenhamobservatories.org/`); CROSS (`http://wwww.cortinasetelle.it/snindex.htm`); LSSS: La Sagra Sky Survey (`http://www.minorplanets.org/OLS/LSSS.html`); PASS: Perth Automated Supernova Search (`http://www.perthobservatory.wa.gov.au/research/spps.html`); Williams 1997); PIKA: Comet and Asteroid Search Program (`http://www.observatorij.org/Pika.html`); PanStarrs: (`http://pan-starrs.ifa.hawaii.edu/public/`); THCA Supernova Survey (`http://www.thca.tsinghua.edu.cn/en/index.php/TUNAS`)

Continued on Next Page...

Table 2.3 – Continued

SN[a]	RA[b]	DEC[b]	Host[c]	Morphology[d]	$z_{\rm helio}$[e]	Discovery[c]	Discovery Group[f]
07bz	194.22395	22.37313	IC 3918	SC	0.0218	CBET 941	SNF
07ca	202.77451	-15.10175	MCG -02-34-61	Sc pec sp	0.0141	CBET 945	LOSS
07co	275.76493	29.89715	MCG +05-43-16	···	0.0270	CBET 977	Nicolas
07cq	333.66839	5.08017	Anon	···	0.0262	CBET 983	POSS
07fb	359.21827	5.50886	UGC 12859	Sbc	0.0180	CBET 992	LOSS
07hj	345.44869	15.58642	NGC 7461	SB0	0.0141	CBET 1048	LOSS
07if	17.71421	15.46103	Anon	···	0.0742	CBET 1059	ROTSE-III
07ir	38.42500	37.66909	UGC 2033	SB(s)b	0.0352	CBET 1067	LOSS
07kk	55.59698	39.24178	UGC 2828	SB(rs)bc	0.0410	CBET 1096	LOSS
07le	354.70186	-6.52269	NGC 7721	SA(s)c	0.0067	CBET 1100	Monard
07nq	14.38999	-1.38874	UGC 595	E	0.0450	CBET 1106	ROTSE-III
07qe	358.55408	27.40916	Anon	···	0.0240	CBET 1138	ROTSE-III
07rx	355.04908	27.42097	Anon	···	0.0301	CBET 1157	ROTSE-III
07sr	180.46995	-18.97269	NGC 4038	SB(s)m pec	0.0054	CBET 1172	CSS
07ss	190.27548	50.39138	NGC 4617	Sb	0.0155	CBET 1175	Ichimura
07sw	183.40384	46.49343	UGC 7228	···	0.0252	CBET 1185	ROTSE-III
07ux	152.33324	14.99249	Anon	···	0.0309	CBET 1187	LOSS
08A	24.57248	35.37029	NGC 634	Sa	0.0165	CBET 1193	Ichimura
08C	104.29794	20.43723	UGC 3611	S0/a	0.0166	CBET 1195	POSS
08Z	145.81364	36.28439	Anon	···	0.0210	CBET 1243	POSS
08ae	149.01322	10.49965	IC 577	S?	0.0301	CBET 1248	POSS
08af	224.86846	16.65325	UGC 9640	E	0.0335	CBET 1248	Boles
08ar	186.15826	10.83797	IC 3284	SBa(r)	0.0261	CBET 1273	ROTSE-III
snf02	202.30350	11.27236	UGC 8472	S0	0.0221	ATEL 1532	SNF
snf00	204.19796	5.14200	SDSS?	···	0.0472	SNF	SNF
snf11	229.99519	4.90454	SDSS?	···	0.0397	SNF	SNF
08dg	8.79716	23.25406	Anon	···	0.0430	CBET 1409	CSS
08fr	17.95488	14.64068	Anon	···	0.0490	CBET 1513	ROTSE-III
08fv	154.23873	73.40986	NGC 3147	SA(rs)bc	0.0093	CBET 1520	Itagaki
08fx	32.89166	23.87998	Anon	···	0.0590	CBET 1523	CSS
08gb	44.48821	46.86566	UGC 2427	Sbc	0.0376	CBET 1527	POSS
08gl	20.22829	4.80531	UGC 881	E	0.0340	CBET 1545	CHASE
08ha	353.71951	18.22659	UGC 12682	Im	0.0046	CBET 1567	POSS
08hj	1.00869	-11.16846	MCG -02-1-14	SB(rs)c?	0.0379	CBET 1579	POSS
08hm	51.79540	46.94421	2MFGC 02845	Spiral	0.0197	CBET 1586	LOSS

(a) Non-IAUC SN Name abbreviations in **bold**: **snf02**=snf20080514-002, **snf00**=snf20080522-000, **snf01**=snf20080522-011, **psb26**=snpsb26, **10bjs**=snPTF10bjs, **10icb**=snPTF10icb

(b) SN RA, DEC positions [in decimal degrees] are best fit SN centroid positions appropriate for forced photometry (e.g. DoPHOT) at fixed coordinates (see §4.2.5, §7.2).

(c) Host Galaxy Names, discovery references, and discovery group/individual credits from IAUC List of Supernovae: http://www.cbat.eps.harvard.edu/lists/Supernovae.html. (+ ≡ et al.).

(d) Host galaxy morphologies taken from the NASA/IPAC Extragalactic Database (NED; http://ned.ipac.caltech.edu/) where available. Anonymous host galaxies in NED (Anon) or hosts with unknown morphologies are denoted by ···

(e) Heliocentric redshifts $z_{\rm helio}$ are from NED. Otherwise, redshifts are from CfA optical spectra or IAUC/ATEL/CBET discovery references.

(f) References/URLs: LOSS: Lick Observatory Supernova Search (see Li et al. 2000; Filippenko 2005, and references therein); Tenagra II (`http://www.tenagraobservatories.com/Discoveries.htm`); ROTSE-III (Quimby 2006); POSS: Puckett Observatory Supernova Search (`http://www.cometwatch.com/search.html`); BRASS: (`http://brass.astrodatabase.net`); SDSS-II: Sloan Digital Sky Survey II (Frieman et al. 2008b); CSS: Catalina Sky Survey (`http://www.lpl.arizona.edu/css/`); SNF: Nearby Supernova Factory (`http://snfactory.lbl.gov/`); CHASE: CHilean Automatic Supernova sEarch (`http://www.das.uchile.cl/proyectoCHASE/`); CRTS: Catalina Real-Time Transient Survey (`http://crts.caltech.edu/`); Itagaki (`http://www.k-itagaki.jp/`); Boles: Coddenham Astronomical Observatory, U.K. (`http://www.coddenhamobservatories.org/`); CROSS (`http://wwww.cortinasetelle.it/snindex.htm`); LSSS: La Sagra Sky Survey (`http://www.minorplanets.org/OLS/LSSS.html`); PASS: Perth Automated Supernova Search (`http://www.perthobservatory.wa.gov.au/research/spps.html`); Williams 1997); PIKA: Comet and Asteroid Search Program (`http://www.observatorij.org/Pika.html`); PanStarrs: (`http://pan-starrs.ifa.hawaii.edu/public/`); THCA Supernova Survey (`http://www.thca.tsinghua.edu.cn/en/index.php/TUNAS`)

Continued on Next Page...

Table 2.3 – Continued

SN[a]	RA[b]	DEC[b]	Host[c]	Morphology[d]	$z_{\rm helio}$[e]	Discovery[c]	Discovery Group[f]
08hs	36.37335	41.84311	NGC 910	E+	0.0173	CBET 1598	LOSS
08hv	136.89178	3.39240	NGC 2765	S0	0.0125	CBET 1601	CHASE
08hy	56.28442	76.66533	IC 334	S?	0.0085	CBET 1608	POSS
09D	58.59495	-19.18194	MCG -03-10-52	Sb	0.0250	CBET 1647	LOSS
09Y	220.59865	-17.24675	NGC 5728	(R1)SAB(r)a	0.0093	CBET 1684	PASS; LOSS
09ad	75.88914	6.66000	UGC 3236	Sbc	0.0284	CBET 1694	POSS
09al	162.84201	8.57833	NGC 3425	S0	0.0221	CBET 1705	CSS
09an	185.69715	65.85145	NGC 4332	SB(s)a	0.0092	CBET 1707	Cortini+; Paivinen
09bv	196.83538	35.78433	MCG +06-29-39	···	0.0367	CBET 1741	PIKA
09dc	237.80042	25.70790	UGC 10064	S0	0.0214	CBET 1762	POSS
09do	188.74310	50.85108	NGC 4537	S	0.0397	CBET 1778	LOSS; POSS
09ds	177.26706	-9.72892	NGC 3905	SB(rs)c	0.0192	CBET 1784	Itagaki
09fw	308.07711	-19.73336	ESO 597-6	SA(rs)0-?	0.0282	CBET 1836	CHASE
09fv	247.43430	40.81153	NGC 6173	E	0.0293	CBET 1834	POSS
09ig	39.54843	-1.31257	NGC 1015	SB(r)a	0.0088	CBET 1918	LOSS
09im	53.34204	-4.99903	NGC 1355	S0 sp	0.0131	CBET 1925	Itagaki
09jr	306.60846	2.90889	IC 1320	SB(s)b?	0.0165	CBET 1964	Arbour
09kk	57.43441	-3.26447	2MFGC 03182	···	0.0129	CBET 1991	CSS
09kq	129.06316	28.06711	MCG +05-21-1	Spiral	0.0116	CBET 2005	POSS
09le	32.32152	-23.41242	ESO 478-6	Sbc	0.0178	CBET 2022	CHASE
09lf	30.41513	15.33290	Anon	···	0.0450	CBET 2023	CSS
09na	161.75577	26.54364	UGC 5884	SA(s)b	0.0210	CBET 2098	POSS
10H	121.60082	1.03585	IC 494	SA0	0.0152	CBET 2130	LOSS
10Y	162.76658	65.77966	NGC 3392	E?	0.0109	CBET 2168	Cortini
psb26	160.67450	58.84392	Anon	···	0.0313	PanStarrs	PanStarrs
10bjs	195.29655	53.81604	MCG +09-21-83	···	0.0300	ATEL 2453	PTF
10ag	255.97330	31.50152	UGC 10679	Sb(f)	0.0338	CBET 2195	POSS
10ai	194.84999	27.99646	Anon	E	0.0184	CBET 2200	ROTSE-III; Itagaki
10cr	202.35442	11.79637	NGC 5177	S0	0.0216	CBET 2281	Itagaki; PTF
10dl	323.75440	-0.51345	IC 1391	···	0.0300	CBET 2296	CSS
10icb	193.70484	58.88198	Anon	···	0.0086	ATEL 2657	PTF
10dw	230.66775	-5.92125	Anon	···	0.0381	CBET 2310	PIKA
10ew	279.29933	30.63026	CGCG 173-018	S	0.0255	CBET 2345	POSS
10ex	345.04505	26.09894	CGCG 475-019	Compact	0.0228	CBET 2348	Ciabattari+
10gn	259.45832	40.88128	Anon	Disk Gal	0.0300	ATEL 2720	PTF

(a) Non-IAUC SN Name abbreviations in **bold**: **snf02**=snf20080514-002, **snf00**=snf20080522-000, **snf01**=snf20080522-011, **psb26**=snpsb26, **10bjs**=snPTF10bjs, **10icb**=snPTF10icb

(b) SN RA, DEC positions [in decimal degrees] are best fit SN centroid positions appropriate for forced photometry (e.g. DoPHOT) at fixed coordinates (see §4.2.5, §7.2).

(c) Host Galaxy Names, discovery references, and discovery group/individual credits from IAUC List of Supernovae: http://www.cbat.eps.harvard.edu/lists/Supernovae.html. (+ ≡ et al.).

(d) Host galaxy morphologies taken from the NASA/IPAC Extragalactic Database (NED; http://ned.ipac.caltech.edu/) where available. Anonymous host galaxies in NED (Anon) or hosts with unknown morphologies are denoted by ···

(e) Heliocentric redshifts $z_{\rm helio}$ are from NED. Otherwise, redshifts are from CfA optical spectra or IAUC/ATEL/CBET discovery references.

(f) References/URLs: LOSS: Lick Observatory Supernova Search (see Li et al. 2000; Filippenko 2005, and references therein); Tenagra II (`http://www.tenagraobservatories.com/Discoveries.htm`); ROTSE-III (Quimby 2006); POSS: Puckett Observatory Supernova Search (`http://www.cometwatch.com/search.html`); BRASS: (`http://brass.astrodatabase.net`); SDSS-II: Sloan Digital Sky Survey II (Frieman et al. 2008b); CSS: Catalina Sky Survey (`http://www.lpl.arizona.edu/css/`); SNF: Nearby Supernova Factory (`http://snfactory.lbl.gov/`); CHASE: CHilean Automatic Supernova sEarch (`http://www.das.uchile.cl/proyectoCHASE/`); CRTS: Catalina Real-Time Transient Survey (`http://crts.caltech.edu/`); Itagaki (`http://www.k-itagaki.jp/`); Boles: Coddenham Astronomical Observatory, U.K. (`http://www.coddenhamobservatories.org/`); CROSS (`http://wwww.cortinasetelle.it/snindex.htm`); LSSS: La Sagra Sky Survey (`http://www.minorplanets.org/OLS/LSSS.html`); PASS: Perth Automated Supernova Search (`http://www.perthobservatory.wa.gov.au/research/spps.html`); Williams 1997); PIKA: Comet and Asteroid Search Program (`http://www.observatorij.org/Pika.html`); PanStarrs: (`http://pan-starrs.ifa.hawaii.edu/public/`); THCA Supernova Survey (`http://www.thca.tsinghua.edu.cn/en/index.php/TUNAS`)

Continued on Next Page...

Table 2.3 – Continued

SN[a]	RA[b]	DEC[b]	Host[c]	Morphology[d]	$z_{\rm helio}$[e]	Discovery[c]	Discovery Group[f]
10it	55.48965	-4.70584	NGC 1417	SAB(rs)b	0.0137	CBET 2498	LOSS
10iw	131.31205	27.82325	UGC 4570	SABdm	0.0215	CBET 2505	CSS
10jm	56.51525	12.70477	Anon	···	0.0231	CBET 2537	LSSS
10ju	85.48321	18.49746	UGC 3341	SBab	0.0152	CBET 2549	LOSS
10jv	111.86051	33.81143	NGC 2379	SA0	0.0135	CBET 2549	LOSS
10kg	70.03505	7.34995	NGC 1633	SAB(s)ab	0.0166	CBET 2561	LOSS
10ko	83.20592	-14.09628	NGC 1954	SA(rs)bc pec	0.0104	CBET 2569	Leonini
10lq	128.16968	-24.04593	ESO 495-16	S0-a	0.0264	CBET 2613	Leonini+
11B	133.95016	78.21693	NGC 2655	SAB(s)0/a	0.0047	CBET 2625	Itagaki
11K	71.37662	-7.34808	Anon	···	0.0145	CBET 2636	CSS
11aa	114.17727	74.44319	UGC 3906	S	0.0125	CBET 2653	POSS
11ae	178.70514	-16.86280	MCG -03-30-19	···	0.0060	CBET 2658	CSS
11ao	178.46267	33.36277	IC 2973	SB(s)d	0.0107	CBET 2669	POSS
11at	142.23977	-14.80573	MCG -02-24-27	SB(s)d	0.0068	CBET 2676	POSS
11ay	105.64134	50.59055	NGC 2315	S0/a	0.0210	CBET 2678	LOSS
11by	178.93951	55.32592	NGC 3972	SA(s)bc	0.0028	CBET 2708	Jin+
11de	235.97179	67.76196	UGC 10018	(R')SB(s)bc	0.0292	CBET 2728	POSS
11df	291.89008	54.38632	NGC 6801	SAcd	0.0145	CBET 2729	POSS

(a) Non-IAUC SN Name abbreviations in **bold**: **snf02**=snf20080514-002, **snf00**=snf20080522-000, **snf01**=snf20080522-011, **psb26**=snpsb26, **10bjs**=snPTF10bjs, **10icb**=snPTF10icb

(b) SN RA, DEC positions [in decimal degrees] are best fit SN centroid positions appropriate for forced photometry (e.g. DoPHOT) at fixed coordinates (see §4.2.5, §7.2).

(c) Host Galaxy Names, discovery references, and discovery group/individual credits from IAUC List of Supernovae: http://www.cbat.eps.harvard.edu/lists/Supernovae.html. (+ ≡ et al.).

(d) Host galaxy morphologies taken from the NASA/IPAC Extragalactic Database (NED; http://ned.ipac.caltech.edu/) where available. Anonymous host galaxies in NED (Anon) or hosts with unknown morphologies are denoted by ···

(e) Heliocentric redshifts $z_{\rm helio}$ are from NED. Otherwise, redshifts are from CfA optical spectra or IAUC/ATEL/CBET discovery references.

(f) References/URLs: LOSS: Lick Observatory Supernova Search (see Li et al. 2000; Filippenko 2005, and references therein); Tenagra II (`http://www.tenagraobservatories.com/Discoveries.htm`); ROTSE-III (Quimby 2006); POSS: Puckett Observatory Supernova Search (`http://www.cometwatch.com/search.html`); BRASS: (`http://brass.astrodatabase.net`); SDSS-II: Sloan Digital Sky Survey II (Frieman et al. 2008b); CSS: Catalina Sky Survey (`http://www.lpl.arizona.edu/css/`); SNF: Nearby Supernova Factory (`http://snfactory.lbl.gov/`); CHASE: CHilean Automatic Supernova sEarch (`http://www.das.uchile.cl/proyectoCHASE/`); CRTS: Catalina Real-Time Transient Survey (`http://crts.caltech.edu/`); Itagaki (`http://www.k-itagaki.jp/`); Boles: Coddenham Astronomical Observatory, U.K. (`http://www.coddenhamobservatories.org/`); CROSS (`http://wwww.cortinasetelle.it/snindex.htm`); LSSS: La Sagra Sky Survey (`http://www.minorplanets.org/OLS/LSSS.html`); PASS: Perth Automated Supernova Search (`http://www.perthobservatory.wa.gov.au/research/spps.html`); Williams 1997); PIKA: Comet and Asteroid Search Program (`http://www.observatorij.org/Pika.html`); PanStarrs: (`http://pan-starrs.ifa.hawaii.edu/public/`); THCA Supernova Survey (`http://www.thca.tsinghua.edu.cn/en/index.php/TUNAS`)

2.5 PAIRITEL: the 1.3-m Peters Automated InfraRed Imaging TELescope

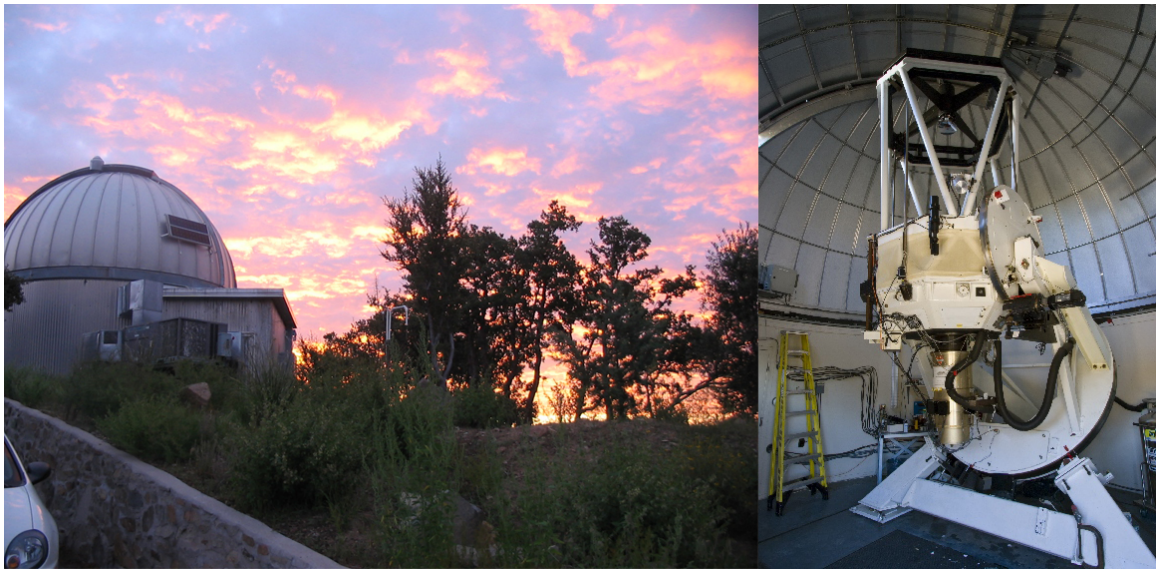

Figure 2.1.— PAIRITEL Dome and Telescope on Mount Hopkins, Arizona

The dome (**left**) and telescope (**right**) of the fully robotic PAIRITEL f/13.5 1.3-meter Peters Automated Infrared Imaging TELescope at the Fred Lawrence Whipple Observatory (FLWO) on Mount Hopkins, Arizona (Bloom et al. 2006; `http://www.pairitel.org/`). Thanks to PAIRITEL P.I. Professor Joshua Bloom and collaborators, who roboticized the old 2MASS north telescope which became PAIRITEL, the friendly PAIRITEL robot miraculously allowed me to be a lazy astronomer, obtaining my thesis data from the comforts of my office chair.

Dedicated in October 2004, PAIRITEL uses the Two Micron All Sky Survey (2MASS; Skrutskie et al. 2006) northern telescope together with the 2MASS southern camera. PAIRITEL is a fully automated, robotic telescope with the sequence of observations controlled by an intelligent queue-scheduling database (Bloom et al. 2003, 2006). Two dichroic mirrors allow simultaneous observing in JHK_s (1.2, 1.6, and 2.2 μm; Cohen et al. 2003; Skrutskie et al. 2006) with three 256×256 pixel HgCdTe NICMOS3 arrays. The image scale of 2″/pixel provides a field of view (FOV) of 8.53′×8.53′ for each filter. Images are obtained with standard

double-correlated reads with the long (7.8-second) minus short (51-millisecond) frames in each filter treated as the "raw" frame in the mosaic reduction pipeline (§3.1). The telescope is dithered ($< 2'$) every fourth exposure to aid with reductions (see Figure 3.1). After combining the dithered images into mosaics, the instrument achieves an average image quality of 2.5 arcsec FWHM (Bloom et al. 2003; See §3.1). Figure 2.2 shows an example false color RGB composite image of SN 2006D, created by combining the mosaicked images in each of the JHK_s-bands.

Since the SN observations are conducted with the instrument that defines the 2MASS photometric system, we use the 2MASS point source catalog (Cutri et al. 2003) to establish the photometric zero points. Typical 30 minute (1800-second) observations (including slew overhead) reach signal-to-noise-ratio (SNR=10) sensitivity limits of $\sim 18, 17.5$, and 17 mag for J, H, and K_s respectively. For fainter sources, $10 - \sigma$ point source sensitivities of 19.4, 18.5, and 18 mag are achievable with 1.5 hours (5400-seconds) of dithered imaging (Bloom et al. 2003). This allows PAIRITEL to go significantly deeper than the six 1.3-second exposures used by 2MASS, equivalent to a 7.8-second total exposure time, which achieved 10-σ point source sensitivities of 15.8, 15.1, 14.3 in JHK_s, respectively (Skrutskie et al. 2006). Simultaneous JHK_s observations and nearly nightly cadence allow for densely sampled PAIRITEL NIR LCs, from as many as ~ 15 days before B-band maximum brightness to ~ 80 days past maximum (See §4).

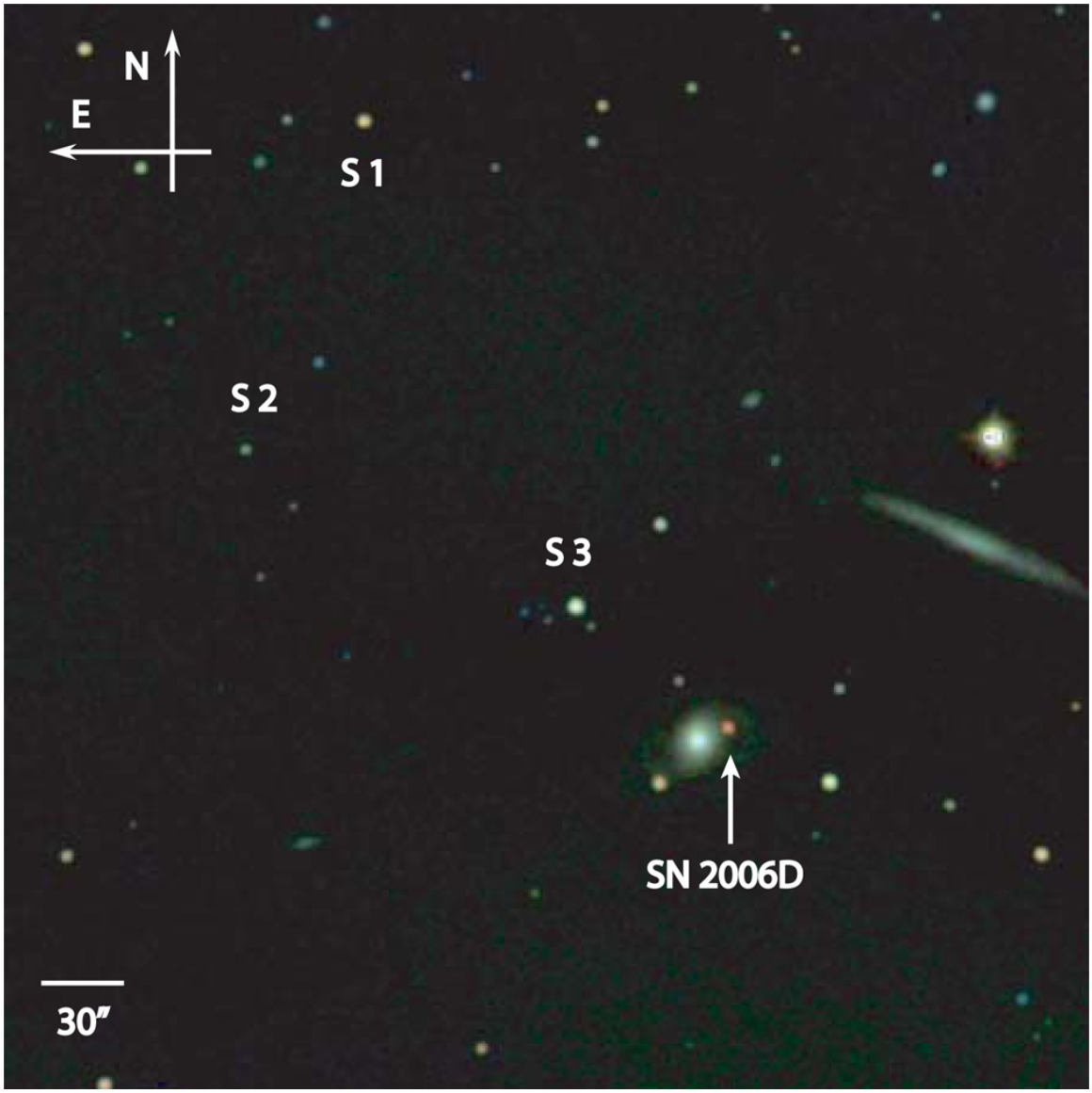

Figure 2.2.— PAIRITEL JHK_s False Color Image

Reproduced with permission from Wood-Vasey et al. 2008. PAIRITEL JHK_s composite color image of SN 2006D (orange-red dot to upper right of galaxy in lower-right corner) at a week past maximum light when the SN Ia had IR magnitudes of $(J, H, K) \approxeq (16.1, 14.8, 15.0)$. The image shown is $9' \times 9'$ in size. There are $\sim$ 30 2MASS stars in this field that were used for the photometric calibration of our PAIRITEL images of SN 2006D. The S1, S2, and S3 labels indicate three representative 2MASS stars with JHK_s magnitudes of S1: (14.11, 13.76, 13.71), S2: (16.02, 15.335, 14.830), and S3 (13.23, 12.61, 12.41).

2.6 Observing Strategy

The automation of PAIRITEL has made it possible to study SN with unprecedented temporal coverage in the NIR, responding quickly to new SN and revisiting targets frequently (Bloom et al. 2006; WV08). The PAIRITEL SN project follows up SN discovered by optical searches at $\delta \gtrsim -30$ degrees with $V \lesssim 18$ mag, with significant discovery contributions from both amateur and professional astronomers (See Table 2.3). SN candidates that also have a favorable observation window and airmass < 2.5 from Mount Hopkins are considered for the PAIRITEL observation queue. We observe SN of all types but place highest priority on the brightest SN Ia discovered early or close to maximum brightness. SN candidates meeting these criteria are often added to the queue even before spectroscopic typing, in order to observe the early time LC whenever possible. If the SN is subsequently found to be fainter than our 1-hour exposure sensitivity limits ($J \gtrsim 19$), weeks past maximum brightness, or of a spectroscopic type that is lower priority for our project, we may remove the object from our observing queue. Since $\sim 1/3$ of the optically discovered SN of all types brighter than $V < 18$ mag are also spectroscopically typed by our group at the CfA or other groups within 1-3 days of discovery, we rarely spend more than a few observations on PAIRITEL objects we decide to deactivate soon after typing. All CfA supernovae are spectroscopically classified using the SuperNova IDentification code (SNID; Blondin & Tonry 2007). The 172 nearby SN we have observed with PAIRITEL since 2005 include 72% SN Ia, 16% SN Ib/c, 12% SN II, and 2 SN of unknown type (See Table 2.4 and Figure 2.3).

From 2005-2011, $\sim$ 20–30 SN per year were discovered that are bright enough to observe with the PAIRITEL 1.3 m, with $\sim$ 3–6 available on any given night from Mount Hopkins. Since we perform follow-up NIR observations and are not conducting a NIR search to discover SN with PAIRITEL, we suffer from all the heterogeneous sample selection effects and biases incurred by each of the independent discovery efforts. A full analysis of the completeness of our sample is beyond the scope of this work. However, with $\sim$ 30% of the time on a robotic telescope available for supernova observations, we have been able to observe $\gtrsim 2/3$ of candidate SN that meet our follow-up criteria. After the SN has faded below our detection limits $\sim$ 6–12 months after discovery, we also obtain host galaxy template images (SNTEMP) for all SN with PAIRITEL (See §3.4).

PAIRITEL conducts two observation campaigns during each observing season (e.g. 2010-11), aligned with typical academic semesters (e.g. Semester2010A, Semester2011B). Semester A runs from September 1 to January 31 of the following year while Semester B runs from February 1 to July 31. The FLWO observatory is typically closed August 1-31 due to the Arizona monsoon season. While this leaves 334 nights per year where PAIRITEL is potentially available for observations, weather, scheduling conflicts, and mechanical failures typically limit this to $\sim$250-300 nights per year. Scheduling conflicts are determined by the robotic queue scheduler, which attempts to optimize observations for objects from all PAIRITEL projects using their requested observing parameters along with the relative priorities of each object within a project (e.g. SN or SNTEMP) and the global priorities of each project. For example, the Gamma-Ray Burst (GRB) project has the highest PAIRITEL priority and can interrupt SN observations (Bloom et al. 2003, 2006).

Table 2.4. PAIRITEL SN Observed by Type, Season, Since 2005

Type/Season	04-05[a]	05-06	06-07	07-08	08-09	09-10	10-11	Total	Fraction
Ia	7	20	12	22	22	21	18	122	71.76%
Ibc	5	6	8	3	2	3	0	27	15.88%
II	2	0	2	3	6	3	3	19	11.18%
unk	0	1	0	0	0	0	1	2	1.18%
Total	14	27	22	28	30	27	22	170	100.00%

Note. — 04-05 only includes data from Spring 2005 as Fall 2004 included the PAIRITEL commissioning and calibration.

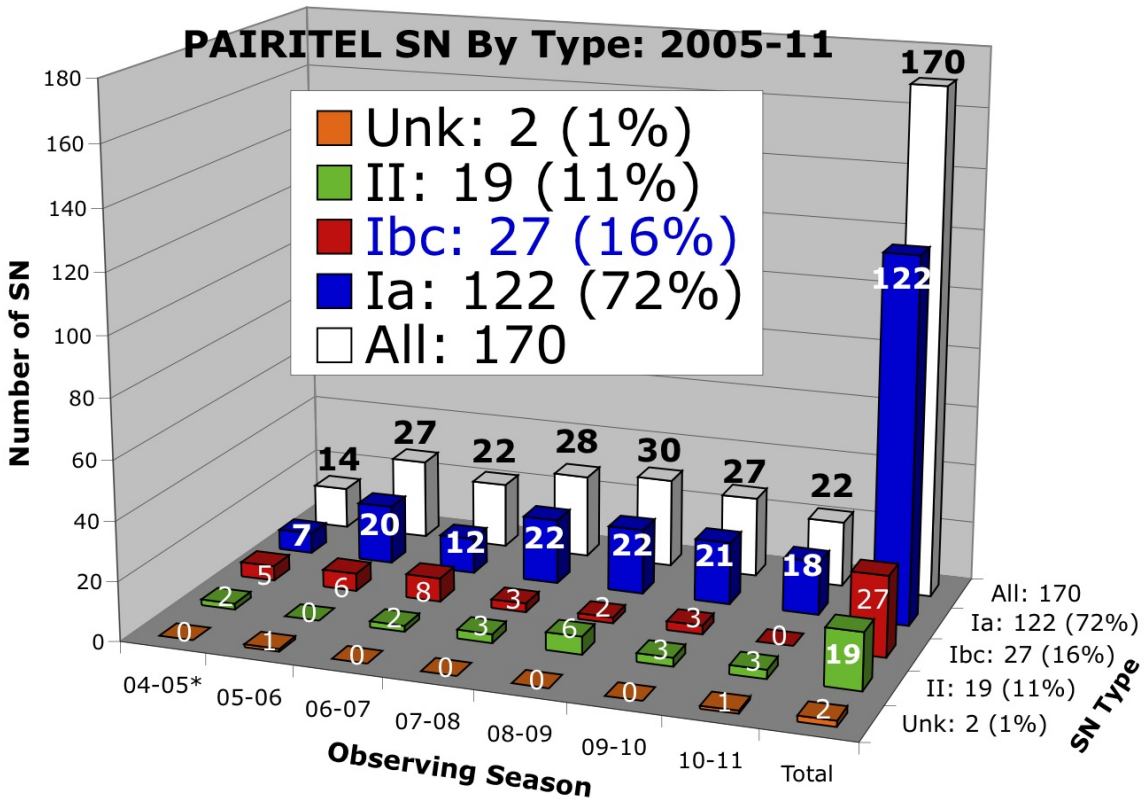

Figure 2.3.— Census of PAIRITEL data from 2005-2011.

The figure shows the number of SN observed per season, by type. Also see Table 2.4.

When managing the SN and SNTEMP project queues, we can remotely activate and deactivate objects, change observation parameters, and set relative priorities for observations, but even with perfect weather and a functioning telescope, there is no guarantee that requested objects will be scheduled and observed on any given night. These unavoidable limitations of a queue scheduled robotic telescope are far outweighed by the convenience of remote observing and the quantity of observations obtainable. As mentioned, we have been fortunate to be granted $\sim 30\%$ of the time on PAIRITEL since 2005, with average awards of 300 hours per semester, effectively amounting to over 6 months of time on the sky.

Pre-NIR-maximum data are still difficult to obtain because (a) NIR follow-up observations occur only after optical discovery, and (b) the time of the first peak of the light curve in the NIR bands typically occurs $\sim$ 3–5 days before $t_{B\mathrm{max}}$, the time of maximum in the B-band (Kasen 2006; Krisciunas et al. 2004a, 2007; Wood-Vasey et al. 2008; §5.2.1). Nevertheless, out of the 122 SN Ia observed by PAIRITEL from 2005-2011, 58 (48%) have NIR observations before $t_{B\mathrm{max}}$, while 34 (28%) have observations at least 5 days before $t_{B\mathrm{max}}$. These fractions of early time observations are comparable to similar SN Ia follow-up work by the CSP (Contreras et al. 2010; Stritzinger et al. 2011). We discuss the lack of early time data in constructing NIR template light curves in §5.1–§5.2.1.

Chapter 3

Data Reduction

Data Reduction

Since the publication of 21 PAIRITEL SN Ia JHK_s LCs in Wood-Vasey et al. 2008 (hereafter also WV08), we have implemented several substantial upgrades to our data reduction software, including both our pipelines for combining the raw data into mosaics and for performing photometry on the mosaicked images. In this section, we describe our current data reduction process with emphasis on recent improvements. All CfAIR2 data were processed homogeneously with a single mosaicking pipeline that co-adds and registers PAIRITEL raw images into mosaics (§3.1). The mosaics, and their associated noise and exposure maps, were then fed to single photometry pipeline, originally developed to handle optical data for the ESSENCE and SuperMACHO projects (Rest et al. 2005; Garg et al. 2007; Miknaitis et al. 2007) and modified to perform host galaxy subtraction and photometry (§3.4–3.5) on the NIR mosaicked images, with contributions from A. Rest, W.M. Wood-Vasey, G. Narayan, M. Modjaz., M. Hicken, P. Challis, and A. Friedman. Earlier versions of this photometry pipeline have also been used for previously published PAIRITEL SN photometry (Tominaga et al. 2005; Modjaz 2007; Wood-Vasey et al. 2008), with recent modifications by A. Friedman and W.M. Wood-Vasey to process the CfAIR2 data set. The current photometry pipeline also takes as input new and improved noise mosaics to estimate the noise in the mosaicked images (§3.2), registers the images to a common reference frame with SWarp (Bertin et al. 2002), subtracts off host galaxy light at the SN position using reference images with HOTPANTS (Becker et al. 2004, 2007), and performs point-spread function (PSF) photometry using DoPHOT (Schechter et al. 1993). Photometry is extracted

from either the un-subtracted or the subtracted images by forcing DoPHOT to measure the PSF-weighted flux of the object at a fixed position in pixel coordinates (see §3.4, §7.2). Since the SN observations are conducted with the telescope and camera that defines the 2MASS photometric system, we use the 2MASS point source catalog (Cutri et al. 2003) to establish the photometric zero points.

This section is organized as follows. In §3.1, we describe our mosaic pipeline and detail recent modifications and improvements. In §3.2, we describe the sky subtraction process and our improved algorithm to estimate noise in the mosaicked images and produce corresponding noise mosaics. In §3.3, we describe our image quality control algorithm for rejecting bad mosaics unsuitable for photometry. In §3.4 we detail the host galaxy subtraction process and describe our method for performing photometry on the subtracted or un-subtracted images. In §3.5, we summarize how we have implemented the major recent improvements to our combined mosaic and photometry pipelines for the CfAIR2 data set.

3.1 Mosaics

Due to absorption, emission, and scattering by molecules in our atmosphere with prominent electronic transitions in the NIR, at NIR wavelengths the night sky itself is extremely bright compared to the night sky at optical wavelengths, which appears quite dark to the human eye. The basic fact of the optical darkness of the night sky — which we usually take for granted — makes possible the entire enterprise

of performing optical astronomy at night or at all![1] However, to an observer with Infrared detectors as eyes, the night sky at NIR wavelengths would appear as bright as the daytime sky appears to humans at optical wavelengths! As a result, individual night time exposures with the PAIRITEL Infrared camera in the JHK_s-bands can easily saturate the detector in under 10 seconds (Skrutskie et al. 2006). In order to observe faint objects that require exposures greater than 10 seconds — which includes most supernovae of interest — we must use a method different than the typical long lasting single exposures that are possible at optical wavelengths.

The solution is to combine multiple, short exposures, which are taken at different dithered positions on the sky, and combine them into a stitched-together "mosaic" with a total effective exposure time much greater than 10 seconds in each pixel. The dithering itself helps aid in the data reduction process by allowing different portions of the light from the image to fall on different detector pixels over the course of the spatially varying dither pattern. Dithering helps us to remove contributions from individual bad pixels which systematically over or underestimate the number of photons at the corresponding point in the image (see Figure 3.1). Dithering also allows us to estimate the overall contribution of the background counts from the sky and the detector itself, for example, by using a pixel-by-pixel weighted average through an unregistered stacked time series of dithered images (see §3.2). This is crucial since we must subtract off background counts that would otherwise cause us to overestimate the flux at the positions of the sources of interest

[1]Unlike the case of daytime radio wavelength astronomy, the daytime NIR and optical sky are both too bright to include any meaningful daytime astronomy due to the luminous presence of our favorite star, the sun, both the source of all life on Earth and the nemesis of would-be daytime Optical and NIR astronomers.

of image, including point sources like stars and supernovae and extended sources like the supernova host galaxy. The dithering and mosaic creation process allows PAIRITEL to observe objects as faint as $J \sim 18$–19 mag, with standard hour long dithered image progressions. However, sophisticated software must be employed to obtain mosaic solutions for each dithered sequence of observations in order to output a mosaicked image suitable for performing photometry.

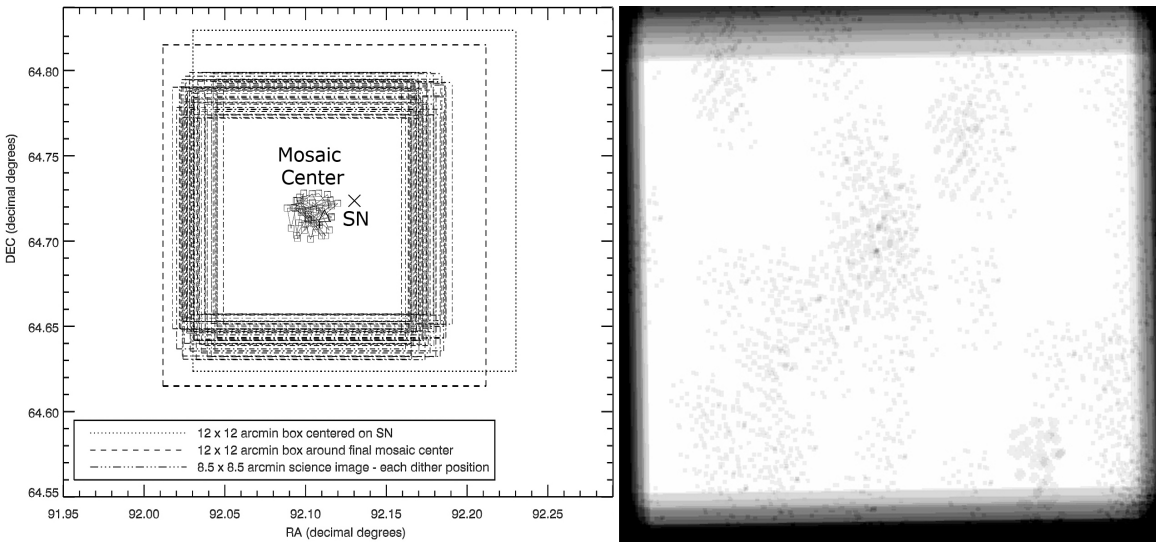

Figure 3.1.— Example PAIRITEL Dither Pattern and Exposure Map

(**Left**) Randomized dither pattern shown for the PAIRITEL JHK_s observations of SN 2006N taken on February, 6th 2006 displayed on grid with celestial coordinates Right Ascension and Declination on the x and y-axes, respectively. The coordinates of SN 2006N are marked with an "X" and the centers of each dither position are marked with open squares that cluster around the final dither position. The centers of individual dithered science exposures are displayed as open squares which cluster around the center of all mosaicked imaging, slightly off center to the lower left of the SN coordinates. Individual dithered exposures have a field of view (FOV) of $8.5 \times 8.5'$ (corresponding to the 256×256 pixel detector), displayed as boxes with alternating dashes and dots surrounding the dither centers. Larger $12 \times 12'$ boxes corresponding to the final mosaic FOV are displayed centered on the SN position and the Mosaic Center with dotted and dashed lines, respectively.

(**Right**) J-band exposure map for the mosaicked image corresponding to the dither pattern shown on the left, cropped to a final size of 512×512 pixels. The exposure map weights the effective exposure time of each pixel, based on the dither pattern with the exposure map scaled in white near the mosaic center where the effective exposure time is highest to black near the mosaic edges where the effective exposure time is lowest (and potentially zero if the dither pattern never overlapped with that part of the sky). The persistent darker gray patterns in the exposure map come from a deficit of counts which have been removed from individual exposures due to persistent bad pixels in the 256×256 pixel detector which move across the sky as the dither pattern progresses. Allowing different detector pixels to detect different parts of the sky over the dither pattern helps us identify and remove bad pixels, one of the major benefits of dithering.

PAIRITEL data were processed into mosaics at Harvard/CfA using Mosaic Pipeline version 3.6 implemented in python. Mosaic Pipeline 3, was developed by C. Klein, D. Starr, and J.S. Bloom at UC Berkeley (versions 3.0-3.5), with recent modifications by A. Friedman at Harvard/CfA (version 3.6). Pipeline 3.0 was an upgrade over Mosaic Pipeline 2.0, originally developed by D. Starr, J.S. Bloom, and C. Blake at UC Berkeley and Harvard/CfA, which we used to process most of the mosaics for the photometry published in WV08. Mosaic Pipeline 1.0 was originally developed by J.S. Bloom and C. Blake at Harvard/CfA, when PAIRITEL was first being roboticized and commissioned in late 2004 and early 2005 (Bloom et al. 2003, 2006). The latest Mosaic Pipeline 3.6 contains small but significant upgrades over versions 3.0–3.5 and several major upgrades compared to previous Mosaic Pipelines 1.0 and 2.0 (see Bloom et al. 2003, 2006; Kocevski et al. 2007; Modjaz 2007; Wood-Vasey et al. 2008; Modjaz et al. 2009, for details of older pipelines). While the WV08 data used mosaics reduced with Pipelines 1.0 and 2.0, and a modified Pipeline 2.0 for SN with large host galaxies, all the images in this work were processed uniformly with Pipeline 3.6, making the CfAIR2 data set the largest homogeneously reduced sample of NIR SN Ia light curves to date.

Images are obtained with standard double-correlated reads with the long (7.8-second) minus short (51-millisecond) frames in each filter treated as the "raw" frame input to the PAIRITEL mosaic reduction pipeline. These raw 256×256 pixel images are of ~ 7.8 second duration with a plate scale of $2\ ''$/pixel and a $8.53' \times 8.53'$ FOV. Three raw images are observed at each dither position, then coadded into "triplestacks" before mosaicking. To aid with reductions, the telescope is dithered every fourth exposure with a step size $< 2'$ based on a randomized dither

pattern covering a typical $\sim 12' \times 12'$ mosaicked FOV (See Figure 3.1). Including slew overhead for the entire dither pattern, typical exposure times range from 600 to 3600 seconds, yielding $\sim$ 50–150 raw images for mosaicking. Mosaic Pipeline 3.6 processes all raw images by flat correction, dark current and sky subtraction, registration, and stacking to create a final mosaic in each of the JHK_s bands using SWarp (Bertin et al. 2002). Bad pixel masks are created dynamically and flat fields — which are relatively stable — were created from archival images. The seeing over long time periods (several months) is limited by the thermal properties of the dome and remains relatively constant at 1.5–2.5″. Since the short-timescale seeing also remains roughly constant in the several seconds of slew time between dithered images, we did not find it necessary to convolve the raw images to the seeing of a raw reference image before mosaicking. The raw images are resampled from a raw image plate scale of 2″/pixel into final mosaics with 1″/pixel sampling with SWarp (Bertin et al. 2002). The typical FWHM in the final PAIRITEL mosaics is $\sim$ 2.5–3.0″, consistent with the average image quality obtained by 2MASS (Skrutskie et al. 2006).

The desired telescope pointing center for all dithered images is set to the SN RA and DEC coordinates from the optical discovery images. Unfortunately, due to software deficiencies and persistent mechanical issues — for example problems with the RA drive motor — the PAIRITEL 1.3-m telescope pointing accuracy is highly variable and can be off by $\sim 1 - 30$ arcminutes from night to night. Fatal pointing errors can result in the SN being absent in all of the raw images and not in the $\sim 12' \times 12'$ mosaic FOV. More often, non-fatal pointing errors result in the SN being absent or off-center in some fraction of the raw images. In the previous mosaic pipeline 2.0 used for WV08, the mosaic center was constrained to be the SN

coordinates. While desirable for later image registration and consistent standard stars across each SN image, this resulted in a significant fraction of failed mosaics or low SNR mosaics constructed from an insufficient number of raw images. For p3.0 (and p3.6 mosaics used in CfAIR2), the constraint fixing the SN at the mosaic center was relaxed and the mosaic center was allowed to be the center of all imaging (see Figure 3.2). This resulted in $\sim 15\%$ more mosaic solutions than p2.0, and we are thus able to include additional observations for the SN Ia published in WV08.

Figures 3.3–3.9 present a gallery of J-band mosaics for all 122 SN Ia observed with PAIRITEL from 2005-2011. 104 of these have LCs included in CfAIR2.

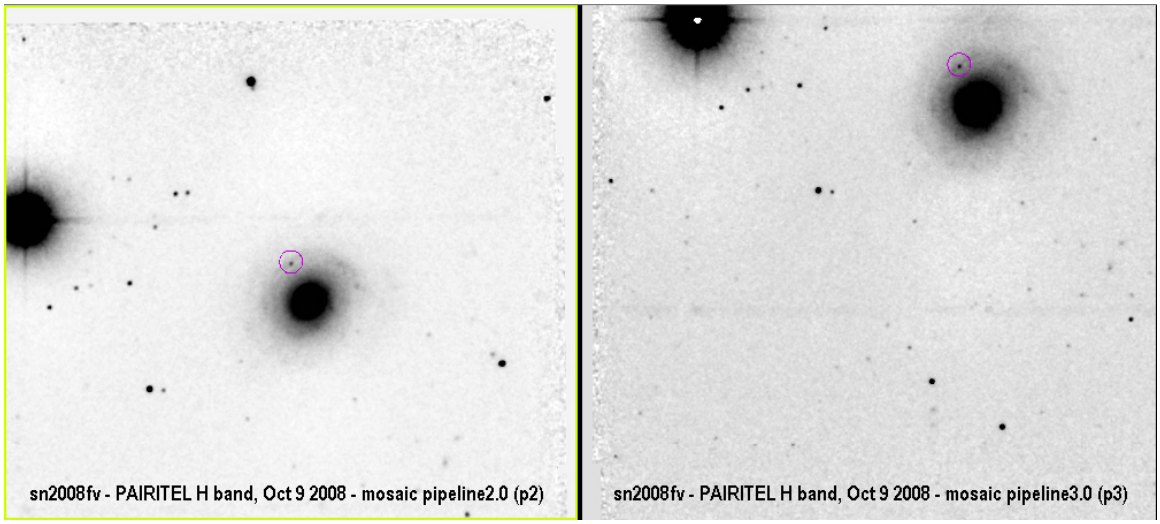

Figure 3.2.— Example p2.0 and p3.0 Mosaics

Mosaics for the PAIRITEL H-band images of SN 2008fv (circled) taken on 10/9/2008 reduced using mosaic pipeline p2.0 (**left**) and mosaic pipeline p3.6 (**right**). While the mosaic center for p2.0 images was constrained to be the SN position, for p3.0 images (up through version p3.6), the mosaic center is allowed to be the center of all imaging. Because the pointing for PAIRITEL is sometimes off by several arcminutes, and the mosaicked FOV is ~ 12 arcmin, relaxing the constraint of the mosaic center forced at the SN coordinates allows for $\sim 15\%$ more p3.0–p3.6 mosaics to be processed that would otherwise have failed p2.0. This allows for more light curve points, but requires larger photometric catalogs from 2MASS, and may results in certain standard stars not being present in all mosaics for a given SN (see Table 4.1), since mosaics processed for the same SN on different nights may have had variable pointing.

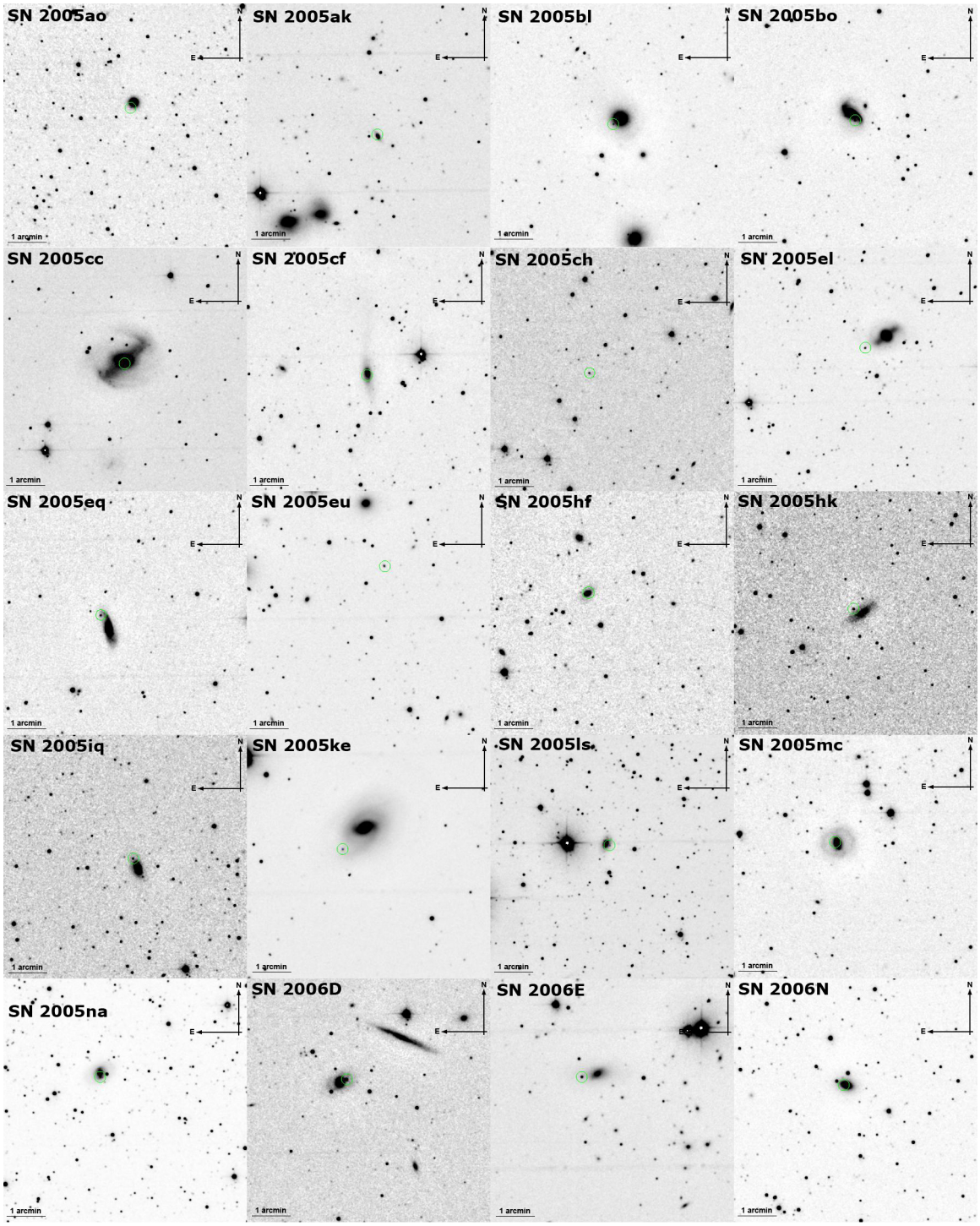

Figure 3.3.— Gallery of 20 PAIRITEL J-band Mosaics

A subset of 20 PAIRITEL J-band Mosaics from the set of 122 total SN Ia observed with PAIRITEL from 2005-2011. 104 have light curves presented here in CfAIR2. SN Ia are marked by green circles.

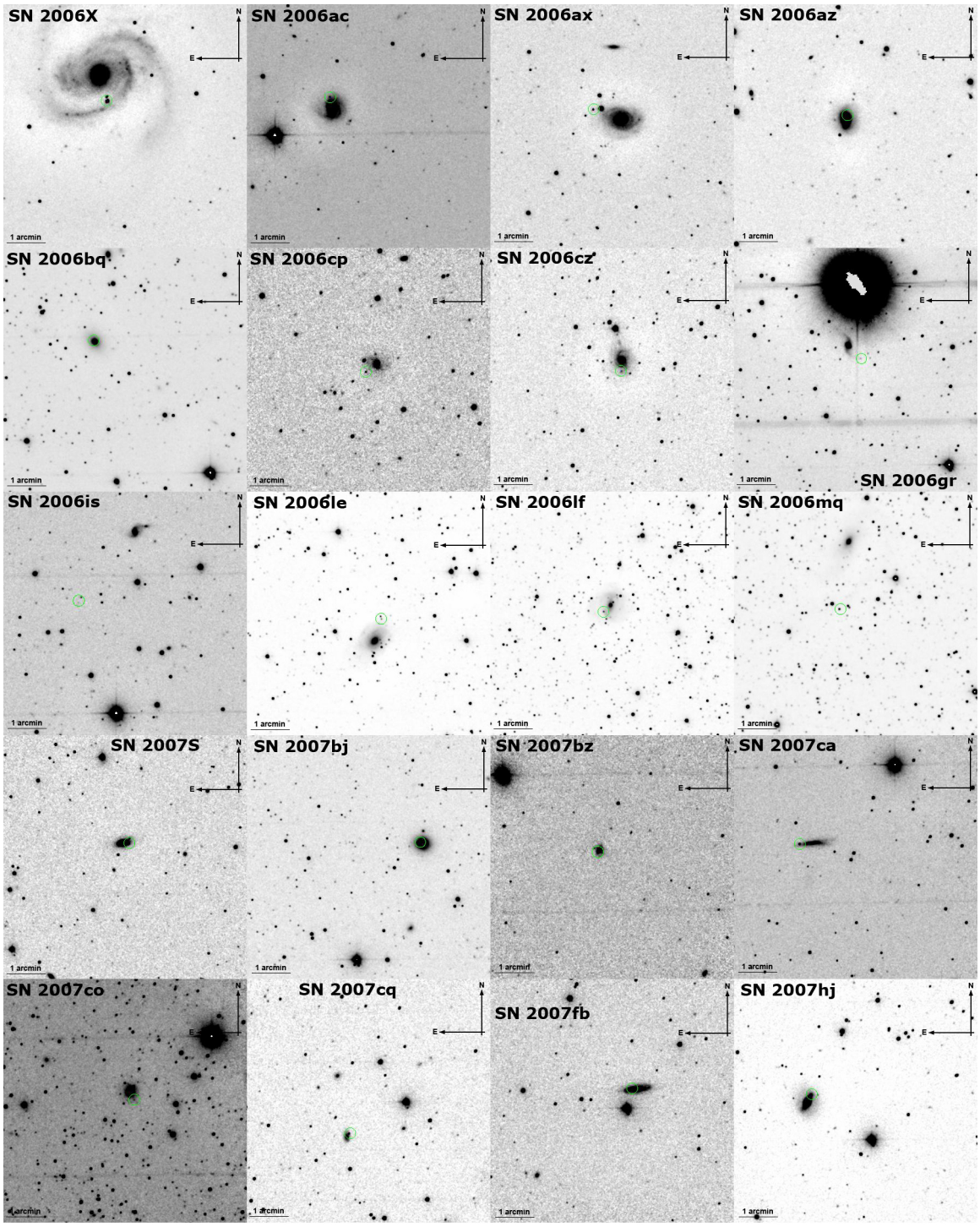

Figure 3.4.— Gallery of 20 PAIRITEL J-band Mosaics

A subset of 20 PAIRITEL J-band Mosaics from the set of 122 total SN Ia observed with PAIRITEL from 2005-2011. 104 have light curves presented here in CfAIR2. SN Ia are marked by green circles.

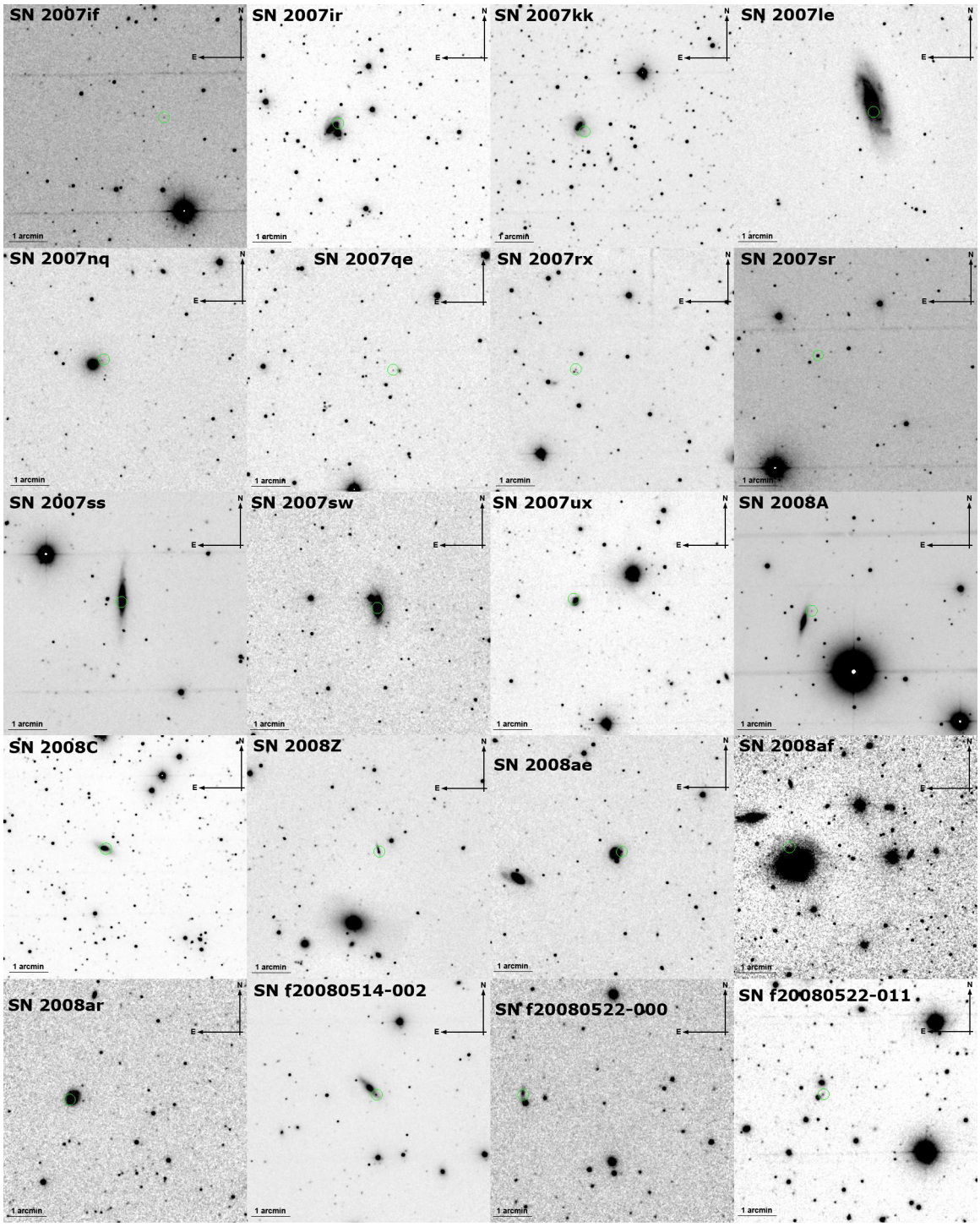

Figure 3.5.— Gallery of 20 PAIRITEL J-band Mosaics

A subset of 20 PAIRITEL J-band Mosaics from the set of 122 total SN Ia observed with PAIRITEL from 2005-2011. 104 have light curves presented here in CfAIR2. SN Ia are marked by green circles.

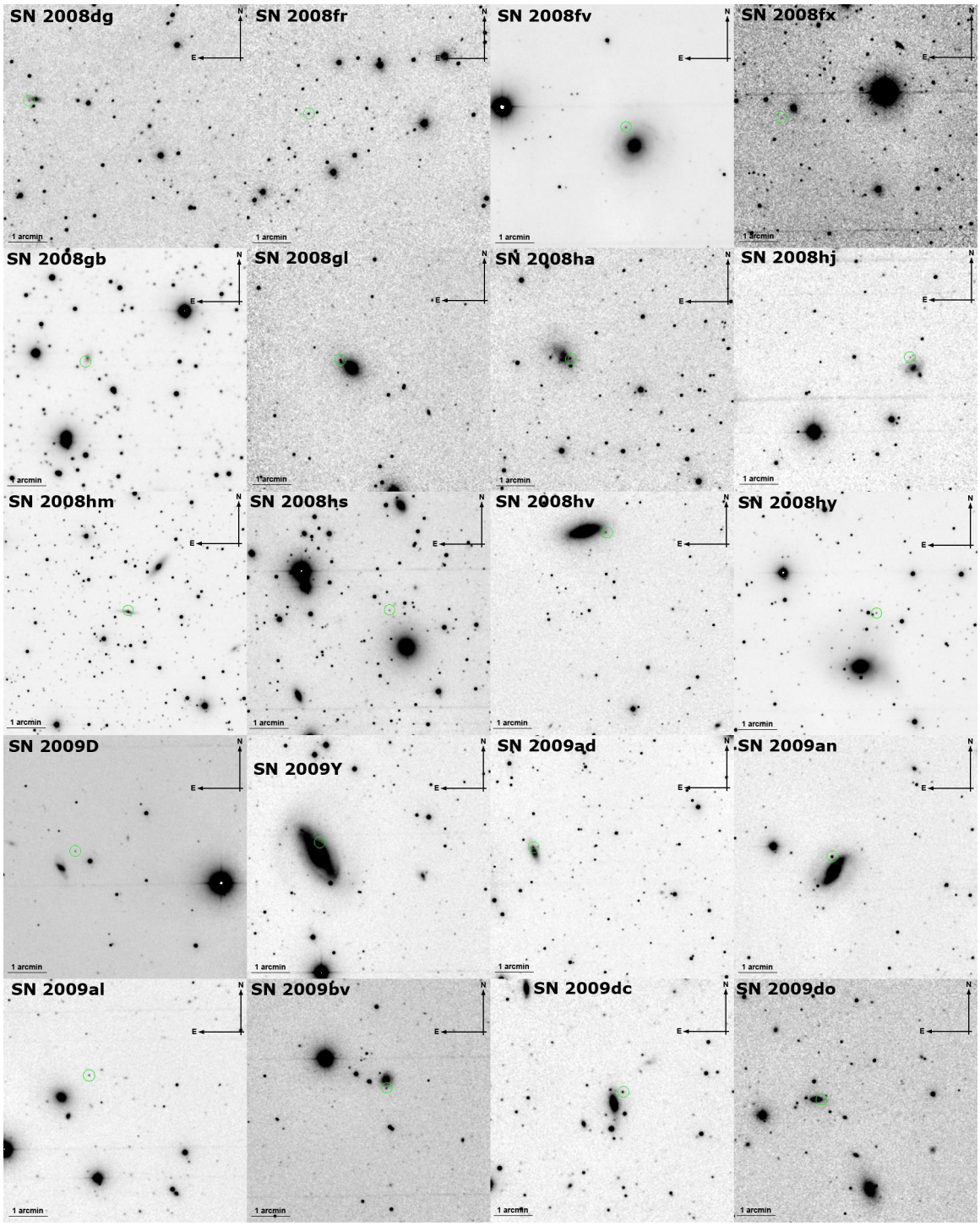

Figure 3.6.— Gallery of 20 PAIRITEL J-band Mosaics

A subset of 20 PAIRITEL J-band Mosaics from the set of 122 total SN Ia observed with PAIRITEL from 2005-2011. 104 have light curves presented here in CfAIR2. SN Ia are marked by green circles.

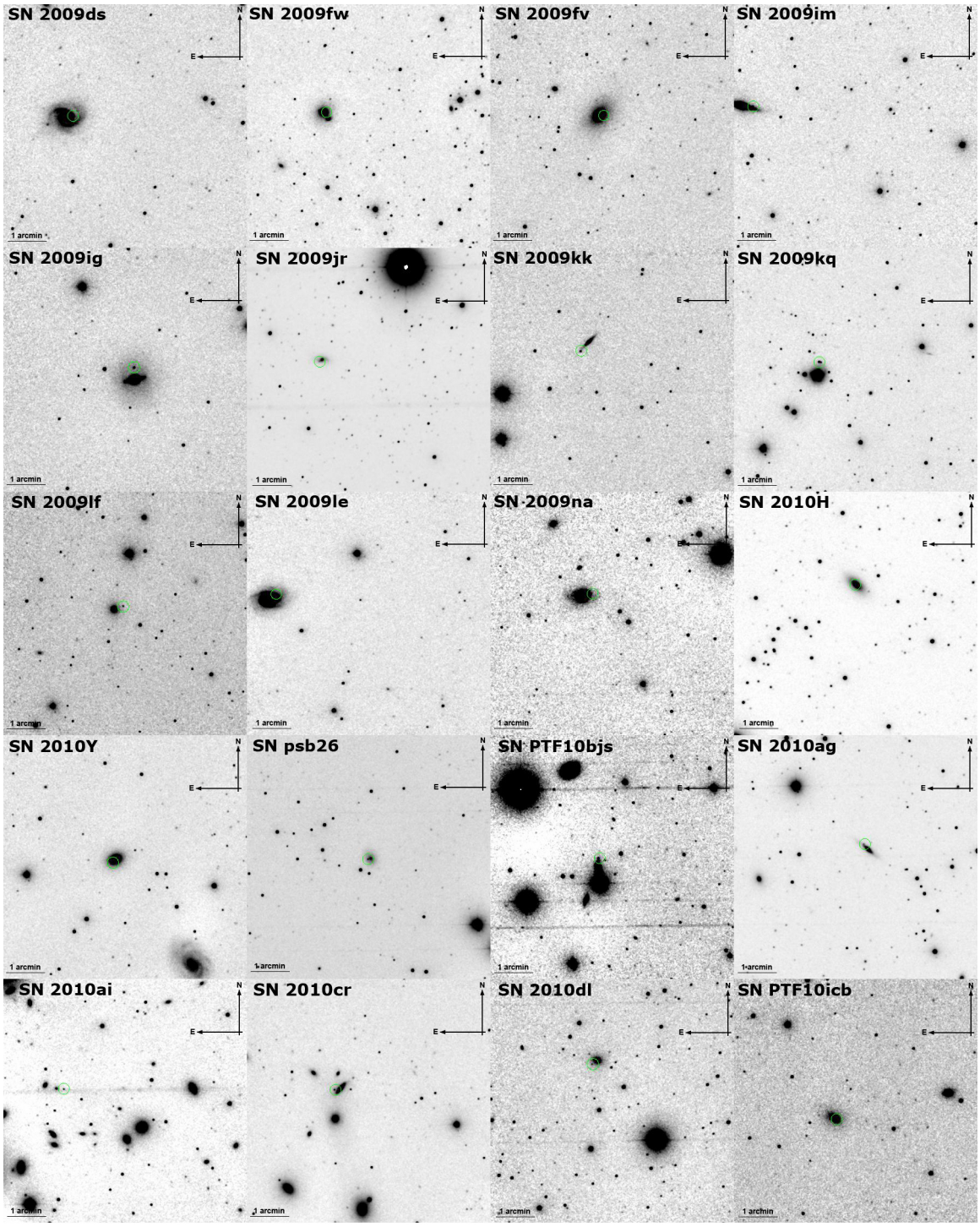

Figure 3.7.— Gallery of 20 PAIRITEL J-band Mosaics

A subset of 20 PAIRITEL J-band Mosaics from the set of 122 total SN Ia observed with PAIRITEL from 2005-2011. 104 have light curves presented here in CfAIR2. SN Ia are marked by green circles.

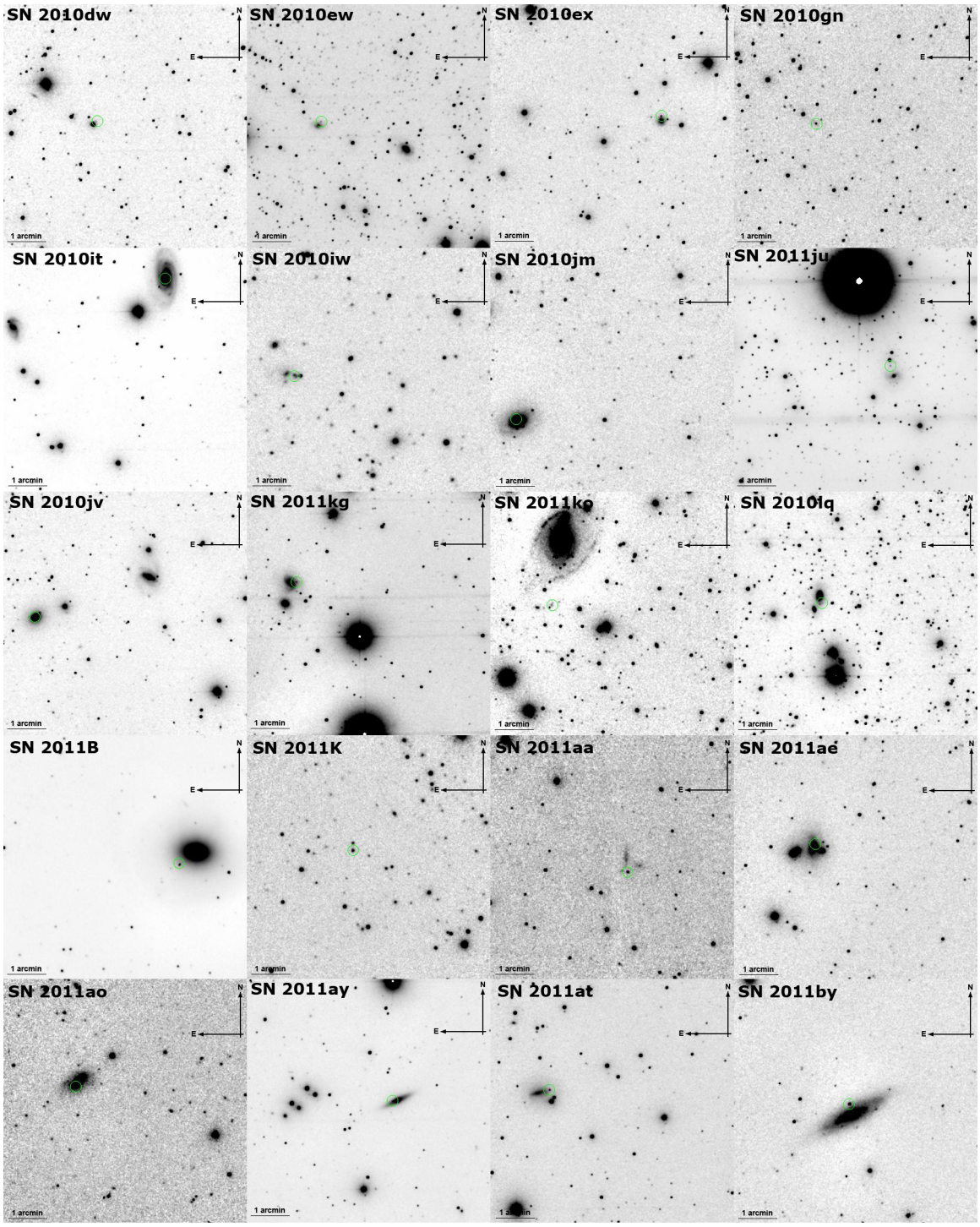

Figure 3.8.— Gallery of 20 PAIRITEL J-band Mosaics

A subset of 20 PAIRITEL J-band Mosaics from the set of 122 total SN Ia observed with PAIRITEL from 2005-2011. 104 have light curves presented here in CfAIR2. SN Ia are marked by green circles.

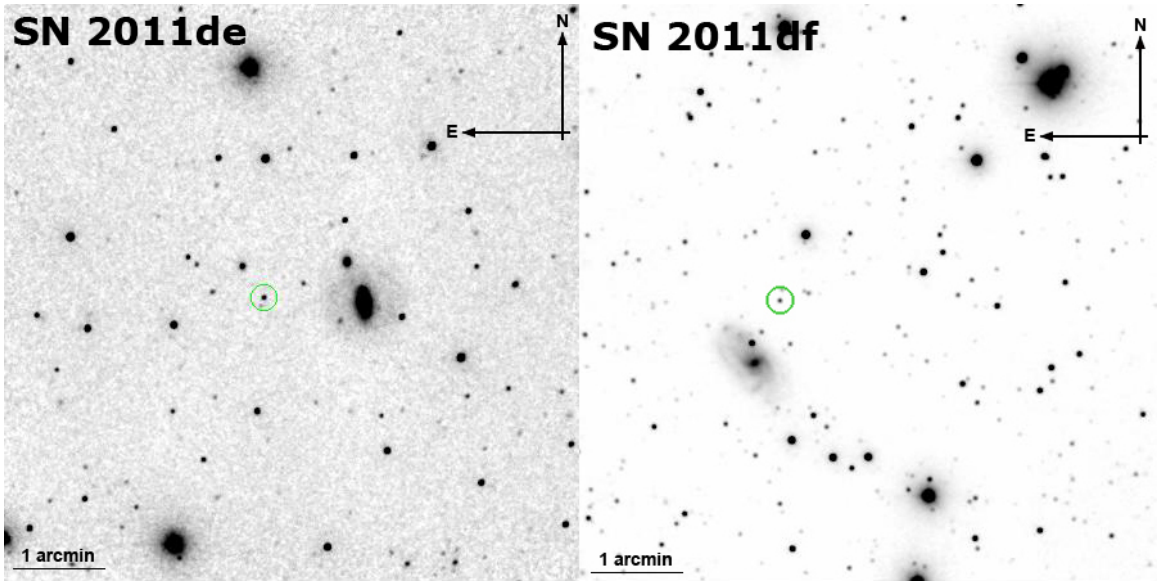

Figure 3.9.— Gallery of 2 PAIRITEL J-band Mosaics

A subset of 2 PAIRITEL J-band Mosaics from the set of 122 total SN Ia observed with PAIRITEL from 2005-2011. 104 have light curves presented here in CfAIR2. SN Ia are marked by green circles.

3.2 Sky Subtraction and Noise Maps

The PAIRITEL camera has no shutter, so dark current cannot be measured independently, and background frames include both sky and dark photons ("skark"). PAIRITEL SN observations did not include on-off pointings alternating between the source and a nearby sky field, so skark frames were created for each raw image in the mosaic by applying a pixel-by-pixel robust average through the stack of a time series of unregistered raw frames and removing the highest and lowest pixel values in the stack. The time window of the stack is set to be ± 5 minutes around the time of each raw image, under the technically false — but practically reasonable — assumption that the skark values at each sky position are approximately constant on timescales less than 10 minutes. Note that sky values at a given time can and do

vary across the image FOV on sub-arcminute spatial scales (see 3.10). Pipeline 2.0 implemented a similar procedure that involved a pixel-by-pixel spline fit to the time series of skark values in order to reconstruct a skark image corresponding to a given raw science image.

Although the telescope is dithered ($< 2'$) every fourth exposure to aid with reductions, for host galaxies with large angular size $\gtrsim 2 - 5'$ (in the $8.53'$ raw image FOV), host galaxy flux contamination introduces additional systematic uncertainty by biasing skark count estimates toward larger values. When the skark values are calculated from a pixel-by-pixel robust average or median through a time series stack of unregistered dithered images, large galaxies increase the likelihood that unregistered pixels near the mean galaxy position will have landed on galaxy light versus sky light, biasing the mean sky value in the pixel-by-pixel average upwards and leading to *over-subtraction* of sky light in those pixels (see §4.2.4). Still, the relatively large PAIRITEL $8.53'$ FOV combined with a dither step size comparable or greater than the $\sim 1 - 2'$ angular size of typical PAIRITEL galaxies allows us to safely estimate the sky from the raw frames in most cases. Estimating the sky from the raw frames ultimately gives us more time on the target compared to on-off pointing, which is required for other telescopes with a smaller FOV, for example the $3.4'$ FOV of the CSP Swope 1.0-m (Hamuy et al. 2006; see Table 2.1). Avoiding off target sky exposures is one of the key factors that allowed PAIRITEL to obtain more individual observations than CSP over a comparable time span (see Table 2.2). Overall, with PAIRITEL we chose to spend more time observing the target at the expense of potential systematic sky over-subtraction for SN and stars near larger galaxies. In §4.2.4, we argue that this choice is justified because we estimate sky

over-subtraction to be a small systematic effect, biasing SN photometry toward fainter values by at most $\sim$ 1–2 hundredths of a magnitude in JHK_s.

Prior to the current Mosaic Pipeline 3.6, in Mosaic Pipeline 3.5, the median value of each 256 $\times$ 256 pixel skark frame corresponding to each raw image ($MEDSKARK_{256}$) was stored in the fits header. We then estimated the median skark counts subtracted from each mosaic pixel as a single number, $MEDSKARK$, calculated by taking the median $MEDSKARK_{256}$ value over all the raw skark frames. Skark frames itself were deleted after mosaicking. Pipelines 3.5 and earlier thus discarded most of the information in the skark frames after using them to subtract the skark counts from the mosaics, and effectively made the approximate assumption that the sky plus dark current background counts were constant across the mosaic by retaining only a single number to describe the skark mosaic properties (See Fig. 3.10). Pipeline 3.6 improves upon this in several ways by retaining the most important information from the skark frames. Before deleting the skark frames, pipeline 3.6 coadds each triplet of skarks into tripleskarks, and copies the WCS information in the corresponding triplestacks to the tripleskark header. The tripleskarks are then coadded and registered with SWarp in the same way as the triplestacks, resulting in skark mosaics, which contain the actual number of counts subtracted from each mosaic pixel rather than a single median value. This turns out to be essential for more accurately estimating the relative noise across the mosaic image for photometry (See §4). The mosaics and skark mosaics are then used to construct noise mosaics, which contain the estimated noise per pixel from the source, sky, dark, readnoise, and other sources (See Eq. 7.1 in §7.1). Noise mosaics are the final data products that represent the most important upgrade between Pipeline

3.5 and 3.6, and between Pipelines 1.0 and 2.0 —which also retained only a single representative skark number in the fits header — that were used to reduce mosaics for Wood-Vasey et al. 2008 and previously published PAIRITEL SN observations (Tominaga et al. 2005; Kocevski et al. 2007; Modjaz 2007; Modjaz et al. 2009). See §7.1 for the assumptions we used to estimate the noise per pixel in our mosaics.

Final Mosaic Pipeline 3.5 and earlier mosaic reductions have been automatically reduced nightly with a pipeline implemented on a xGrid based, parallelized Mac G5 cluster at the University of California Berkeley, originally developed by Joshua Bloom and Cullen Blake, and further developed by Dan Starr and Chris Klein. Final pipeline 3.6 mosaics are currently reduced at the CfA on a small cluster of two, 4-core Linux machines, each with a 2.66 GHz processor, sharing 16 GB of RAM. Jobs are processed with the unix parallel program, implemented on the mini-cluster by B. Wyatt and A. Friedman. Re-processing $\sim$ 6000 sets of JHK_s observations for all PAIRITEL SN and SNTEMP images of all types observed from 2005-2011 took $\sim$ 2 weeks running continuously. Automating the nightly PAIRITEL pipeline 3.6 mosaic reductions at the CfA has recently been implemented and the process is currently in the testing phase.

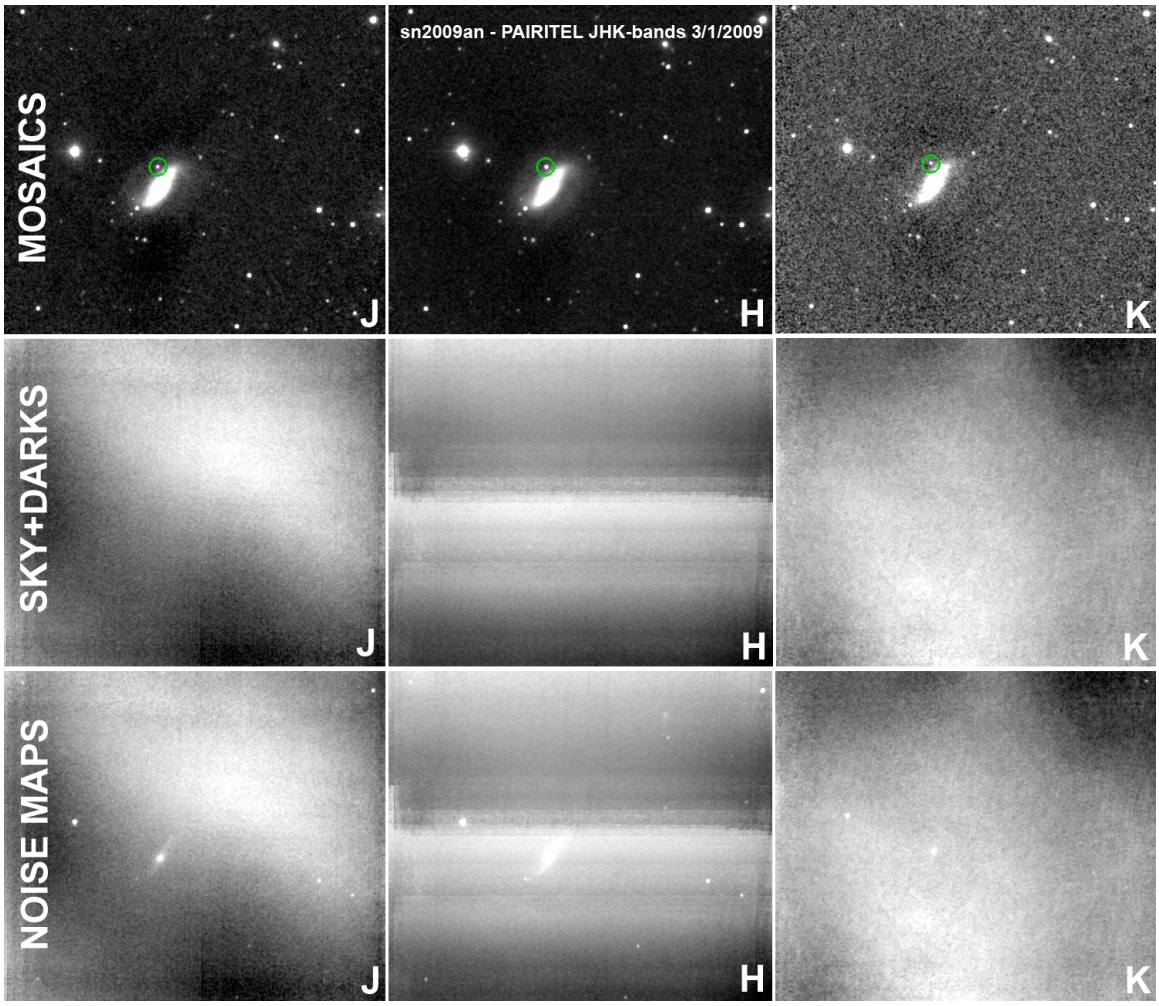

Figure 3.10.— PAIRITEL Source, Skark, and Noise Mosaics

Mosaics (**first row**), Skark Mosaics (**second row**), and Noise Mosaics (**third row**) for the PAIRITEL JHK_s band images of SN 2009an taken on 3/1/2009. Images are displayed with the same 99% scaling in SAOimage ds9, in grayscale with counts increasing from black to white. The skark images contain the number of sky counts and dark current counts (skark counts) subtracted from each mosaic pixel. Median skark counts for these images were ~ 800, 6700, and $19,600$ counts for JHK_s, respectively, reflecting the fact that the sky noise increases towards longer wavelengths in the NIR, and is worst in K_s-band, which also incurs more dark current noise versus J and H due to the thermal properties of the detector. The large scale patterns in the skark mosaics come both from arcminute scale spatial variations in the sky brightness, and from the relatively stable dark current patterns in each of the JHK_s detectors, which get smeared out over the mosaic dither pattern. The noise mosaics use the source counts from the mosaic, the skark counts from the skark mosaics, and noise from other sources to calculate the noise per pixel associated with each mosaic pixel. See §7.1 for the assumptions we used to estimate the noise per pixel.

3.3 Excluding Bad Mosaics

Many mosaics which do not suffer from fatal pointing problems still are not of sufficient quality for photometry. We must take care to exclude SN measurements from these mosaics avoid systematic photometric errors in the LC. Bad mosaics can result from many factors. Often $\lesssim 30$ raw images are processed into a mosaic due to pointing problems in a large fraction of the raw images, telescope interruptions due to weather, mechanical failures, or a higher priority time sensitive Gamma-Ray burst (GRB) observations, which can override and interrupt any dithered sequence of SN observations. These mosaics may have a lower effective exposure time and may have SNR $\lesssim 3$ at the positions of point sources in the mosaic, insufficient to detect the SN and many standard stars, especially for the faintest SN we can observe ($J \gtrsim 18$ mag). Other mosaics suffer from failed processing and result in image artifacts in the mosaic (see Fig. 3.12), which happens most frequently in K-band where the sky brightness can be factors of $\sim 10 - 20$ larger than the sky brightness in J and H, respectively (See Fig. 3.10). Up to $\sim$1/3 of our K-band mosaics must be excluded due to large mosaic sky variance alone. Some mosaics must be excluded because too few standard stars are detected, or because pointing problems placed the SN itself too close to the edge of the 512×512 pixel mosaic, where the SNR is lowest.

Visual inspection is sufficient to identify good and bad images in most cases. However, with over $15,000$ JHK_s images input to CfAIR2, some automation was necessary. Figures 3.11, 3.12, and 3.13 show examples of of good and bad images for individual SN Ia LCs, emphasizing cases which are easy to identify in an automated way (e.g. failed pointing where the SN is not in the mosaic FOV), and more difficult

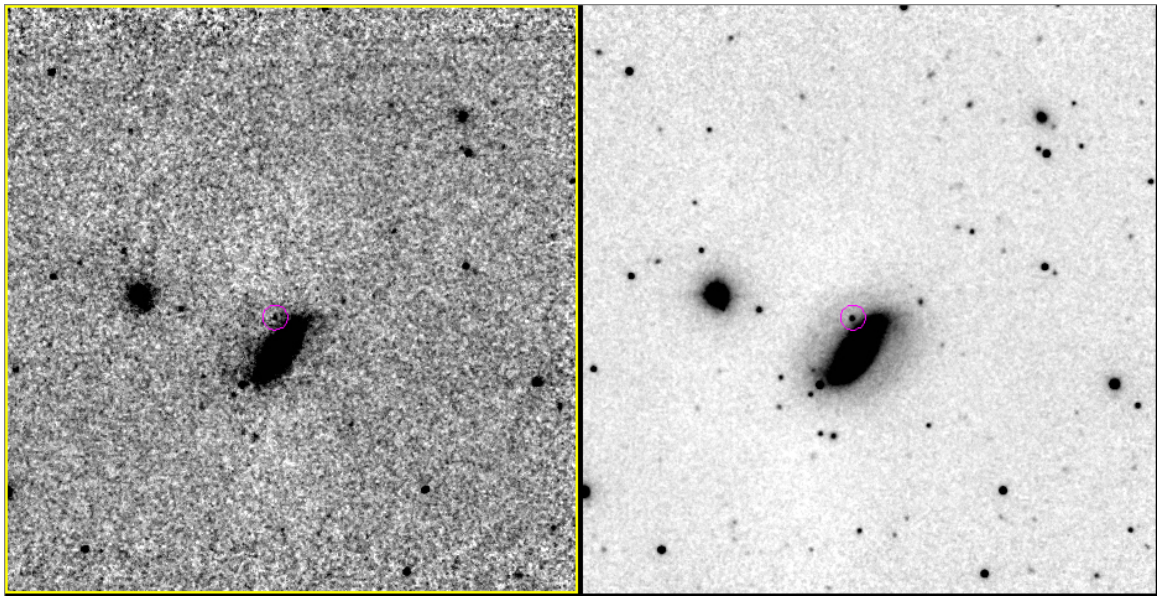

Figure 3.11.— Example Good and Bad PAIRITEL Mosaics

Example bad (**left**) and good (**right**) PAIRITEL J-band p3.6 mosaics for SN 2009an. The bad image has a sky variance $> 3-\sigma$ the median sky variance of all images in the SN 2009an J-band LC, a threshold that correlates with systematically inaccurate photometry (see §3.3).

cases that required a more sophisticated bad-image detection algorithm and/or manual visual rejection of bad images.

Automating bad-image detection is a difficult image classification problem which we attempted to approximately solve using the following algorithm. First, manual lists of bad images were constructed for a subset of $\sim$ 20 SN Ia LCs, including those that were independently observed by the CSP (See 4.3.2). Manual bad image rejection for these LCs was required to ensure the most accurate PAIRITEL LCs to compare with CSP LCs of the same SN Ia (See §4.3.2). Mosaics for these LCs, which comprise $\sim$ 20% of the images in our data set, were used to train our algorithm for automatically detecting bad images until we had achieved a $\sim$90% success rate ($\sim$10% false negative rate) for identifying bad images and a $\sim$10% false positive rate where otherwise good images are rejected as bad. However, since these rates

were not deemed to be sufficient, we found that they were best used as a guide in the bad image rejection process which still required a final manual check of images flagged as bad to exclude good images improperly flagged as bad (false positives) and post-photometry software to screen out LC points from remaining bad images improperly flagged as good by the bad image rejection algorithm (false negatives).

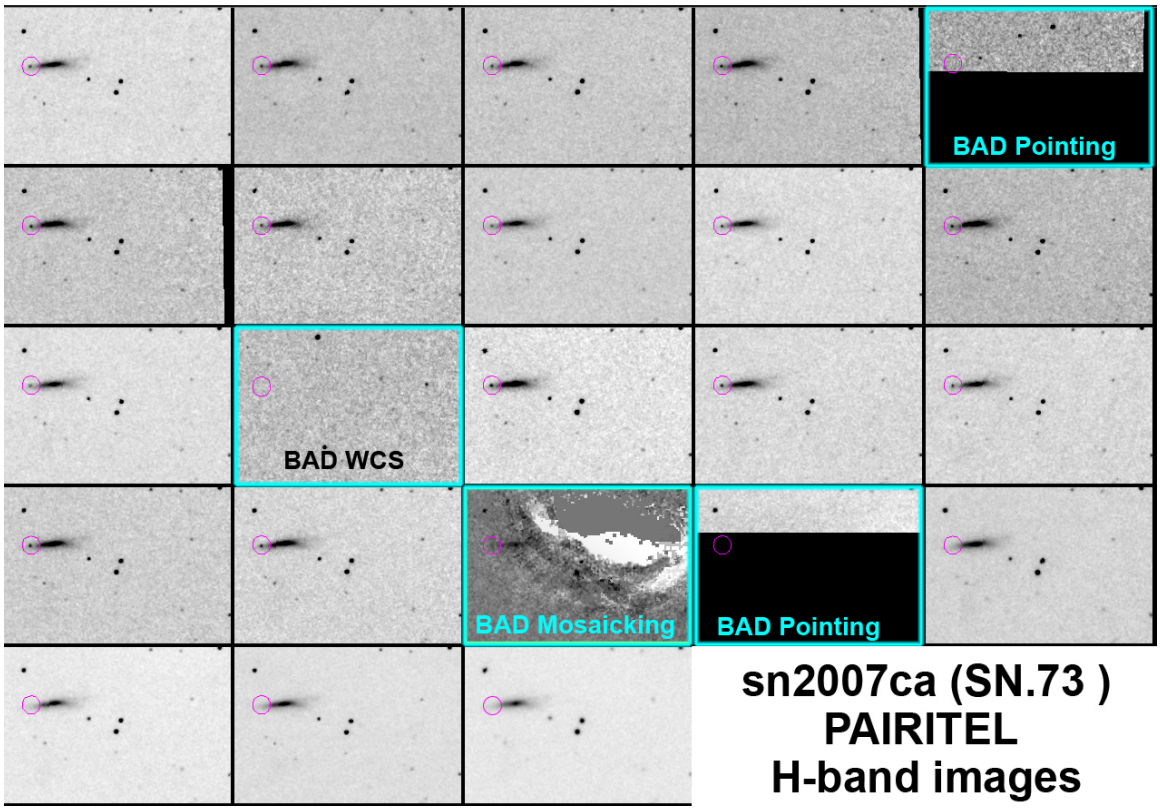

Figure 3.12.— Detecting Bad Mosaics: Easy Example

Example *H*-band mosaics for SN 2007ca. Bad images due to bad telescope pointing, bad WCS solutions, or failed mosaicking, are easily distinguishable from good images both by eye and by automated software. These can be automatically excluded prior to the photometry pipeline or by modules within photometry pipeline itself.

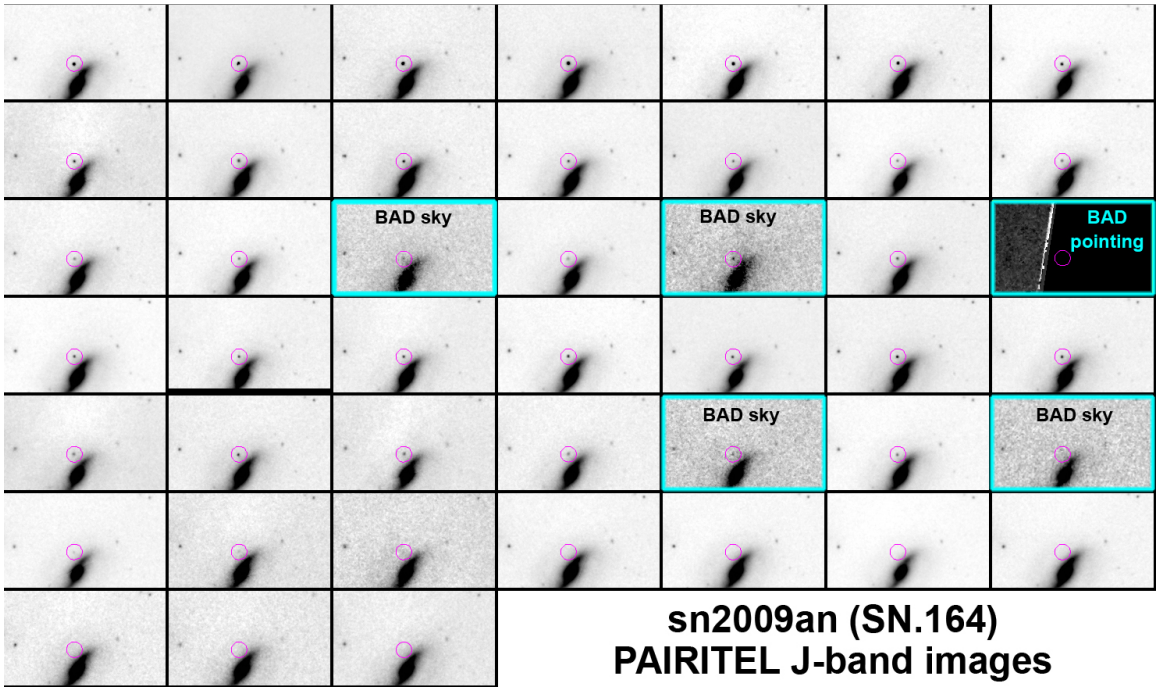

Figure 3.13.— Detecting Bad Mosaics: Difficult Example

Example *J*-band mosaic images for SN 2009an, including both SN images and host galaxy template (SNTEMP) images. 5 bad SN images are noted, including 4 with increased sky variance due to bad weather and/or few raw frames processed into the mosaic and 1 with bad pointing and failed mosaicking. Bad images due to bad telescope pointing, bad WCS solutions, or failed mosaicking, are easily distinguishable from good images both by eye and by automated software. These can be automatically excluded prior to the photometry pipeline or by modules within photometry pipeline itself. Bad images due to bad weather, increased sky variance, or mosaicking defects can be excluded with automated software, but thresholds must be trained with manual lists of good and bad images to increase the proportion of true bad image detections and decrease the number of false positives (good images that the software rejects as bad.) Our automated bad image rejection software currently has a ∼90% success rate (or a ∼10% false negative rate) at detecting bad images and a ∼10% false positive rate, but still benefits from a final manual check of images flagged as bad to exclude good images improperly flagged as bad (false positives) and post photometry software to screen out LC points from remaining bad images flagged as good (false negatives). The algorithm was trained on manual bad image lists prepared for the subset of CfAIR2 SN Ia that are common to both the PAIRITEL and CSP data sets.

The algorithm used several parameters which are highly correlated with image quality in opposite senses for good and bad images. Training the algorithm consisted of adjusting the upper and lower thresholds for these parameters until the desired success and false positive rates had been achieved for the manual bad image lists created for the training subset. These parameters included statistics from DoPHOT photometry on the un-subtracted mosaics and statistics quantifying outliers in the standard star photometry. The DoPHOT image statistics which correlated strongly with bad image quality included: the reduced χ^2 of the photometric zero point fit to the 2MASS standard stars, the telescope airmass (secant(z)), the number of raw 7.8-s images used to construct the mosaic, the number of stars successfully matched to 2MASS catalog, the number of objects identified as stars by DoPHOT, the variance of the residual sky in the mosaic, and the full width half maximum (FWHM) of the DoPHOT measured PSF.

In addition, we used our DoPHOT photometry of 2MASS standard stars to identify bad images by finding nights where some number of standard stars $N_{\rm badstar}$ differed by greater than $N_\sigma \times \sigma$ from the weighted mean residual standard star LC (See 4.1.2). The residuals were calculated by subtracting the weighted mean PAIRITEL magnitude from the nightly measured PAIRITEL magnitude for each standard star. We did not use the residuals of PAIRITEL photometry - 2MASS photometry for this metric because PAIRITEL observes deeper than 2MASS, resulting in more accurate photometry, especially for the faintest standard stars (see §4.1.3). $N_{\rm badstar}$ and N_σ were bandpass-dependent parameters which we trained in the manner described above. For example, $N_{\rm badstar} = 4$ and $N_\sigma = 2.25$ seemed to optimize our bad-image detection algorithm for J-band mosaics. Combining these

parameters and training their thresholds proved sufficient to achieve reasonably acceptable bad image rejection. However, to supplement the algorithm, a final round of manual inspection of the images flagged as bad was also employed to achieve optimal bad image rejection. In addition, we implemented post-photometry software to help reject LC points from remaining bad images flagged as good and missed by the bad image rejection algorithm (See the NNT method in §3.4.2).

An alternative algorithm, which used N_σ clipping of the residuals from a SN Ia mean template LC to identify bad images produced similar results with $N_\sigma \sim 3-5$. Nevertheless, we preferred to use a bad image rejection algorithm which only used information from the images themselves and from standard star photometry (See §4.1.2) rather than looking for LC template outliers from the SN Ia photometry, because the latter process introduces a bias which makes a given SN Ia LC look more like the mean template LC in that bandpass. More specifically, this bias is greatest when $N_\sigma \lesssim 3$ and negligible if $N_\sigma \gtrsim 5$, a more conservative rejection where only major outliers are excluded. This bias is worth avoiding since individual SN Ia do show real intrinsic deviations from the mean LC template which we do not want to inadvertently ignore through blind data processing (See §5.1).

3.4 Host Galaxy Subtraction

In all cases, we obtain host galaxy template images (SNTEMP) after the SN has faded below detection for the PAIRITEL Infrared camera, typically $\gtrsim$ 6–12 months after the last SN observation. We then use these SNTEMP images to subtract the underlying host galaxy light at the SN position (see §3.4.1). To limit the effects of

variable observational conditions and sensitivity to individual template observations of poor quality, we obtain at least 2 — and as many as 10 — SNTEMP images for each SN LC, requiring a minimum of 1 SNTEMP images that satisfy our image quality requirements (see §3.3, §3.4.2). To subtract SNTEMP images from SN images which were obtained under different seeing conditions, we must solve for the convolution kernel to transform the PSF of one image to the PSF of the other. We solve for the kernel to transform in both directions, but ultimately convolve the image with the narrower PSF to the image with wider PSF and poorest seeing, which can be either the SN or SNTEMP image. This convolution kernel is calculated using the algorithm of Alard & Lupton 1998; Alard 2000, with recent improvements by Becker et al. 2004 and Miknaitis et al. 2007, using the open source C/C++ code developed by Becker and collaborators (HOTPANTS: High Order Transform of Psf ANd Template Subtraction; Becker et al. 2004). Each image is divided into substamps, where stars in each substamp are used to calculate the PSF of each image before solving for the convolution kernel to transform between the two PSFs. With proper masking of the non-overlap regions in the SWarped SN and SNTEMP images (See §3.1), difference images ideally contain only the SN flux and residual noise from imperfect subtractions or masked regions. See Fig. 3.14 for example SN and SNTEMP images and their subtracted difference image.

In WV08, when we used image subtraction to remove host galaxy flux, we primarily used the NN2 method, where all $N \times (N-1)/2$ unique pairs of SN and/or SNTEMP images ($N = N_{\rm SN} + N_{\rm SNTEMP}$) were subtracted to produce our final host galaxy subtracted LCs (see §4.3.1). We ultimately found that NN2 did not perform well for our data in WV08, so for the CfAIR2 data set, we adopt the NNT method,

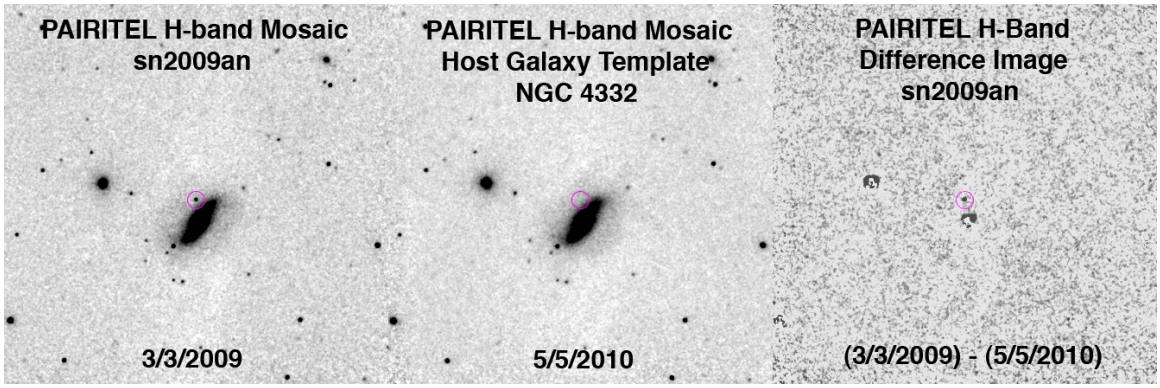

Figure 3.14.— PAIRITEL Host Galaxy Subtraction

Host Galaxy subtraction for an example H-band image of SN 2009an in NGC 4332.

(Left) The mosaicked SN image was observed on March 3, 2009, with SN 2009an circled and clearly visible in the image center. Although the SN is well separated from the nucleus of the host galaxy, NGC 4332, some galaxy light is present at the SN position.

(Middle) Over a year later on May 5, 2010, after the SN light had faded well below detection level for the PAIRITEL Infrared camera, we observed a host galaxy template (SNTEMP) image. The SN is clearly no longer visible at the same circled position.

(Right) To remove the contribution of galaxy light at the SN position, we subtract the SNTEMP image from the SN image, leaving a difference image which aims to leave only SN light at the circled position. Other features in the difference image are residual noise from the subtraction process and features which were masked out such as bright foreground stars in our own Milky Way galaxy or the bright core of the galaxy NGC 4332. We ultimately perform PSF photometry at the SN position in the difference image, calibrated using 2MASS standard stars in the field of the SN image. See §3.4 for a detailed description of the host galaxy subtraction process.

which uses fewer individual subtractions than NN2, where all $N_{\rm SN} \times N_{\rm SNTEMP}$ SN and SNTEMP image pairs were subtracted to produce $N_{\rm SNTEMP}$ LCs which were averaged on a night by night basis (see §3.4.2). In practice, each image subtraction may add or remove flux from the SN in the difference image, a potential source of systematic uncertainty which is reduced by averaging over subtractions from multiple SNTEMP images with NNT at the cost of an increased statistical uncertainty from the NNT averaging process. We discuss the statistical and systematic uncertainty incurred from host galaxy subtraction with NNT in §4.2.2.

3.4.1 Forced DoPHOT Photometry on Un-subtracted Images

Forced DoPHOT photometry at a fixed position was performed on the un-subtracted SN images as an initial step for all SN Ia observed with PAIRITEL. The forced DoPHOT LCs provide a good cross check for the final galaxy subtracted photometry. In particular, forced DoPHOT photometry on the un-subtracted images provides an excellent approximation to the final galaxy subtracted LC for those SN Ia that were clearly separated from their host galaxy and had little underlying contaminating light (See §4.2.2). Approximately 30% of the CfAIR2 SN Ia are well-isolated from the host galaxy and bright enough so that the measured galaxy flux at the SN position is $\lesssim 10\%$ of the SN flux at peak brightness. For these and other SN where the host galaxy flux at the SN position is a small fraction of the SN peak flux, galaxy subtraction introduces only a small correction to the SN LC and is technically not required. However, we perform galaxy subtraction on all CfAIR2 SN Ia in order to reduce the data with a method as homogeneous as possible (see §3.4.2). Instead, we use 20 of these bright, well-isolated SN Ia to perform internal consistency checks to test for any systematic errors incurred from the host galaxy subtraction process (§4.2.2).

In WV08, problems with our image subtraction process led us to adopt a two-pronged approach to host galaxy subtraction. For bright SN that were well-isolated from their host galaxies, the galaxy flux correction derived in WV08 was often comparable to — or significantly smaller than — both the photometric errors and the uncertainty introduced due to the NN2 subtraction process itself. For

these supernovae where the underlying galaxy contribution was a small fraction of the supernova light, in WV08, direct DoPHOT photometry on the un-subtracted images was preferable to photometry on the subtracted images. In practice, the standard background annulus subtraction used by DoPHOT to estimate the local sky was sufficient to remove any remaining contaminating galaxy light in the mosaics which were already corrected with sky subtraction. In each of these cases, the contribution from underlying galaxy light was less than 10% of the SN Ia light at maximum, so in WV08, we neglected any additional systematic uncertainty from over or under-subtracting this approximate correction for host galaxy contamination.

In lieu of full galaxy subtraction, rather than using the DoPHOT sky annulus surrounding the SN Ia in the SN image, we can alternatively measure the mean amount of galaxy light in the DoPHOT PSF at the location of the supernova in the host galaxy reference SNTEMP images and subtract this estimate from the supernova flux as an approximate host galaxy correction. This requires the assumption that the PSF of the SN and SNTEMP are the same, requiring no convolution. Seeing at PAIRITEL is limited by the dome seeing and remains relatively constant from 1.5–2.5″. A positive side-effect of this dome-limited seeing is that the amount of contaminating galaxy light within the PSFs used is nearly constant, usually to within a factor of $\sim$ 2–4. As such, this approximation also yields a reasonable correction for the host galaxy light contribution at the SN position requiring only the estimation of the PSF in each SNTEMP image, without the need for full image subtraction. While it is difficult to accurately estimate the PSF for an undersampled image, it is much more difficult to estimate the convolution kernel to transform between the PSFs of two different undersampled images.

For bright, well-isolated, SN, either of these approaches yields comparable results and is sometimes superior to full image subtraction on undersampled images. In practice, in WV08, we used the DoPHOT sky annulus approach for these SN because it is technically simpler and is independent of the quantity and quality of SNTEMP images, which in practice are each observed under different seeing conditions, even if the seeing is nearly constant. In the WV08 data set, SN Ia with LCs derived from direct forced DoPHOT photometry on the un-subtracted images with an approximate host galaxy subtraction correction from the DoPHOT sky annulus include 9 out of 21 objects: SN 2005el, SN 2005hk, SN 2005ke, SN 2006ac, SN 2006cp, SN 2006D, SN 2006gr, SN 2006lf, and SN 2006X while the remaining 12 objects used primarily NN2 difference imaging (see §4.3.1). However, improvements in our galaxy subtraction process have led us to use galaxy subtracted NNT photometry for all CfAIR2 SN Ia (see §3.4.2).

3.4.2 Forced DoPHOT Photometry on Difference Images

For all CfAIR2 SN Ia, we used subtraction-based photometry following Miknaitis et al. (2007). Unlike WV08, we used the same method both for bright and/or well-isolated SN Ia that required little host galaxy subtraction and for SN Ia clearly embedded inside their host galaxy that required signicant host galaxy subtraction. For all these SN Ia, the SN flux in the difference images is measured with forced DoPHOT photometry at fixed pixel coordinates, usually determined by averaging the SN centroids determined from J-band or CfA optical V-band difference images with photometric detections of the object that had a signal-to-noise ratio > 5. See

§7.2 for a discussion of how we compute the optimal SN coordinates for forced DoPHOT photometry from the subtracted images or other methods. See §4.2.5 for a discussion of systematic bias in photometry from errors in forced SN coordinates. Forced DoPHOT photometry at this fixed position in the difference images is done using the DoPHOT PSF calculated from the standard stars in the un-convolved image. For the difference images the calibrated zero point from the template is used, with suitable correction for the convolution of the SNTEMP image as detailed by Miknaitis et al. (2007). Flux measurements are calibrated to the 2MASS system using the photometric solutions to the 2MASS catalogs (Cutri et al. 2003).

In WV08, we employed the NN2 method of Barris et al. 2005 (as used in Miknaitis et al. 2007) by subtracting all $N \times (N-1)/2$ unique pairs of SN and SNTEMP images ($N = N_{\rm SN} + N_{\rm SNTEMP}$) to ostensibly minimize the sensitivity to subtraction errors for host galaxy template images of poor quality. NN2 has been shown to provide more accurate photometry for optical observations compared to cases where the subtractions are performed on a single SNTEMP image of poor image quality, for example an image with a larger than average FWHM or sky variance after sky subtraction (Barris et al. 2005; Miknaitis et al. 2007). However, for cases with 1 or more high signal-to-noise SNTEMP observations with adequate sampling of the PSF, NN2 on optical data was shown to provide diminishing returns, giving comparable results to subtraction of a single, high quality template (Barris et al. 2005). In addition, the photometric uncertainty estimates from NN2 could not be derived analytically and used approximations for which the authors expressed caution (Barris et al. 2005). Specifically, NN2 is predicated on the approximate assumption that subtraction errors are uncorrelated between different image pairs,

an assumption which the authors admit is certainly false in principle, but may be approximately true in practice for certain data sets.

Unfortunately, the NN2 process proved problematic for PAIRITEL images as employed in WV08. The PAIRITEL Infrared camera is undersampled because the $2''$ detector pixels are larger or comparable to the atmospheric seeing conditions at FLWO, with a typical FWHM of 1.5–2.5$''$. As a result, PAIRITEL can not fully sample the PSF of the detected image. In hopes of achieving some sub-pixel sampling, PAIRITEL does implement a randomized dither pattern with step sizes $\lesssim 2''$. In principle, dithering can help recover some of the image information lost from undersampling. However large pixels with dithered imaging cannot fully replace a fully sampled imaging system (Lauer 1999; Fruchter & Hook 2002; Rowe et al. 2011), and in practice, dithering does not always reliably produce the desired sub-pixel sampling. Early PAIRITEL mosaic pipelines (p1.0) did employ the Drizzle method originally developed to deal with dithered, undersampled, images for HST (Fruchter & Hook 2002). However, while the PAIRITEL Infrared camera is of similar type to the HST 256×256 pixel NICMOS3 array, we found that the computational overhead of Drizzle was not commensurate with the mosaicking results, which performed as good or better with a simpler, computationally faster co-addition with Swarp (Bertin et al. 2002). Because PAIRITEL data are not critically sampled, and because our images are constructed by SWarped mosaicking, which involved resampling from the detector pixel scale of $2''$/pixel to the mosaic pixel scale of $1''$/pixel, the reliability of the PAIRITEL image subtraction is not as good as the subtractions for the non-mosaicked optical images on which the NN2 method was used in Barris et al. (2005) and Miknaitis et al. (2007). In WV08, our photometric

pipeline automatically detected and screened out subtractions with problems, but because so many subtractions were flagged as poor, this process resulted in fewer high-quality light-curve points than would have been obtained in the case of perfect or improved subtractions. Furthermore, the SN Ia LCs for which we used NN2 in WV08 show some significant systematic deviations for fainter LC points from the galaxy subtracted photometry published by the CSP for the same objects above and beyond the deviations expected from small bandpass differences without S-corrections (Contreras et al. 2010; M. Phillips – private communication; also see §4.3.2-§4.3.3). This led us to consider the NNT as an alternative galaxy subtraction method to NN2 for the SN Ia in CfAIR2, noting that the p3.0–p3.6 PAIRITEL mosaics suffered from the same undersampling problems as p2.0 and earlier mosaics.

For the CfAIR2 data set, to minimize our sensitivity to accumulated systematic errors from the host galaxy subtraction process on undersampled images, and to allow our photpipe to include more LC points obtained from photometry on the difference images, we opted to reduce the number of individual difference images used in the host galaxy subtraction process. We achieved this by using the NNT method instead of the NN2 method in the subtraction process. In the NNT method, we obtain $N_{\rm SNTEMP}$ host galaxy SNTEMP images for each SN that meet our image quality requirements (See §3.3). For each of the $N_{\rm SN}$ mosaicked images containing the SN that also meet our image quality requirements, we subtract each of the $N_{\rm SNTEMP}$ SNTEMP images, yielding $N_{\rm SN} \times N_{\rm SNTEMP}$ individual subtractions. To distinguish from the $N \times (N-1)/2$ individual subtractions in the NN2 method, we call this the NNT (or NNTEMP) method. The NNT method yields $N_{\rm SNTEMP}$ realizations of the LC which can be combined into a final galaxy subtracted LC by

performing a night-by-night weighted average of the photometry along with robust 3-σ rejection, which tended to exclude individual bad subtractions with an approach superior to letting our photpipe screen out bad subtractions in an automated way, as we did in WV08.

Figure 3.15 illustrates the NNT method for 2 example SN Ia, SN 2006D and SN 2006X. The left panels of Figure 3.15 show the subtracted LCs for each of the $N_{\rm SNTEMP} = 6$ and $N_{\rm SNTEMP} = 4$ SNTEMP images for SN 2006D and SN 2006X, respectively. The right panels of Figure 3.15 show the LCs after NNT weighted averaging. By obtaining $N_{\rm SNTEMP} \sim$ 2–10 realizations of the host galaxy image — including additional SNTEMP observations since WV08 — most SN Ia had $N_{\rm SNTEMP} \gtrsim 4$ images suitable for host galaxy subtraction. With these additional realizations of the host galaxy template, the NNT method allowed us to downweight individual bad subtractions that have not already been removed by our bad image rejection algorithm by averaging over the variance in the galaxy subtraction process. This allows us to produce SN Ia LCs for CfAIR2 that suffered from smaller systematic galaxy subtraction errors compared to NN2 for WV08 (See §4.2.2). These new NNT LCs from the CfAIR2 data set also show increased agreement with CSP photometry for the same objects compared to WV08 (§4.3.2).

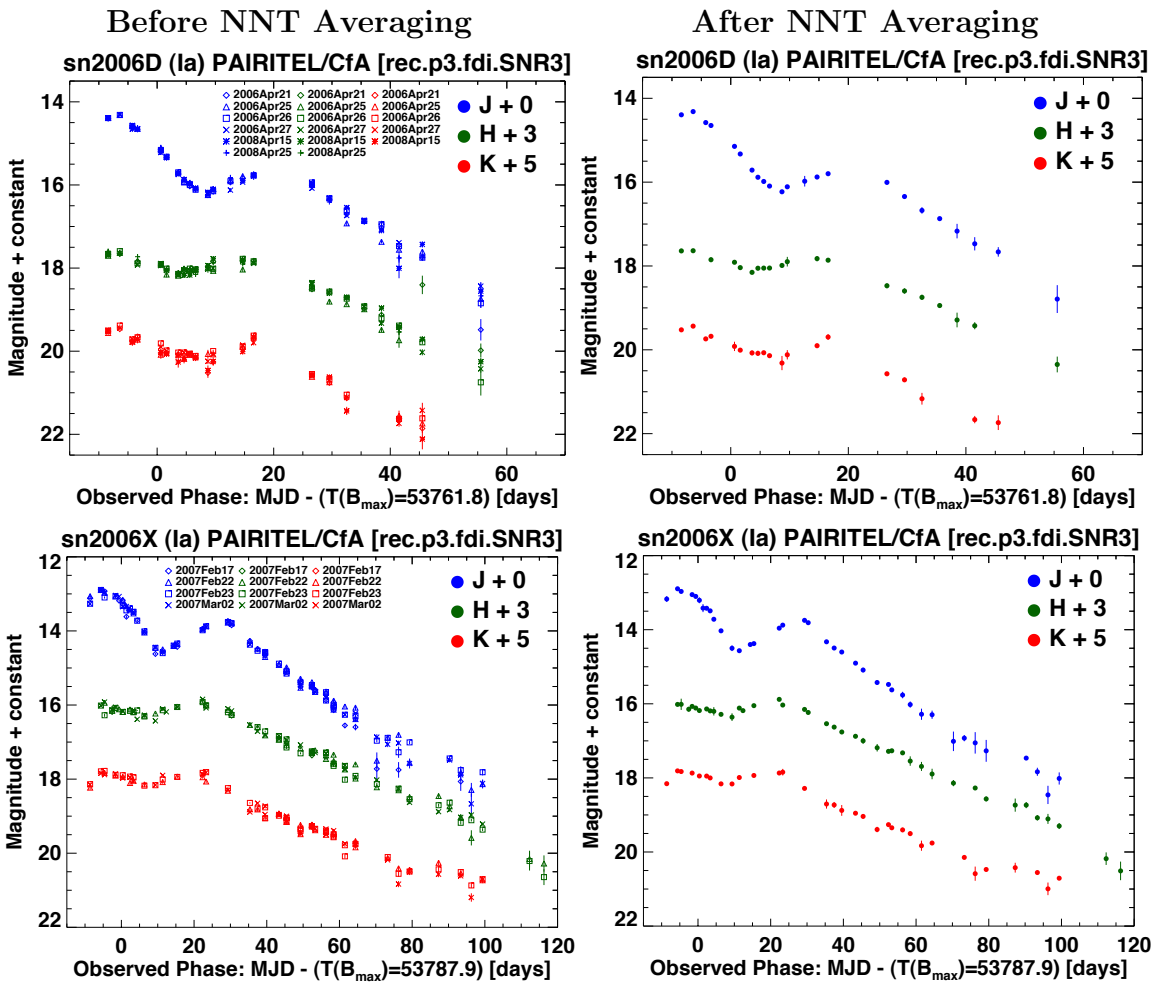

Figure 3.15.— Illustration of the NNT Averaging Process.

(**Left Column**) LCs for SN 2006D and SN 2006X *before* NNT night-by-night weighted averaging. The JHK_s LCs are displayed in blue, green, and red, respectively, offset vertically for clarity. LCs from subtractions for each of the SNTEMP images ($N_{\rm SNTEMP} = 6$ and $N_{\rm SNTEMP} = 4$ for SN 2006D and SN 2006X, respectively) are shown with different plot symbols for each band, corresponding to the dates of the SNTEMP observation in the legend.

(**Right Column**) LCs for SN 2006D and SN 2006X *after* NNT. The magnitudes from DoPHOT photometry on multiple subtracted images are combined with a weighted average. To account for the random over or under-subtraction of flux from difference imaging on undersampled images, we add the standard deviation of the individual subtraction based magnitude measurements for each night in quadrature with the error on the weighted mean, weighted by the nightly DoPHOT photometric errors. This can be seen most clearly in error bars for the late time points which are fainter and often show larger scatter between individual subtractions on a given night.

3.5 Photometry Pipeline Improvements

In Wood-Vasey et al. 2008, we used the photometry pipeline originally developed to process optical observations for the ESSENCE and SuperMACHO projects, and adapted it to process PAIRITEL NIR p2.0 mosaic images. We have since incorporated several major new improvements in the content and implementation of the pipeline to produce the CfAIR2 data set. The new photometry pipeline takes p3.6 mosaics instead of p2.0 mosaics as input (See §3.1). By letting the mosaic center be the center of all imaging rather than the SN coordinates, 15% more mosaics were created with p3.6 compared to p2.0. This allows us to publish additional observations for the SN Ia with LCs published in WV08 and include more observations for the newest SN Ia than would have been possible with p2.0. However, the new p3.6 mosaics required several significant changes to work with our photometry pipeline.

Because the p3.6 mosaic center is the center of all imaging — which varies from night to night as a result of different randomized dither patterns and pointing errors — successful p3.6 mosaics will contain the SN somewhere in the mosaic, but not necessarily in the mosaic center as it was forced to be for p2.0. For example, the SN could end up in the upper left corner of a given p3.6 mosaic, a case that would have caused p2.0 to fail. As a result, p3.6 mosaics do not necessarily contain all the same field stars from night to night (See Tables 4.1–4.2). This issue did not affect p2.0 images, where the constraint of the SN in the mosaic center forced all successful p2.0 mosaics to contain essentially all the same field stars. More specically, when we register all p3.6 mosaics for a given SN to a common spatial frame with SWarp, and

place the SN in the center of the SWarped mosaics, individual 2MASS standard stars at the edges of images will not necessarily be present in all images for a given SN. To account for this, we modified our photometry pipeline to include larger 2MASS photometric catalogs with search radii ∼5 times the radius of the catalogs we used in WV08 (Also see §4.1). This allows us to perform DoPHOT photometry on the SWarped images, calibrated with a larger set of 2MASS standard stars.

We also incorporated the new p3.6 noise mosaics into the photometry pipeline. In WV08, we used an estimate of the background "skark" noise from the sky and dark current which was assumed to be constant throughout the image (See §3.2). As seen in Figure 3.10, the assumption of a constant skark background is a bad approximation, due both to arcminute scale spatial sky brightness variations across the mosaic FOV and the spatially persistent, characteristic dark current patterns in each of the JHK_s detectors which get smeared out over the mosaic dither pattern. In fact, the estimated skark noise actually varies by $\sim$ 10–100% across individual skark mosaics. By allowing the modeled noise to vary across the mosaic, we now have more reliable *differential* noise estimates at the positions of all standard stars and the SN, although our *absolute* estimate of the noise is underestimated since the noise mosaics do not model all sources of uncertainty (See §7.1). To account for this, we also incorporate a procedure for empirically calculating the inevitable underestimate of the noise using our standard star photometry, and correcting for this in the SN Ia photometry (see §4.1). Accurate noise estimates are crucial when the pipeline performs DoPHOT photometry on point sources in the subtracted or un-subtracted images.

In addition to employing the NNT method instead of NN2 for host galaxy

subtraction, we have also improved the difference imaging process itself for photpipe since WV08. The new p3.6 noise mosaics are now also fed as inputs to HOTPANTS, our difference imaging module for host galaxy subtraction (See §3.4). This leads to improved difference imaging versus Wood-Vasey et al. 2008, where we fed HOTPANTS a constant skark background value which it used to construct its own approximate noise maps. However, because the mosaic center can vary from night to night for a given SN, this complicates the difference imaging process. To subtract any two images taken on different nights, for example a SN image and a SNTEMP host galaxy reference image, we first align them to a common pixel coordinate frame with SWarp, placing the SN in the center of the SWarped images. SN generally have different pixel coordinates in each original 512×512 pixel p3.6 mosaic image, which yields an overlap region for the SWarped images smaller than 512×512 pixels. In order to subtract the SWarped images, we must correctly mask out the non-overlap regions to exclude them from the subtraction process, to avoid residuals of the non-overlap regions in the difference images which can confound or prevent the solution for the kernel to convolve one image to the PSF of the other (See §3.4).

3.5.1 Computational Improvements

We also made a major technical change to implement our photometry pipeline on a new computational architecture, moving the data and pipeline software from the CfA Hydra cluster, run by the Harvard-Smithsonian Center for Astrophysics to the Harvard FAS Odyssey cluster, run through the Harvard Faculty of Arts and

Sciences Research Computing Group[2]. The Odyssey cluster offered larger disk space, improved disk speed, better technical support, and significantly more processing power, giving us access to hundreds of computational nodes through the powerful LSF batch job queue scheduling system. Each independent software module we needed for our pipeline, for example, a particular version of python or perl, could be loaded as a separate module at run time as needed. The ESSENCE version of the photometry pipeline was first installed and tested on the Odyssey cluster by A. Rest, W.M. Wood-Vasey, and G. Narayan. The PAIRITEL NIR version of the pipeline for p3.6 mosaics was branched from the ESSENCE pipeline, set up, and modified considerably by W.M. Wood-Vasey and A. Friedman. A. Friedman wrote software to run all sub-steps of the photometry pipeline from images to light curves in an optimal automated fashion using the LSF queue system and bsub job control software. This involved partitioning the pipeline into as many independent computational sub-steps as possible, sending these out to be executed in parallel as individual serial jobs on different computational nodes as they became available, and using the LSF queue bsub job condition control software to make sure that groups of computational sub-steps were automatically executed in the correct order only after all their pre-requisite sub-steps were complete. This near-full automation allows us to reprocess the entire photometric data set, including nearly 15,000 images overnight in $\sim 5-7$ hours depending on node availability, dramatically speeding up the testing and improvement of the pipeline software and its light curve output. By comparison, a similar task would have taken weeks to months using the computational infrastructure we were using at the time of Wood-Vasey et al. 2008.

[2]See `http://rc.fas.harvard.edu/` for details on the Harvard FAS Odyssey cluster.

Chapter 4

Photometry

Photometry

In this section we discuss various tests used to assess the accuracy and precision of PAIRITEL photometry, utilizing internal consistency checks and comparison with comparable external data sets with NIR photometry for the same objects. In §4.1, we discuss photometric calibration of PAIRITEL, presenting PAIRITEL photometry for 2MASS stars which we use to test the precision and accuracy of PAIRITEL DoPHOT photometry. In §4.2, we investigate potential systematic errors in the photometry, including those from host galaxy subtraction, sky subtraction, forced photometry coordinates, and other sources. In §4.3, we compare our original PAIRITEL WV08 photometry to the new CfAIR2 photometry along with external consistency checks comparing PAIRITEL photometry to published CSP photometry for an overlapping subset of the SN Ia in CfAIR2. In §4.4, we present our final SN Ia photometry for the CfAIR2 data set.

4.1 Photometric Calibration

Since the PAIRITEL 1.3-m telescope uses the 2MASS northern telescope along with the transplanted 2MASS southern camera, the 2MASS point source catalog (Cutri et al. 2003) is the natural astrometric and photometric reference system for these observations. Even though p3.6 mosaicked images do not have the same standard stars in all images for a given SN, in a typical $12' \times 12'$ FOV, there were $\sim$6–90 2MASS stars in each filter, most of which were present in multiple mosaics across different nights (see Table 4.1 and Fig. 4.1). For the tests in §4.1, we only include

2MASS stars that are present in at least 5 $\times$ p3.6 mosaics and thus have at least 5 photometric measurements for a given SN Ia LC. For photometry on individual images, we also require a minimum of 5 different 2MASS stars in a given mosaic to compute a zero point solution. We perform DoPHOT photometry on all 2MASS stars (and all other point sources detected as stars by DoPHOT) in all PAIRITEL SN fields, although we only use 2MASS stars to estimate the photometric zero point for each image. As we move toward longer wavelength, a decreasing average number of 2MASS stars detected by DoPHOT meet our selection criteria. More specifically, for all SN Ia, the mean and standard deviation for the number of standard stars in at least 5 mosaic images was 39 ± 22, 38 ± 22, and 34 ± 21 in JHK_s, respectively. In addition, the minimum and maximum number of standard stars in at least 5 mosaic images were $8, 6, 6$ and $92, 91, 91$ in JHK_s, respectively (see Table 4.1).

Table 4.1. Number of 2MASS Stars in 122 PAIRITEL JHK_s SN Ia Fields

SN Name	N_J	N_H	N_K	SN Name	N_J	N_H	N_K	SN Name	N_J	N_H	N_K
sn2011df	81	81	81	sn2009ds	14	15	···	sn2007hj	47	50	36
sn2011de	31	29	25	sn2009do	22	19	22	sn2007fb	···	···	···
sn2011by	17	17	16	sn2009dc	37	37	34	sn2007cq	36	34	26
sn2011at	66	66	48	sn2009bv	14	14	14	sn2007co	77	77	72
sn2011ay	···	···	···	sn2009al	20	20	15	sn2007ca	39	36	24
sn2011ao	11	8	11	sn2009an	24	26	24	sn2007bz	12	10	···
sn2011ae	32	32	25	sn2009ad	70	69	63	sn2007bj	72	72	49
sn2011aa	53	50	47	sn2009Y	58	56	43	sn2007S	27	28	23
sn2011K	47	47	39	sn2009D	21	18	20	sn2006mq	92	91	91
sn2011B	36	33	35	sn2008hy	88	87	78	sn2006lf	71	70	70
sn2010lq	···	···	···	sn2008hv	33	33	29	sn2006le	86	84	83
sn2010ko	70	70	60	sn2008hs	···	···	···	sn2006is	48	47	42
sn2010kg	75	73	68	sn2008hm	81	81	81	sn2006gr	52	52	42
sn2010jv	···	···	···	sn2008hj	18	19	13	sn2006cz	42	38	···
sn2010ju	71	69	68	sn2008ha	28	28	22	sn2006cp	20	20	15
sn2010jm	8	12	···	sn2008gl	20	21	14	sn2006bq	73	75	68
sn2010iw	42	40	38	sn2008gb	72	72	71	sn2006az	16	18	16
sn2010it	20	16	10	sn2008fx	15	18	16	sn2006ax	26	25	19
sn2010gn	25	15	···	sn2008fv	···	···	···	sn2006ac	17	19	19
sn2010ex	···	6	6	sn2008fr	22	21	17	sn2006X	29	26	24
sn2010ew	24	23	7	sn2008dg	41	42	25	sn2006N	66	66	59
sn2010dw	60	55	32	snf20080522-011	42	39	28	sn2006E	40	39	38
snPTF10icb	11	11	···	snf20080522-000	10	···	6	sn2006D	16	16	16
sn2010dl	22	27	20	snf20080514-002	16	15	19	sn2005na	76	76	75
sn2010cr	21	21	25	sn2008ar	12	12	8	sn2005mc	43	46	42
sn2010ai	27	36	39	sn2008af	27	24	23	sn2005ls	87	86	85
sn2010ag	60	58	53	sn2008ae	21	22	17	sn2005ke	22	22	20
snPTF10bjs	12	14	14	sn2008Z	19	17	16	sn2005iq	33	33	28
snpsb26	29	27	27	sn2008C	82	80	80	sn2005hk	28	31	24
sn2010Y	21	22	19	sn2008A	60	52	51	sn2005hf	28	27	26
sn2010H	76	71	63	sn2007ux	23	25	22	sn2005eu	55	55	53
sn2009na	21	19	17	sn2007sw	13	12	11	sn2005eq	22	21	18
sn2009le	16	17	14	sn2007ss	27	26	23	sn2005el	63	63	52
sn2009lf	24	25	24	sn2007sr	39	40	39	sn2005ch	31	31	27
sn2009kq	38	36	27	sn2007rx	27	26	26	sn2005cf	50	49	44
sn2009kk	28	27	23	sn2007qe	28	26	24	sn2005cc	26	26	26
sn2009jr	57	58	55	sn2007nq	21	18	15	sn2005bo	27	27	21
sn2009ig	21	21	12	sn2007le	29	27	24	sn2005bl	18	18	19
sn2009im	33	35	29	sn2007kk	65	64	63	sn2005ak	30	30	27
sn2009fv	45	45	33	sn2007ir	72	72	52	sn2005ao	52	53	43
sn2009fw	66	64	52	sn2007if	20	19	20	···	···	···	···

Note. — N_X, $(X = J, H, K)$ is the number of 2MASS standard stars found in at least 5 PAIRITEL mosaicked images for each SN Ia light curve in JHK_s. For each image, a subset of these stars that are found in the image are used to calculate the photometric zero point for each SN Ia. Due to the pointing variability of PAIRITEL, the same standard stars are not necessarily in all mosaicked images for a given SN Ia light curve, so these numbers indicate the maximum number of 2MASS stars present in a given mosaic for that SN Ia. However, most stars appear in almost all mosaics for a given SN Ia (See §3.1 and Table 4.2). The ellipsis ··· indicates that no stars were matched to the 2MASS catalog in at least 5 mosaicked images for that SN Ia in that bandpass. For the 6 cases where ··· is listed in each of the JHK_s bands (sn2007fb, sn2008fv, sn2008hs, sn2010jv, sn2010lq, and sn2011ay), the SN actually had successful photometry but there was an error in the script that outputs DoPHOT star photometry information used to compile the above table.

Because PAIRITEL photometry is deeper than 2MASS photometry (See §2.5), the ∼6–90 2MASS stars per filter were sufficient to calibrate the images to the 2MASS JHK_s system firmly enough that the underlying 3% 2MASS calibration uncertainty is the dominant systematic error in the photometric calibrations for the light curves presented here[1]. Cohen et al. (2003) and Skrutskie et al. (2006) describe the 2MASS JHK_s filter system in detail while Carpenter (2001) and Leggett et al. (2006) provide color transformations to convert observations from other widely used photometric systems to the 2MASS filter system. More recently, Contreras et al. 2010 perform photometry on 2MASS stars in the fields of CSP SN Ia, calculating zero point filter offsets and color terms to approximately transform between the CSP natural system and the 2MASS J and H bands (See §4.3.3), although the most accurate transformations require S-corrections using SN Ia SEDs (e.g Stritzinger et al. 2002). A major advantage of PAIRITEL compared to other ground-based Infrared telescopes is that the natural system photometry is already on the standard 2MASS JHK_s system. PAIRITEL thus avoids an additional source of systematic uncertainty from using S-corrections based on highly uncertain SN Ia SEDs from the currently limited NIR spectral sample (e.g. Hsiao et al. 2007; Marion et al. 2009).

Section 4.1 is organized as follows. In §4.1.1 we present light curves of 2MASS stars observed by PAIRITEL for example SN Ia fields along with PAIRITEL mean photometric measurements and uncertainties[2] of all 2MASS stars in the CfAIR2 data set, essentially the PAIRITEL version of the 2MASS catalog for all the SN Ia

[1]Other sources of systematic uncertainty including systematic errors incurred from host galaxy image subtraction are discussed in §4.2.

[2]The PAIRITEL uncertainties for 2MASS stars in Table 4.2 have been corrected for DoPHOT uncertainty estimates as described in §4.1.3.

fields we observed. In §4.1.2-4.1.3, we qualitatively and quantitatively address two major questions as an internal consistency check of our photometry using only PAIRITEL data and the 2MASS catalog calibration. In §4.1.2, we test whether DoPHOT is correctly estimating photometric uncertainties for PAIRITEL point sources and in §4.1.3, we assess whether the global mean of all PAIRITEL standard star photometry agrees with 2MASS photometry given our best estimate of the photometric uncertainties. The former question helps us assess our photometric precision, to test whether we have correctly estimated our errors and to empirically compute a correction factor if we have underestimated our uncertainties. The latter question tests our photometric accuracy to rule out any major systematic differences with 2MASS, which would indicate problems with PAIRITEL DoPHOT photometry on the un-subtracted images.

4.1.1 PAIRITEL Photometry of 2MASS Standard Stars

Figure 4.1 presents light curves of all 2MASS stars in the fields of 2 example SN Ia, SN 2005ao and SN 2005eq, shown in order of decreasing 2MASS catalog magnitude. Standard star light curves are plotted as residuals of the the nightly PAIRITEL photometry pipeline magnitude minus the weighted mean PAIRITEL magnitude over all nights as a function of the Modified Julian Date (MJD), offset by a constant to keep the x-axis values between 0 and 100 days. For clarity, photometric uncertainties on the residuals are not shown in Figure 4.1, but they are discussed in detail in §4.1.2. Overplotted are the residuals for the weighted mean PAIRITEL magnitude (solid line) and the 2MASS catalog magnitude (dashed line), with the

2MASS catalog magnitude shown in the lower left of each panel. We interpret the error on the weighted mean of the PAIRITEL photometric measurements to be the uncertainty in the measurement of the mean PAIRITEL magnitude for that 2MASS star (See Appendix §7.3 for mathematical details). Table 4.2 presents weighted mean PAIRITEL photometric measurements and uncertainties for all 2MASS stars in 122 SN Ia fields observed by PAIRITEL. A global comparison of PAIRITEL and 2MASS star measurements is presented in §4.1.2–4.1.3.

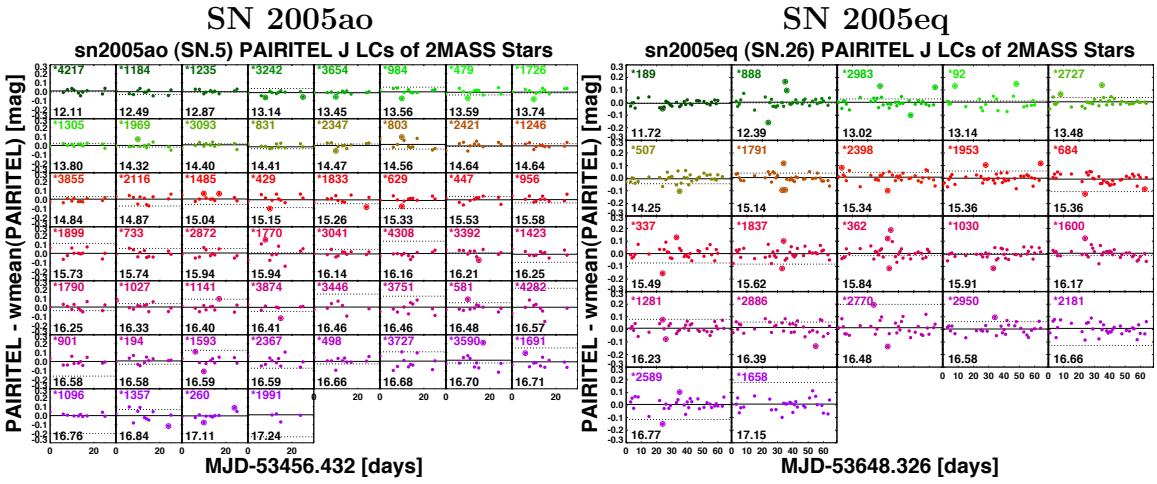

Figure 4.1.— PAIRITEL J-band LCs of 2MASS Stars in Example SN Ia Fields

PAIRITEL J-band LCs of 52 and 22 2MASS J-band standard stars used to determine the photometric zero points for SN 2005ao and SN 2005eq, respectively. Standard star light curves are plotted as residuals of the nightly PAIRITEL photometry pipeline magnitude minus the weighted mean PAIRITEL magnitude over all nights as a function of the Modified Julian Date (MJD), offset by a constant to keep the x-axis values between 0 and 100 days. Light curves are ordered by decreasing 2MASS catalog brightness, displayed in bold black in the lower left corner of each panel. Overplotted are the residuals for the weighted mean PAIRITEL magnitude (solid line) and the 2MASS catalog magnitude (dashed line). Individual measurements more than 3-σ away from the weighted mean PAIRITEL magnitude are marked with a large open circle around the data point (small solid circle). Nights with > 4 stars measured as $\gtrsim$ 3-σ outliers allow us to identify nights with poor image quality that should be excluded from our SN Ia LCs by our bad image rejection algorithm (See § 3.3).

Table 4.2:: PAIRITEL JHK_s Photometry of 2MASS Standard Stars in SN Ia Fields

SN	Star [a]	α(2000)	δ(2000)	N_J [b]	$m_J^{\rm PTL}$ [mag][c]	$\sigma_{m_J}^{\rm PTL}$ [mag][d]	$m_J^{\rm 2M}$ [mag][e]	$\sigma_{m_J^{\rm 2M}}$ [mag][e]	N_H [b]	$m_H^{\rm PTL}$ [mag][c]	$\sigma_{m_H}^{\rm PTL}$ [mag][d]	$m_H^{\rm 2M}$ [mag][e]	$\sigma_{m_H^{\rm 2M}}$ [mag][e]	N_K [b]	$m_K^{\rm PTL}$ [mag][c]	$\sigma_{m_K}^{\rm PTL}$ [mag][d]	$m_K^{\rm 2M}$ [mag][e]	$\sigma_{m_K^{\rm 2M}}$ [mag][e]
sn2005ak																		
SN	Star	α(2000)	δ(2000)	N_J	$m_J^{\rm PTL}$	$\sigma_{m_J}^{\rm PTL}$	$m_J^{\rm 2M}$	$\sigma_{m_J}^{\rm 2M}$	N_H	$m_H^{\rm PTL}$	$\sigma_{m_H}^{\rm PTL}$	$m_H^{\rm 2M}$	$\sigma_{m_H}^{\rm 2M}$	N_K	$m_K^{\rm PTL}$	$\sigma_{m_K}^{\rm PTL}$	$m_K^{\rm 2M}$	$\sigma_{m_K}^{\rm 2M}$
05ak	01	14:40:18.45	+03:30:55.44	34	16.549	0.007	16.504	0.159	35	15.940	0.009	16.024	0.183	30	15.675	0.012	15.251	0.173
05ak	02	14:40:18.56	+03:34:12.76	34	15.918	0.006	15.858	0.097	33	15.230	0.008	15.230	0.105	33	15.024	0.010	15.075	0.148
05ak	03	14:40:19.41	+03:30:22.95	34	15.112	0.006	15.118	0.056	35	14.768	0.007	14.822	0.085	33	14.686	0.008	14.814	0.112
05ak	04	14:40:20.77	+03:27:36.99	34	16.404	0.006	16.430	0.150	35	15.793	0.009	16.057	0.219	34	15.549	0.012	15.326	0.197
05ak	05	14:40:20.94	+03:33:41.82	33	15.013	0.006	15.071	0.049	34	14.408	0.007	14.511	0.071	34	14.301	0.007	14.285	0.074
05ak	06	14:40:22.26	+03:31:18.61	33	17.032	0.007	16.521	0.147	33	16.386	0.010	16.101	0.215	29	16.153	0.014	15.598	0.255
05ak	07	14:40:22.58	+03:32:56.39	35	15.637	0.006	15.665	0.066	35	15.001	0.007	15.133	0.089	34	14.765	0.008	14.946	0.148
05ak	08	14:40:26.00	+03:31:41.52	34	13.255	0.005	13.233	0.024	35	12.617	0.006	12.608	0.030	35	12.406	0.007	12.404	0.032
05ak	09	14:40:26.55	+03:30:58.65	34	14.780	0.006	14.762	0.037	35	14.212	0.007	14.121	0.035	35	13.967	0.007	14.003	0.071
05ak	10	14:40:29.45	+03:32:34.68	35	16.402	0.006	16.596	0.163	35	15.757	0.008	15.736	0.152	32	15.571	0.011	15.228	0.173
05ak	11	14:40:29.89	+03:28:05.44	33	14.455	0.006	14.444	0.038	34	14.160	0.006	14.114	0.035	33	14.055	0.007	14.095	0.072
05ak	12	14:40:30.02	+03:30:15.93	34	15.424	0.005	15.319	0.072	33	14.958	0.007	15.021	0.090	35	14.793	0.008	14.624	0.123
05ak	13	14:40:31.33	+03:28:33.93	24	15.472	0.010	15.589	0.082	28	14.814	0.011	15.169	0.100	31	14.488	0.010	14.898	0.150
05ak	14	14:40:31.52	+03:32:31.31	36	14.373	0.005	14.367	0.036	36	14.171	0.007	14.212	0.042	36	14.145	0.007	14.277	0.086
05ak	15	14:40:31.74	+03:29:10.30	35	15.420	0.006	15.304	0.056	34	14.804	0.007	14.823	0.070	35	14.574	0.008	14.704	0.116
05ak	16	14:40:32.31	+03:31:13.54	34	16.087	0.006	15.902	0.090	36	15.501	0.008	15.476	0.132	...	...	...	...	...
05ak	17	14:40:32.43	+03:33:34.39	28	14.766	0.010	14.756	0.056	26	14.069	0.012	14.143	0.085	29	13.836	0.011	13.802	0.070

(**This Table will be available in its entirety in a machine-readable form in the online electronic version of this paper, Friedman et al. 2012** *in preparation to be submitted to the Astrophysical Journal (ApJ)*. **A portion is shown here for guidance regarding its form and content).**

(a) The superscripts PTL and 2M denote PAIRITEL and 2MASS, respectively. Missing data is denoted by ...
(b) N_X is the number of PAIRITEL SN images in band $X = J, H, K$ with this standard star used to measure $m_X^{\rm PTL}$ and $\sigma_{m_X}^{\rm PTL}$.
(c) The PAIRITEL magnitudes $m_X^{\rm PTL}$ are computed as the weighted mean PAIRITEL magnitude over all N_X SN images with that star.
(d) The PAIRITEL uncertainties $\sigma_{m_X}^{\rm PTL}$ are computed as the error on the weighted mean of the N_X measurements, each of which have already been corrected for DoPHOT uncertainty estimates as described in §4.1.3. The error on the weighted mean is given approximately by the standard deviation of all PAIRITEL magnitude measurements for each star divided by $\sqrt{N_X}$ (see §7.3).
(e) The 2MASS magnitudes $m_X^{\rm 2M}$ and uncertainties $\sigma_{m_X}^{\rm M}$ for each star are from the 2MASS point source catalog (Cutri et al. 2003).

4.1.2 Photometric Precision

In this section, we assess the repeatability of DoPHOT measurements of 2MASS stars to quantify the photometric precision of PAIRITEL. This internal consistency check tests whether we have correctly estimated our uncertainties for point sources measured on individual nights. *A priori*, we expect that we are underestimating our photometric errors, because we do not model all known sources of uncertainty in computing our noise mosaics (See §3.2 and §7.1). Assuming 2MASS stars are well modeled by constant LCs, the measured scatter can be used to assess if the PAIRITEL DoPHOT photometric uncertainties are under or overestimated. We quantify this by computing the standard deviation of the error normalized residuals for each standard star LC (see Appendix §7.3 for mathematical details). Empirical tests using DoPHOT photometry of 2MASS stars in the un-subtracted images confirm we are underestimating our photometric magnitude uncertainties by factors of $\sim$ 1.5–3, depending on the brightness of the point source and the filter. We then multiply the uncorrected DoPHOT magnitude uncertainties ($\sigma_{\rm do}$) for individual points in the SN Ia LCs by this empirically measured, magnitude-dependent, correction factor (See Figure 4.4). Our tests assume that light curves of 2MASS stars are approximately constant within the PAIRITEL measured uncertainties over the timescales of SN LCs. Although all stars are variable at some level , we do not expect this to significantly affect our results when using $\gtrsim$ 4000 2MASS thousand stars for each filter from 122 SN Ia fields observed by PAIRITEL (See Table 4.2).

Figure 4.2 shows PAIRITEL J-band photometry for 2MASS stars in the field of SN 2005ao (also see Figure 4.1) along with histograms of the associated error

normalized residuals for each star, color coded and in the same order as the light curves, displayed by decreasing 2MASS catalog magnitude. The standard deviations of the J-band error normalized residuals ($\sigma_{\hat{r_{\rm P}}}$) for individual stars in Figure 4.2 are empirically measured to be $\sigma_{\hat{r_{\rm P}}} \sim 1.5$–4. After removing $3-\sigma$ outliers, the aggregated J-band error normalized residuals for all standard stars in the field of SN 2005ao in Figure 4.2 have standard deviation $\sigma_{\hat{r_{\rm P}}} = 2.84$, indicating that our DoPHOT errors are underestimated by an average factor of ~ 3 for the stars in this SN Ia field. Figure 4.3 shows the same information as Figure 4.2 for SN 2005ao for each of the JHK_s bands with the standard star LCs, the associated histograms of the error normalized residuals for each standard star, and the aggregated error normalized residuals shown in the first, second, and third rows of Figure 4.3, respectively. After removing $3-\sigma$ outliers — which may have also been identified as measurements from images excluded by our bad image rejection algorithm (see §3.3) — we find aggregated standard deviations of $\sim$3 in each band, or more specifically $\sigma_{\hat{r_{\rm P}}} = 2.84$, 3.09, and 3.09 in JHK_s, respectively, for SN 2005ao.

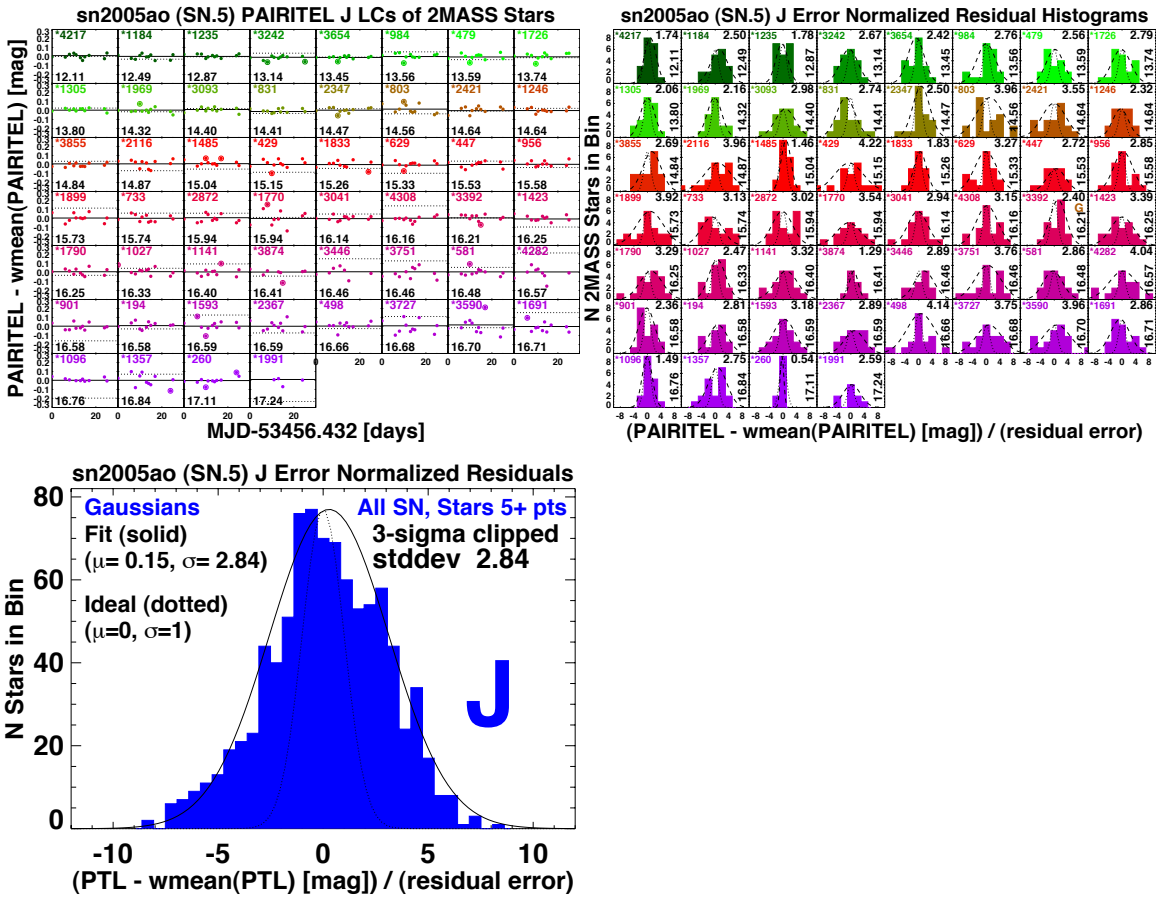

Figure 4.2.— SN 2005ao 2MASS Star J-band LCs and Error Normalized Residual Histograms

(**Upper left**) PAIRITEL J-band LCs for 2MASS standard stars in the field of SN 2005ao (see caption of Figure 4.1, where already shown), displayed left to right top to bottom by decreasing 2MASS star brightness, which is listed in black in the lower left of each panel.

(**Upper Right**) Histograms of associated J-band error normalized residuals for each standard star, color coded and in the same order as the light curves in the top row. The 2MASS catalog magnitude is shown on the upper left of each panel in black below the star ID number. The standard deviations of the error normalized residuals for each star ($\sigma_{\hat{r_P}}$) are displayed in the upper right of each panel, empirically measured to be $\sigma_{\hat{r_P}} \sim 1.5$–4.

(**Bottom Left**) Histogram of aggregated J-band error normalized residuals for all standard stars in the field of SN 2005ao after removing $3-\sigma$ outliers, with aggregated standard deviation $\sigma_{\hat{r_P}} = 2.84$. This indicates that our DoPHOT errors are underestimated for this SN Ia by an average factor of ~ 3.

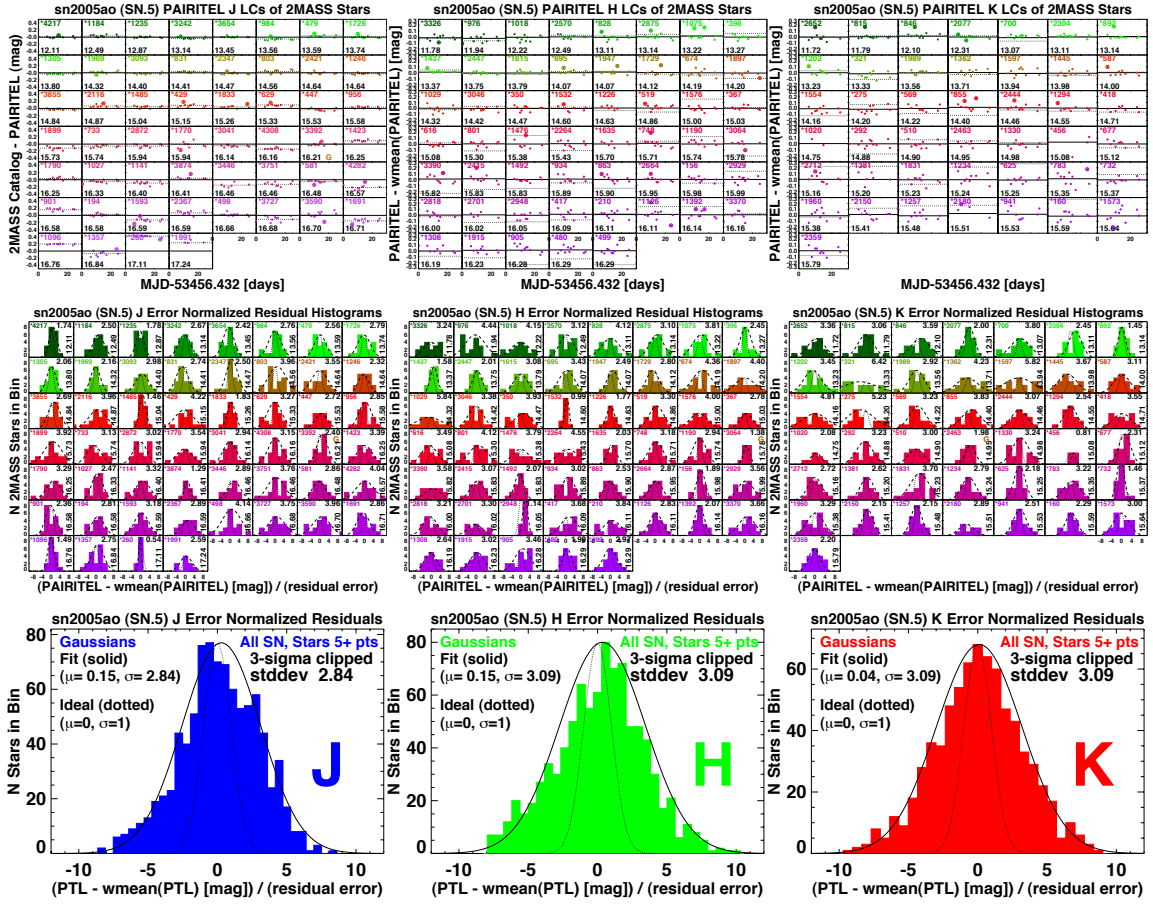

Figure 4.3.— SN 2005ao 2MASS Star JHK_s LCs, Error Normalized Residuals, and Aggregated Histograms

Figure 4.3 figure shows the same information as displayed only for the J-band in Figure 4.2 for SN 2005ao, shown here for the JHK_s bands in each column.

(**First row**) Standard star LCs for SN 2005ao.

(**Second row**) Associated histograms of error normalized residuals for each standard star.

(**Third row**) Aggregated error normalized residuals for all standard stars in the field of SN 2005ao after removing 3-σ outliers, with aggregated standard deviations of $\sigma_{\hat{r_P}} = 2.84$, 3.09, and 3.09 in JHK_s, respectively. This indicates that our DoPHOT errors are underestimated for this SN Ia by an average factor of ~ 3 in each of the JHK_s bands.

A more statistically powerful sample is obtained by aggregating the error normalized residuals for all 2MASS stars in JHK_s for all SN Ia in our sample. The left panel of Figure 4.4 shows this global aggregate of the error normalized residuals for all 2MASS stars for all SN Ia fields. Similar to the results shown for our example SN Ia, SN 2005ao, aggregated error normalized residuals for all SN show that we have also globally underestimated our uncertainties on the residuals by mean factors of $C \sim 2.9$–3.2 in JHK_s, or $C_J = 2.85, C_H = 3.18$, and $C_{K_s} = 2.88$, in JHK_s respectively. We assume that our uncertainty underestimates on the residuals comes fundamentally from underestimating $\sigma_{\rm do}$ on individual nights. We then derive the function relating the required DoPHOT correction factor $C = C(\sigma_{\hat{r_{\rm P}}}, \sigma_{\rm do}, \sigma_{\tilde{m_{\rm P}}}) \approx \sigma_{\hat{r_{\rm P}}}$ to the standard deviation of the error normalized residuals (see Figure 4.4, and Appendix §7.3).

In the right panel of Figure 4.4, we show that the DoPHOT correction factor C — and therefore also the standard deviation of the error normalized residuals $\sigma_{\hat{r_{\rm P}}}$ — depends on the standard star brightness, with an initial increase for the brighter stars in J and H followed by a decrease for stars fainter than some turnover magnitude $m_J^{\rm turn} \sim 14.5$, $m_H^{\rm turn} \sim 13$, and $m_{K_s}^{\rm turn} \sim 11$ in JHK_s, respectively. We interpret these relations as an indicator of the tradeoff between our DoPHOT underestimates of the noise from the source, which dominates for brighter stars, and the noise from the sky + dark current (skark), which dominates for fainter stars. The turnover magnitude is the brightness at which these contributions are approximately equal, and we find that, as expected, $m_J^{\rm turn} > m_H^{\rm turn} > m_{Ks}^{\rm turn}$ because the sky+dark noise becomes increasingly dominant toward longer NIR wavelengths. The K_s-band turnover at $m_{Ks}^{\rm turn} \sim 11$ mag demonstrates that the skark noise is the dominant noise

source in K_s for essentially the entire star brightness range $\sim$ 11 to 17 mag. This underscores the difficulty of making accurate and precise K_s-band measurements. The curves also show decreasing scatter toward decreasing brightness mainly because we achieve greater statistical power from measurements of many more standard stars at the fainter end. Overall, the standard deviation of the error normalized residuals tells us how much we are underestimating our DoPHOT uncertainties for sources of any brightness in the range 11 to 17 mag. These relations in the right panel Figure 4.4 are fit with 2-degree polynomials which we use to empirically correct our SN Ia photometry errors by multiplying our original uncertainty estimates by these factors as a function of their brightness and filter for each SN Ia measurement. The corrected DoPHOT errors are given by $\tilde{\sigma_{\rm do}} = C_X(m) \times \sigma_{\rm do}$, where $\sigma_{\rm do}$ are the the uncorrected DoPHOT photometric uncertainties based only on the input noise mosaics and $C = C_X(m)$ is a function of the source brightness m in magnitudes for each bandpass X, given by the second order polynomial fits shown in Figure 4.4.

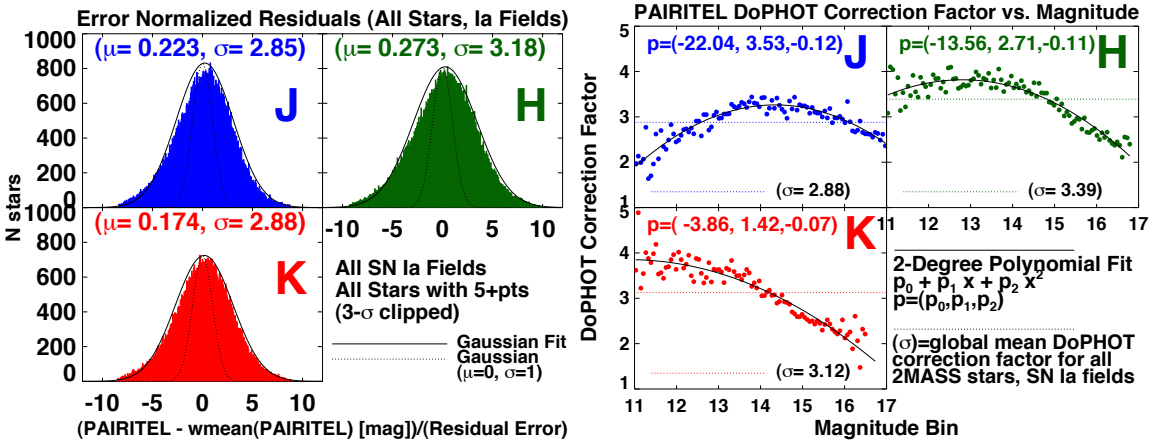

Figure 4.4.— Testing PAIRITEL Photometric Precision for 2MASS Stars

(**Left panel**) Histograms of the JHK_s error normalized residuals aggregated for all stars in all PAIRITEL CfAIR2 SN Ia fields. The standard deviation of the aggregated error normalized residuals $\sigma_{\hat{r_{\rm P}}}$ is a function of the mean global factor $C = C(\sigma_{\hat{r_{\rm P}}}, \sigma_{\rm do}, \sigma_{\tilde{m_{\rm P}}}) \approx \sigma_{\hat{r_{\rm P}}}$ by which we are underestimating our DoPHOT photometric errors on individual measurements (**) (Also see Appendix 7.3). Empirically, $C \sim 2.9$–3.2 in JHK_s including all 2MASS stars between 11 and 17 mag, or more specifically the mean correction factors are $C_J = 2.85$, $C_H = 3.18$, and $C_{K_s} = 2.88$, in JHK_s respectively.

(**Right panel**) We plot the DoPHOT correction factor versus magnitude. Clear trends with an initial increase followed by a decrease fainter than some turnover magnitude can be seen in JH (with a decrease in K_s over all magnitude bins), illustrating the tradeoff between our underestimate of uncertainty from the point source, which dominates for brighter stars and uncertainty from the sky+dark current (skark), which dominates for fainter stars. The turnover magnitude $m_J^{\rm turn} \sim 14.5$, $m_H^{\rm turn} \sim 13$, and $m_{K_s}^{\rm turn} \sim 11$ in the JHK_s curves is the magnitude at which these contributions are equal. As expected, $m_J^{\rm turn} > m_H^{\rm turn} > m_{Ks}^{\rm turn}$ because the sky+dark noise becomes increasingly dominant toward longer NIR wavelengths. In K_s, the skark noise is the dominant noise source over essentially the entire star brightness range ∼11 to 17 mag. The overplotted dashed line is the mean DoPHOT correction factor over all 2MASS stars in the $[11, 17]$ mag range, with means of $C_J = 2.85$, $C_H = 3.18$, and $C_{K_s} = 2.88$ in JHK_s. The curves are fit with a second order polynomial (overplotted solid line) of the form $C_X(m) = p_0 + p_1 m + p_2 m^2$, where $X = J, H$, or K_s, m is the apparent magnitude of the star or SN, and the $\{p_i, i = 0, 1, 2\}$ are the polynomial coefficients, shown as $\vec{p} = (p_0, p_1, p_2)$ for JHK_s in each panel. We can correct the SN Ia photometric magnitude uncertainties empirically by multiplying our errors by a factor determined from these polynomial fits as a function of measured SN brightness and filter.

(**) The DoPHOT correction factor is given by $C(\sigma_{\hat{r_{\rm P}}}, \sigma_{\rm do}, \sigma_{\tilde{m_{\rm P}}}) \approx \sigma_{\hat{r_{\rm P}}} \times \sqrt{1 + \left[1 + \sigma_{\hat{r_{\rm P}}}^{-2}\right] \left(\sigma_{\tilde{m_{\rm P}}}/\sigma_{\rm do}\right)^2}$.

$C(\sigma_{\hat{r_{\rm P}}}, \sigma_{\rm do}, \sigma_{\tilde{m_{\rm P}}}) \approx \sigma_{\hat{r_{\rm P}}}$ in the limit where $\sigma_{\tilde{m_{\rm P}}} << \sigma_{\rm do}$.

4.1.3 Photometric Accuracy

In this section we quantify whether PAIRITEL and 2MASS star photometry are consistent within the estimated uncertainties *after* correcting the PAIRITEL DoPHOT uncertainties using the method discussed in §4.1.2. This allows us to test the photometric accuracy of PAIRITEL and to identify any statistically significant systematic offsets from 2MASS for each SN Ia field and globally for 2MASS stars in all SN Ia fields. We do expect PAIRITEL and 2MASS photometry to agree in the mean averaged over many stars *by construction*, since PAIRITEL uses the same telescope (2MASS north) and camera (2MASS south) and is calibrated with the 2MASS point source catalog (Cutri et al. 2003). This test is merely a self-consistency check to rule out any glaring systematic problems with PAIRITEL DoPHOT photometry. For these tests, we measure the PAIRITEL-2MASS residuals for each 2MASS star, essentially the difference between the weighted mean PAIRITEL magnitudes for each star and the 2MASS catalog magnitudes shown in Table 4.2. Note that because PAIRITEL photometry goes deeper than 2MASS for individual images (with effective exposure times of 600-5400-seconds for PAIRITEL vs. 7.8-seconds for 2MASS; see §2.5), and because the weighted mean PAIRITEL magnitude for each 2MASS star is determined from multiple measurements (typically $\sim$ 25–40) over the SN Ia LC, we do not expect the 2MASS catalog magnitude and the weighted mean PAIRITEL magnitude to be strictly equal for all standard stars. In fact, we expect the weighted mean PAIRITEL magnitude to be closest to the 2MASS catalog magnitude for the brightest 2MASS stars with decreasing agreement and more scatter as the 2MASS catalog brightness decreases, as expected if their measurements are drawn from a distribution given the uncertainties.

This can be seen in Figure 4.5 for our example SN Ia SN 2005ao. In the upper left, upper right, and lower left panels of Figure 4.5, we plot the standard star LCs in the JHK_s bands for all 2MASS stars the field of SN 2005ao, plotted as residuals of the nightly PAIRITEL magnitude minus the 2MASS catalog magnitude. In the lower right panel of Figure 4.5, we plot the weighted mean PAIRITEL photometry pipeline magnitude minus the residual 2MASS catalog magnitude as a function of magnitude for all 2MASS stars in the JHK_s bands in the field, with the 2MASS 1-σ and 2-σ error envelopes overplotted. Residuals for each standard star in the lower right panel are color coded to match the respective standard star LCs in the other panels. As the lower right panel of Figure 4.5 shows, stars have mean PAIRITEL-2MASS residuals that do not all lie strictly along the 0 line, which would be the case for perfect agreement of PAIRITEL and 2MASS photometry. Rather, the residuals are distributed about the zero line, with most star residuals bounded by the overplotted 1-σ and 2-σ 2MASS error envelopes, indicating a residual consistent with 0 within the uncertainties at the associated level of confidence. In Figure 4.6, we present plots similar to the lower right panel of Figure 4.5 for 6 other example SN Ia, including SN 2011df, SN 2010ju, SN 2010Y, SN 2007S, SN 2006D, and a global aggregate for all PAIRITEL CfAIR2 SN Ia, demonstrating the consistency between PAIRITEL and 2MASS photometry from observations taken over a 6 year span from 2005-2011. As Figures 4.5–4.6 show, PAIRITEL and 2MASS photometry agree, with residuals for most stars consistent with 0 at the 2-σ or better level, with the occasional 3-σ or greater outlier.

By aggregating data from plots similar to Figures 4.5–4.6 for all 2MASS stars in all SN Ia fields in JHK_s (see Figures 4.6–4.7), we rule out any major statistically

significant global offsets between PAIRITEL and 2MASS photometry. As shown in the left panel of Figure 4.7, we find weighted mean global PAIRITEL-2MASS residuals of 0.0014 ± 0.0006, 0.0014 ± 0.0007, and -0.0055 ± 0.0007 in JHK_s, respectively, where the uncertainties are the standard errors of the mean. This shows that, when averaging over thousands of stars, PAIRITEL and 2MASS agree to within a few thousandths of a magnitude in JHK_s, with evidence for a small, but statistically significant PAIRITEL-2MASS offsets of ~ 0.001, 0.001, and -0.006 mag in JHK_s, respectively, at the $\sim$ 2–3σ level. The overall agreement between PAIRITEL and 2MASS is most clearly demonstrated in the right panel of Figure 4.7, where each PAIRITEL-2MASS star residual is shown versus its 2MASS catalog magnitude, with the 2MASS 1-σ and 2-σ upper limit error envelopes overplotted. For each 2MASS star, we determine if 2MASS and PAIRITEL photometry agree by calculating whether the mean residual is consistent with 0 to within 1, 2, or greater than 3-σ, although the uncertainties in the residuals are not shown, for clarity. The standard deviations of the error normalized PAIRITEL-2MASS residuals are determined to be 1.17, 1.11, and 1.21 in JHK_s, respectively. Since these would be 1 if we were perfectly estimating our uncertainties in the PAIRITEL-2MASS residuals, we interpret this to mean that we are slightly *underestimating* the uncertainties in the residuals by factors of ~ 1.2 in JHK_s, or an additional $\sim 20\%$ even after correcting the PAIRITEL DoPHOT uncertainties by factors of $\sim$ 150%–300%. If we correct for the slight underestimation of our uncertainties in the PAIRITEL-2MASS residuals, we find that $\sim$68%, $\sim$95%, and $\sim$99% of the standard stars have PAIRITEL-2MASS residuals consistent with 0 to 1, 2, and 3-σ respectively, as expected with correctly estimated Gaussian errors (also see §7.4 for additional mathematical details).

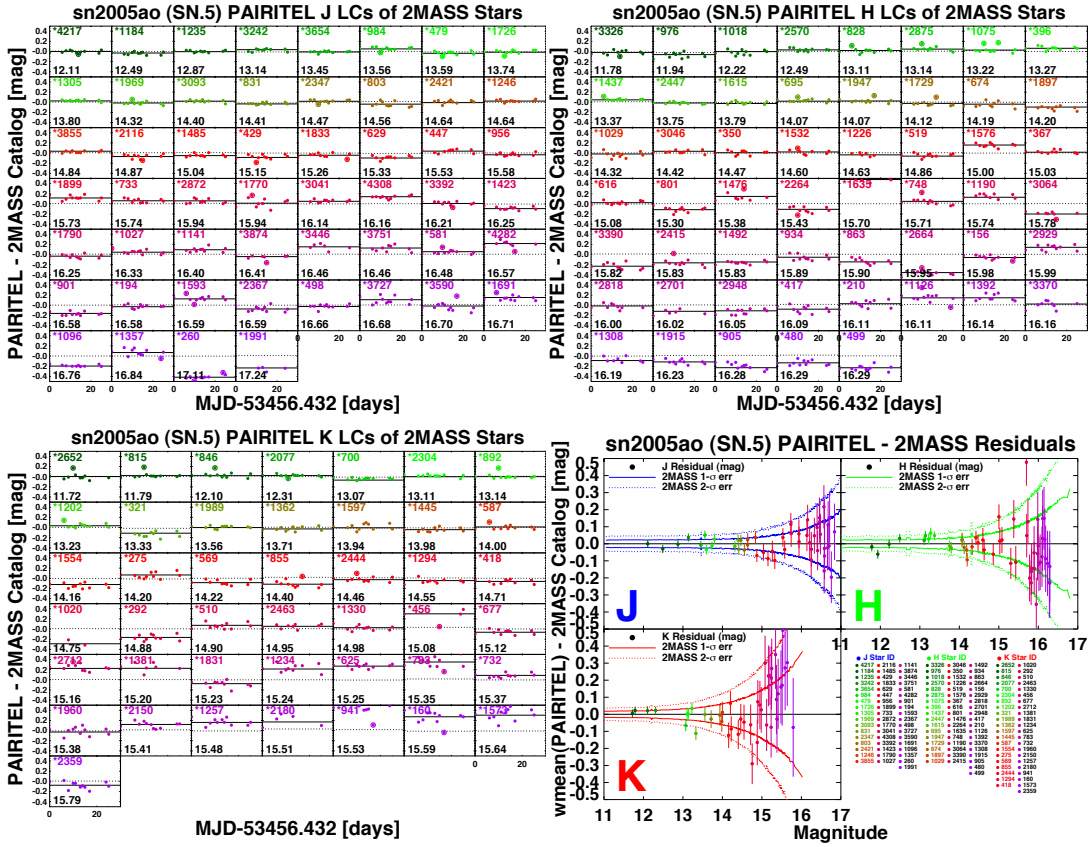

Figure 4.5.— Testing PAIRITEL Photometric Accuracy for 2MASS Stars in the Field of SN 2005ao

(**Upper left, upper right, and lower left**) Standard star LCs in the JHK_s bands for all 2MASS standard stars the field of SN 2005ao plotted as residuals of the PAIRITEL nightly magnitude minus the 2MASS catalog magnitude vs. the Modified Julian Date (MJD), offset by a constant to keep the x-axis values between 0 and 100 days. The 2MASS residual is marked as a dashed line (near 0 residual by definition), and the weighted mean PAIRITEL magnitude is marked with a solid line. This demonstrates that PAIRITEL and 2MASS do not agree perfectly in their mean measurements for each standard star, but rather are drawn from a distribution that would be expected given the uncertainties.

(**Lower right**) Weighted Mean PAIRITEL-2MASS catalog magnitude residuals over the entire standard star LC plotted as a function of magnitude for all 2MASS stars in the JHK_s bands in the field of SN 2005ao, with the 2MASS 1-σ and 2-σ error envelopes overplotted as blue, green, and red solid and dashed lines for JHK_s, respectively. Residuals for each standard star in the lower right panel are color coded to match the respective standard star LCs in the other panels. The y-axis error bars on the residuals are computed as the quadrature sum of the 1-σ uncertainties on the weighted mean PAIRITEL magnitude and the 2MASS catalog magnitude for each standard star LC (see Table 4.2). PAIRITEL and 2MASS photometry generally show good agreement, with a mean PAIRITEL-2MASS residual consistent with 0 at the 2-σ or better level for most stars, with the occasional 3-σ or greater outlier.

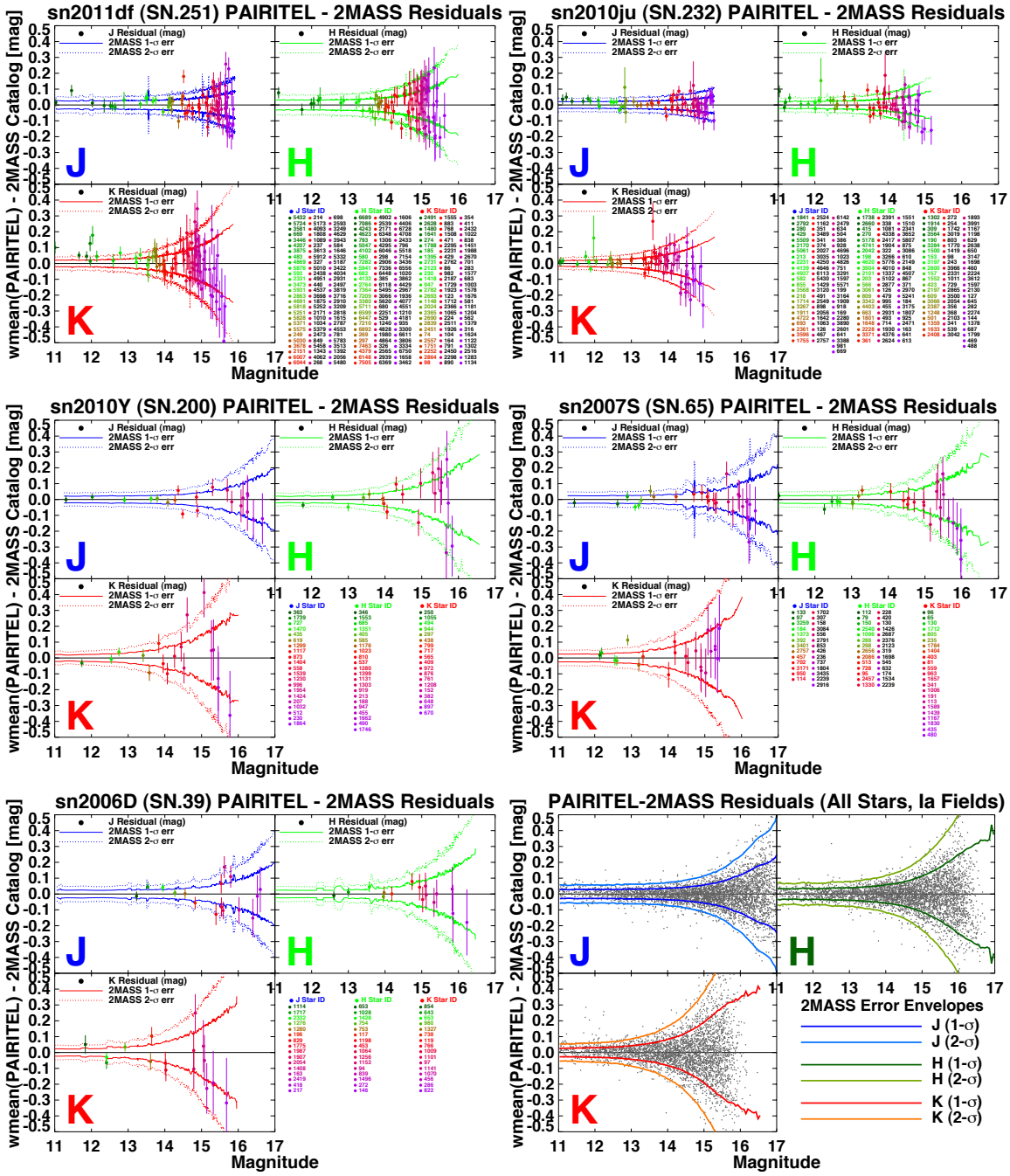

Figure 4.6.— Testing PAIRITEL Photometric Accuracy of 2MASS stars in SN Fields

PAIRITEL weighted mean - 2MASS catalog residuals (See Table 4.2) vs. magnitude for all JHK_s-band 2MASS stars in the fields of SN Ia SN 2011df, SN 2010ju, SN 2010Y, SN 2007S, SN 2006D, along with an aggregate plot for all PAIRITEL CfAIR2 SN Ia (Also see Fig 4.7) with the 2MASS 1-σ and 2-σ error envelopes overplotted. Plotted uncertainties are described in the Figure 4.5 caption, where the PAIRITEL contribution to the error on the PAIRITEL-2MASS residuals has already been corrected for DoPHOT uncertainty underestimates (See §4.1.2). PAIRITEL and 2MASS photometry generally show good agreement, with a mean residuals consistent with 0 at the 2-σ or better level for most stars, with the occasional 3-σ or greater outlier. These plots demonstrate the consistency between PAIRITEL and 2MASS photometry from PAIRITEL observations taken over a 6 year span from 2005-2011.

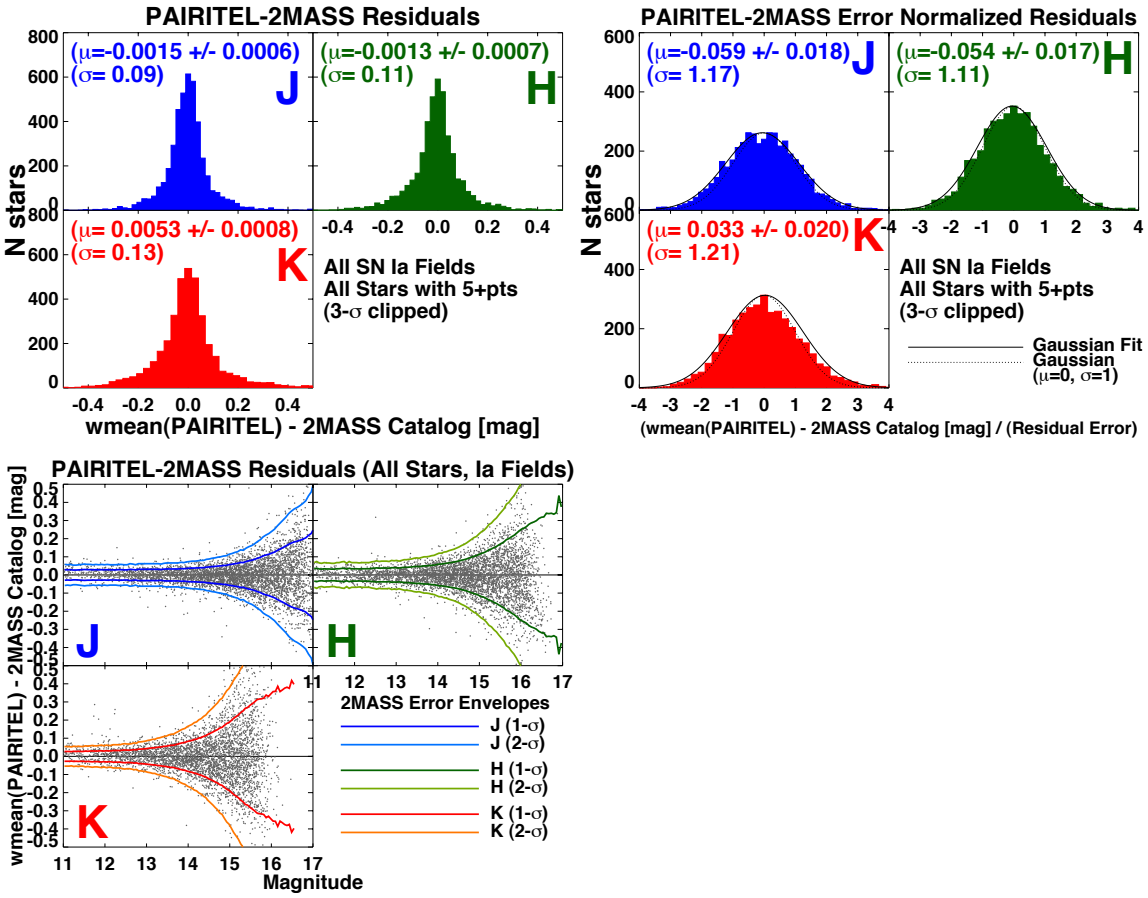

Figure 4.7.— Testing the Photometric Accuracy of PAIRITEL

(**Upper Left**) Histograms of the PAIRITEL-2MASS residuals in JHK_s for all 2MASS stars in the 11 to 17 mag range in all PAIRITEL SN Ia fields. The PAIRITEL and 2MASS mean magnitudes and uncertainties can be found in Table 4.2, where the mean PAIRITEL uncertainties have already been corrected for DoPHOT underestimates. We find global weighted means for all residuals of 0.0014 ± 0.0006, 0.0014 ± 0.0007, and -0.0055 ± 0.0007 in JHK_s, respectively, where the uncertainties are the errors on the weighted mean. This shows that globally, when averaging over thousands of stars, PAIRITEL and 2MASS agree to within a few thousandths of a magnitude in JHK_s, with evidence for a small, but statistically significant PAIRITEL-2MASS offsets of $\sim$ 0.001, 0.001, and -0.006 mag in JHK_s, respectively, at the $\sim$ 2–3σ level. This demonstrates the overall agreement between PAIRITEL and 2MASS using observations for all 2MASS standard stars in all SN Ia fields over a 6-year span from 2005-2011.

(**Upper Right**) Histograms of the PAIRITEL-2MASS error normalized residuals in JHK_s for all 2MASS stars in the 11 to 17 mag range in all PAIRITEL SN Ia fields. The standard deviations of the error normalized PAIRITEL-2MASS residuals are determined to be 1.17, 1.11, and 1.21 in JHK_s, respectively. This indicates that, even after correcting the PAIRITEL DoPHOT magnitude uncertainty underestimates by factors of $\sim$ 1.5–3 ($\sim$ 150%–300%), we are slightly underestimating the errors on the PAIRITEL-2MASS residuals by $\sim$ 10%–20%. This suggests that either the 2MASS catalog uncertainties or the weighted mean PAIRITEL uncertainties are slightly underestimated by $\sim$ 10%–20%. We think the latter is more likely.

(**Lower Left**) As also shown in Figure 4.6, we plot the PAIRITEL-2MASS mean residuals vs. magnitude, with the 2MASS 1-σ and 2-σ upper limit error envelopes overplotted. For each standard star, we determine if PAIRITEL and 2MASS photometry agree by calculating whether the mean residual is consistent with 0 to within 1, 2, or greater than 3-σ. The PAIRITEL uncertainty contribution to the residuals has already been corrected for DoPHOT uncertainty underestimates. The uncertainties in the residuals are not shown, for clarity. If we correct for the underestimation of our uncertainties in the PAIRITEL-2MASS residuals, multiplying by factors of 1.17, 1.11, and 1.21 in JHK_s, respectively (as derived from the Upper Right panel plot), we find that $\sim$68%, $\sim$95%, and $\sim$99% of the standard stars have PAIRITEL-2MASS residuals consistent with 0 to 1, 2, and 3-σ respectively, as expected with correctly estimated Gaussian errors. This is a good cross check that we are correctly handling the uncertainties.

4.2 Photometry Systematics

In §4.2 we discuss internal consistency checks which test for other statistical and systematic errors which could effect PAIRITEL SN photometry. In §4.2.1–§4.2.3, we asses the systematic and statistical uncertainty from the host galaxy subtraction process, both for bright, well-isolated objects and for objects potentially embedded deep within host galaxies. In §4.2.4, we discuss the potential photometry systematics from errors in sky subtraction. In §4.2.5, we outline systematic errors that could results from astrometric errors in forced DoPHOT photometry at the putative SN centroid position. In §4.2.6–§4.2.7, we briefly discuss other potentially important sources of potential systematic uncertainty that are beyond the scope of this thesis.

4.2.1 Galaxy Subtraction: Statistical & Systematic Errors

As discussed in §3.4, we have made several improvements to the PAIRITEL host galaxy subtraction process since WV08. These include feeding improved noise maps to HOTPANTS, our difference imaging module, and using NNT rather than NN2 to perform a nightly average of the forced DoPHOT LCs on subtracted images from different host galaxy templates. Still, because PAIRITEL images are fundamentally undersampled, our images do not capture enough information to fully resolve the observed PSF. In the galaxy subtraction process, when HOTPANTS attempts to solve for the convolution kernel to transform one image to the PSF of another image observed under different seeing conditions (for example an SN and SNTEMP image), the undersampling introduces uncertainties into both the calculation of the PSF for each image and the estimate of the convolution kernel solution. Some additional

uncertainty is thus an inevitable result of the host galaxy subtraction process on undersampled images. In §4.2.2, we attempt to quantify the statistical uncertainty from NNT and we also test whether NNT introduces a net systematic bias using, bright, well-isolated objects. Overall, both for bright, well-isolated objects and SN that may be more deeply embedded in the host galaxy (see §4.2.3), we find that our galaxy subtraction produces no net systematic bias, provided that there are a sufficient number of host galaxy template images (typically $N_{\rm SNTEMP} \gtrsim 4$). While the subtraction process with sufficient host galaxy template images yields no net systematic uncertainty (bias), it does result in additional statistical uncertainty (scatter), which we can measure and include in the final photometric error budget. For bright, and or well-isolated SN, the additional statistical uncertainty from NNT still generally yields LCs with many points that exceed our signal-to-noise cut of $SNR > 3$. For fainter objects and/or SN more deeply embedded in the host galaxy, the additional statistical uncertainty from host galaxy subtraction is more likely to yield too few LC points that meet our signal-to-noise cuts. In these cases, the LCs are sometimes of quality insufficient for publication (e.g. see Figure 4.33).

4.2.2 Galaxy Subtraction for Bright, Well-Isolated Objects

Even if NNT introduces no net systematic bias when averaged over many subtractions for each LC point, in practice, each realization of the host galaxy template provides a different estimate for the SN flux, and each subtraction potentially adds or subtracts some SN flux which we treat as a random variable. We therefore consider it appropriate to include the scatter from this process in our final statistical error

budget for galaxy subtracted photometry. For an individual night of photometry with $N_{\rm SNTEMP}$ subtractions, the key question is whether the standard deviation of the SN flux measurements from the NNT process ($\sigma_{\rm NNT}$) is comparable to or greater than the photometric errors from DoPHOT ($\tilde{\sigma_{\rm do}}$), which have already been corrected to account for additional noise in the images beyond the estimates in the noise mosaics (see §4.1.2). If $\sigma_{\rm NNT} < \tilde{\sigma_{\rm do}}$, then the galaxy subtraction process introduces an additional uncertainty smaller than the photometric uncertainties from DoPHOT and neglecting $\sigma_{\rm NNT}$ would be a reasonable approximation. However, in practice, we find that $\sigma_{\rm NNT} \gtrsim \tilde{\sigma_{\rm do}}$ in most cases and we interpret any remaining source of statistical uncertainty to be from the NNT host galaxy subtraction process itself. We therefore add the corrected flux errors from DoPHOT and NNT in quadrature to produce our final photometric uncertainties for SN LCS using NNT host galaxy subtraction, $\sigma_{\rm tot} = \sqrt{(\tilde{\sigma_{\rm do}})^2 + (\sigma_{\rm NNT})^2}$. For rare cases where $N_{\rm SNTEMP} = 1$ and only one SNTEMP image meets our image quality requirements, it is not possible to measure $\sigma_{\rm NNT}$, so we estimate $\sigma_{\rm NNT}$ using the $\bar{\sigma_{\rm NNT}}$, the typical standard deviation incurred from NNT estimated using a group of 20 bright and/or well-isolated SN with $N_{\rm SNTEMP} > 1$. (see the following section). However, $N_{\rm SNTEMP} = 1$ can always be remedied in principle by obtaining additional future SNTEMP observations, which we continue to do with PAIRITEL as needed rather than extrapolating the $\sigma_{\rm NNT}$ uncertainty from other objects with $N_{\rm SNTEMP} > 1$. Unlike the transient SN, fortunately, the host galaxy can be repeatedly imaged indefinitely.

While we know that the NNT process introduces an additional statistical uncertainty, we also test here whether host galaxy subtraction, on average, introduces any additional systematic bias to the subtracted LCs. Certainly, individual SN

with an insufficient number of high quality SNTEMP images and subtractions ($N_{\rm SNTEMP} \lesssim 3$), may incur a systematic error from NNT host galaxy subtraction, motivating additional SNTEMP observations for these objects, which are relatively easy to obtain with PAIRITEL. However, we expect that the NNT averaging process should limit the overall systematic error incurred from over or under-subtracted flux estimates using individual SNTEMP images, provided there are a sufficient number of good SNTEMP images for a given SN, which we find to be $N_{\rm SNTEMP} \gtrsim 4$ in practice. To test this expectation and the host galaxy subtraction process globally for PAIRITEL data, we can average over many subtractions for a large set of SN.

The best objects for such tests are SN that are either well isolated from the nucleus of their host galaxy or bright enough that the host galaxy flux at the SN position is a small fraction of the SN flux over many epochs. For these SN, photometry on the un-subtracted images gives a good approximation to the final galaxy subtracted LC at most phases and provides an internal consistency check of the host galaxy subtraction process (See the bottom row of Figure 4.8). However, even for bright, well isolated SN, there is some galaxy flux at the SN position, and the galaxy flux contribution may only be negligible over a finite phase range. For an individual SN, observations at early times may have a high ratio of SN flux to host galaxy flux, whereas observations at late times may have a lower such ratio as the SN fades in brightness and the host galaxy flux remains nearly constant. For the purposes of this test, we make the assumption that the host galaxy flux to SN flux ratio should be small in the phase range of $[-10, 50]$ days and we test to see if the weighted mean residuals of the un-subtracted and subtracted LCs are consistent with zero to within 1-σ in this phase range, where σ is estimated as

the standard deviation of the residuals in this phase range for individual SN. Two example bright and/or well-isolated SN Ia (SN 2007sr, and SN 2009dc) are shown in the top row of Fig. 4.8. SN that meet these criteria also need not be limited to SN Ia, so for these tests, we include other SN Ib/c and SN II for which we have PAIRITEL photometry. Overall, we use a total of 20 bright and/or well-isolated SN, including 15 SN Ia (SN 2005el, SN 2005eq, SN 2006D, SN 2006E, SN 2006X, SN 2006mq, SN 2007le, SN 2007sr, SN 2008hy, SN 2009D, SN 2009al, SN 2009an, SN 2009dc, SN 2010ai, SN 2011aa), 2 SN Ib/c (SN 2009er, SN 2009iz), and 3 SN II (SN 2007aa, SN 2008ax, SN 2008ip). Plots of both the un-subtracted and host galaxy subtracted LCs and their residuals for these SN are shown in Figures 4.9–4.10 with SN 2007sr and SN 2009dc LCs shown Fig. 4.8. After removing 3-σ outliers and points with $SNR < 3$, the weighted means of the aggregated residuals for all 20 SN are easily consistent with 0, with weighted means (and errors) of $-0.0009\pm$ 0.0016, $0.0006\pm$ 0.0019, and $0.0007\pm$ 0.0026 magnitudes in JHK_s respectively. In addition, the standard deviations of the aggregated residuals for the 20 PAIRITEL SN listed above are $\sigma_{\bar{\rm NNT}} = 0.072$, 0.079, and 0.138 mag in JHK_s, respectively. We interpret these numbers ($\sigma_{\bar{\rm NNT}}$), as estimates of the typical mean statistical error budget due to the NNT averaging process in each bandpass. For bright, well isolated SN with $N_{\rm SNTEMP} = 1$, where it is not possible to compute the standard deviation, we could add these numbers in quadrature to our photometric errors. However, in these cases, we prefer to simply observe more host galaxy templates for that object. In any case, since these numbers are typically comparable to or greater than the mean statistical DoPHOT photometric errors over all phases, it is very important to include them in the final photometric error budget for galaxy subtracted PAIRITEL CfAIR2 LCs.

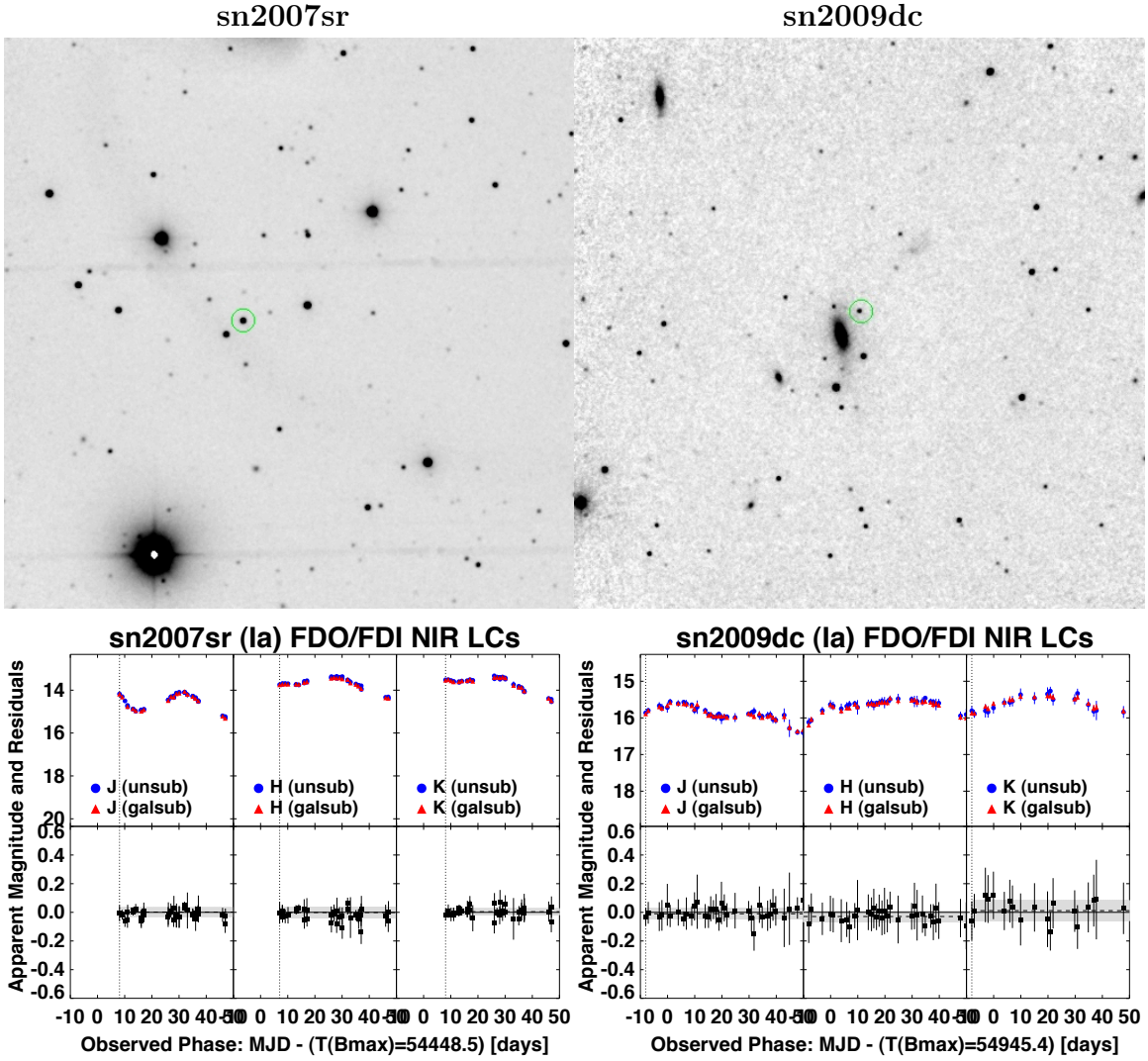

Figure 4.8.— Subtracted and Un-subtracted LC for SN 2007sr & SN 2009dc

(**First Row**) Sample J-band mosaicked images for 2 example SN Ia (SN 2007sr and SN 2009dc) that are sufficiently bright and well isolated from their host galaxies so that little galaxy subtraction is needed. The SN Ia are each marked by green circles.

(**Second Row Top Panels:**) PAIRITEL JHK_s forced DoPHOT LCs for these example SN Ia are shown both for the unsubtracted images (blue circles) and the host galaxy subtracted difference images (red triangles). Each LC was constructed from NNT averaging of the subtractions, although SN 2007sr only had one SNTEMP image ($N_{\rm SNTEMP} = 1$) compared to $N_{\rm SNTEMP} = 7$ SNTEMP image subtractions for SN 2009dc. The extra scatter in the SN 2009dc LCs come from including the standard deviation of each of the subtractions (NNT) in the final photometric error budget for the galaxy subtracted LC. Cases where $N_{\rm SNTEMP} = 1$ are discussed in §4.2.2.

(**Second Row Bottom Panels**) Residuals (black squares) of the flux differences between the forced DoPHOT LCs on the unsubtracted and subtracted images observed at the same phases. The weighted mean of the residuals in the $[-10, 50]$ day phase range is overplotted as a dashed line and 1-σ uncertainty region is overplotted in gray, where σ is the standard deviation of the residuals in this phase range. Over the phase range $[-10, 50]$ days in each of the JHK_s bands, the mean residuals are consistent with zero, as can be seen from the fact that the 1-σ gray error region overlaps with a residual of zero (solid line). This gives us confidence that the host galaxy subtraction process is not systematically over or under-subtracting flux from the SN Ia LC. For bright, well isolated objects like SN 2007sr, a single good quality SNTEMP image may be sufficient for galaxy subtraction, although $N_{\rm SNTEMP} \gtrsim 4$ is preferred.

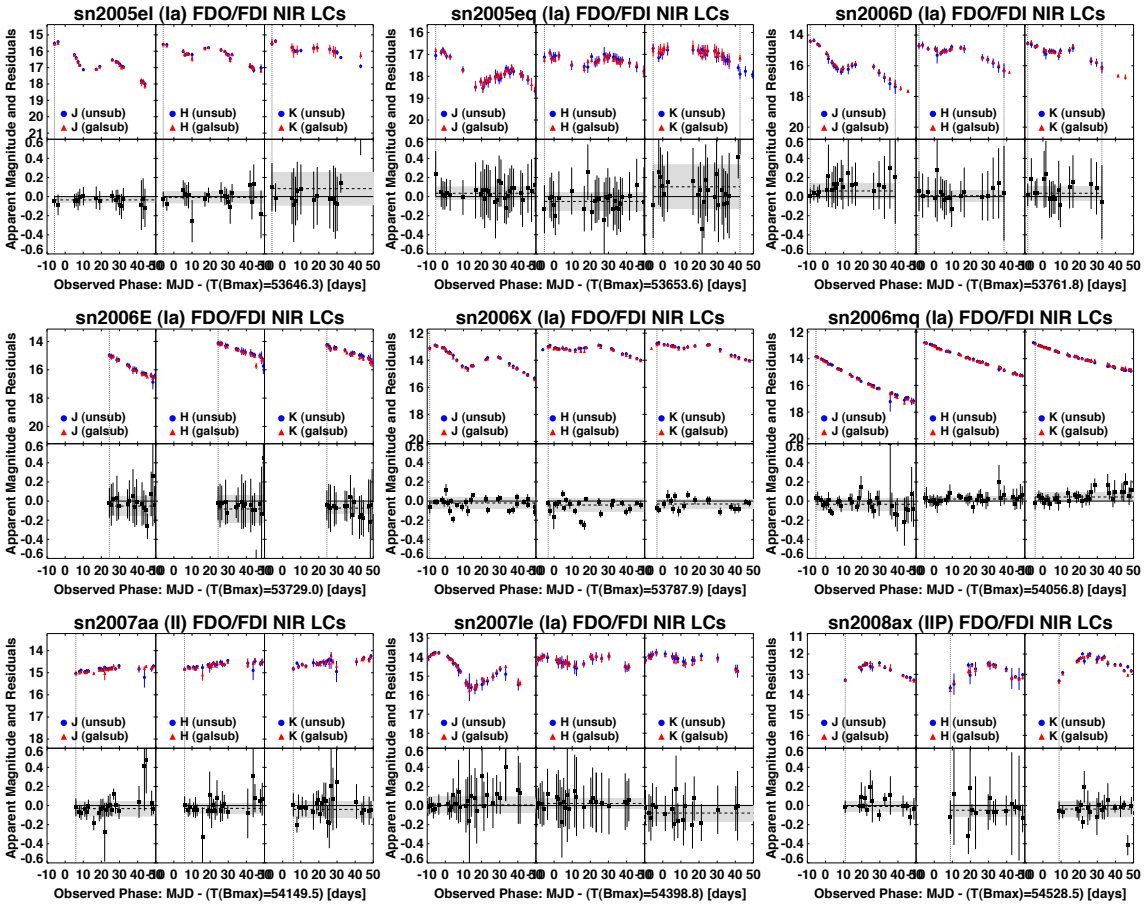

Figure 4.9.— Subtracted and Un-subtracted LCs of Bright, Well-Isolated SN

(**Top Panels**) PAIRITEL JHK_s forced DoPHOT LCs on both the unsubtracted images (blue circles) and host galaxy subtracted difference images (red triangles) for 9 example SN of all types that are bright and/or well isolated from their host galaxies, requiring little host galaxy subtraction over a wide phase range.

(**Bottom Panels**) Residuals (black squares) are computed as direct data differences between the forced DoPHOT LCs on the un-subtracted and subtracted images since data points for each method are observed at the same phase. The weighted mean of the residuals in the $[-10, 50]$ day phase range is overplotted as a dashed line and 1-σ uncertainty region is overplotted in gray, where σ is the standard deviation of the residuals in this phase range. Over the phase range $[-10, 50]$ days in each of the JHK_s bands, the mean residuals are consistent with zero to within 1-σ for essentially all of the 20 bright, well-isolated SN LCs shown in Figs. 4.8–4.10, with occasional exceptions where the residuals are only consistent with zero to within 2-σ for individual SN in specific bands (especially in K_s-band, where our images and subtractions are of poorer quality). A weighted mean residual consistent with zero to 1-σ can be seen whenever the 1-σ gray error region overlaps with a residual of zero (solid line). This gives us confidence that the host galaxy subtraction process is not systematically over or under-subtracting flux from the SN Ia LC.

At phase points where the residuals are consistent with zero to within 1-σ, where the host galaxy flux contribution is negligible compared to the SN flux, the standard deviation of the residuals (σ) helps quantify the typical statistical uncertainties incurred from the NNT averaging process combining host galaxy subtractions for several SNTEMP images. After removing 3-σ outliers and data points with $SNR < 3$, the standard deviations of the aggregated residuals for these 20 bright, and/or well-isolated PAIRITEL SN from Figures 4.8–4.10 are 0.072, 0.079, and 0.138 mag in JHK_s, respectively. We could add these magnitude error in quadrature to our photometric errors for all CfAIR2 galaxy subtracted photometry for SN Ia with only a single SNTEMP observation ($N_{\rm SNTEMP} = 1$) to account for the typical statistical errors incurred from the NNT averaging process. For SN Ia with $N_{\rm SNTEMP} \geq 2$, we computed $\sigma_{\rm NNT}$ from the data directly although $N_{\rm SNTEMP} \gtrsim 4$ is preferable to avoid systematic uncertainties from galaxy subtraction. As expected the typical host galaxy subtraction NNT uncertainties $\sigma_{\rm NNT}$ increase toward longer wavelength, reflecting the decrease in image quality and subtractions as we move from J to H to K_s.

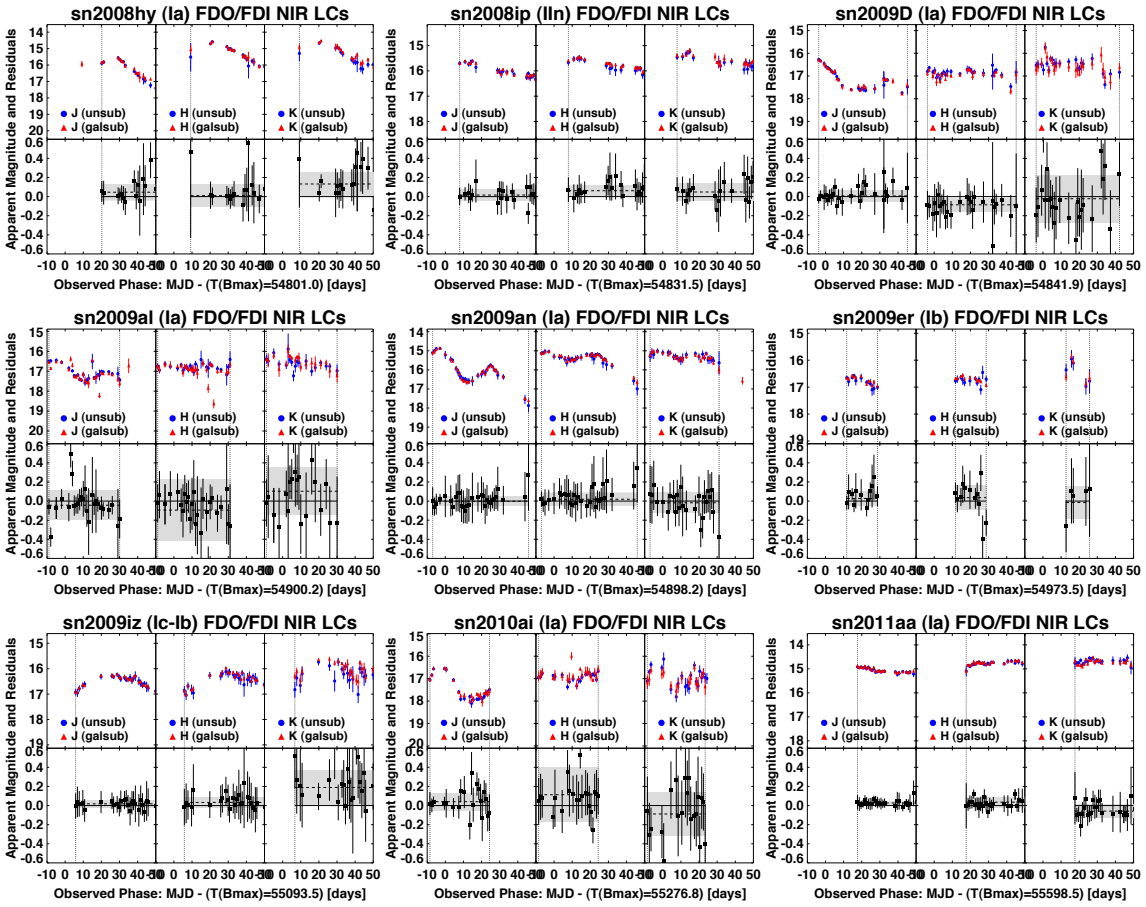

Figure 4.10.— Subtracted and Un-subtracted LCs of Bright, Well-Isolated SN

(**Top Panels**) PAIRITEL JHK_s forced DoPHOT LCs on both the unsubtracted images (blue circles) and host galaxy subtracted difference images (red triangles) for 9 example SN of all types that are bright and/or well isolated from their host galaxies, requiring little host galaxy subtraction over a wide phase range.

(**Bottom Panels**) Residuals (black squares) are computed as direct data differences between the forced DoPHOT LCs on the un-subtracted and subtracted images since data points for each method are observed at the same phase. The weighted mean of the residuals in the $[-10, 50]$ day phase range is overplotted as a dashed line and 1-σ uncertainty region is overplotted in gray, where σ is the standard deviation of the residuals in this phase range. Over the phase range $[-10, 50]$ days in each of the JHK_s bands, the mean residuals are consistent with zero to within 1-σ for essentially all of the 20 bright, well-isolated SN LCs shown in Figs. 4.8–4.10, with occasional exceptions where the residuals are only consistent with zero to within 2-σ for individual SN in specific bands (especially in K_s-band, where our images and subtractions are of poorer quality). A weighted mean residual consistent with zero to 1-σ can be seen whenever the 1-σ gray error region overlaps with a residual of zero (solid line). This gives us confidence that the host galaxy subtraction process is not systematically over or under-subtracting flux from the SN Ia LC.

At phase points where the residuals are consistent with zero to within 1-σ, where the host galaxy flux contribution is negligible compared to the SN flux, the standard deviation of the residuals (σ) helps quantify the typical statistical uncertainties incurred from the NNT averaging process combining host galaxy subtractions for several SNTEMP images. After removing 3-σ outliers and data points with $SNR < 3$, the standard deviations of the aggregated residuals for these 20 bright, and/or well-isolated PAIRITEL SN from Figures 4.8–4.10 are 0.072, 0.079, and 0.138 mag in JHK_s, respectively. We could add these magnitude error in quadrature to our photometric errors for all CfAIR2 galaxy subtracted photometry for SN Ia with only a single SNTEMP observation ($N_{\rm SNTEMP} = 1$) to account for the typical statistical errors incurred from the NNT averaging process. For SN Ia with $N_{\rm SNTEMP} \geq 2$, we computed $\sigma_{\rm NNT}$ from the data directly although $N_{\rm SNTEMP} \gtrsim 4$ is preferable to avoid systematic uncertainties from galaxy subtraction. As expected the typical host galaxy subtraction NNT uncertainties $\sigma_{\rm NNT}$ increase toward longer wavelength, reflecting the decrease in image quality and subtractions as we move from J to H to K_s.

4.2.3 Galaxy Subtraction for Embedded Objects

The tests in §4.2.2 were specifically for bright, well-isolated objects for which we expect the un-subtracted LC to be a good approximation to the true, galaxy subtracted LC because the amount of galaxy light at the SN position is small compared to the SN light. We then tested the host galaxy subtraction process by empirically measuring whether the weighted mean residuals of the subtracted and un-subtracted LCs are zero in a suitable phase range. This test of the subtraction process is similar to testing whether the weighted mean residual LCs are constant with zero flux at the positions of stars in the difference images that are far from the host galaxy where we expect very little galaxy light to be present. In other words, the tests we performed in §4.2.2, and tests at the positions of stars — which we did not perform — both theoretically test how well the subtraction process works at image points where there is no significant host galaxy contribution. In the case of the SN position, we expect only the mean SN flux and residual noise to be present in the difference image LC. For the positions of stars, we expect the mean flux in the difference image to be zero with some uncertainty.

However, for objects deeply embedded in the SN host galaxy, we can not make the same comparison in the absence of a suitable un-subtracted reference LC. In these cases, we test the subtraction process by performing forced DoPHOT NNT photometry on the galaxy subtracted difference images at positions near the host galaxy where the SN *could conceivably have been*. We achieve this by performing forced photometry on a 3×3 grid of positions with evenly spaced increments of $15' = 15$ pixels centered around the SN position (see Figures 4.11–4.12). Since

the SN is highly likely to be near the galaxy, these $3 \times 3 = 9$ position grids are likely to contain one or more grid positions that are embedded within the galaxy. Grid positions farther from the galaxy nucleus serve as additional controls of the subtraction process since we expect the mean flux in the difference images to be consistent with zero at those positions as well, but with smaller scatter than at positions with significant host galaxy light. Overall, if the subtraction process is working correctly, we expect the LCs on the difference images to have a weighted mean of zero flux at all grid positions *except* for the central position with the SN. For grid positions highly embedded in the host galaxy, we expect a larger scatter about a weighted mean flux of zero due to the presence of host galaxy light at that grid position, but we still consider the subtraction process to be successful if the weighted mean LC is zero (no systematic bias) at the position embedded in the host galaxy.

This is demonstrated in Figures 4.11–4.12, for the fields of SN Ia SN 2005eq and SN 2006D, respectively. In each of the 8 grid positions surrounding the SN, we find that the weighted mean difference imaging NNT LC, averaged over $N_{\rm SNTEMP} = 3$ and 5 host galaxy template subtractions per night for SN 2005eq and SN 2006D, respectively, is consistent with zero to within 1-σ, as shown by the gray strips in Figures 4.11–4.12, which surround the black line indicating zero flux. Here we take the standard deviation of the LC as an estimate of the 1-σ uncertainty in the weighted mean. Since we expect each individual subtraction to yield a systematically brighter or dimmer flux measurement, it is not appropriate to divide the uncertainty by $\sqrt{N}$, where N is the number of LC points. However, since we expect this systematic to be a random variable with a mean of zero, it should average out over many subtractions via NNT on each night and averaged over the entire LC.

As expected, the scatter increases at grid positions embedded within the host galaxy, for example, at grid positions 9 and 8 in Figure 4.11 and grid positions 4, 7, and 8 in Figure 4.12. The scatter also increases towards longer wavelength since the signal-to-noise ratio decreases from J to H to K due to the presence of additional contaminating sky light and thermal noise (see §3.2). Although the scatter increases for highly embedded positions, the weighted mean flux at embedded host galaxy positions in the difference images is still zero over the entire LC for these embedded positions, as shown in each grid below the RA and DEC coordinates listed for each grid position. This indicates no systematic bias from NNT galaxy subtraction even at these highly embedded positions inside the galaxy.

We performed this test for all SN Ia fields but show only two example host galaxies for concision in Figures 4.11–4.12. These examples are representative of the typical host galaxies observed by PAIRITEL for which is possible to obtain publication quality SN photometry with sufficient signal-to-noise at the SN position for many LC points. SN that are fainter than $J \sim 18$ mag at the brightest LC point are often too faint for PAIRITEL, especially if the SN is deeply embedded in the galaxy (see Figure 4.33). Provided that enough host galaxy template images are obtained ($N_{\rm SNTEMP} \gtrsim 4$ is preferred), Figures 4.11–4.12 demonstrate that the NNT host galaxy subtraction process does not result in a net systematic bias even for objects at positions embedded within host galaxies. The additional statistical error (scatter) incurred for SN embedded within the host is accounted for by $\sigma_{\rm NNT}$, the standard deviation of the flux measurements (eventually converted to a magnitude uncertainty) for all subtractions on each night in the NNT process, as described in §4.2.1.

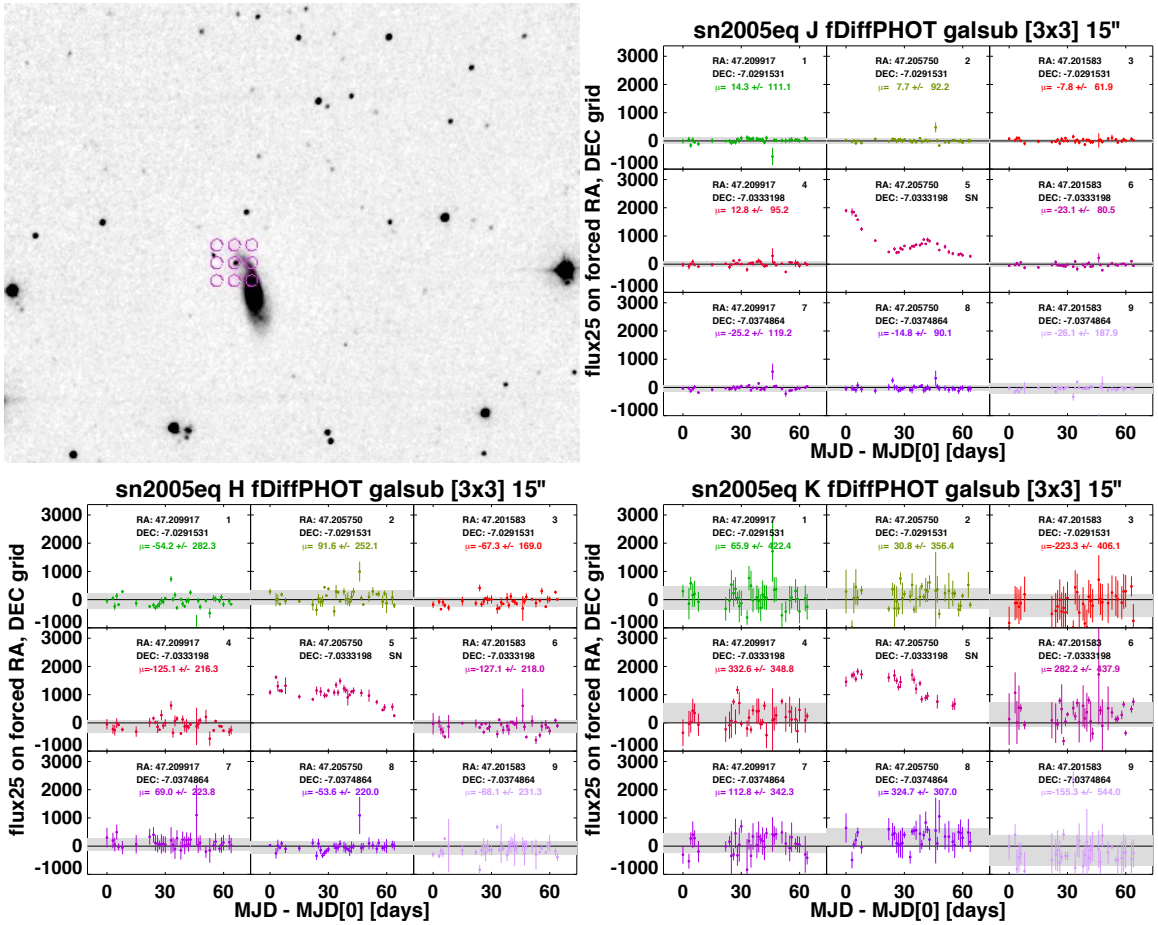

Figure 4.11.— Testing Galaxy Subtraction at Points Embedded in the Host Galaxy for SN 2005eq

(**Upper Left**) J-band mosaic image for SN 2005eq. The 3×3 grid, with evenly spaced increments of $15'' = 15$ pixels, are shown centered on pink circles, with the SN at the central grid position. Forced DoPHOT photometry was performed at the center of each grid position. Light curves on the $N_{\rm SNTEMP}$ difference images per night were constructed by the NNT process described in §3.4.2, with a weighted average of each of the $N_{\rm SNTEMP}$ subtractions on each night ($N_{\rm SNTEMP} = 3$ for SN 2005eq). The 3×3 LC grid is displayed for the JHK_s bands, in the **Upper Right**, **Lower Left**, and **Lower Right** panels respectively. In each of the $3 \times 3 = 9$ grid panels in each bandpass, $flux_{25}$ LCs are displayed, where $flux_{25}$ is the measured flux normalized to a zero point of 25 magnitudes, with the uncertainty for each point given by the quadrature sum of the error on the corrected DoPHOT photon uncertainties $\tilde{\sigma_{\rm do}}$ and $\sigma_{\rm NNT}$ over each difference image for that night (see §4.2.2). In each case, the central grid panel shows the SN LC, whereas the other panels show the LCs at the remaining 8 grid positions. As expected, the LCs at the 8 surrounding grid positions have weighted means consistent with $flux_{25} = 0$ to within 1-σ (gray strips surrounding the black line indicating zero flux), where the standard deviation of the $flux_{25}$ measurements over the entire LC is taken as the estimate of the uncertainty on the weighted mean flux over the entire LC (See §4.2.3). While the scatter at positions embedded within the host galaxy (e.g. grid position 9 for SN 2005eq) is larger than at non embedded positions — and in general for longer wavelength bands — the weighted mean flux is consistent with zero at all grid positions surrounding the SN as displayed in each grid LC plot under the RA and DEC forced coordinates. This confirms that, in cases where there are enough host galaxy template images with which to construct the difference imaging LC with the NNT method, we find no systematic bias due to host galaxy subtraction. The additional statistical uncertainty due to host galaxy subtraction is taken into account by including $\sigma_{\rm NNT}$ in the error budget for each LC point.

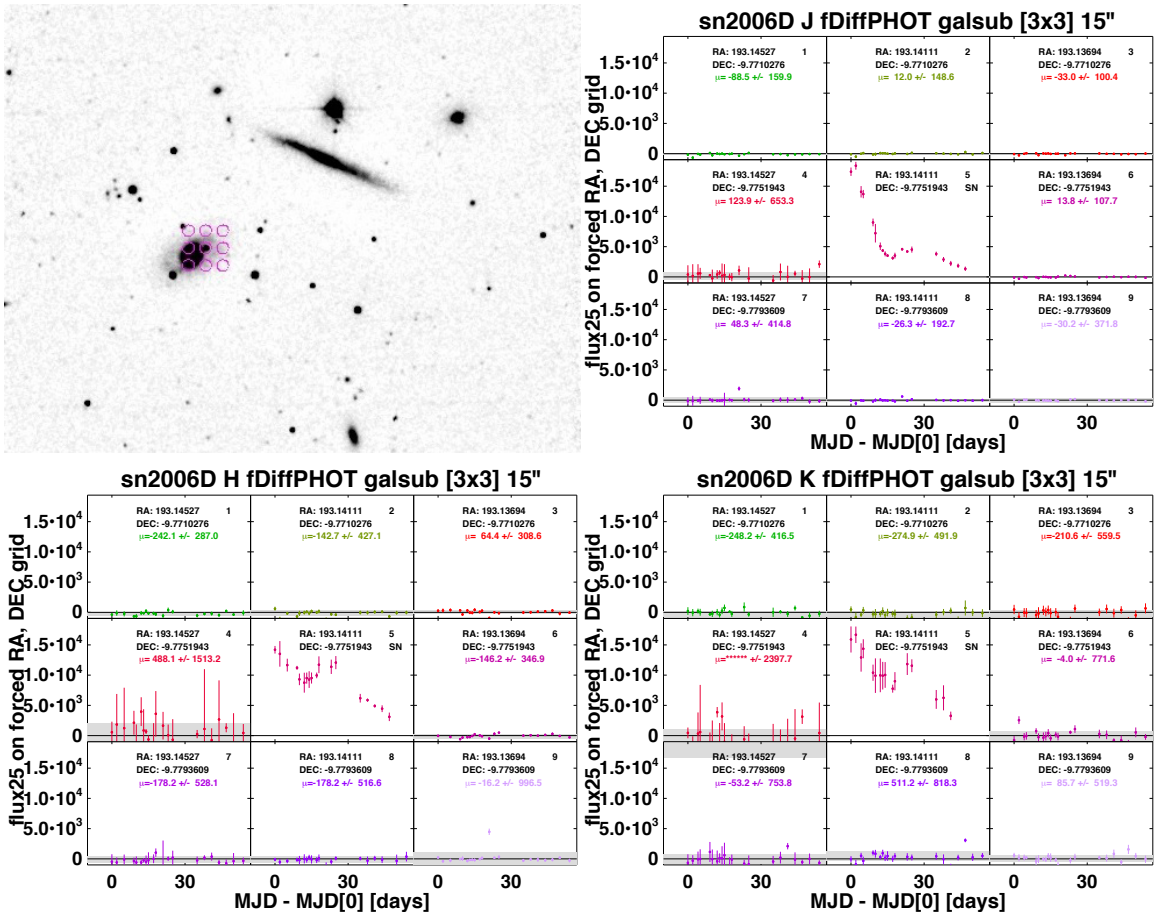

Figure 4.12.— Testing Galaxy Subtraction at Points Embedded in the Host Galaxy for SN 2006D

(**Upper Left**) J-band mosaic image for SN 2006D. The 3×3 grid, with evenly spaced increments of $15'' = 15$ pixels, are shown centered on pink circles, with the SN at the central grid position. Forced DoPHOT photometry was performed at the center of each grid position. Light curves on the $N_{\rm SNTEMP}$ difference images per night were constructed by the NNT process described in §3.4.2, with a weighted average of each of the $N_{\rm SNTEMP}$ subtractions on each night ($N_{\rm SNTEMP} = 5$ for SN 2006D). The 3×3 LC grid is displayed for the JHK_s bands, in the **Upper Right**, **Lower Left**, and **Lower Right** panels respectively. In each of the $3 \times 3 = 9$ grid panels in each bandpass, $flux_{25}$ LCs are displayed, where $flux_{25}$ is the measured flux normalized to a zero point of 25 magnitudes, with the uncertainty for each point given by the quadrature sum of the error on the corrected DoPHOT photon uncertainties $\tilde{\sigma_{\rm do}}$ and $\sigma_{\rm NNT}$ over each difference image for that night (see §4.2.2). In each case, the central grid panel shows the SN LC, whereas the other panels show the LCs at the remaining 8 grid positions. As expected, the LCs at the 8 surrounding grid positions have weighted means consistent with $flux_{25} = 0$ to within 1-σ (gray strips surrounding the black line indicating zero flux), where the standard deviation of the $flux_{25}$ measurements over the entire LC is taken as the estimate of the uncertainty on the weighted mean flux over the entire LC (See §4.2.3). While the scatter at positions embedded within the host galaxy (e.g. grid positions 4, 7, and 8 for SN 2006D) is larger than at non embedded positions — and in general for longer wavelength bands — the weighted mean flux is consistent with zero at all grid positions surrounding the SN as displayed in each grid LC plot under the RA and DEC forced coordinates. This confirms that, in cases where there are enough host galaxy template images with which to construct the difference imaging LC with the NNT method, we find no systematic bias due to host galaxy subtraction. The additional statistical uncertainty due to host galaxy subtraction is taken into account by including $\sigma_{\rm NNT}$ in the error budget for each LC point.

4.2.4 Sky Subtraction

Here we argue that sky subtraction contributes a systematic positive magnitude bias which dims typical SN LCs by $\lesssim 0.01$ mag in the JH bands and $\lesssim 0.02$ mag in K_s. However, we choose to ignore sky subtraction systematics in the final photometric errors we report in Table 4.3, since they are negligible in the overall error budget, which is dominated by the statistical and systematic errors from host galaxy subtraction (see §4.2.2). Our tests — which we ultimately interpret as measuring typical sky subtraction systematics — were initially designed to investigate whether point source photometry showed any radial dependence on the detector position. Since the mosaicking process smears out the radial detector information in each of the individual $8.5 \times 8.5'$ exposures, we decided to perform a cruder test to see if point source photometry displayed any radial dependence with respect to the position of the SN in the final $12 \times 12'$ mosaics. Although the SN is not necessarily at the center of individual p3.0 mosaics, stars near the SN are *on average* closer to the mosaic center than stars far from the SN.

Our results are shown in Figure 4.13, which plot PAIRITEL - 2MASS star magnitude residuals from Table 4.2 as a function of radius from the SN in arcminutes. Weighted mean residuals are binned in 15 equally spaced bins from $1'$ to $7'$. Beyond $8'$, closer to the edges of the mosaic, there are too few stars to get good statistics. In each of the JHK_s bands, we find statistically significant but small PAIRITEL - 2MASS star residuals with a maximum absolute value of $\sim$ 0.01–0.02 mag in the range of radii up to $7'$ from the SN. Each filter in Figure 4.13 also shows a similar trend versus radius from the SN. Assuming that 2MASS sky subtraction estimates

are less systematically biased than PAIRITEL, we interpret this radial dependence in Figure 4.13 as evidence for sky over-subtraction near the SN / host galaxy and sky under-subtraction far from the SN and galaxy. We interpret the PAIRITEL - 2MASS residuals for stars at positions $\lesssim 3'$ from the SN as the typical systematic magnitude bias due to sky over-subtraction near host galaxies which is representative of sky over-subtraction at typical SN positions (see §3.2).

From the similar pattern of residuals vs. radius from the SN in each filter, we conclude that the trends are due to a common factor affecting all filters. One might naturally suspect common feature of the optics or the detectors. However, each of the JHK_s detectors for each band are on separate chips with distinct properties, for example, differing bad pixel maps (see §4.2.6) and relatively stable but distinct dark current patterns (see §3.2). Similarly, the dichroic mirrors that split the NIR light for simultaneous JHK_s observing send the light for each bandpass down different optical paths (Skrutskie et al. 2006). We therefore do not think the results are due to common features of the optical system or detectors. Ultimately, we hypothesize that the radial dependence of the residuals is due to a common causal factor in the mosaic reduction process, most likely due to systematic errors in the sky subtraction process. The reason is that galaxies observed by PAIRITEL typically subtend $\sim$ 1–4$'$ on the sky, which can be a substantial fraction of the $8.5 \times 8.5'$ raw frames. Since we estimate the sky in each raw frame from a pixel-by-pixel weighted average through a time series of dithered raw frames (see §3.2), rather than on-off pointing, galaxy light may bias the estimates of the sky for stars near the galaxy (and near the SN) by overestimating the amount of sky light at the SN position near the galaxy, with the opposite effect far from the SN/galaxy. The observed effect in Figure 4.13 also

has the correct sign that would be expected for sky over-subtraction with PAIRITEL - 2MASS residuals > 0 near the SN (dimmer photometric measurements due to subtracting too much sky light from the point source), with the opposite effect far from the SN and host galaxy.

Fortunately, any systematic effects at positions near the SN are on the order of $\lesssim 0.01$–0.02 mag in all NIR bands and are negligible contributions to the overall error budget, which is dominated by host galaxy subtraction (see §4.2.2). As such, we choose to ignore this small systematic effect of sky over-subtraction in our SN photometry error budget presented in Table 4.3. As discussed in §3.2, the relative unimportance of sky subtraction systematics in this interpretation also lends justification to our observational choice to not employ on-off pointings and estimate the sky from the data themselves, which allows us to spend a much greater fraction of our telescope time observing targets rather than nearby sky regions without SN.

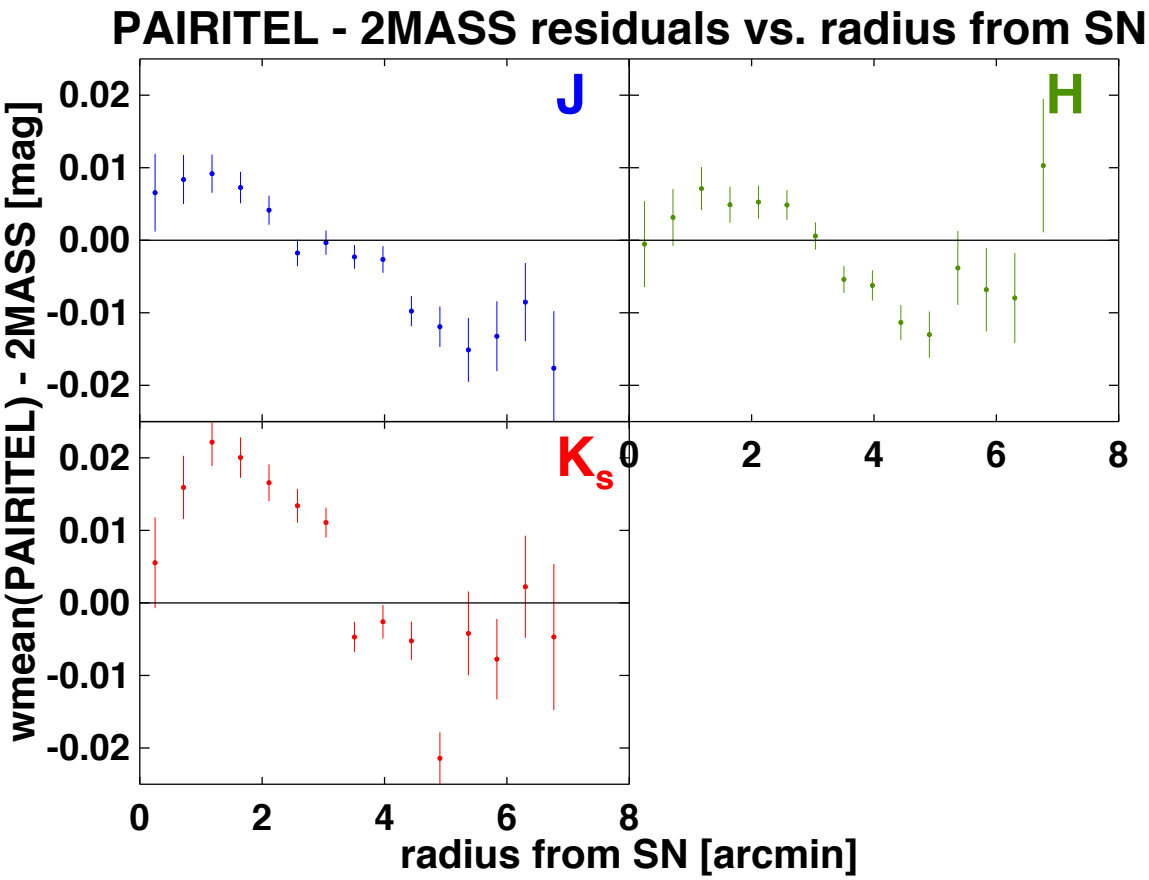

Figure 4.13.— PAIRITEL Sky Subtraction Systematics

We compute the weighted mean PAIRITEL - 2MASS catalog magnitude residuals of 2MASS stars in all PAIRITEL SN Ia fields from Table 4.2 and compute the radius of each star from the SN in arcminutes. We then compute the weighted mean of the binned residuals in 15 equally spaced radius bins in the range $[0, 7]$ $'$ and display the results for the JHK_s bands. A similar trend is seen in each filter. For bins $\lesssim$ 2–3 $'$, the residuals are positive with a maximum of $\sim$ 0.01 mag in JH and $\sim$ 0.02 mag in K, whereas for bins $\gtrsim$ 3 $'$, the residuals are negative with maxima of $\sim -0.02, -0.015$, and -0.02 in JHK_s, respectively. The sign of these residuals is what we would expect if they are due to radially dependent sky subtraction systematic errors for PAIRITEL relative to 2MASS, which we would expect to yield positive magnitude residuals (dimmer PAIRITEL measurements) for sky over-subtraction near the SN/host galaxy and negative magnitude residuals for sky under-subtraction far from the SN/host galaxy (see §3.2). For stars separated by $r \gtrsim 3'$, (beyond the scale of typical SN and host galaxies observed by PAIRITEL), we interpret this as evidence for a slight under-subtraction of sky light with a maximum systematic negative bias of $\lesssim 0.02$ mag in JHK_s, which does not apply to SN photometry near the host galaxy. For stars separated by $r \lesssim 3'$ of the SN (within the size of typical galaxies observed by PAIRITEL in redshift range of $z \sim 0.01$–0.08), we interpret this as evidence for systematic over-subtraction of sky light introducing maximally positively biased systematic photometric errors $\lesssim 0.01$ mag in JH and $\lesssim 0.02$ mag in K_s. Since these systematic photometric uncertainties are small compared to the statistical uncertainties, which are dominated by host galaxy subtraction errors, we ignore their negligible contribution to our overall SN photometric error budget reported in Table 4.3.

4.2.5 Forced DoPHOT Coordinates

Rather than letting DoPHOT determine the best fit centroid for the SN position, we found more accurate centroid estimates using other methods (see §7.2). However, if we force DoPHOT to perform PSF photometry at a position systematically offset from the true centroid, we expect systematically dimmer measurements (a positive magnitude bias), since less SN flux will fall inside the image PSF, which falls off with radius from the true centroid. We test this by performing forced DoPHOT NNT photometry on the host galaxy subtracted difference images in a 13×13 grid with equally spaced increments of $0.25'$ centered on the best estimate of the SN centroid position. We show the results of these tests for 4 example SN in Figure 4.14. For each example SN field in each of the JHK_s bands, Figure 4.14 displays the expected trend, where systematic radial offsets from the best SN centroid yield LCs which are systematically dimmer than the LC at the nominal best SN centroid position. The trends appear to be linear with radius from the true centroid for radial offsets $\gtrsim 0.5''$ and flat (consistent with 0) for radial offsets $\lesssim 0.5''$. Since these 4 example SN are representative of the tests for other SN Ia fields, we conclude that as long as the SN centroid is estimated to within $\lesssim 0.5''$ (equivalent to 0.5 pixels in the mosaic with a plate scale of $1''$ / pixel), we expect no systematic bias in the photometry due to forced DoPHOT coordinate errors. The SN centroid estimation methods described in §7.2 consistently yield better than $\sim 0.2''$ SN astrometry, so we do not consider this to be an important systematic for most SN fields, although we double check the accuracy of the SN coordinates in specific cases where we must choose the best of the three centroid estimation methods described in §7.2.

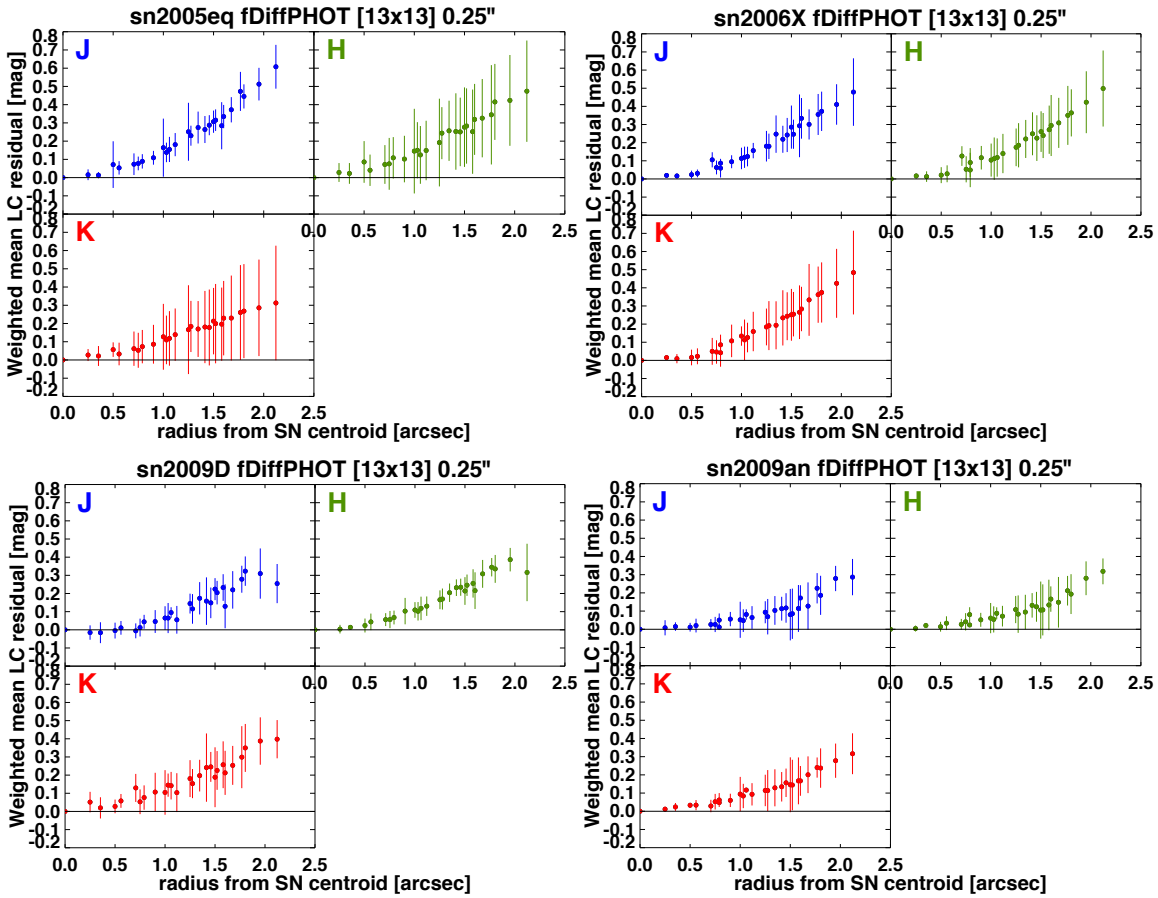

Figure 4.14.— Systematic Uncertainty from Inaccurate SN centroid coordinates for forced DoPHOT Photometry on difference images

We form an evenly spaced 13×13 grid with increments of $0.25'' = 0.25$ pixels centered on the best fit SN centroid (see §7.2). At each of the $13 \times 13 = 169$ grid positions, we perform forced DoPHOT photometry at that position in the host galaxy subtracted difference image. At each grid point we compute the weighted mean residual between the entire time series of the difference image light curve at that position and the difference image light curve at the reference position in the grid center at the best fit SN position. We convert each of the cartesian grid positions into a radius from the grid center and bin the weighted mean residuals for multiple points at the same radius. This approximation assumes spherical symmetry, which would be broken and biased in the direction of a galaxy not completely subtracted from the difference image. We plot the weighted mean, radius-binned, magnitude residuals of the entire JHK_s band LC time series with respect to the putative SN LC versus radius for 4 example SN LCs, SN 2005eq (**Upper Left**), SN 2006X (**Upper Right**), SN 2009D (**Lower Left**), and SN 2009an (**Lower Right**). In each case, the magnitude residuals are flat (0) for radii $r \lesssim 0.5$ ″, then positive and increasing roughly linearly with radius $r \gtrsim 0.5$ ″ indicating a potential systematic bias in favor of dimmer LCs (greater magnitudes) with increasing radius from the true SN coordinates on the order of ~ 0.1–0.2 mag / ″ of displacement from the true SN centroid. While the slopes in the linear regime are different for different SN fields, the trends for all fields shown above indicate that we expect no systematic magnitude bias as long as the SN centroid coordinates are accurate to better than $0.5'' = 0.5$ pixels, astrometry which is easily achievable for our SN centroid estimation methods which are typically accurate to better than $\sim 0.2''$ ($= 0.2$ pixels), (§7.2).

4.2.6 Time Variation of Detector Properties

As the detector ages and degrades, the number of bad pixels increases. If an increasing fraction of the array becomes defective it would require longer effective exposures to reach the same sensitivity in a given bandpass. Eventually, this could make the camera unusable. However, since the bad pixels are masked out, and the dithering process allows light from the sky to fall on different pixels during the dither pattern, we do not expect this effect to systematically bias point source photometry as long as the time variation of bad pixel degradation is slow compared to the timescales of light curves (months) and as long as the fraction of bad pixels in the array remains small. The increase in the fraction of bad pixels for the PAIRITEL camera is shown in Figure 4.15, where the fraction of bad pixels in the 256×256 array increased from $0.2\% \rightarrow 1.2\%$, $2.3\% \rightarrow 2.5\%$, and $1.8\% \rightarrow 2.2\%$ in the JHK_s bands, respectively in a 5 plus year span from 2001 to 2006 as the camera transitioned from 2MASS to PAIRITEL. Figure 4.15 thus shows that the bad pixel fraction of the 2MASS southern camera changed by $\lesssim 1\%$ in JHK_s over a 5 year span between its transition from 2MASS to PAIRITEL. Overall, a 256×256 pixel array with $\sim 1 - 2\%$ of the $65,536$ total pixels flagged as bad still has more than enough good pixels (more than $64,000$) with which to construct a mosaic and perform photometry. In addition, since, bad pixel masks are recreated dynamically for each mosaic, we automatically account for time variation the bad pixel distribution. This approach is superior to using archival bad pixel masks, which could systematically effect measurements by including new bad pixels in the non-masked data. The bad pixel masks as of February 2012 showed bad pixel fractions of 2.1%, 3.3%, and 2.2% in JHK_s, respectively. Overall, we do not expect

the increasing bad pixel fraction to systematically effect PAIRITEL SN photometry since the bad pixel fraction is still quite small.

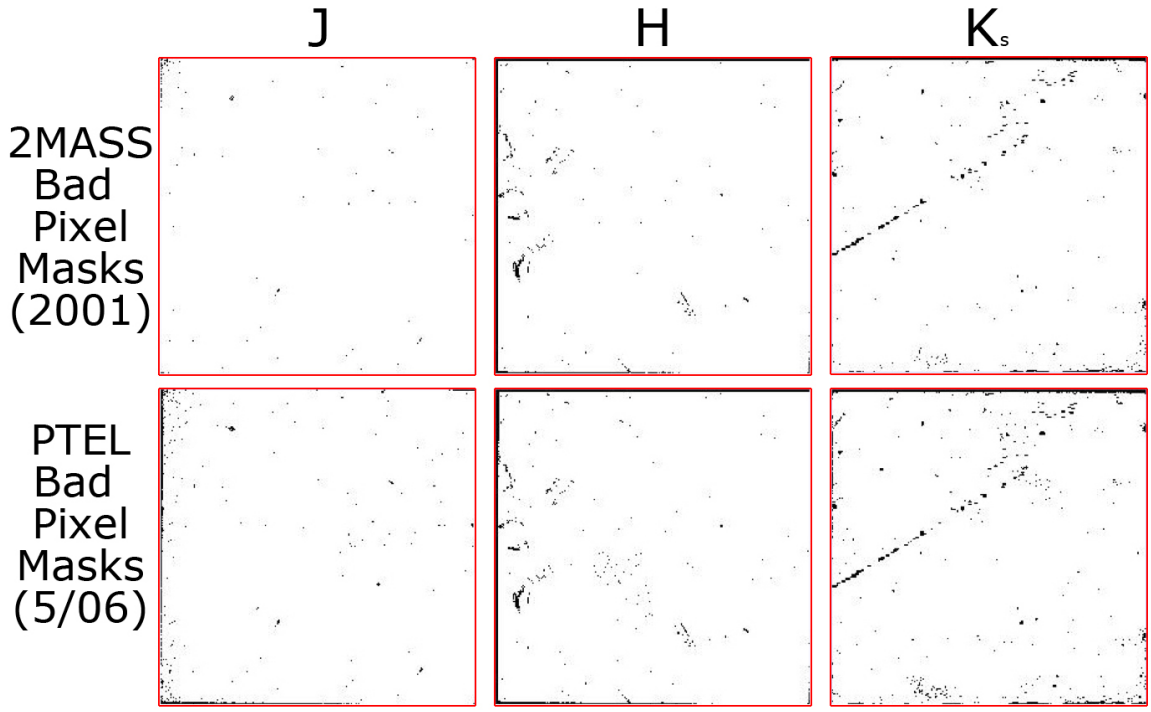

Figure 4.15.— Time Variation of PAIRITEL Bad Pixel Masks 2001-2006

Each of PAIRITEL JHK_s bands has a separate 256×256 pixel NICMOS3 HgCTe detector. The fraction of bad pixels in these 256×256 arrays increased from $0.2\% \rightarrow 1.2\%$, $2.3\% \rightarrow 2.5\%$, and $1.8\% \rightarrow 2.2\%$ in the JHK_s bands, respectively in a 5 plus year span from 2001 to 2006 as the camera was transitioned from 2MASS to PAIRITEL. The bad pixel masks as of February 2012 showed bad pixel fractions of 2.1%, 3.3%, and 2.2% in JHK_s, respectively.

4.2.7 Atmospheric Water Vapor

The total transmission function of the PAIRITEL/2MASS system includes the convolution of the effects from atmosphere, telescope and camera optics, and the quantum efficiency of the detector. The most uncertain of these effects is the transmission of the atmosphere, due to the presence of precipitable water vapor, a time-variable phenomenon which can significantly change the effective NIR JHK_s bandpasses. Atmospheric absorption and scattering by additional water vapor has the effect of shrinking the size of the effective bandpass, lowering the sensitivity, and changing the effective zero point of the filter relative to well understood calibration stars. Water vapor has the biggest potential systematic impact in the J-band, leading to more significant seasonal variations in the J-band filter zero point (Skrutskie et al. 2006), with the worst transmission losses and systematic biases toward lower sensitivities at Mount Hopkins present at the start and end of the summer monsoon which lasts from late July to early September. The observatory is typically shut down for all of August during the monsoon.

While the 2MASS survey painstakingly removed these water vapor induced zero-point variations via hourly observations of calibration fields, PAIRITEL did not do so. As such, PAIRITEL observations, which use 2MASS stars as calibrators, may suffer from seasonal systematic biases in the effective zero point of the JHK_s filters, especially in the J-band (see Figure 7 of Skrutskie et al. 2006). Fortunately, the signal-to-noise for PAIRITEL is highest in J, mitigating the severity of this potential systematic. Additionally, the zero point variation found by 2MASS from 2000-2001 ranges only from ~ -0.05 to 0.05 mag from late September to early July

in the H and K_s bands, which is small compared to the statistical uncertainties from host galaxy subtraction and sky + dark subtraction in those bands. Unfortunately, larger zero point offsets (with respect to calibrator magnitudes) were seen by 2MASS in the J-band of ranges from ~ -0.15–0.15 mag. As such, PAIRITEL J-band LCs observed with data points in late July and early September are most susceptible to this source of systematic uncertainty, while observations from late September to early July, where most of our observations are taken, are less susceptible to water vapor zero point filter systematics.

Since the effective NIR bandpasses are narrower in the presence of water vapor, especially in J, one might suspect this could lead to systematic photometric biases in the direction of less flux (larger magnitudes) when there is more water vapor present and in the opposite direction otherwise. However, since the PAIRITEL LCs are calibrated by measuring 2MASS stars, any effect would be a second order effect which would depend crucially on the features of the spectra of standard stars, especially if the stars had strong features which could fall in and out of the effective bandpass depending on the amount of water vapor, changing the measured colors of the calibration stars. We can only conclude that water vapor does *not necessarily* imply a systematic bias in SN photometry calibrated with 2MASS stars, as long as the shift in the effective filter zero point does not lead to large changes in the 2MASS star colors as measured by PAIRITEL. Overall, in the absence of detailed information on the spectra of 2MASS stars, we can not draw conclusions regarding the systematic bias on SN photometry from changing effective NIR bandpasses due to water vapor. While atmospheric water vapor is potentially an important systematic for PAIRITEL, a full investigation is beyond the scope of this thesis.

4.3 Internal and External Consistency Checks

In §4.3, we perform internal and external consistency checks, comparing our new data with previously published light curves for the same objects. In §4.3.1 we perform an internal consistency check, comparing new PAIRITEL F12 photometry (Friedman et al. 2012 *in preparation*)[3] to older PAIRITEL WV08 photometry for the subset of 21 SN Ia LCs previously published in Wood-Vasey & Friedman et al. 2008. In §4.3.2, we compare both our old WV08 and our new F12 photometry to the 19 SN Ia LCs also observed by the Carnegie Supernova Project (CSP).

4.3.1 Comparing CfAIR2 to WV08 Photometry

We present new F12 photometry for 20 out of the 21 SN Ia LCs presented in WV08 (with the exception of SN 2005cf, which failed our new photometry pipeline), compared directly in Figures 4.17–4.19. This allows us to perform another internal consistency check of the output from the old and new versions of our photometry pipeline using the p2.0 and p3.6 input mosaics, respectively. Objects in the F12/WV08 overlap set of 21 SN Ia include 18 normal SN Ia (SN 2005ao, SN 2005cf, SN 2005ch, SN 2005el, SN 2005eq, SN 2005eu, SN 2005iq, SN 2005na, SN 2006D, SN 2006N, SN 2006X, SN 2006ac, SN 2006ax, SN 2006cp, SN 2006gr, SN 2006le, SN 2006lf, SN 2007cq) and 3 peculiar SN Ia (SN 2005bl, SN 2005hk, SN 2005ke). As expected, the brightest, most well-isolated, SN Ia with little host galaxy light at the SN position have F12/WV08 photometry largely in agreement as seen in

[3]To clarify, CfAIR2 is the subset of publication-worthy SN Ia data derived from F12 photometry.

Figures 4.17–4.19. In these cases, F12 used NNT galaxy subtracted photometry and WV08 used forced DoPHOT photometry with an approximate host galaxy subtraction correction. The SN Ia that used forced DoPHOT photometry (fdo) in WV08 include 9 out of 21 objects: SN 2005el, SN 2005hk, SN 2005ke, SN 2006ac, SN 2006cp, SN 2006D, SN 2006gr, SN 2006lf, and SN 2006X. On the other hand, fainter SN Ia that required significant host galaxy subtraction show the most disagreement — as seen in Figures 4.17–4.19 — between F12 and WV08 due mainly to the differences between NN2 used in WV08 and NNT used in F12. The SN Ia that used NN2 difference imaging photometry in WV08 include 11 out of 21 objects: SN 2005ao, SN 2005bl, SN 2005ch, SN 2005eq, SN 2005eu, SN 2005iq, SN 2005na, SN 2006N, SN 2006ac, SN 2006le, and SN 2007cq. In WV08, one additional object, SN 2005cf used difference imaging with a single template (effectively NNT with $N_{\rm SNTEMP} = 1$) but not NN2.[4] Unfortunately, we were not able to successfully produce a F12 LC for SN 2005cf with our new photometry pipeline, so we present the WV08 LC for this object in all Figures or Tables where SN 2005cf is displayed. The problems with NN2 photometry from WV08 becomes evident in the the most important subset of the F12/WV08 SN Ia, namely the set of 9 WV08 SN Ia also observed by the CSP which are discussed in §4.3 along with 10 additional SN Ia new to CfAIR2. Because we believe the CSP photometry to be of higher quality than PAIRITEL photometry (better accuracy and precision) due to fundamental

[4]Note that the list of fdo vs. NN2 from WV08 presented here supersedes the text of Wood-Vasey et al. 2008, where the WV08 text has some errors. The WV08 text says "DoPHOT photometry on the images was used for those SNe Ia that were clearly separated from their host galaxy and had little underlying contaminating light (SN 2005ao, SN 2005cf, SN 2005el, SN 2005hk, SN 2005ke, SN 2005eu, SN 2005iq, SN 2005na, SN 2006N, and SN 2006X)." This would imply that all other SN Ia were reduced with NN2. In fact, the correct list should read as above.

differences between our telescopes, instruments, observing sites, and host galaxy subtraction processes (see §2.2 and Table 2.1), the significantly improved agreement between F12 and CSP photometry, as compared to WV08 and CSP photometry gives us perhaps our strongest evidence that F12 photometry represents a significant improvement to the WV08 photometry.

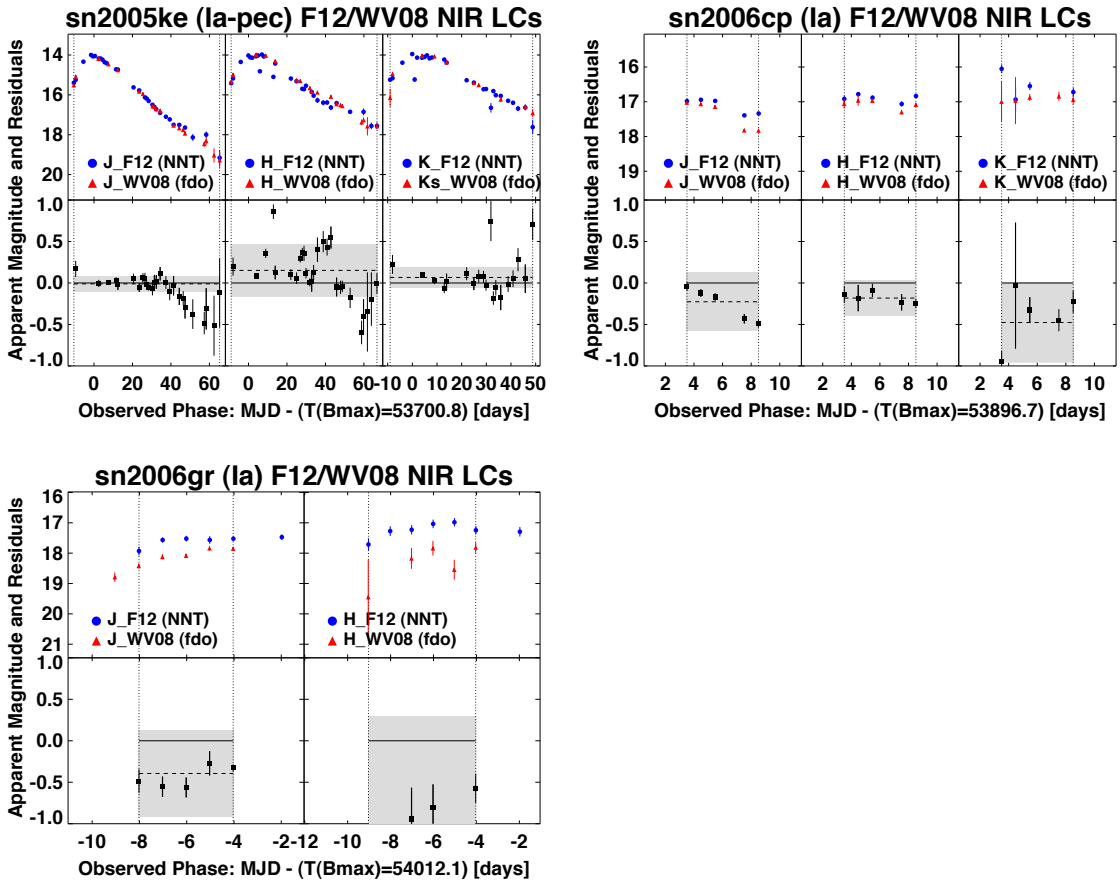

Figure 4.16.— F12/WV08 Photometry Comparison for SN Ia SN 2005ke, SN 2006cp, SN 2006gr.

(Top panels) JHK_s SN Ia LCs from PAIRITEL CfAIR2 NNT galaxy subtracted photometry (blue circles) and WV08 forced DoPHOT photometry with an approximate host galaxy subtraction correction (red triangles).

(Bottom panels) Residuals (black squares) are computed as direct data differences. No model fit is needed to compute residuals, since overlapping data are from the same observed phase. The residuals for most objects are consistent with zero within the individual 1-σ uncertainties over most phases, although the late time residuals for some SN Ia show the presence of galaxy flux at late times (the mean residuals rising above the zero residual line) in the LC that were neglected by using forced DoPHOT photometry on the un-subtracted images in WV08.

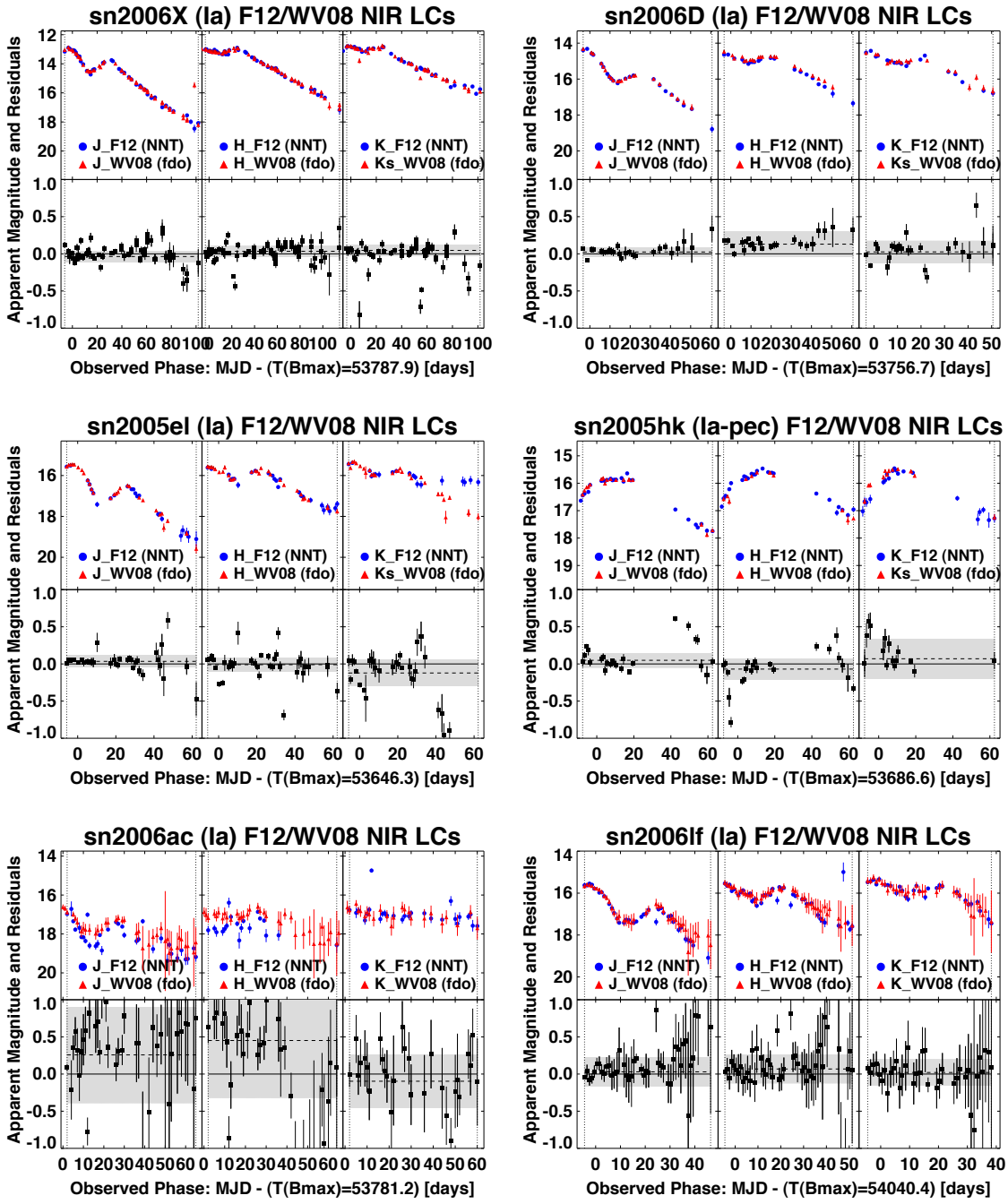

Figure 4.17.— F12/WV08 Photometry Comparison for SN Ia SN 2005el, SN 2005hk, SN 2006ac, SN 2006D, SN 2006lf, and SN 2006X.

(Top panels) JHK_s SN Ia LCs from PAIRITEL CfAIR2 NNT galaxy subtracted photometry (blue circles) and WV08 forced DoPHOT photometry with an approximate host galaxy subtraction correction (red triangles).

(Bottom panels) Residuals (black squares) are computed as direct data differences. No model fit is needed to compute residuals, since overlapping data are from the same observed phase. The residuals for most objects are consistent with zero within the individual 1-σ uncertainties over most phases, although the late time residuals for some SN Ia show the presence of galaxy flux at late times (the mean residuals rising above the zero residual line) in the LC that were neglected by using forced DoPHOT photometry on the un-subtracted images in WV08.

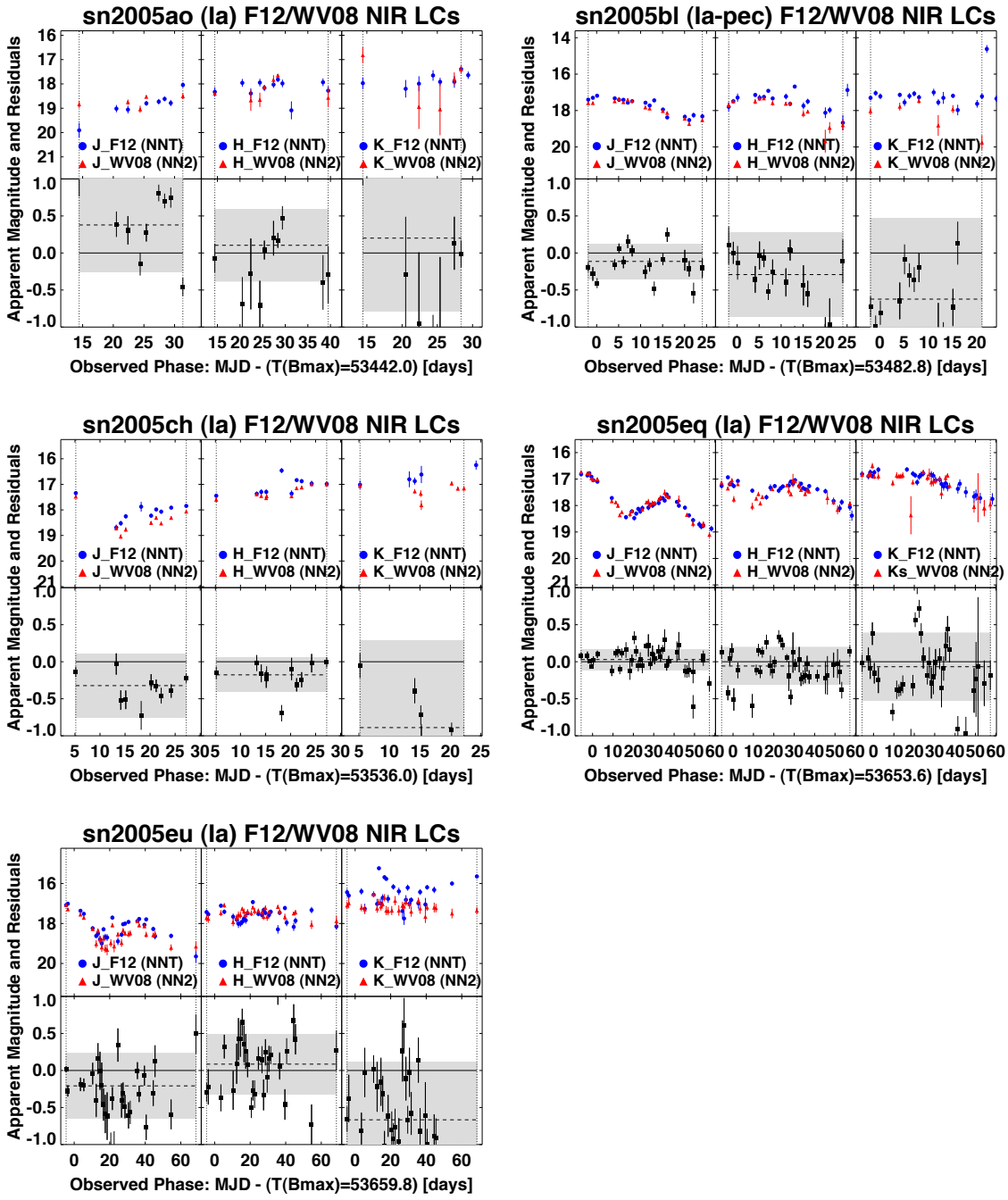

Figure 4.18.— F12/WV08 Photometry comparison for SN Ia SN 2005ao, SN 2005bl, sn2005ch, SN 2005eq, and SN 2005eu.

(Top panels) JHK_s SN Ia LCs from PAIRITEL CfAIR2 NNT galaxy subtracted photometry (blue circles) and WV08 NN2 galaxy subtracted photometry (red triangles).

(Bottom panels) Residuals (black squares) are computed as direct data differences. No model fit is needed to compute residuals, since overlapping data are from the same observed phase. The weighted mean residual is overplotted as a dashed line and ± the standard deviation of the residuals is overplotted as a gray region around the weighted mean residual.

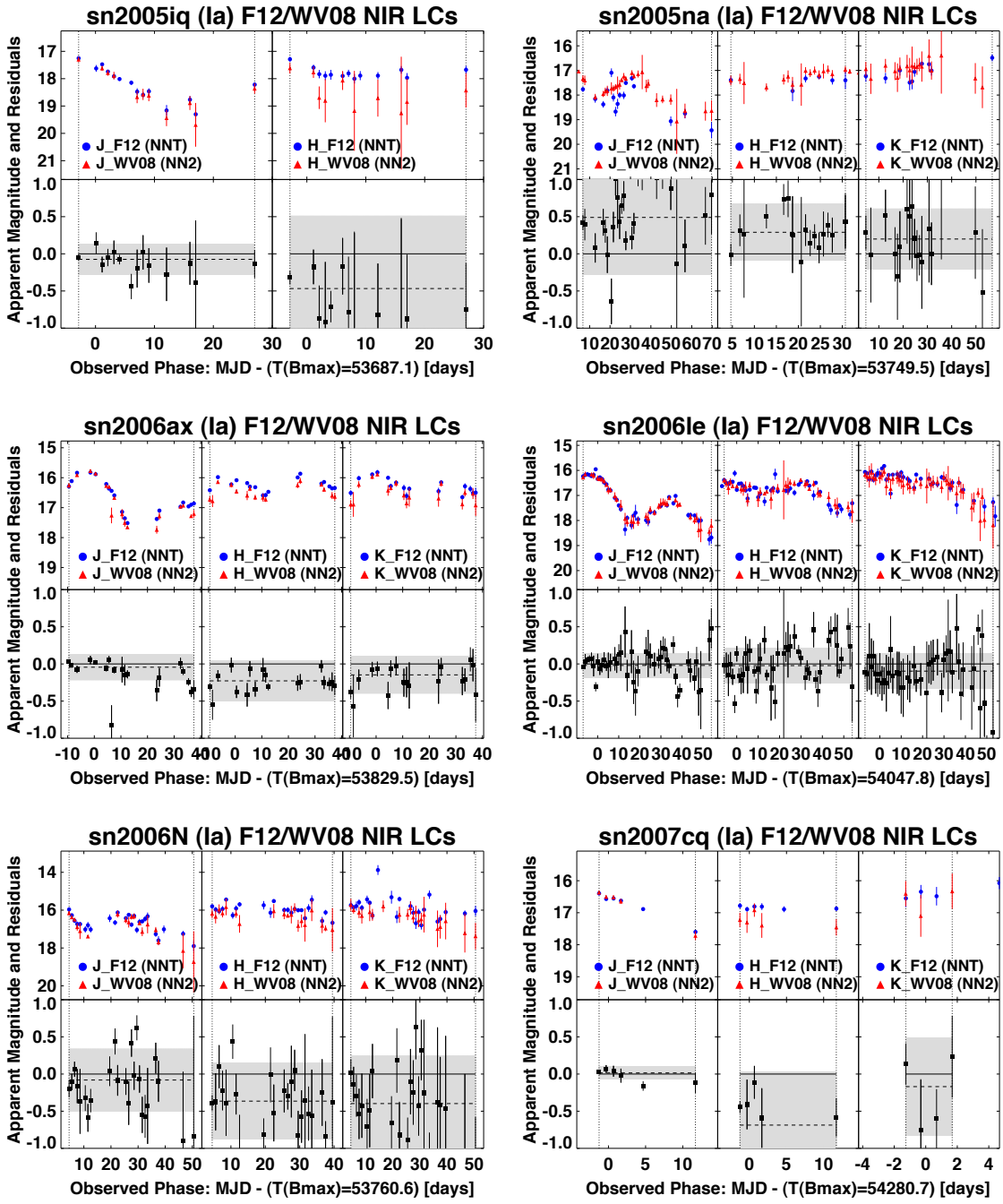

Figure 4.19.— F12/WV08 Photometry comparison for SN Ia SN 2005iq, SN 2005na, SN 2006ax, SN 2006le, SN 2006N, SN 2007cq.

(Top panels) JHK_s SN Ia LCs from PAIRITEL CfAIR2 NNT galaxy subtracted photometry (blue circles) and WV08 NN2 galaxy subtracted photometry (red triangles).

(Bottom panels) Residuals (black squares) are computed as direct data differences. No model fit is needed to compute residuals, since overlapping data are from the same observed phase. The weighted mean residual is overplotted as a dashed line and ± the standard deviation of the residuals is overplotted as a gray region around the weighted mean residual.

4.3.2 Comparing PAIRITEL and CSP Photometry

Although the CfA and CSP observatories with NIR capabilities are in the northern and southern hemispheres, respectively, an overlapping subset of 19 SN Ia were observable by both groups, presenting a unique opportunity to compare independent photometric measurements (See Figures 4.20–4.26). Most of the originally published PAIRITEL SN Ia photometry (WV08; Wood-Vasey et al. 2008) was consistent with Carnegie Swope photometry for the same objects (CSP; Phillips et al. 2007; Contreras et al. 2010) modulo the photometric uncertainties and bandpass differences. However, direct comparison did reveal a significant disagreement between a small subset of the WV08 and CSP objects that required significant host galaxy subtraction (first identified by M. Phillips — private communication). We now find that, with a few exceptions, our newest PAIRITEL F12 galaxy subtracted photometry is consistent with CSP photometry for the overlap objects and in essentially all cases agrees better with CSP than our original WV08 photometry, which likely incurred significant systematic errors from the NN2 host galaxy subtraction process and DoPHOT uncertainty underestimates due to approximate assumptions about the noise in the un-subtracted images which we have since improved upon (see §4.1.2). The increased agreement of PAIRITEL F12 photometry with the high quality CSP photometry results from a combination of several upgrades to our data reduction and photometry pipelines including improved p3.6 mosaics, noise maps, bad image rejection (See §3), correction for underestimation of our nightly DoPHOT uncertainties with tests using 2MASS stars (§4.1.2), and especially our decision to use NNT instead of NN2 subtractions (See §3.4, §4.2.1).

Objects in the PAIRITEL/CSP NIR overlap set of 19 SN include 15 normal SN Ia (SN 2005el, SN 2005eq, SN 2005iq, SN 2005na, SN 2006D, SN 2006X, SN 2006ax, SN 2006is, SN 2007S, SN 2007ca, SN 2007le, SN 2007nq, SN 2007sr, SN 2008C, SN 2008hv), 2 peculiar, fast-decining SN Ia (SN 2005hk, SN 2005ke), and 2 overluminous, slowly-declining objects (SN 2007if, SN 2009dc). Of these, 9 had data published in WV08 (SN 2005el, SN 2005eq, SN 2005iq, SN 2005na, SN 2006D, SN 2006X, SN 2006ax, SN 2005hk, SN 2005ke) and 10 are new to F12 (SN 2006is, SN 2007S, SN 2007ca, SN 2007if, SN 2007le, SN 2007nq, SN 2007sr, SN 2008C, SN 2008hv, SN 2009dc), although we present revised F12 photometry for all WV08 objects except for SN 2005cf. CSP data is shown for the following SN Ia and references: (SN 2005hk: Phillips et al. 2007), (SN 2007sr: Schweizer et al. 2008), (SN 2009dc: Taubenberger et al. 2011), (SN 2005el, SN 2005eq, SN 2005iq, SN 2005na, SN 2006D, SN 2006X, SN 2006ax: Contreras et al. 2010), and (SN 2006is, SN 2007S, SN 2007ca, SN 2007le, SN 2007nq, SN 2007sr, SN 2008C, SN 2008hv: Stritzinger et al. 2011). 3 other SN Ia (SN 2005bo, SN 2005bl, SN 2005mc) have PAIRITEL JHK_s observations and CSP optical observations but no CSP NIR observations (SN 2005bl: Taubenberger et al. 2008; SN 2005bo, SN 2005mc: Contreras et al. 2010), so they are not included in the PAIRITEL/CSP NIR comparison set. Similar to Table §2.3 presented here, Table 1 of Contreras et al. 2010 and Table 1 of Stritzinger et al. 2011 present the general properties of 35 and 50 SN Ia observed by the CSP, respectively, 19 of which were also independently observed by PAIRITEL.

Figures 4.20–4.26 overplot PAIRITEL and CSP SN Ia LCs for direct comparison. The top row panels show the JHK_s SN Ia LCs where available (often CSP K-band

is missing) with PAIRITEL and CSP data denoted with blue circles and red triangles, respectively. The overplotted black line is an N-degree ($N = 8 - 12$) polynomial model fit to the joint PAIRITEL+CSP data that uses the WV08 SN Ia template LC to inform the fit for missing data (See §5.2). For all fits, to account for intrinsic variation of the NIR light curve shapes and luminosities, the data is given greater weight than the template in contributing to the model fit. Model fits for peculiar SN Ia were direct fits to the data and did not use the normal SN Ia template LC to help fill in missing data, although the template LC was used to help fit the 2 overluminous, peculiar SN Ia (SN 2007if, SN 2009dc), yielding a poor fit for SN 2007if which led us to ignore the residuals for that object in Figure 4.26 and for tests comparing the CSP and PAIRITEL zero point offsets (§4.3.3). The bottom rows of Figures 4.20–4.26 show residuals computed as the difference between the data and the joint model fit with the same plot symbols and colors used for the data in the upper panel to distinguish PAIRITEL and CSP data. It is usually not possible to compute direct data differences because PAIRITEL and CSP observations generally occurred at slightly different phases. We thus require a smooth model fit to interpolate from to compute relative residuals. Late time residuals are often dominated by the uncertainty in the model fit, so direct visual comparison of the late time PAIRITEL and CSP data is a better qualitative indicator of agreement or disagreement for the faintest late time LC points.

Figures 4.20–4.22 demonstrate the improvement in agreement between PAIRITEL and CSP using the original WV08 and the revised F12 photometry. Qualitatively, agreement between PAIRITEL and CSP can be seen as the lack of any systematic offset from the mean residual for either PAIRITEL or CSP

above or below the black zero line, and a decrease in scatter of the residuals from WV08/CSP to F12/CSP. All F12 data shown is for galaxy subtracted NNT photometry. WV08 data in the overlap set used galaxy subtracted NN2 photometry for 4 objects (SN 2005eq, SN 2005iq, SN 2005na, SN 2006ax), and forced DoPHOT photometry with an approximate host galaxy subtraction correction for 6 objects (SN 2005bl, SN 2005el, SN 2006D, SN 2006X, SN 2005hk, SN 2005ke). Problems with NN2 galaxy subtraction likely caused the biggest systematic differences between WV08/CSP, specifically for SN 2005eq, SN 2006ax, SN 2005iq, and SN 2005na, which now agree much better with F12 NNT photometry (although SN 2005iq and SN 2005na are both quite faint for PAIRITEL). F12 LCs also agree as well or better with CSP for the brightest SN Ia well isolated from their host galaxy that used forced DoPHOT photometry corrected with approximate galaxy subtraction in WV08: SN 2005hk, SN 2005el, SN 2006D, and SN 2006X, and SN 2005ke.

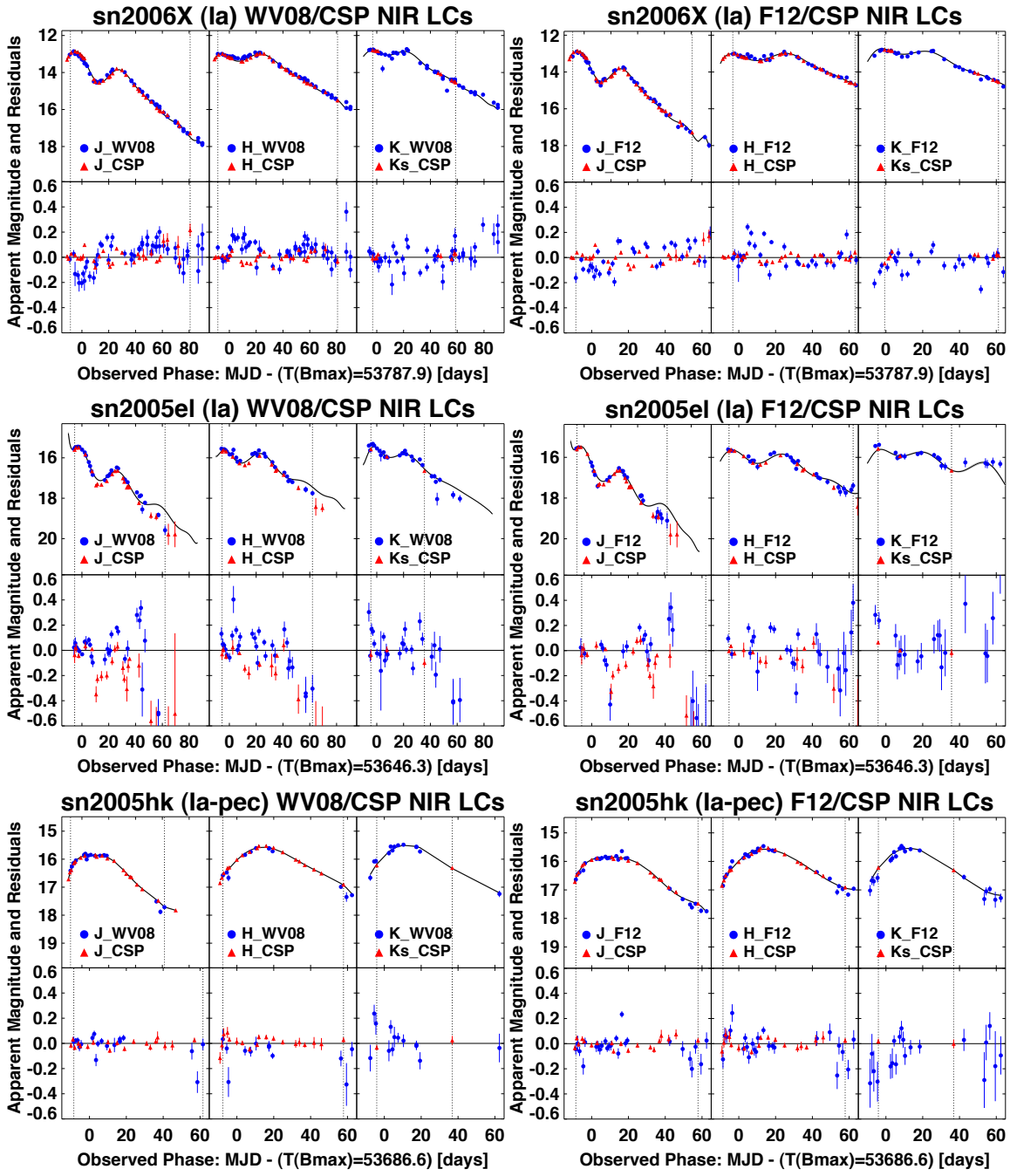

Figure 4.20.— Comparing WV08 and F12 (CfAIR2) to CSP Photometry

(Left Column) WV08 and CSP Photometry for the same SN Ia

(Right Column) F12 and CSP Photometry for the same SN Ia

(Top panels) JHK_s SN Ia LCs from PAIRITEL F12 galaxy subtracted photometry (blue circles) and CSP (red triangles). The black line is a N-degree ($N = 8 - 12$) polynomial model fit to the joint PAIRITEL+CSP data that uses the WV08 template LC to fit for missing data for normal SN Ia.

(Bottom panels) Residuals are computed as the difference between the data and the joint model fit with the same plot symbols and colors used for the data in the upper panel.

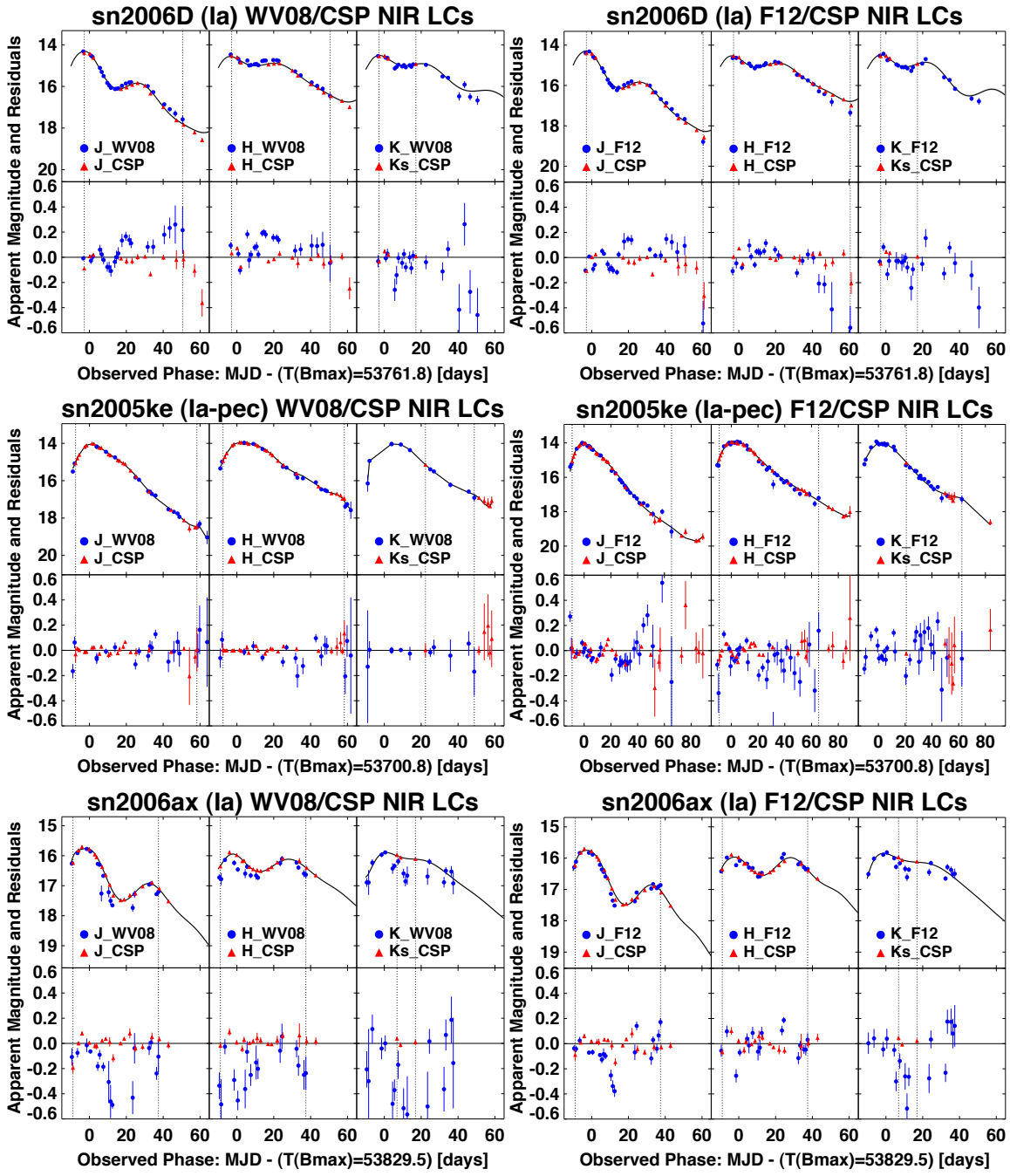

Figure 4.21.— Comparing WV08 and F12 (CfAIR2) to CSP Photometry

(Left Column) WV08 and CSP Photometry for the same SN Ia

(Right Column) F12 and CSP Photometry for the same SN Ia

(Top panels) JHK_s SN Ia LCs from PAIRITEL F12 galaxy subtracted photometry (blue circles) and CSP (red triangles). The black line is a N-degree ($N = 8 - 12$) polynomial model fit to the joint PAIRITEL+CSP data that uses the WV08 template LC to fit for missing data for normal SN Ia.

(Bottom panels) Residuals are computed as the difference between the data and the joint model fit with the same plot symbols and colors used for the data in the upper panel.

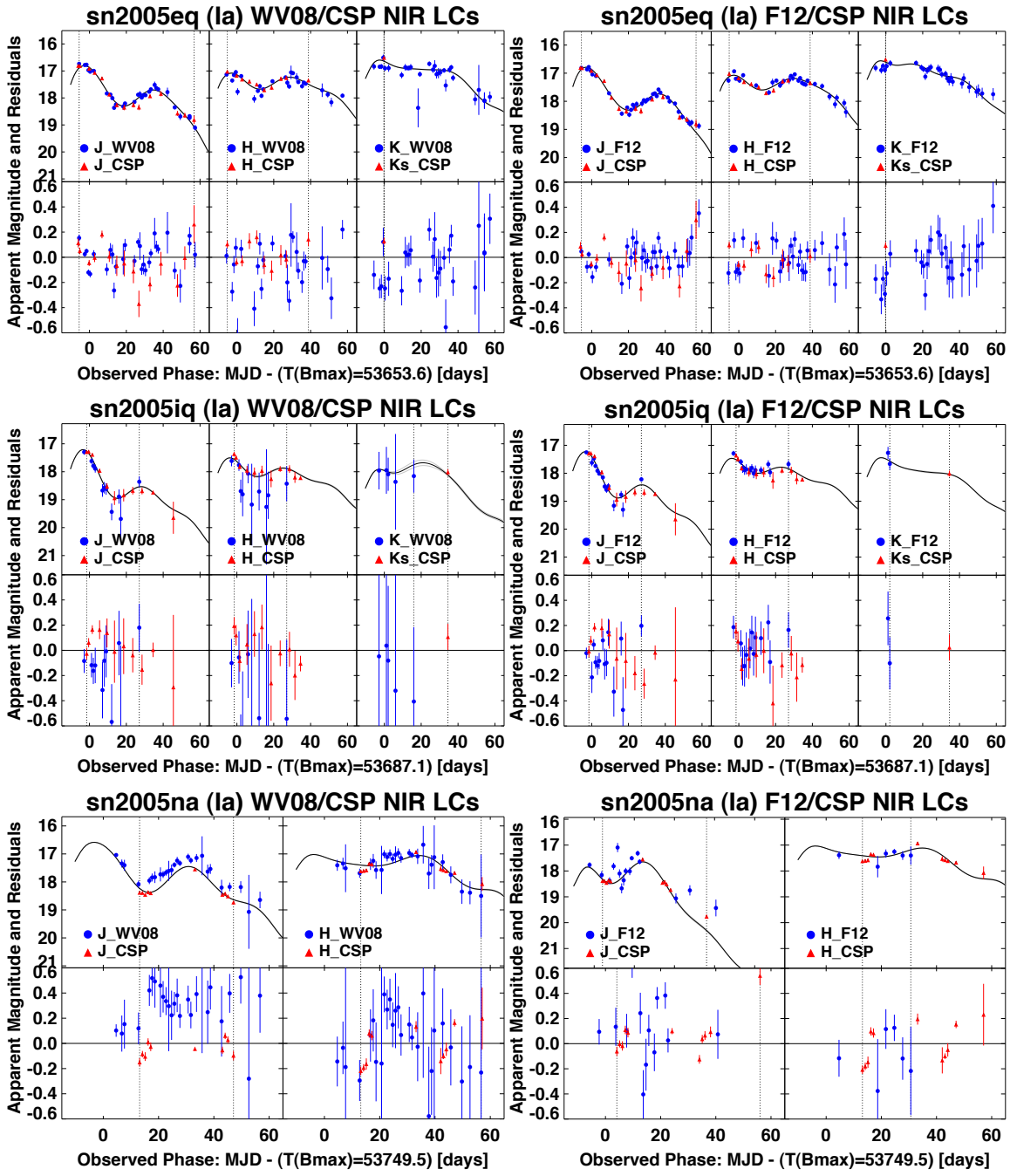

Figure 4.22.— Comparing WV08 and F12 (CfAIR2) to CSP Photometry

(Left Column) WV08 and CSP Photometry for the same SN Ia

(Right Column) F12 and CSP Photometry for the same SN Ia

(Top panels) JHK_s SN Ia LCs from PAIRITEL F12 galaxy subtracted photometry (blue circles) and CSP (red triangles). The black line is a N-degree ($N = 8 - 12$) polynomial model fit to the joint PAIRITEL+CSP data that uses the WV08 template LC to fit for missing data for normal SN Ia.

(Bottom panels) Residuals are computed as the difference between the data and the joint model fit with the same plot symbols and colors used for the data in the upper panel.

Figures 4.23–4.26 compare PAIRITEL F12 photometry to CSP photometry for all 19 overlapping SN Ia, including those already shown in Figures 4.20–4.22. F12 photometry now agrees well with CSP for most SN Ia with data originally published in WV08 including: SN 2005eq, SN 2005iq, SN 2005el, SN 2005hk, SN 2005ke, SN 2005na, SN 2006D, SN 2006X, and SN 2006ax (Figures §4.24–4.25). Many new F12 SN Ia also agree well with CSP including: SN 2007S, SN 2007ca, SN 2007le, SN 2008hv, SN 2007sr and SN 2009dc (Figure 4.23). Overall, the scatter in the residuals for objects that show good agreement is consistent with what would be expected from photometric uncertainties, bandpass differences, and uncertainties due to the model fit, which often dominate the residuals at late times due to a lack of late-time data in the objects and in the WV08 LC template. We quantify the weighted mean NIR residuals from joint PAIRITEL and CSP measurements of the same SN Ia and from joint measurements of 2MASS stars in §4.3.3.

Some fainter SN still exhibit disagreements beyond what would be expected from photometric uncertainties and bandpass differences, but this is most likely because we are reaching the limit of PAIRITEL measurements. As shown in Figure 4.25, exceptions that show significant disagreement include: SN 2006is (bad forced DoPHOT coordinates?, SN too faint), SN 2007nq (sparse data, problem with the model fit that makes the residuals meaningless), SN 2007if (overluminous peculiar SN Ia, not enough data to fit model without template for these objects). In all cases, these objects are either very faint for PAIRITEL and/or in need of better galaxy subtractions with additional SNTEMP images, which we are in the process of obtaining. These PAIRITEL data may not all be suitable for publication in the CfAIR2 data set to be presented in F12 (Friedman et al. 2012 *in preparation*).

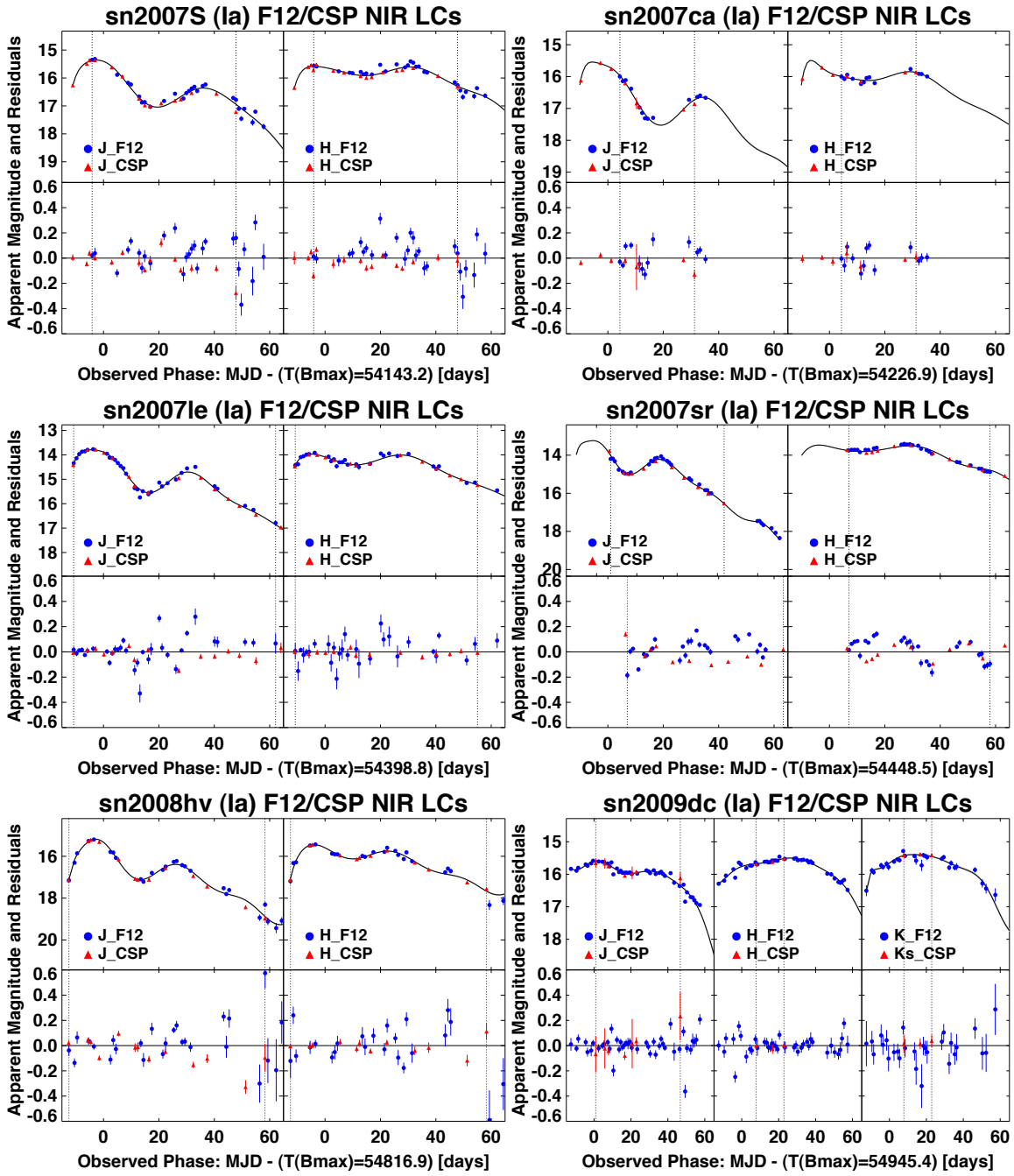

Figure 4.23.— Comparing F12 (CfAIR2) to CSP Photometry

(Top panels) JHK_s SN Ia LCs from PAIRITEL CfAIR2 galaxy subtracted photometry (blue circles) and CSP (red triangles). The black line is a N-degree ($N = 8 - 12$) polynomial model fit to the joint PAIRITEL+CSP data that uses the WV08 template LC to fit for missing data for normal SN Ia.

(Bottom panels) Residuals are computed as the difference between the data and the joint model fit with the same plot symbols and colors used for the data in the upper panel.

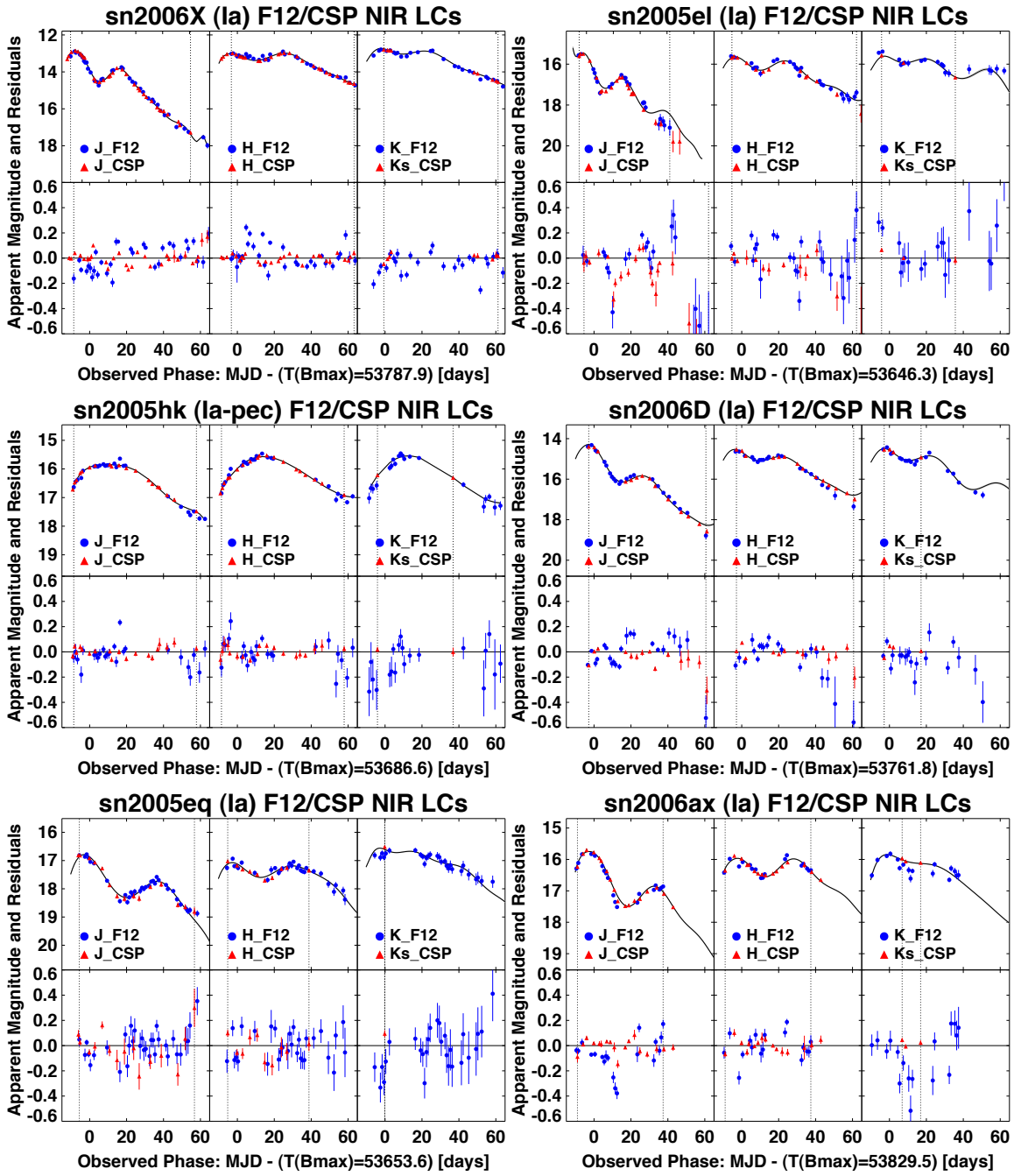

Figure 4.24.— Comparing F12 (CfAIR2) to CSP Photometry

(Top panels) JHK_s SN Ia LCs from PAIRITEL CfAIR2 galaxy subtracted photometry (blue circles) and CSP (red triangles). The black line is a N-degree ($N = 8 - 12$) polynomial model fit to the joint PAIRITEL+CSP data that uses the WV08 template LC to fit for missing data for normal SN Ia.

(Bottom panels) Residuals are computed as the difference between the data and the joint model fit with the same plot symbols and colors used for the data in the upper panel.

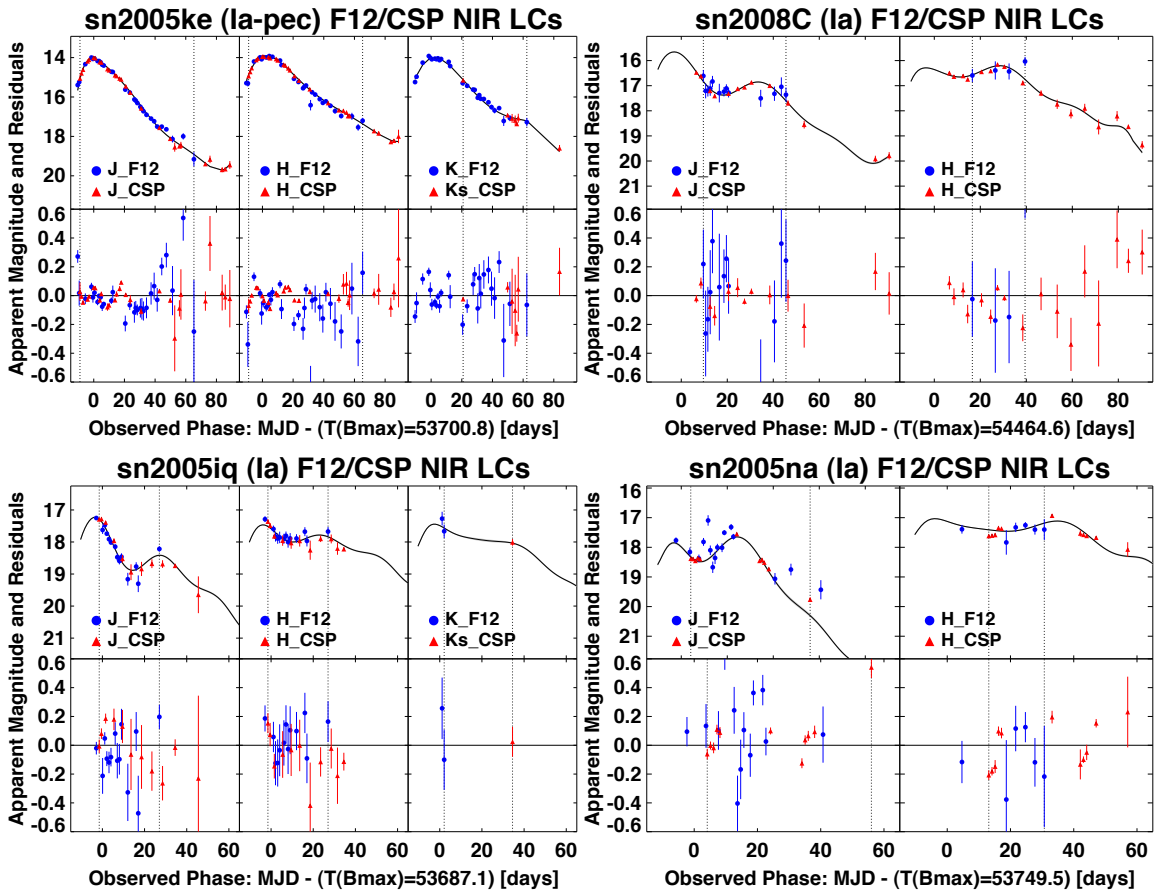

Figure 4.25.— Comparing F12 (CfAIR2) to CSP Photometry

(Top panels) JHK_s SN Ia LCs from PAIRITEL CfAIR2 galaxy subtracted photometry (blue circles) and CSP (red triangles). The black line is a N-degree ($N = 8 - 12$) polynomial model fit to the joint PAIRITEL+CSP data that uses the WV08 template LC to fit for missing data for normal SN Ia.

(Bottom panels) Residuals are computed as the difference between the data and the joint model fit with the same plot symbols and colors used for the data in the upper panel.

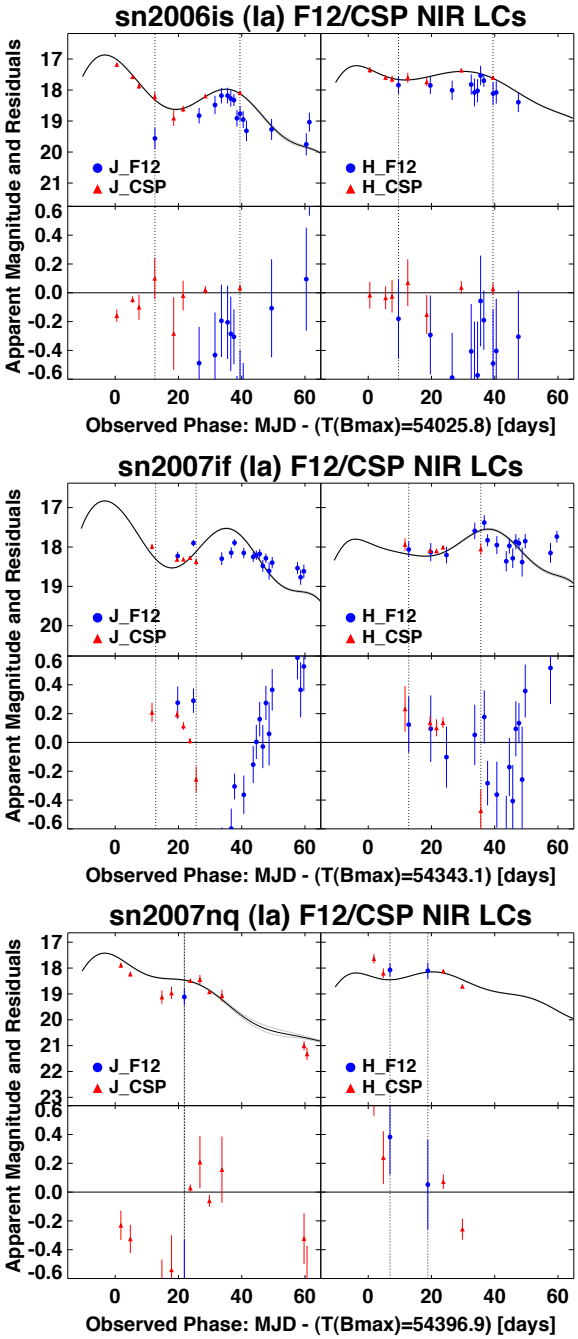

Figure 4.26.— Comparing F12 (CfAIR2) to CSP Photometry

(Top panels) JHK_s SN Ia LCs from PAIRITEL CfAIR2 galaxy subtracted photometry (blue circles) and CSP (red triangles). The black line is a N-degree ($N = 8 - 12$) polynomial model fit to the joint PAIRITEL+CSP data that uses the WV08 template LC to fit for missing data for normal SN Ia.

(Bottom panels) Residuals are computed as the difference between the data and the joint model fit with the same plot symbols and colors used for the data in the upper panel.

4.3.3 CSP - PAIRITEL Zero Point Offsets and Color Terms

Some remaining scatter in the CSP - PAIRITEL SN Ia LC residuals at all phases results from slight bandpass differences, since we have not transformed the CSP data into the PAIRITEL/2MASS system with any zero point offsets or color terms derived from stars or S-corrections derived using SN Ia SEDs. Stritzinger et al. 2002 discuss how to use S-corrections to transform magnitudes published in the natural system of a given telescope (e.g. CSP Swope) to other widely used photometry systems (e.g. 2MASS). One of the major advantages of PAIRITEL is that we are already on the widely used 2MASS system and thus require no S-corrections to the JHK_s bands, which would require knowledge of the SN Ia SEDs which are currently highly uncertain in the NIR due to a limited spectral sample (Hsiao et al. 2007; Marion et al. 2009; Boldt et al. 2012 *in preparation*).

Zero Point Offsets from SN Ia Photometry

In lieu of S-corrections, we can estimate the mean zero point offsets between CSP and PAIRITEL SN Ia photometry and compare that to zero points and color terms derived from stars. To estimate the weighted mean CSP - PAIRITEL F12 SN Ia LC residuals, we aggregate the residuals shown in Figures 4.23–4.26 in the phase range of $[-10, 60]$ days, excluding two objects with bad fits in JH (SN 2007if and SN 2006is), along with one object with a bad K_s-band fit (SN 2005eq) to avoid including nonsensical residuals. This yields 614 and 561 CSP - PAIRITEL residual measurements from 17 SN Ia in JH, respectively and 175 measurements from 8

SN Ia in K_s (see §4.3.2), with weighted mean residuals and errors found as:

$$\begin{aligned} J_{CSP} - J_{PTL} &= 0.010 \pm 0.003 \text{ mag} \\ H_{CSP} - H_{PTL} &= 0.034 \pm 0.005 \text{ mag} \\ K_{sCSP} - K_{sPTL} &= 0.027 \pm 0.014 \text{ mag} \end{aligned} \tag{4.1}$$

Zero Point Offsets from Photometry of 2MASS Stars

Contreras et al. 2010 used CSP measurements of 984 J and H-band 2MASS stars in their SN fields to derived zero point offsets and color terms between the 2MASS and CSP bandpasses in the J and H bands, finding mean zero point offsets:

$$\begin{aligned} J_{CSP} - J_{\rm 2M} &= 0.010 \pm 0.003 \text{ mag} \\ H_{CSP} - H_{\rm 2M} &= 0.043 \pm 0.003 \text{ mag} \end{aligned} \tag{4.2}$$

The zero point offset from Equations 4.1 and 4.2 agree to better than 1–σ in J and to within 2–σ in H indicating that, since PAIRITEL is on the 2MASS system, the mean CSP - PAIRITEL SN photometric differences arise mainly from differences in the effective bandpasses of the CSP Swope natural system and the PAIRITEL/2MASS system. Contreras et al. 2010 did not derive zero point offsets or color terms in K_s due to what the authors considered an insufficient number of 2MASS star observations (only 41 2MASS stars in K_s), since the CSP/LCO K_s filter was only available on the Wide Field Infrared Camera (WIRC) on the 2.5-meter duPont telescope, not on RetroCam on the 1.0-meter Swope telescope, which observes in YJH (Contreras et al. 2010; also see Table 2.1).

While Contreras et al. 2010 compared CSP measurements of 2MASS stars to 2MASS measurements of those stars from the 2MASS point source catalog (Cutri et al. 2003), here we also compare CSP measurements of 2MASS stars to PAIRITEL measurements of those stars from Table 4.2 to derive our own estimates of the zero points and look for evidence for any color terms between PAIRITEL and CSP photometry. Although PAIRITEL is on the 2MASS natural system, PAIRITEL observations are deeper than 2MASS, so PAIRITEL measurements of 2MASS stars are more appropriate when trying to discover the source of any differences between PAIRITEL and CSP photometry for SN or stars. Of the 19 SN Ia observed by both PAIRITEL and CSP, standard star photometry for the local sequences was only available in usable form in the literature for 16 objects (Contreras et al. 2010; Stritzinger et al. 2011; Taubenberger et al. 2011), and unavailable for three objects (SN 2005hk, SN 2006ax, and SN 2007sr). Although the local sequences and finding charts for SN 2005hk were published in Phillips et al. 2007, the star coordinates were not, so we were originally unable to incorporate them. The optical and NIR LCs of SN 2006ax were published in Contreras et al. 2010, but the local sequences seem to have been inadvertently left out of their machine-readable Table 3 in the online version. Similarly, the LCs for SN 2007sr were published in Schweizer et al. 2008, but the local sequences were not. Fortunately, the local sequences for these 3 SN fields not available in the literature were provided to us by the CSP (Max Stritzinger — private communication).

In the 19 SN Ia fields, we find 269, 264, and 24 2MASS stars observed both by PAIRITEL and CSP in JHK_s, respectively, limited to the color range $0.2 < (J-H)_{CSP} < 0.7$ mag also used by Contreras et al. 2010. We compute

the CSP - PAIRITEL residuals for each 2MASS star in JHK_s and interpret the weighted mean residuals and the error on the weighted mean as our estimate of the zero point offset between the CSP natural system (JH Swope, K_s duPont) and the PAIRITEL/2MASS system. Our estimates show a slight dependence on whether the uncertainties on the weighted mean PAIRITEL magnitudes of 2MASS stars are estimated as the error on the weighted mean (as presented in column 6 of Table 4.2) or as the RMS of the nightly magnitude measurements, which is the method reported by the CSP, who use the RMS magnitude measurements over several photometric nights to estimate their local sequence uncertainties (Contreras et al. 2010; Stritzinger et al. 2011).

If we use the error on the weighted mean for PAIRITEL measurements of 2MASS stars, we find smaller mean stellar photometry errors compared to the RMS, which yields larger uncertainty estimates. The error on the weighted mean ($\approx$ standard deviation / $\sqrt{N}$)[5] is appropriate if we assume 2MASS stars are strictly constant in brightness and we are simply taking repeated measurements of a truly fixed quantity with only measurement noise, justifying the effective division by $\sqrt{N}$, where N is the number of observations of that star. The RMS (or standard deviation) is more appropriate if we assume 2MASS stars are intrinsically variable at a non-negligible level, where the nightly intrinsic variation can be treated as a random variable with mean zero. This seems to be implicit in the CSP choice to use the RMS as an estimator of their local sequence uncertainties. Rather than address the larger question of NIR stellar variability of 2MASS stars, which is beyond the

[5]The error on the weighted mean reduces to the standard deviation of the nightly magnitude measurements divided by $\sqrt{N}$, where N is the number of measurements, in the limit where all nightly uncertainties are equal (See §7.3).

scope of this thesis, Figures 4.27–4.28 present CSP - PAIRITEL zero point estimates using both error assumptions for the PAIRITEL measurements of 2MASS stars. Using the weighted mean uncertainty (column 6 in Table 4.2), we find these zero point offsets (also shown in the left panel of Figure 4.27):

$$\begin{aligned} J_{CSP} - J_{PTL} &= 0.022 \pm 0.001 \text{ mag} \\ H_{CSP} - H_{PTL} &= 0.039 \pm 0.001 \text{ mag} \\ K_{sCSP} - K_{sPTL} &= 0.054 \pm 0.004 \text{ mag} \end{aligned} \tag{4.3}$$

while using the RMS uncertainty for PAIRITEL measurements of 2MASS stars, we find the following zero point offsets (also shown in the right panel of Figure 4.27):

$$\begin{aligned} J_{CSP} - J_{PTL} &= 0.018 \pm 0.002 \text{ mag} \\ H_{CSP} - H_{PTL} &= 0.038 \pm 0.003 \text{ mag} \\ K_{sCSP} - K_{sPTL} &= 0.077 \pm 0.011 \text{ mag} \end{aligned} \tag{4.4}$$

The JHK_s CSP - PAIRITEL zero point offsets from Equations 4.3–4.4 agree with the zero point offsets found by Contreras et al. 2010 given by Equation 4.2 somewhat for the H-band but less so in J. The zero point estimates might be brought into closer agreement if our estimated uncertainties are underestimated. However, Equations 4.3–4.4 are technically the offsets we measured between CSP and PAIRITEL, not the offsets between CSP and 2MASS, which Contreras et al. 2010 measured using about 4 times as many 2MASS stars. If we believe either of Equations 4.3–4.4, this could potentially be indirect evidence for a change in the effective J bandpass between PAIRITEL and 2MASS, perhaps due a the presence of differing average amounts of atmospheric water vapor in the 7 years PAIRITEL has been in operation compared to 2MASS (see §4.2.7). This effect would not have

been detected with the photometric accuracy tests we performed in §4.1.3, since the mean PAIRITEL - 2MASS magnitude is expected to be consistent with zero by construction because the PAIRITEL nightly zero point is calibrated with the 2MASS catalog. In any case, we would need $\sim$ 3–4 times as many stars to form a sample comparable to that analyzed by Contreras et al. 2010, so we withhold judgement on the meaning of the slight differences between zero point offsets derived using the methods presented here and in Contreras et al. 2010. In either case, we do not consider the zero point estimates for K_s in Equations 4.3–4.4 to be reliable since they are based on only 24 2MASS stars measured by both groups.

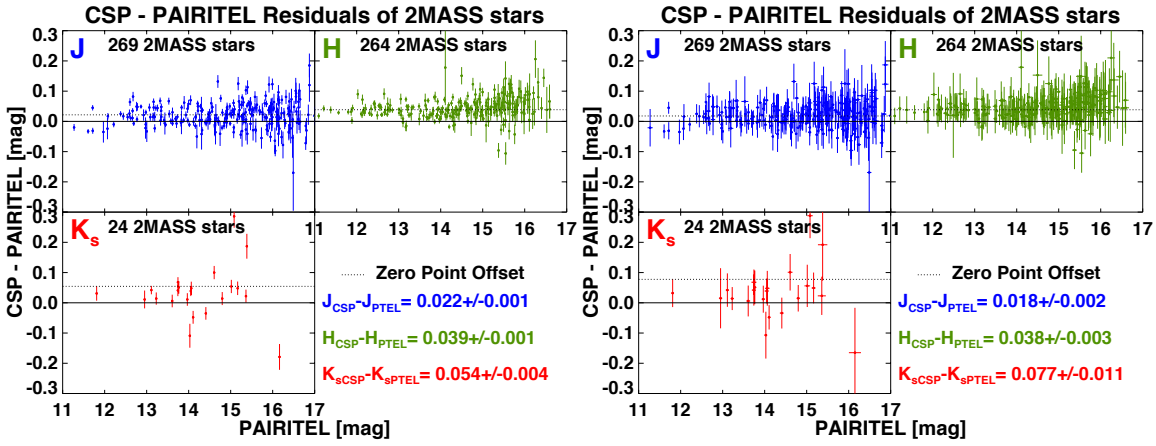

Figure 4.27.— Zero Point Offsets of PAIRITEL and CSP JHK_s Filters Derived from Common Observations of 2MASS stars in SN Ia fields.

In the 19 SN Ia fields observed by both PAIRITEL and the CSP, we find 269, 264, and 24 2MASS stars observed both groups in JHK_s, respectively, in the color range $0.2 < (J-H)_{CSP} < 0.7$ mag also used by Contreras et al. 2010. The plots show CSP - PAIRITEL magnitude residuals on the y-axis for all of these stars in JHK_s versus the PAIRITEL star magnitude on the x-axis. Errors on the residuals are the quadrature sum of the quoted CSP errors and the PAIRITEL errors on the weighted mean magnitude of 2MASS stars. The Left and Right panels differ only in the assumptions made regarding the measurement errors for PAIRITEL observations of 2MASS stars (see §4.3.3).

(**Left**) Error bars shown assume errors on the weighted mean from the PAIRITEL measurements of 2MASS stars (column 6 in Table 4.2). Fitted zero point offsets are $J_{CSP} - J_{PTL} = 0.022 \pm 0.001$ mag, $H_{CSP} - H_{PTL} = 0.039 \pm 0.001$ mag, and $K_{sCSP} - K_{sPTL} = 0.054 \pm 0.004$ mag.

(**Right**) Error bars show assume larger RMS errors for PAIRITEL (not shown in Table 4.2). Fitted zero point offsets are $J_{CSP} - J_{PTL} = 0.018 \pm 0.002$ mag, $H_{CSP} - H_{PTL} = 0.038 \pm 0.003$ mag, and $K_{sCSP} - K_{sPTL} = 0.077 \pm 0.011$ mag.

CSP - PAIRITEL Color Terms

Considering only 2MASS stars in the color range $0.2 < (J-H)_{CSP} < 0.7$ mag, Contreras et al. 2010 obtained the following linear fits for the JH bands:

$$J_{CSP} - J_{2\mathrm{M}} = (-0.045 \pm 0.008) \times (J-H)_{CSP} + (0.035 \pm 0.067) \text{ mag} \quad (4.5)$$

$$H_{CSP} - H_{2\mathrm{M}} = (0.005 \pm 0.006) \times (J-H)_{CSP} + (0.038 \pm 0.080) \text{ mag}$$

Contreras et al. 2010 thus find some evidence for a small color term slope in J with a negligible color term in H. With only 41 2MASS stars observed in K_s by the CSP, Contreras et al. 2010 do not attempt to derive any color terms involving K_s[6].

Following Contreras et al. 2010, we test for any significant linear color terms relating the CSP and PAIRITEL filters and limit ourselves to the 263 2MASS stars with both J and H band measurements due to the lack of 2MASS stars observed in K_s by both groups. The left and right panels of Figures 4.28 use the smaller error on the weighted mean and the larger RMS error for the PAIRITEL measurement errors of 2MASS stars, respectively. For the smaller errors, the linear color term fits are poor $\chi^2_\nu \gtrsim 3$, whereas for the larger RMS errors, the linear color term fits yield $\chi^2_\nu < 1$ indicating that while the fits may be trustworthy, the errors have been overestimated. This indicates that the true errors lie somewhere in between these extremal error estimates. Still, the best fit linear color term parameters are similar between both fits, so we take the conservative approach of quoting only the color

[6]Carpenter 2001 find the following fits for the Las Campanas Observatory (LCO) K_s band which uses the Persson Standard stars: $K_{sCSP} - K_{s2\mathrm{M}} = (-0.015 \pm 0.004) \times (J-K_s)_{CSP} + (0.002 \pm 0.004)$ mag. The Carpenter 2001 color transformations have been updated at `http://www.astro.caltech.edu/~jmc/2mass/v3/transformations/` as of 2003 and we present those here. Carpenter 2001 find a fairly small color term for the K_s filter (the CSP K_s filter is currently only on the 2.5-m duPont telescope at LCO).

term fits for the larger RMS errors and better fits here:

$$J_{CSP} - J_{PTL} = (-0.014 \pm 0.017) \times (J-H)_{CSP} + (0.025 \pm 0.009) \text{ mag} \quad (4.6)$$

$$H_{CSP} - H_{PTL} = (0.042 \pm 0.022) \times (J-H)_{CSP} + (0.020 \pm 0.011) \text{ mag}$$

This would indicate evidence for a small color term slope in H, but is consistent with zero slope in J, seemingly the reverse of what Contreras et al. 2010 found. However, if we look closely, the JH-band color term fits in Equations 4.5 and 4.6 agree in the slopes to within 2-σ and the intercepts within 1–σ. Furthermore, both fits yield the same signs for the slopes and indicate at most small color terms in J and H. In addition, approximately transforming the CSP data to the PAIRITEL/2MASS system using the Contreras et al. 2010 color terms from Equation 4.5 or Equation 4.6 does not significantly reduce the scatter in J or H PAIRITEL-CSP residuals shown in Figures 4.23–4.26, most likely because the PAIRITEL statistical photometric uncertainties themselves are typically $\sim$ 2–3 times larger than the corresponding CSP uncertainties. As such, we consider the weighted mean zero point offsets from Contreras et al. 2010 to be the most reliable way to approximately transform magnitude measurements between PAIRITEL and CSP in the JH bands, in lieu of full S-corrections. This is especially true because the Contreras et al. 2010 zero point offsets used $\sim$4 times as many 2MASS stars as we were able to and because their results are in good agreement with what we found by comparing the residuals of PAIRITEL and CSP SN Ia photometry, which used 614, 561, and 175 measurements of the CSP - PAIRITEL SN Ia photometry residuals, estimated with the help of an interpolating model fit (see §4.3.2).

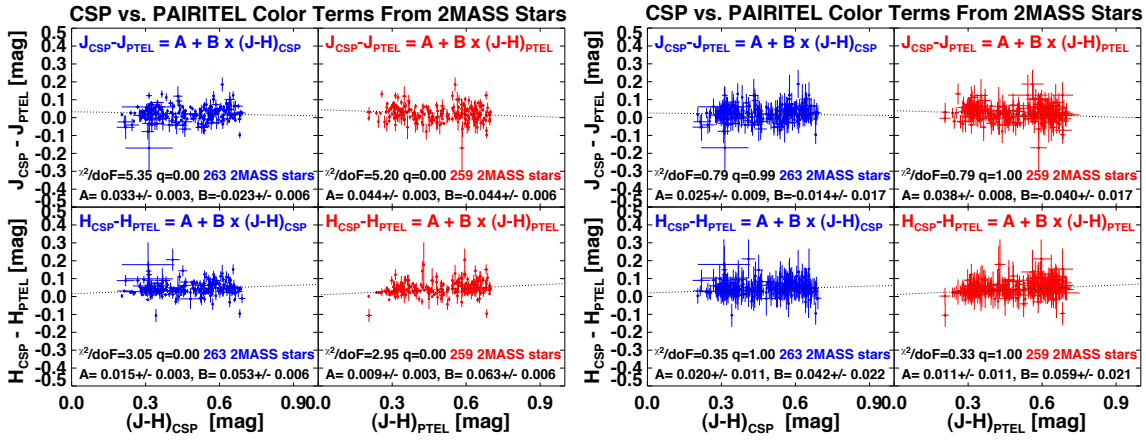

Figure 4.28.— $J-H$ Color Terms between PAIRITEL and CSP J and H filters Derived from Common Observations of 2MASS stars in SN Ia fields.

Plots show linear fits for color terms in the JH bands using 2MASS stars observed by PAIRITEL and CSP. Blue points show fits in terms of $(J-H)_{CSP}$ while red points show fits in terms of $(J-H)_{PTL}$. Following Contreras et al. 2010, we also include only stars with $(J-H)$ colors in the range $[0.2, 0.7]$ mag limiting us to 263 2MASS stars with $(J-H)_{CSP}$ data (blue) and 259 stars with $(J-H)_{PTL}$ data (red). The Left and Right panels differ only in the assumptions made regarding the measurement errors for PAIRITEL observations of 2MASS stars (see §4.3.3).

(**Left**) Error bars shown assume errors on the weighted mean from the PAIRITEL measurements of 2MASS stars (column 6 in Table 4.2). The linear fits are poor ($\chi^2_\nu \gtrsim 3$) due to underestimated errors yielding inconclusive evidence for linear color terms.

(**Right**) Error bars show assume larger RMS errors for PAIRITEL (not shown in Table 4.2). Linear fits have $\chi^2_\nu < 1$ indicating overestimated errors. While true errors lie somewhere in between these extremal error estimates, the most reliable $(J-H)_{CSP}$ color terms here are: $J_{CSP} - J_{PTL} = (-0.014 \pm 0.017) \times (J-H)_{CSP} + (0.025 \pm 0.009)$ mag and $H_{CSP} - H_{PTL} = (0.042 \pm 0.022) \times (J-H)_{CSP} + (0.020 \pm 0.011)$ mag (although see §4.3.3).

4.4 PAIRITEL CfAIR2 JHK_s SN Ia Light Curves

Final, host galaxy subtracted JHK_s LCs for the 104 SN Ia in the PAIRITEL CfAIR2 data set (F12; Friedman et al. 2012 *in preparation*) are presented in Figure 4.29 and Table 4.3 which includes both spectroscopically normal and peculiar SN Ia. The overall PAIRITEL photometric flux error budget $\sigma_{\rm tot} = \sqrt{(\tilde{\sigma_{\rm do}})^2 + (\sigma_{\rm NNT})^2}$ from corrected DoPHOT photometry and host galaxy subtraction is listed in column 7 of Table 4.3, with contributions $\tilde{\sigma_{\rm do}}$ from the corrected DoPHOT nightly uncertainties and $\sigma_{\rm NNT}$, the standard deviation of the brightness measurements for each of the nightly subtractions in the NNT averaging process (see §4.2.2).

While Figure 4.29 presents all 104 spectroscopically normal and peculiar SN Ia in the PAIRITEL CfAIR2 data set, Figure 4.30 shows a subset of 70 of these same SN Ia LCs that are reasonably well-sampled. CfAIR2 JHK_s LCs for all 104 SN Ia are also shown in Figure 4.31 with the fiducial JHK_s template derived in WV08 overplotted for comparison. Figure 4.32 shows CfAIR2 data for the 11 peculiar SN Ia not included in the generation of the F12 mean LC template (See §5.1.1), also overplotted with the mean WV08 template to emphasize the ease with which these objects can be distinguished from normal SN Ia based on LC properties alone. Figure 4.33 shows a subset of 18 NIR SN Ia LCs that were not deemed to be of sufficient quality for publication in Friedman et al. 2012 *in preparation* or inclusion in the CfAIR2 data set at this time, also with the WV08 mean fiducial JHK_s LC templates overplotted for comparison. Figure 4.34 shows LCs for the subset of 21 SN Ia as published in WV08 with the WV08 template LCs overplotted. A full comparison of newer F12 and older WV08 PAIRITEL LCs is discussed in §4.3.1.

Table 4.3:: CfAIR2: 104 SN Ia Light Curves from PAIRITEL (Stub)

sn2005ao							
SN	Type	Date	MJD [days][a]	Band	$flux_{25}$[b]	$\sigma_{flux_{25}}$[c]	N_T[d]
sn2005ao	Ia	2005Mar22	53451.482	J	222.9161	35.3412	5
sn2005ao	Ia	2005Mar27	53456.432	J	76.8863	15.0571	4
sn2005ao	Ia	2005Apr02	53462.510	J	220.0116	56.2229	5
sn2005ao	Ia	2005Apr04	53464.392	J	238.7399	73.4449	5
sn2005ao	Ia	2005Apr07	53467.395	J	294.3632	32.8172	5
sn2005ao	Ia	2005Apr09	53469.419	J	335.2147	37.7611	4
sn2005ao	Ia	2005Apr10	53470.378	J	337.9616	36.7088	5
sn2005ao	Ia	2005Apr11	53471.380	J	386.3172	24.4403	4
sn2005ao	Ia	2005Apr20	53480.348	J	251.5126	38.5133	5
sn2005ao	Ia	2005Mar22	53451.482	H	487.4752	47.0721	3
sn2005ao	Ia	2005Mar27	53456.432	H	334.9146	51.6579	3
sn2005ao	Ia	2005Apr02	53462.510	H	395.8068	76.7445	3
sn2005ao	Ia	2005Apr04	53464.392	H	394.8983	53.4888	2
sn2005ao	Ia	2005Apr07	53467.395	H	501.9858	136.7528	3
sn2005ao	Ia	2005Apr09	53469.419	H	612.5635	101.8288	3
sn2005ao	Ia	2005Apr10	53470.378	H	683.6462	124.8625	3
sn2005ao	Ia	2005Apr11	53471.380	H	427.9493	66.8582	2
sn2005ao	Ia	2005Apr13	53473.361	H	713.8160	63.4607	2
sn2005ao	Ia	2005Mar27	53456.432	K	704.9033	170.1069	6
sn2005ao	Ia	2005Apr06	53466.393	K	908.3426	234.3175	6
sn2005ao	Ia	2005Apr07	53467.395	K	436.0421	128.3725	5
sn2005ao	Ia	2005Apr10	53470.378	K	1028.6644	160.7759	4

(**This Table will be available in its entirety in a machine-readable form in the online electronic version of this paper, Friedman et al. 2012** *in preparation to be submitted to the Astrophysical Journal (ApJ)*. **A portion is shown here for guidance regarding its form and content).**

[a]Modified Julian Date

[b]$flux_{25}$ Flux normalized to a magnitude of 25.

[c]Error on $flux_{25}$ which includes the weighted mean of the photometric errors for each night observation (corrected for DoPHOT underestimates) added in quadrature with the standard deviation of the flux measurements for each subtraction from each host galaxy template image (see §4.2.2).

[d]N_T is the number of host galaxy template images. The final LC is a night by night weighted average over all N_T subtractions (see §3.4, §4.2.2). Missing data is denoted by ... indicating that the LC did not use host galaxy subtraction and is the forced DoPHOT LC in the un-subtracted images at the SN centroid position.

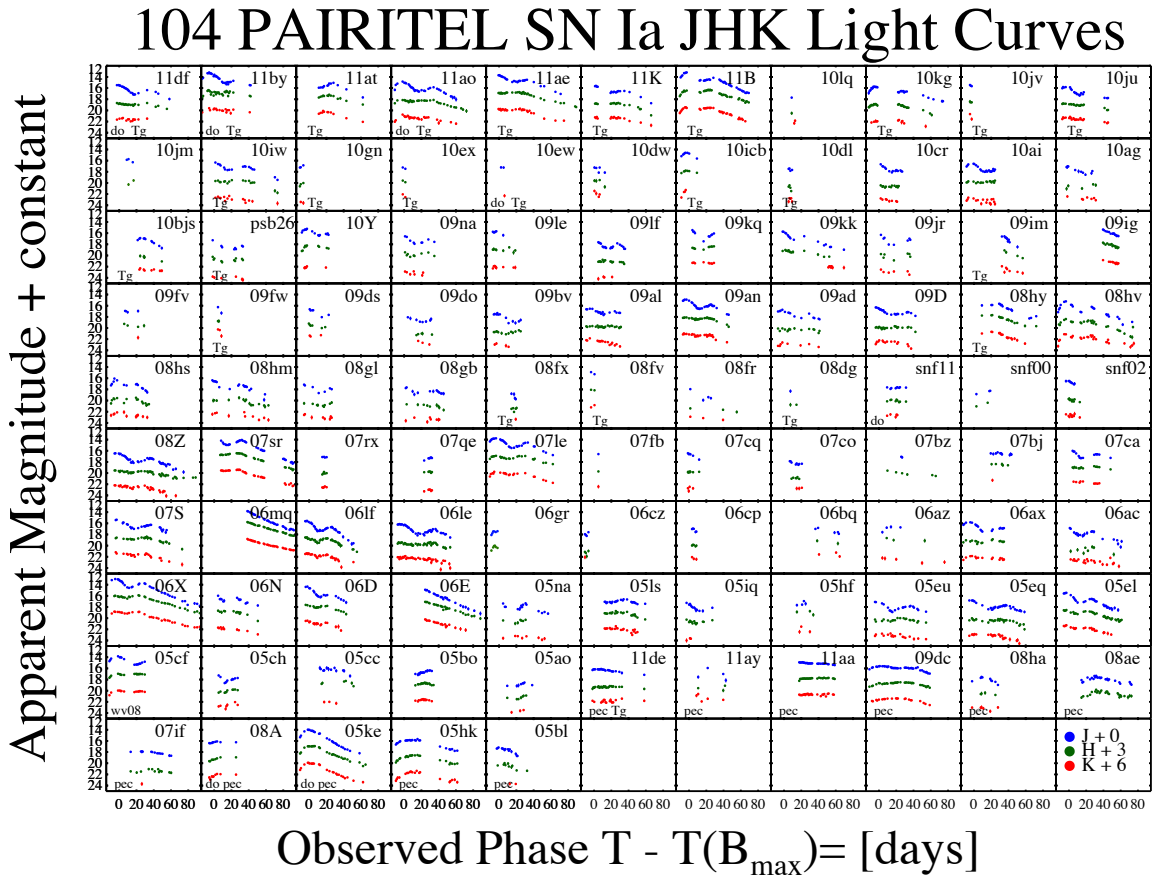

Figure 4.29.— 104 CfAIR2 NIR JHK_s SN Ia LCs from PAIRITEL.

104 CfAIR2 NIR SN Ia LCs. All of these are spectroscopically normal SN Ia. See Figure 4.32 for separate LC plots of the peculiar SN Ia observed by PAIRITEL.

The following notes are sometimes shown in the lower left corner of each LC plot:
do: Indicates forced DoPHOT LCs without host galaxy subtraction.
Tg: If $t_{B\max}$ is estimated from NIR features in the LCs in the absence of optical data (see §5.2.1)
pec: Peculiar SN Ia, which clearly differ from the overplotted JHK_s LC templates.
wv08: Indicates data from WV08 (applies only to SN 2005cf).

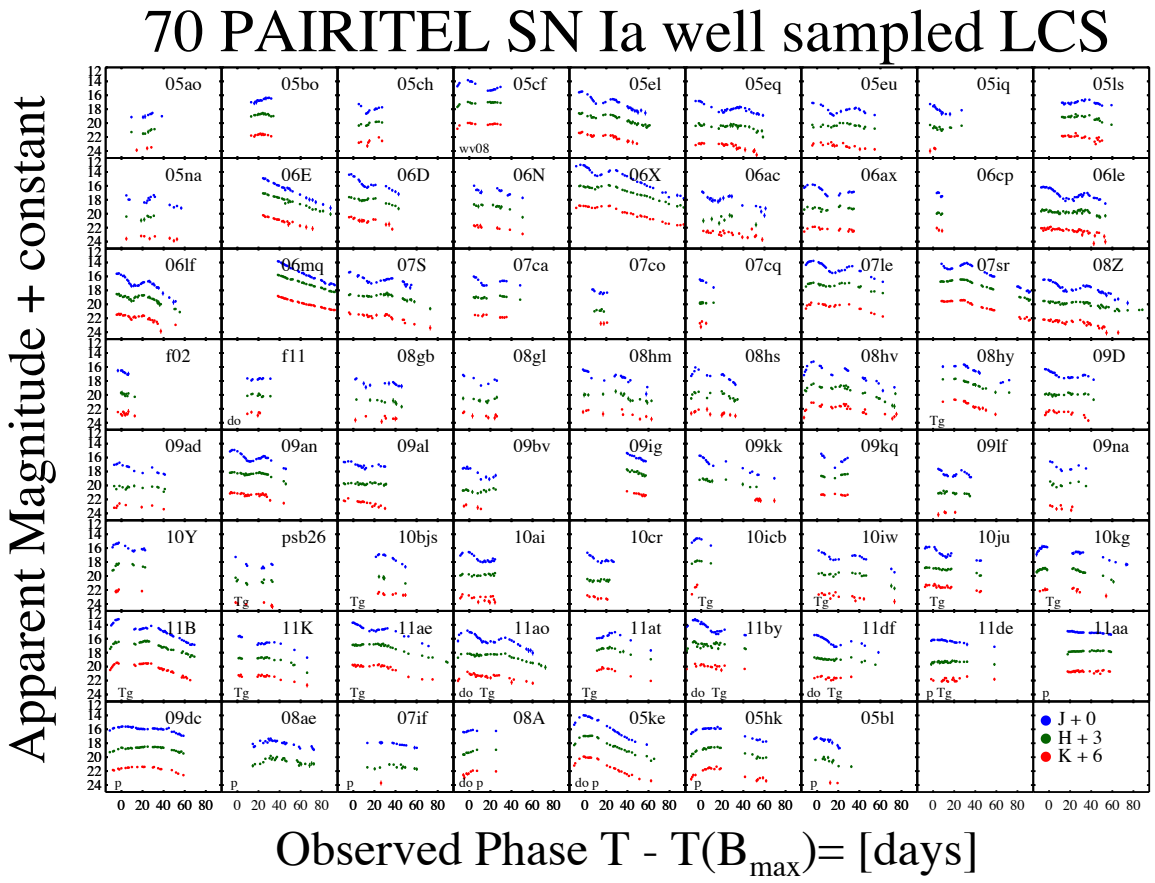

Figure 4.30.— 70 Well Sampled CfAIR2 NIR SN Ia

A subset of 70 CfAIR2 NIR SN Ia normal or peculiar Ia LCs that are reasonably well-sampled.

The following notes are sometimes shown in the lower left corner of each LC plot:
do: Indicates forced DoPHOT LCs without host galaxy subtraction.
Tg: If $t_{B\max}$ is estimated from NIR features in the LCs in the absence of optical data (see §5.2.1)
pec: Peculiar SN Ia, which clearly differ from the overplotted JHK_s LC templates.
wv08: Indicates data from WV08 (applies only to SN 2005cf).

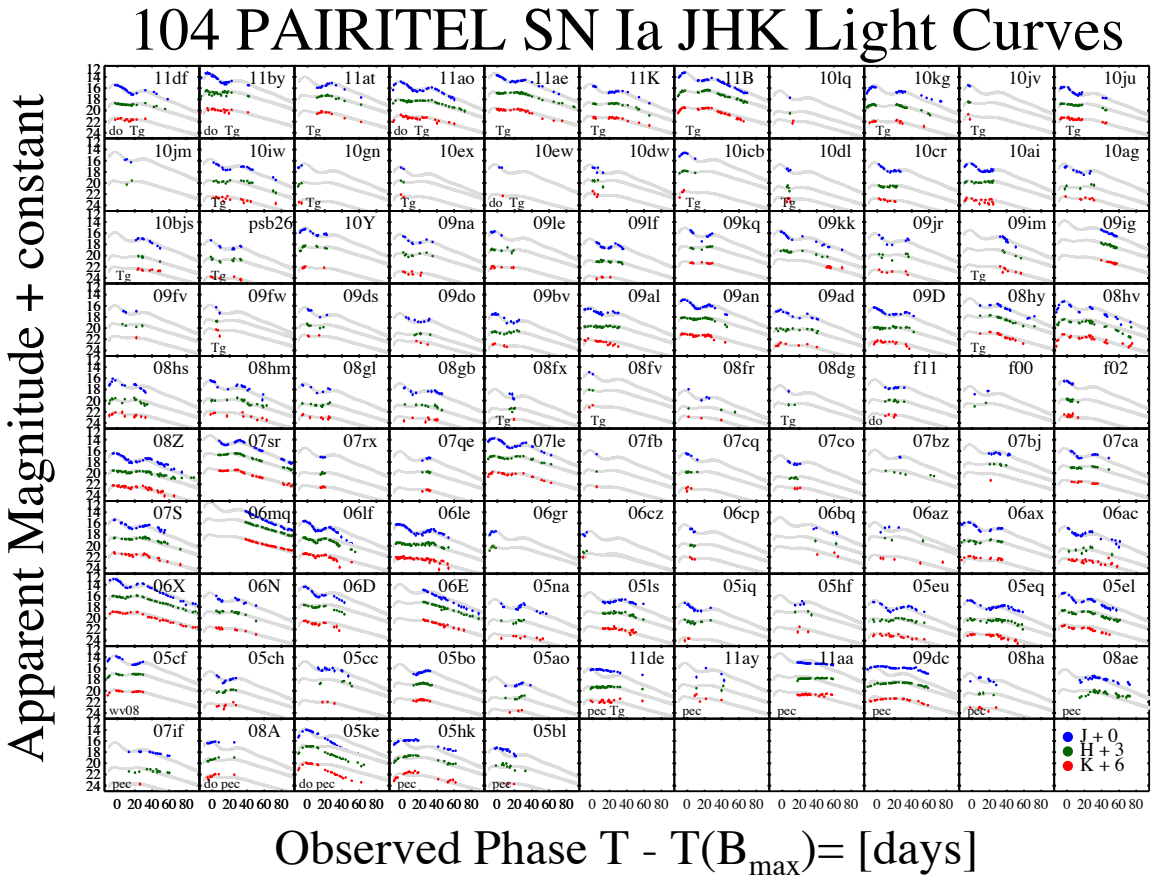

Figure 4.31.— 104 CfAIR2 NIR JHK_s SN Ia LCs from PAIRITEL.

104 CfAIR2 NIR SN Ia LCs (same data as in Figure 4.29) but also with the WV08 mean fiducial JHK_s LC templates overplotted for comparison. All of these are spectroscopically normal SN Ia. See Figure 4.32 for LC plots of the peculiar SN Ia observed by PAIRITEL.

The following notes are sometimes shown in the lower left corner of each LC plot:
do: Indicates forced DoPHOT LCs without host galaxy subtraction.
Tg: If $t_{B\max}$ is estimated from NIR features in the LCs in the absence of optical data (see §5.2.1)
pec: Peculiar SN Ia, which clearly differ from the overplotted JHK_s LC templates.
wv08: Indicates data from WV08 (applies only to SN 2005cf).

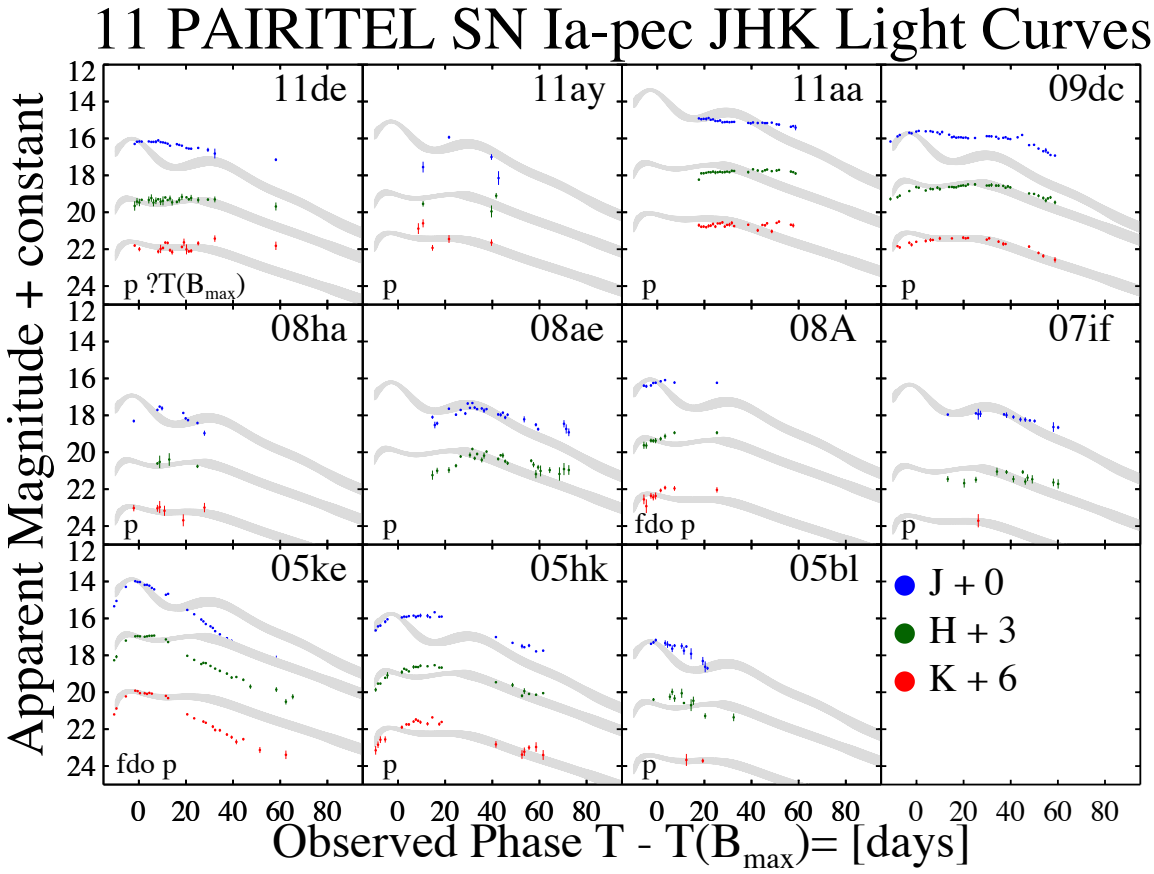

Figure 4.32.— 11 CfAIR2 NIR LCs of Peculiar SN Ia

11 CfAIR2 NIR LCs of peculiar SN Ia with the WV08 mean fiducial JHK_s LC templates overplotted for comparison to emphasize the ease with which these objects can be distinguished from normal SN Ia based on LC properties alone.

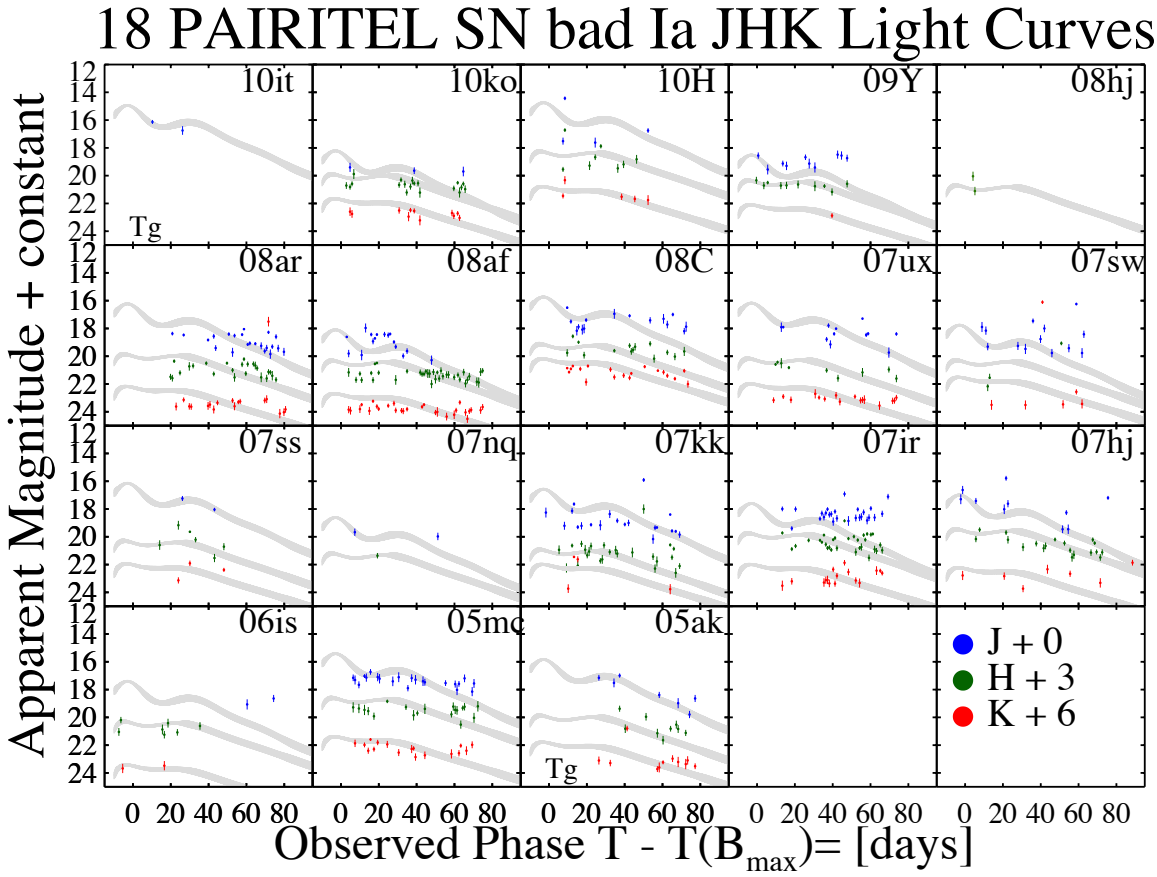

Figure 4.33.— 18 Bad CfAIR2 NIR JHK_s SN Ia LCs from PAIRITEL.

18 PAIRITEL NIR SN Ia LCs that were not deemed to be of sufficient quality for publication in CfAIR2. The WV08 mean fiducial JHK_s LC templates overplotted for comparison. All of these are spectroscopically normal SN Ia.

The following notes are sometimes shown in the lower left corner of each LC plot:
do: Indicates forced DoPHOT LCs without host galaxy subtraction.
Tg: If $t_{B\max}$ is estimated from NIR features in the LCs in the absence of optical data (see §5.2.1)

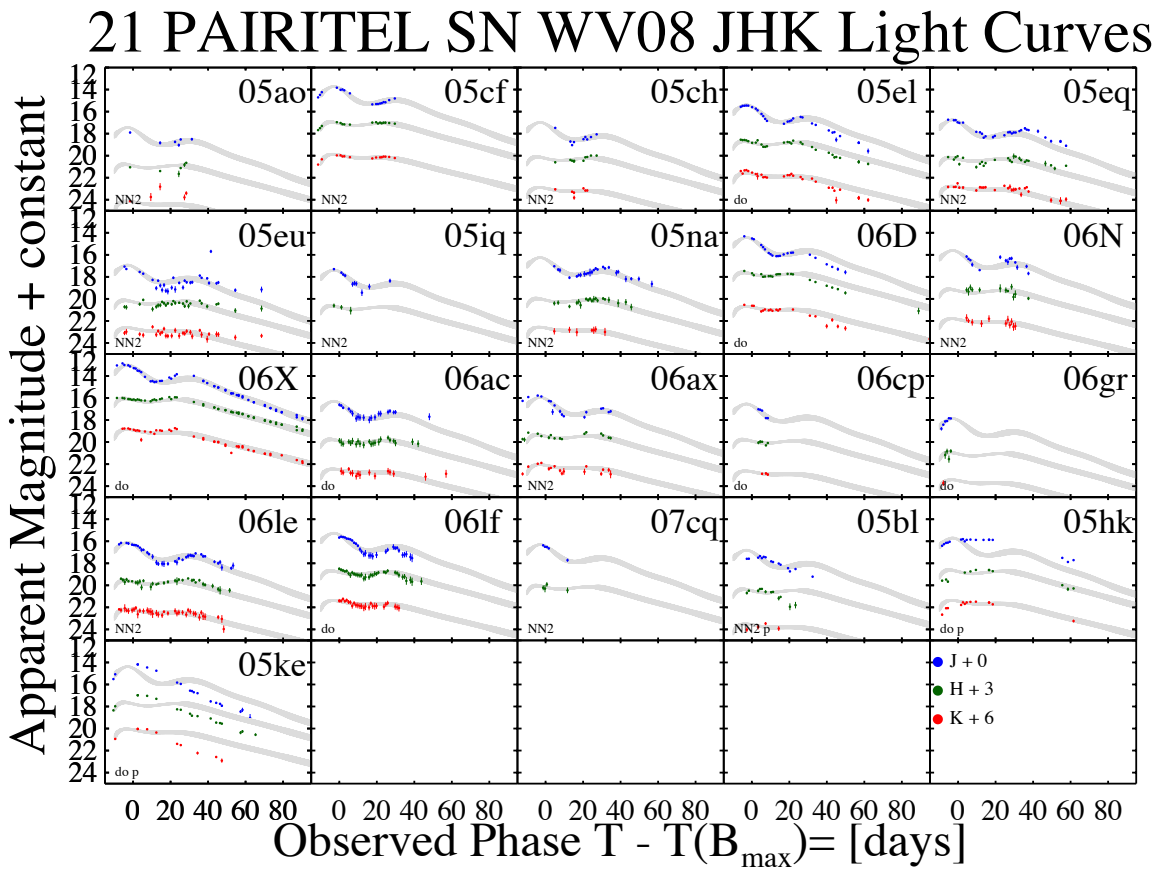

Figure 4.34.— 21 NIR JHK_s SN Ia Light Curves from Wood-Vasey et al. 2008

SN Ia NIR LCs from WV08 with the WV08 mean JHK_s LC templates overplotted for comparison. The 18 normal WV08 SN Ia are shown in the first four rows. 3 peculiar SN Ia are shown (SN 2005bl, SN 2005hk, and SN 2005ke) are not well fit by the mean WV08 NIR LC template derived for spectroscopically normal SN Ia. A comparison of the old WV08 photometry and the new CfAIR2 photometry for these objects is presented in §4.3.1.

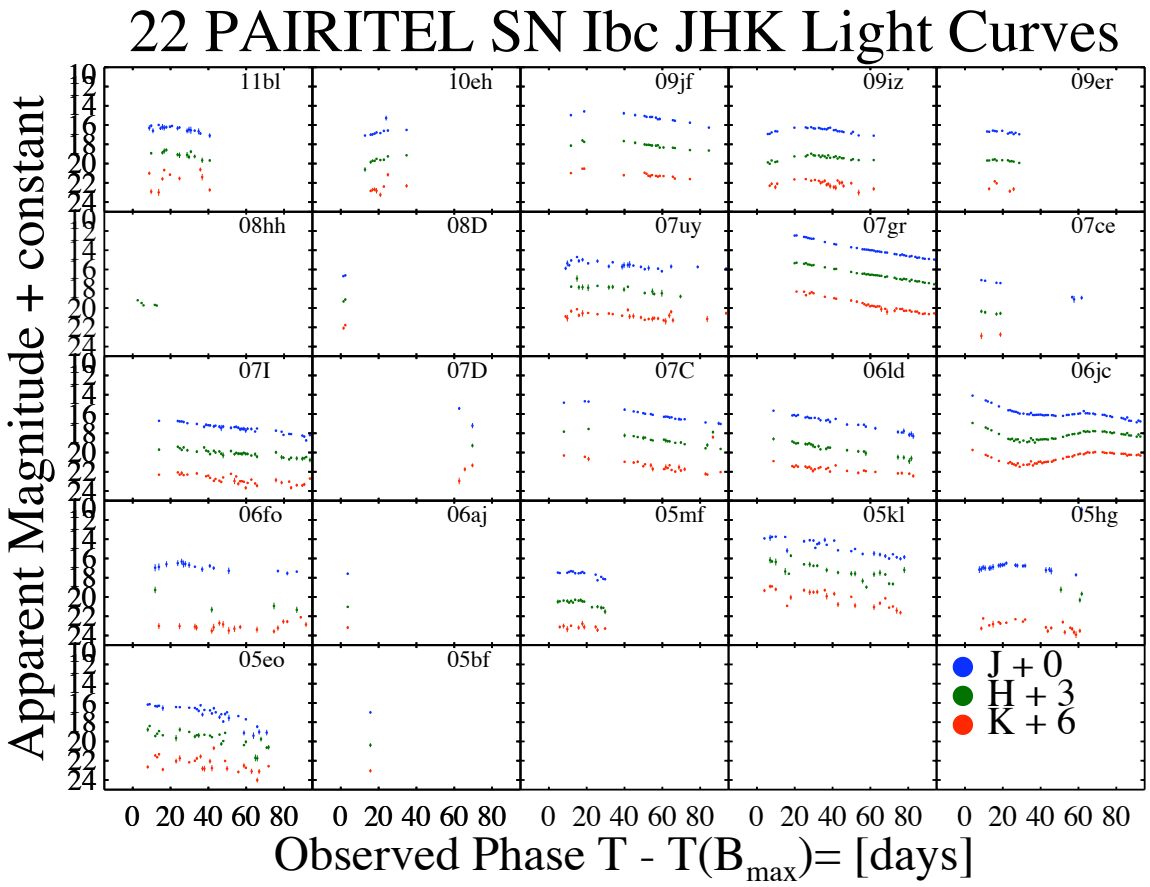

Figure 4.35.— 22 PAIRITEL NIR JHK_s SN Ib/c LCs

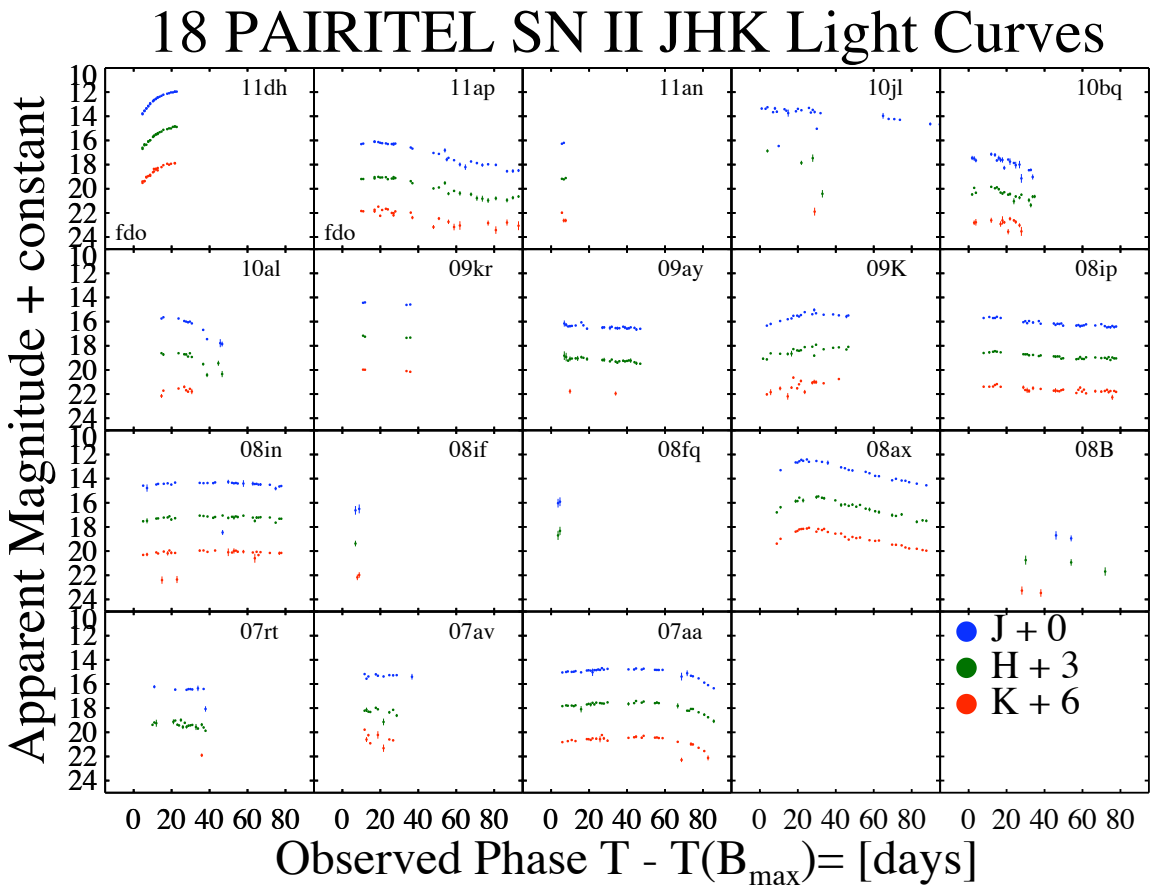

Figure 4.36.— 18 PAIRITEL NIR JHK_s SN II LCs

Although SN of other types are not included in the CfAIR2 SN Ia data set and will not be published in Friedman et al. 2012 *in preparation*, we show PAIRITEL LCs for 22 SN Ib/c and 18 SN II in Figures 4.35–4.36 for completeness since they were also reduced using the same mosaicking and photometry pipelines during the reduction of the CfAIR2 SN Ia LCs. They will be presented in future work.

Chapter 5

Analysis of Data

Analysis and Results

In this section we present a limited analysis of the SN Ia LCs in the CfAIR2 data set, with additional analysis to be presented in future work (Friedman et al. 2012 *in preparation*; Mandel et al. 2012 *in preparation*; also see §6). In §5.1, we combine CfAIR2 data with other NIR SN Ia data from the literature to construct a mean rest-frame LC template in the JHK_s bands. In §5.2 we describe our process to fit models to the JHK_s SN Ia LCs (see Figures 5.1–5.2) in order to extract parameters characterizing the observed properties of the CfAIR2 sample, focusing on the estimated SN Ia apparent magnitudes at $t_{B\max}$, the time of B-band maximum light (Table 5.1), and the typical phases of the prominent NIR LC features with respect to $t_{B\max}$ (§5.2.1). In the Conclusion (§6) we describe previous results and outline future directions for combining optical and NIR SN Ia data to create Hubble Diagrams and to derive host galaxy distance estimates that are more accurate and more precise than those with optical data alone.

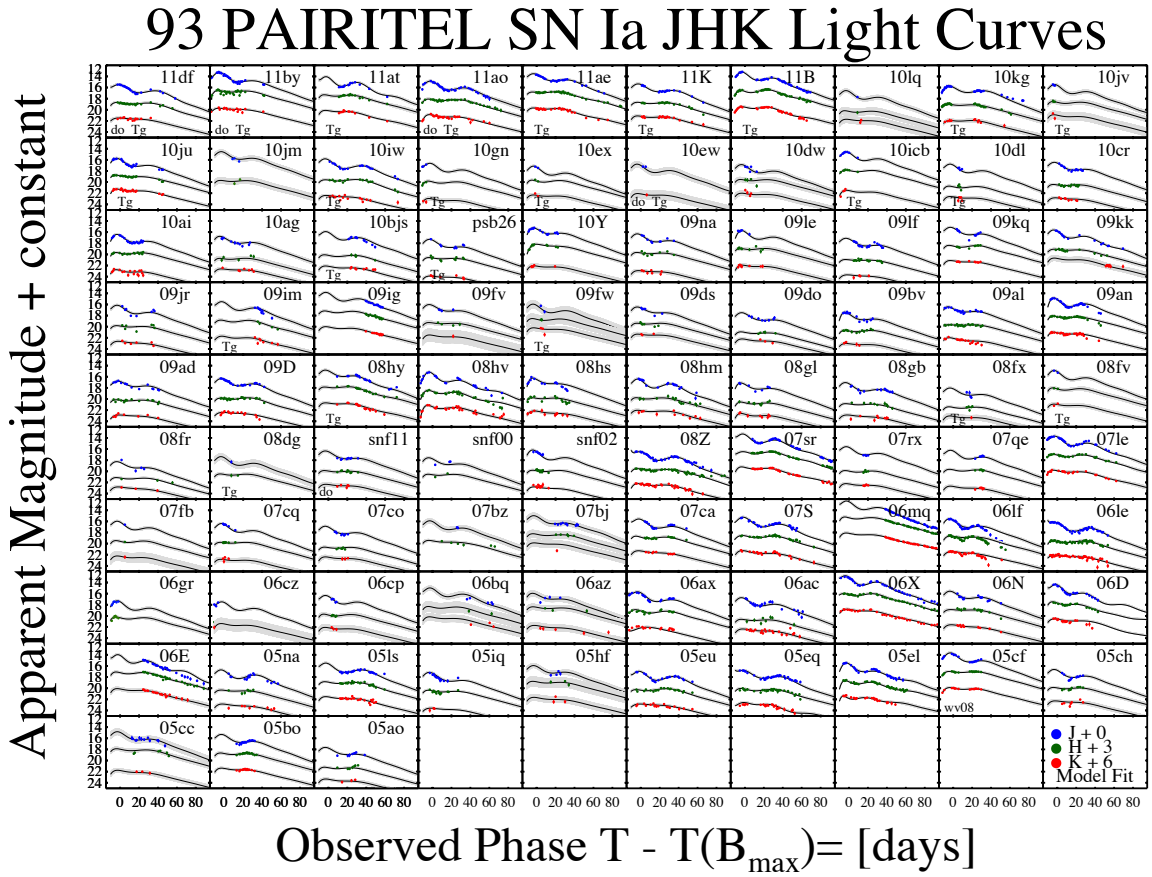

Figure 5.1.— LC Fits for 93 Normal CfAIR2 SN Ia from PAIRITEL.

The LC fitting process for plots shown above is described in §5.2. LC fits allow the inferences of the observed properties of the nearby sample (Table 5.1) and for the determination of Infrared and Optical-Infrared colors (§6.3.2) which help us measure extinction and reddening for each SN Ia and estimate distances that are more accurate and more precise than with optical data alone.

The following notes are sometimes shown in the lower left corner of each LC plot:
do: Indicates forced DoPHOT LCs without host galaxy subtraction.
Tg: If $t_{B\max}$ is estimated from NIR features in the LCs in the absence of optical data (see §5.2.1)
wv08: Indicates data from WV08 (applies only to SN 2005cf).

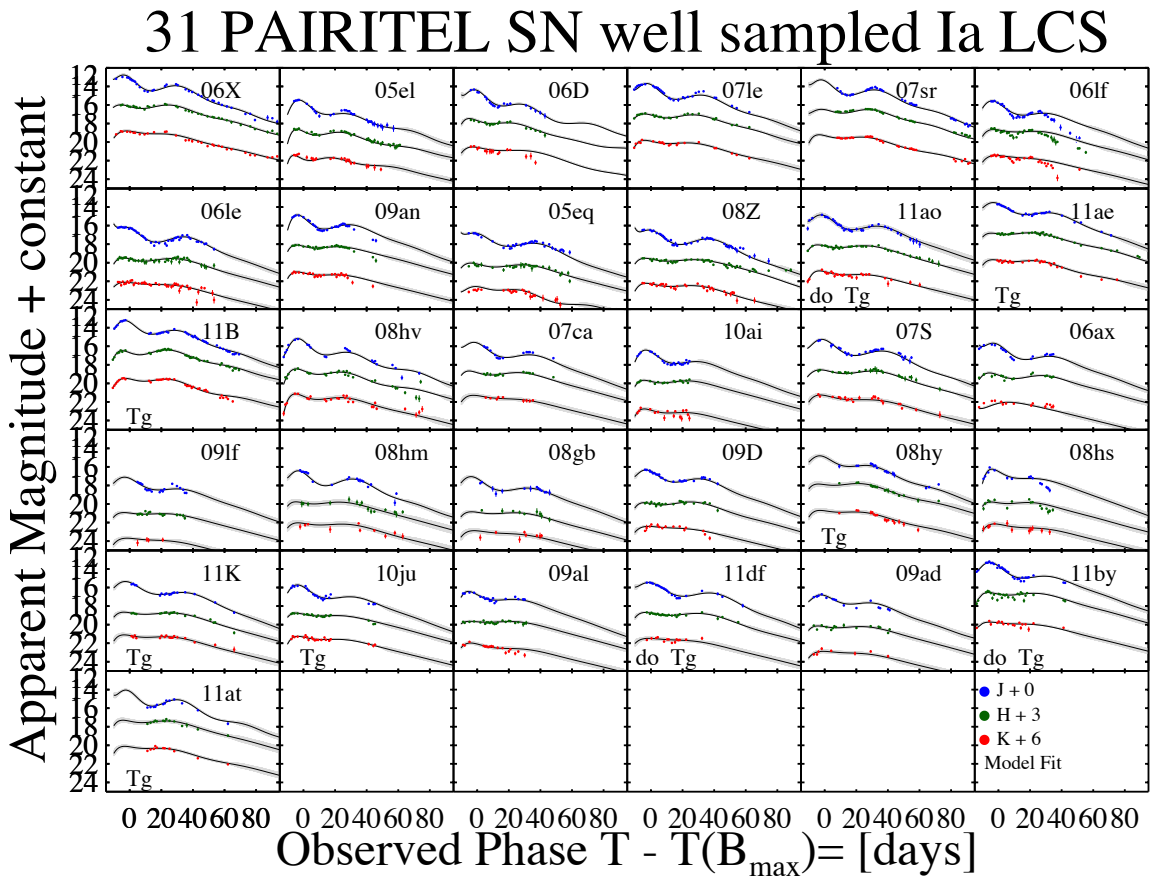

Figure 5.2.— LC FIts for 31 Well-Sampled CfAIR2 SN Ia from PAIRITEL.

The LC fitting process for plots shown above is described in §5.2. LC fits allow the inferences of the observed properties of the nearby sample (Table 5.1) and for the determination of Infrared and Optical-Infrared colors (§6.3.2) which help us measure extinction and reddening for each SN Ia and estimate distances that are more accurate and more precise than with optical data alone.

The following notes are sometimes shown in the lower left corner of each LC plot:
do: Indicates forced DoPHOT LCs without host galaxy subtraction.
Tg: If $t_{B\max}$ is estimated from NIR features in the LCs in the absence of optical data (see §5.2.1)
wv08: Indicates data from WV08 (applies only to SN 2005cf).

Table 5.1:: JHK_s Light Curve Properties for 93 PAIRITEL CfAIR2 SN Ia

SN[a]	Type[b]	$t_{B\max}$[c]	$\sigma_{t_{B\max}}$[c]	$t_{\rm f}^{J}$[d]	$t_{\rm l}^{J}$[d]	$t_{\rm f}^{H}$[d]	$t_{\rm l}^{H}$[d]	$t_{\rm f}^{K_s}$[d]	$t_{\rm l}^{K_s}$[d]	J_0[e]	σ_{J_0}[e]	H_0[e]	σ_{H_0}[e]	K_{s0}[e]	$\sigma_{K_{s0}}$[e]	N_J[f]	N_H[f]	N_{K_s}[f]
sn2005ao	Ia	53442	···	9.48	39.49	9.48	39.49	9.48	39.49	17.76	0.11	18.29	0.09	17.35	0.22	12	12	12
sn2005bo	Ia	53477.16	0.70	13.04	38.04	13.04	38.04	13.04	38.04	15.44	0.11	15.73	0.20	15.40	0.11	15	15	14
sn2005cc	Ia	53508.77	0.56	12.43	54.41	12.43	53.42	12.43	42.43	14.95	0.59	14.97	0.33	15.78	0.39	28	20	14
sn2005cf	Ia	53533.56	0.11	-12.31	29.60	-12.31	28.61	-8.31	6.58	13.91	0.06	14.05	0.09	13.91	0.06	14	22	7
sn2005ch	Ia	53536	···	5.17	27.23	5.17	27.23	5.17	24.22	16.75	0.06	16.95	0.19	16.30	0.29	10	10	5
sn2005el	Ia	53646.27	0.19	7.88	75.80	7.88	75.80	7.88	75.80	15.56	0.01	15.78	0.01	15.20	0.10	27	26	19
sn2005eq	Ia	53653.64	0.25	-13.08	50.81	-13.08	50.81	-13.08	50.81	16.94	0.01	17.14	0.05	16.61	0.01	37	37	36
sn2005eu	Ia	53659	···	-4.55	68.52	-4.55	68.52	-4.55	68.52	17.00	0.09	17.14	0.11	16.79	0.16	30	27	30
sn2005hf	Ia	53661.15	0.93	14.94	52.99	11.97	52.13	16.96	40.01	16.06	0.42	15.85	0.88	15.66	0.58	13	6	4
sn2005iq	Ia	53687	···	-2.87	27.02	-2.87	27.02	-2.87	17.01	17.30	0.01	17.42	0.01	17.55	0.15	14	14	12
sn2005ls	Ia	53713.92	0.16	13.29	59.22	12.32	59.22	12.32	50.26	15.62	0.06	15.92	0.06	15.55	0.09	20	19	23
sn2005na	Ia	53740.49	0.13	-2.29	60.69	-4.35	21.69	-4.35	47.69	16.83	0.12	17.42	0.20	16.88	0.22	22	6	16
sn2006D	Ia	53757.40	0.13	6.89	70.83	6.89	70.83	6.89	70.83	14.42	0.01	14.60	0.01	14.53	0.02	23	22	22
sn2006E	*Ia*	*53743*	···	*24.40*	*88.35*	*24.40*	*88.35*	*24.40*	*88.35*	*14.13*	*0.09*	*14.19*	*0.15*	*14.10*	*0.32*	*27*	*27*	*26*
sn2006N	Ia	53760	···	4.55	50.54	4.55	46.61	4.55	50.54	15.68	0.20	15.95	0.22	15.62	0.25	25	25	23
sn2006X	Ia	53787	···	-8.60	116.26	-8.60	116.26	-8.60	99.38	13.04	0.01	13.17	0.01	12.82	0.09	46	44	39
sn2006ac	Ia	53781	···	2.04	64.99	2.04	64.00	2.04	64.99	16.83	0.13	17.70	0.22	16.37	0.24	32	24	29
sn2006ax	Ia	53829.47	0.03	-12.26	34.70	-12.26	34.70	-12.26	34.70	15.90	0.01	16.10	0.01	16.36	0.03	19	19	19
sn2006az	Ia	53825.28	0.01	-6.16	48.84	-2.24	52.79	-6.16	71.75	16.02	0.53	15.45	0.53	15.73	0.60	16	14	16
sn2006bq	Ia	53842.85	0.20	9.50	63.51	35.48	63.51	9.50	64.47	15.13	0.41	15.41	0.92	14.19	0.62	13	9	10
sn2006cp	Ia	53896	···	3.51	8.52	3.51	8.52	3.51	8.52	16.46	0.10	16.77	0.30	16.06	0.56	5	5	3
sn2006cz	Ia	53913.74	0.41	-10.56	-6.50	-10.56	-6.50	-10.56	-10.56	17.61	0.11	18.47	0.09	15.42	1.02	4	4	1
sn2006gr	Ia	54012.07	0.15	3.69	10.74	3.69	10.74	···	···	17.56	0.10	17.34	0.18	18.44	0.17	7	7	0
sn2006le	Ia	54047	···	-7.43	53.38	-7.43	53.38	-7.43	53.38	16.31	0.01	16.59	0.04	16.13	0.01	40	42	38
sn2006lf	Ia	54044	···	2.95	52.78	2.95	59.77	-0.06	55.75	15.75	0.01	15.84	0.11	15.49	0.09	7	17	36
sn2006mq	*Ia*	*54013*	···	*38.49*	*104.31*	*38.49*	*181.12*	*38.49*	*178.12*	*12.48*	*0.02*	*12.34*	*0.03*	*12.13*	*0.04*	*30*	*41*	*45*
sn2007S	Ia	54143.24	0.17	-2.16	102.75	-2.16	74.74	-2.16	59.76	15.40	0.01	15.60	0.02	15.35	0.21	31	31	27
sn2007bj	Ia	54201.86	0.71	8.51	83.40	8.51	83.40	8.51	73.36	15.11	0.53	15.31	0.68	13.88	0.66	41	33	23
sn2007bz	Ia	54220	···	9.84	65.77	9.84	65.77	8.92	41.78	16.05	0.44	16.51	0.22	15.34	0.59	12	12	4
sn2007ca	Ia	54226.90	0.17	4.31	48.25	4.31	48.25	5.40	35.24	15.74	0.04	15.82	0.05	15.31	0.20	15	15	10

(a) **This Table will be available in its entirety in a machine-readable form in the online electronic version of this paper, Friedman et al. 2012** *in preparation to be submitted to the Astrophysical Journal (ApJ).*
(b) SN type. Ia = spectroscopically normal. Iap = spectroscopically peculiar, including 91-bg like, 91T-like objects and overluminous 09dc-like objects.
(c) MJD of $t_{B\max}$ from MLCS2k2 fits (Jha et al. 2007). When $\sigma_{t_{B\max}}$ is marked with ··· , this indicates that $t_{B\max}$ is an estimate inferred from the NIR LCs (see §5.2.1), or from optical spectra in the absence of available optical LCs. For SN 2006E and SN 2006mq, the SN was discovered weeks to months after maximum, so the $t_{B\max}$ estimates are likely unreliable estimates. The first PAIRITEL observations for SN 2009ig are several weeks after maximum, but $t_{B\max}$ is well determined from earlier optical data. Still for objects where the first PAIRITEL observation is at a phase $\gtrsim 20$ days after $t_{B\max}$ (e.g. SN 2006E, SN 2006mq, SN 2007qe, SN 2009ig, SN 2009im, and SN PTF10bjs), the fit results and quoted uncertainties listed *in italics* are approximate at best.
(d) Phases of the first and last epochs with respect to $t_{B\max}$ in JHK_s.
(e) Magnitudes and 1-σ uncertainties in JHK_s LCs at $t = 0 = t_{B\max}$.
(f) Number of epochs w/ SNR> 3 in the JHK_s lightcurves, respectively.

Continued on Next Page...

Table 5.1 – Continued

SN[a]	Type[b]	$t_{B\max}$[c]	$\sigma_{t_{B\max}}$[c]	$t_{\rm f}^{J}$[d]	$t_{\rm l}^{J}$[d]	$t_{\rm f}^{H}$[d]	$t_{\rm l}^{H}$[d]	$t_{\rm f}^{K_s}$[d]	$t_{\rm l}^{K_s}$[d]	J_0[e]	σ_{J_0}[e]	H_0[e]	σ_{H_0}[e]	K_{s0}[e]	$\sigma_{K_{s0}}$[e]	N_J[f]	N_H[f]	N_{K_s}[f]
sn2007co	Ia	54264.61	0.24	6.77	20.69	6.77	20.69	6.77	20.69	17.00	0.09	17.71	0.12	16.41	0.34	11	10	10
sn2007cq	Ia	54280	···	-1.26	11.71	-1.26	11.71	-1.26	4.67	16.61	0.02	16.80	0.19	16.72	0.41	6	6	4
sn2007fb	Ia	54287.42	0.70	5.04	5.04	5.04	5.04	5.04	5.04	16.11	0.07	16.55	0.20	16.24	0.84	1	1	1
sn2007le	Ia	54398.83	0.14	-10.43	62.46	-10.43	62.46	-10.43	62.46	13.86	0.01	14.08	0.01	13.84	0.10	36	34	28
sn2007qe	*Ia*	*54428.87*	*0.15*	*23.24*	*32.19*	*23.24*	*32.19*	*23.24*	*32.19*	*16.36*	*0.06*	*16.74*	*0.07*	*16.69*	*0.25*	*6*	*6*	*6*
sn2007rx	Ia	54441.89	1.49	15.25	20.24	15.25	20.24	15.25	20.24	15.71	0.06	16.96	0.11	16.24	0.22	5	5	5
sn2007sr	Ia	54448	···	7.02	119.84	7.02	119.84	7.02	159.68	13.44	0.01	13.58	0.01	13.25	0.06	35	39	42
sn2008Z	Ia	54514.66	0.19	-5.34	85.51	-5.34	88.50	-5.34	74.54	16.53	0.01	16.61	0.01	16.30	0.01	46	46	39
snf20080514-002	Ia	54611.55	0.42	-3.38	12.60	-3.38	12.60	-3.38	12.60	16.50	0.05	16.88	0.15	16.87	0.04	10	10	9
snf20080522-000	Ia	54621.28	0.48	2.86	18.89	2.86	581.24	2.86	15.90	17.66	0.20	17.61	0.16	16.23	0.46	5	7	2
snf20080522-011	Ia	54616.87	0.73	9.44	60.34	9.44	59.27	13.32	23.34	16.47	0.25	16.95	0.25	16.35	0.35	12	12	4
sn2008dg	Ia	54630	···	7.47	14.45	7.47	14.45	9.45	9.45	17.51	0.58	17.56	0.23	15.20	1.10	3	3	1
sn2008fr	Ia	54732.80	0.67	10.80	66.60	10.80	66.60	10.80	66.60	18.37	0.04	18.21	0.06	16.83	0.26	8	11	7
sn2008fv	Ia	54752	···	12.03	16.03	9.03	16.03	12.03	16.03	15.13	0.18	15.16	0.30	14.89	0.28	2	3	2
sn2008fx	Ia	54729	···	13.34	20.28	14.32	20.28	13.34	20.28	18.15	0.06	18.50	0.08	17.07	0.48	7	6	4
sn2008gb	Ia	54745.46	1.08	1.93	45.80	1.90	45.80	1.90	45.80	17.15	0.13	17.93	0.10	16.90	0.24	21	21	22
sn2008gl	Ia	54768.12	0.28	-5.83	28.13	-5.83	28.13	-5.83	28.13	17.14	0.10	17.71	0.18	16.72	0.32	16	17	17
sn2008hm	Ia	54804.33	0.41	-2.10	62.85	37.79	37.79	-2.10	61.84	16.62	0.01	16.79	0.27	15.94	0.27	27	1	21
sn2008hs	Ia	54812.64	0.15	-9.45	44.45	-9.45	44.45	-9.45	44.45	16.37	0.12	17.00	0.18	16.22	0.25	17	17	17
sn2008hv	Ia	54816.87	0.11	-12.52	75.22	-12.52	75.22	-11.49	76.29	15.34	0.01	15.56	0.01	15.32	0.21	31	32	33
sn2008hy	Ia	54801	···	9.26	65.14	9.26	72.14	9.26	72.14	14.93	0.18	14.91	0.23	14.70	0.21	19	22	21
sn2009D	Ia	54841.93	0.73	-3.74	45.22	-3.74	45.22	-3.74	42.23	16.49	0.02	16.97	0.06	16.41	0.01	23	25	24
sn2009ad	Ia	54886.01	0.05	-0.89	47.12	-0.89	47.12	-0.89	47.12	16.80	0.08	17.20	0.12	16.83	0.19	18	18	14
sn2009an	Ia	54898.22	0.24	-6.99	45.89	-6.99	45.89	-6.99	43.95	15.01	0.01	15.21	0.01	15.08	0.06	35	35	30
sn2009al	Ia	54900	···	-8.95	30.06	-8.95	31.01	-8.95	31.01	16.44	0.10	16.62	0.11	16.17	0.18	25	25	22
sn2009bv	Ia	54926.32	0.38	-6.08	42.90	-6.08	42.90	-6.08	24.98	17.67	0.15	17.71	0.15	16.97	0.31	16	14	12
sn2009do	Ia	54944.91	0.72	4.33	38.27	4.33	38.27	4.33	29.28	17.60	0.13	18.02	0.11	16.23	0.24	24	22	6
sn2009ds	Ia	54960.51	0.38	-0.33	22.64	-0.33	22.64	0.65	22.64	16.54	0.18	16.45	0.25	15.30	0.39	9	11	4
sn2009fw	Ia	54993	···	2.43	9.40	5.42	9.40	4.42	10.42	16.07	0.74	15.62	0.86	14.21	0.56	5	4	5
sn2009fv	Ia	54996.43	1.25	3.83	28.78	3.83	28.78	5.81	21.86	16.14	0.22	16.34	0.34	15.51	1.13	8	5	3
sn2009im	*Ia*	*55063*	···	*32.42*	*57.30*	*32.42*	*57.30*	*32.42*	*56.46*	*15.65*	*0.18*	*15.91*	*0.21*	*15.74*	*0.28*	*11*	*11*	*8*
sn2009ig	*Ia*	*55079.89*	*0.50*	*55.94*	*73.73*	*55.94*	*73.73*	*55.94*	*73.73*	*13.97*	*0.09*	*14.26*	*0.13*	*14.03*	*0.19*	*16*	*14*	*12*
sn2009jr	Ia	55119.83	0.49	2.28	36.26	2.28	36.26	2.28	35.25	16.27	0.15	16.90	0.20	16.65	0.25	6	6	6

(a) **This Table will be available in its entirety in a machine-readable form in the online electronic version of this paper, Friedman et al. 2012** *in preparation to be submitted to the Astrophysical Journal (ApJ).*
(b) SN type. Ia = spectroscopically normal. Iap = spectroscopically peculiar, including 91-bg like, 91T-like objects and overluminous 09dc-like objects.
(c) MJD of $t_{B\max}$ from MLCS2k2 fits (Jha et al. 2007). When $\sigma_{t_{B\max}}$ is marked with ··· , this indicates that $t_{B\max}$ is an estimate inferred from the NIR LCs (see §5.2.1), or from optical spectra in the absence of available optical LCs. For SN 2006E and SN 2006mq, the SN was discovered weeks to months after maximum, so the $t_{B\max}$ estimates are likely unreliable estimates. The first PAIRITEL observations for SN 2009ig are several weeks after maximum, but $t_{B\max}$ is well determined from earlier optical data. Still for objects where the first PAIRITEL observation is at a phase $\gtrsim 20$ days after $t_{B\max}$ (e.g. SN 2006E, SN 2006mq, SN 2007qe, SN 2009ig, SN 2009im, and SN PTF10bjs), the fit results and quoted uncertainties listed *in italics* are approximate at best.
(d) Phases of the first and last epochs with respect to $t_{B\max}$ in JHK_s.
(e) Magnitudes and 1-σ uncertainties in JHK_s LCs at $t = 0 = t_{B\max}$.
(f) Number of epochs w/ SNR> 3 in the JHK_s lightcurves, respectively.

Continued on Next Page...

Table 5.1 – Continued

SN[a]	Type[b]	$t_{B\max}$[c]	$\sigma_{t_{B\max}}$[c]	$t_{\rm f}^{J}$[d]	$t_{\rm l}^{J}$[d]	$t_{\rm f}^{H}$[d]	$t_{\rm l}^{H}$[d]	$t_{\rm f}^{K_s}$[d]	$t_{\rm l}^{K_s}$[d]	J_0[e]	σ_{J_0}[e]	H_0[e]	σ_{H_0}[e]	K_{s0}[e]	$\sigma_{K_{s0}}$[e]	N_J[f]	N_H[f]	N_{K_s}[f]
sn2009kk	Ia	55128.83	0.73	1.43	72.42	1.43	72.42	42.39	72.42	15.74	0.01	16.15	0.19	15.99	0.28	22	22	11
sn2009kq	Ia	55154.58	0.35	3.92	28.87	3.92	28.87	3.92	28.87	15.26	0.05	15.47	0.06	15.12	0.08	10	10	10
sn2009lf	Ia	55148.26	0.87	4.95	35.84	4.95	36.80	4.95	20.92	17.23	0.08	18.01	0.09	17.72	0.16	19	20	4
sn2009le	Ia	55165.41	0.23	-7.19	18.76	-7.19	18.76	-7.19	18.76	15.85	0.09	16.02	0.29	15.94	0.32	8	9	8
sn2009na	Ia	55201.28	0.29	1.08	35.03	1.08	28.08	1.08	28.08	16.41	0.12	16.73	0.20	16.83	0.27	10	10	9
sn2010Y	Ia	55247.76	0.14	-8.42	31.52	-8.42	30.47	-8.42	31.52	15.27	0.06	15.48	0.08	15.90	0.18	17	11	17
snpsb26	Ia	55245	···	-1.72	33.26	-1.72	33.26	-1.72	33.26	17.47	0.08	17.68	0.10	17.86	0.10	10	10	6
snPTF10bjs	*Ia*	*55230*	···	*21.40*	*49.37*	*21.40*	*49.37*	*23.41*	*49.37*	*16.04*	*0.07*	*17.16*	*0.20*	*16.22*	*0.15*	*13*	*12*	*10*
sn2010ag	Ia	55270.21	0.64	-2.72	31.13	-2.72	31.13	-1.77	29.16	16.77	0.22	17.71	0.38	16.45	0.27	19	17	7
sn2010ai	Ia	55276.84	0.13	-8.51	24.35	-8.51	24.35	-8.51	24.35	16.61	0.07	16.74	0.13	16.91	0.20	22	22	16
sn2010cr	Ia	55310.28	1.88	-2.99	21.91	-2.99	17.85	-2.99	19.96	16.57	0.10	17.51	0.22	17.18	0.04	20	12	15
sn2010dl	Ia	55341	···	5.39	9.36	5.39	8.36	5.39	9.36	16.90	0.09	17.82	0.11	16.62	0.25	5	4	5
snPTF10icb	Ia	55360	···	-8.82	9.16	-8.82	9.16	-8.82	-3.82	14.75	0.06	14.94	0.05	15.52	0.20	8	8	4
sn2010dw	Ia	55357.75	0.65	0.45	12.46	2.54	6.49	0.45	6.49	16.97	0.27	16.59	0.44	15.96	0.45	5	3	4
sn2010ew	Ia	55379	···	3.30	9.32	3.30	7.30	9.80	9.80	16.88	0.54	16.11	0.48	16.08	0.77	4	3	1
sn2010ex	Ia	55386	···	7.44	7.44	4.43	7.44	-1.57	1.44	17.34	0.11	16.74	0.12	16.24	0.33	1	2	2
sn2010gn	Ia	55394	···	-10.73	-6.70	-10.73	-6.70	-9.72	-6.70	16.76	0.08	16.97	0.18	17.04	0.31	3	3	2
sn2010iw	Ia	55496	···	4.45	73.35	1.42	73.35	1.42	73.35	15.93	0.04	16.69	0.05	16.41	0.20	19	18	15
sn2010jm	Ia	···	···	6.85	15.71	6.85	16.66	···	···	14.66	0.38	16.76	0.55	···	···	5	4	0
sn2010ju	Ia	55525	···	-9.63	43.28	-9.63	43.28	-7.63	45.28	15.88	0.08	15.87	0.08	15.32	0.03	22	23	21
sn2010jv	Ia	55522	···	-4.55	-2.59	-4.55	-2.59	-4.55	-2.59	15.69	0.25	15.64	0.38	14.94	0.71	3	2	2
sn2010kg	Ia	55544	···	-10.84	74.11	-11.84	73.09	-11.84	54.13	15.69	0.17	16.09	0.27	15.83	0.33	32	31	17
sn2010lq	Ia	···	···	8.89	8.89	8.89	12.85	11.90	12.85	16.70	0.34	17.26	0.62	15.71	0.65	1	3	2
sn2011B	Ia	55582	···	-10.69	69.16	-10.69	69.16	-10.69	65.22	13.38	0.04	13.56	0.06	13.46	0.06	48	47	36
sn2011K	Ia	55575	···	6.17	71.11	6.17	71.11	1.17	66.11	15.48	0.06	15.74	0.08	15.08	0.20	20	19	17
sn2011ae	Ia	55622	···	-0.68	89.26	-0.68	89.26	-0.68	75.12	13.58	0.07	13.81	0.08	13.62	0.11	38	37	26
sn2011ao	Ia	55639	···	-10.75	72.19	-10.75	72.19	-10.75	72.19	14.96	0.24	15.19	0.04	14.93	0.03	39	36	30
sn2011at	Ia	55634	···	11.20	62.17	11.20	62.17	11.20	62.17	14.21	0.04	14.39	0.22	14.13	0.13	14	14	11
sn2011by	Ia	55693	···	1.68	57.69	1.68	57.69	-13.82	22.19	13.62	0.01	13.71	0.03	13.76	0.04	26	28	11
sn2011df	Ia	55714	···	6.85	49.77	-2.62	134.16	-2.62	32.32	15.49	0.01	15.80	0.01	15.39	0.18	15	25	14

(a) **This Table will be available in its entirety in a machine-readable form in the online electronic version of this paper, Friedman et al. 2012** *in preparation to be submitted to the Astrophysical Journal (ApJ).*

(b) SN type. Ia = spectroscopically normal. Iap = spectroscopically peculiar, including 91-bg like, 91T-like objects and overluminous 09dc-like objects.

(c) MJD of $t_{B\max}$ from MLCS2k2 fits (Jha et al. 2007). When $\sigma_{t_{B\max}}$ is marked with ··· , this indicates that $t_{B\max}$ is an estimate inferred from the NIR LCs (see §5.2.1), or from optical spectra in the absence of available optical LCs. For SN 2006E and SN 2006mq, the SN was discovered weeks to months after maximum, so the $t_{B\max}$ estimates are likely unreliable estimates. The first PAIRITEL observations for SN 2009ig are several weeks after maximum, but $t_{B\max}$ is well determined from earlier optical data. Still for objects where the first PAIRITEL observation is at a phase $\gtrsim 20$ days after $t_{B\max}$ (e.g. SN 2006E, SN 2006mq, SN 2007qe, SN 2009ig, SN 2009im, and SN PTF10bjs), the fit results and quoted uncertainties listed *in italics* are approximate at best.

(d) Phases of the first and last epochs with respect to $t_{B\max}$ in JHK_s.

(e) Magnitudes and 1-σ uncertainties in JHK_s LCs at $t = 0 = t_{B\max}$.

(f) Number of epochs w/ SNR> 3 in the JHK_s lightcurves, respectively.

5.1 NIR LC Template

We construct mean JHK_s LC templates using the NIR light curves from the PAIRITEL CfAIR2 observations (F12) combined with available NIR data from the CSP (e.g. Contreras et al. 2010; Stritzinger et al. 2011) and other NIR data from the literature (e.g. Krisciunas et al. 2004b and references therein). Out of the 122 SN Ia observed by PAIRITEL from 2005-2011, 58 (48%) have NIR observations before $t_{B\mathrm{max}}$, while 34 (28%) have observations at least 5 days before $t_{B\mathrm{max}}$, a subset of which are included in the template creation process. The new F12 NIR LC templates are shown in Figure 5.6, with interpolated values and uncertainties on 1-day timescales presented in Table 5.2 along with convenient polynomial fit coefficients presented in Table 5.3. These templates can be compared with the WV08 JHK_s NIR LC templates we presented in Wood-Vasey et al. 2008, shown here as Figure 5.3 (also Figure 4 of WV08[1]). We refer to each of these as the F12 and WV08 NIR JHK_s LC templates, respectively, to distinguish between the new and old templates constructed using available data from PAIRITEL and the Literature.

5.1.1 Excluding Peculiar SN Ia

SN Ia exhibit a range of optical decline rates with objects on a spectrum including SN 2003gs, perhaps the fastest declining SN Ia observed to date (Krisciunas et al. 2009), and SN 2001ay, one of the slowest declining SN Ia ever observed (Krisciunas et al. 2011). In constructing the NIR templates, we exclude these spectroscopically

[1](**) Any Figures from WV08 reproduced here do so with permission of the first author, W.M Wood-Vasey at the request of the second author, A. Friedman, the presenter of this thesis.

and photometrically peculiar SN Ia from our overall sample of 104 CfAIR2 SN Ia and 95 SN Ia from CSP and the Literature. Objects in CfAIR2 that are not combined to create our NIR LC Template include peculiar SN Ia: SN 2011ay, SN 2008ha, SN 2008ae, SN 2008A, SN 2005ke, SN 2005hk, and SN 2005bl. SN 2005hk is known to be an unusual SN Ia (Phillips et al. 2007) with a fast decline rate similar to the archetypal fast-decliner, SN 1991bg (Filippenko et al. 1992b; Leibundgut et al. 1993). SN 2005bl (Taubenberger et al. 2008) is another underluminous fast-decline in the SN 1991bg-like category. SN 2005ke is also a SN 1991bg-like SN Ia with possible circumstellar interaction (Patat 2005; Immler et al. 2006). SN 2008ha is one of the most underluminous SN Ia ever observed (Foley et al. 2008).

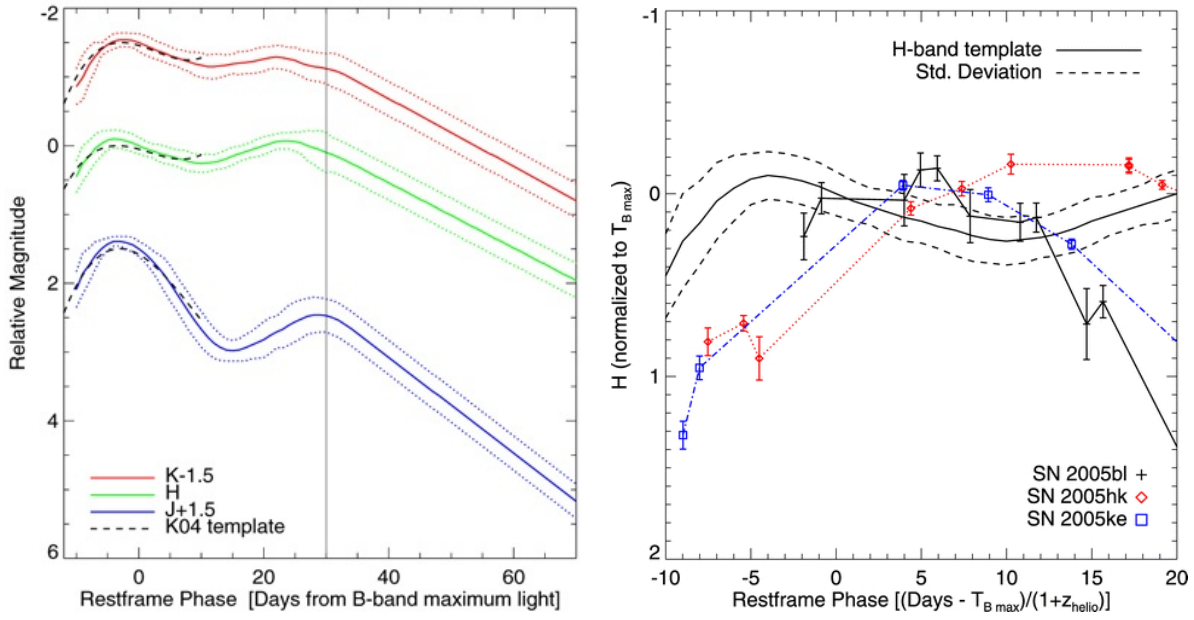

Figure 5.3.— NIR JHK_s Template Light Curves From WV08

(**Left**) [Also Figure 4 of WV08] Infrared LC templates constructed from and then used to fit all of the NIR SN Ia light curves considered in WV08. The 1-σ uncertainties (dashed lines) are based on the sample variance within a 5-day moving window of the SN Ia with respect to the fiducial template. Note that the K_s-band linear fits assumed after $t = 35$ days should have a slope of 0.0425 mag/day (not 0.425 as in the WV08 Table 5 caption).

(**Right**) [Also Figure 3 of WV08] SN 2005hk, SN 2005ke, and SN 2005bl were observed as part of the PAIRITEL campaign but were excluded from the construction of the template because they were known unusual SN Ia. Here we show the comparison of their H-band light curves vs. the normal SN Ia H-band template to demonstrate the clarity with which these can be distinguished from the normal SN Ia used in the Hubble diagram.

We also exclude slow-declining, overluminous objects similar to SN 1991T (Filippenko et al. 1992a; Phillips et al. 1992). Other overluminous SN Ia have given rise to suggestions that the SN Ia may have been the result of a progenitor system with two colliding white dwarf stars with total mass perhaps in excess of the Chandrasekhar mass of 1.4 $M_{\odot}$ (e.g. SN 2006gz: Hicken et al. 2007). In lieu of a better understanding of explosions producing overluminous, slow-declining LCs, we also opt to exclude them from our normal SN Ia template, including two SN Ia observed both in CfAIR2 and by the CSP (SN 2007if: Scalzo et al. 2010 and SN 2009dc: Taubenberger et al. 2011). The clear deviation of an example overluminous SN Ia from the mean JHK_s templates can be seen for SN 2009dc in Figure 5.4, where we compare its JHK_s LCs to the fiducial WV08 template.

Fast-declining SN Ia exhibit only one infrared hump instead of the two exhibited by normal NIR SN Ia (See SN 2005ke in Figure 5.4). In addition, the JHK_s maximum for fast-declining SN Ia occurs *after* the time of B-band maximum light, unlike normal SN Ia for which the JHK_s maxima occur $\sim$ 3–5 rest-frame days before $t_{B\mathrm{max}}$. We confirm these relations between the NIR peak maxima and $t_{B\mathrm{max}}$ with the available sample in §5.2.1 (See Table 5.4). We previously compared WV08 data for SN 2005bl, SN 2005hk, and SN 2005ke to the WV08 SN Ia H-band template in Fig. 5.3 (also Figure 3 of WV08), arguing that these objects can be excluded from the standardizeable candle sample of normal SN Ia based on NIR LC morphology alone. These 3 unusual cases that were excluded from the template construction are easily seen to be far from the H-band template. Fig. 5.3 shows that fitting either SN 2005hk, SN 2005ke, or SN 2005bl with the PAIRITEL WV08 SN Ia H-band template results in a sufficiently bad χ^2/DoF (> 10) that these SN Ia could be

excluded based on that criterion alone. Figure 5.4 further confirms this, showing a comparison of PAIRITEL CfAIR2 JHK_s LCs for the fast-declining SN 2005ke and the slowly-declining, overluminous SN 2009dc, demonstrating that neither are consistent with the fiducial mean NIR LC template from WV08. In both cases, the peak of the data can be seen to be several days *after* the peak of the fiducial normal SN Ia template, demonstrating that these SN Ia can be excluded from template creation and distance fitting for normal SN Ia based on their observed NIR LC morphology alone. Krisciunas et al. 2009 further argue that the clear distinction between the bimodal timing distributions of the NIR first maximum for normal and peculiar SN Ia allows one to exclude peculiar SN Ia without spectroscopy based on the timing of the NIR LC features alone. We discuss this further in §5.2.1.

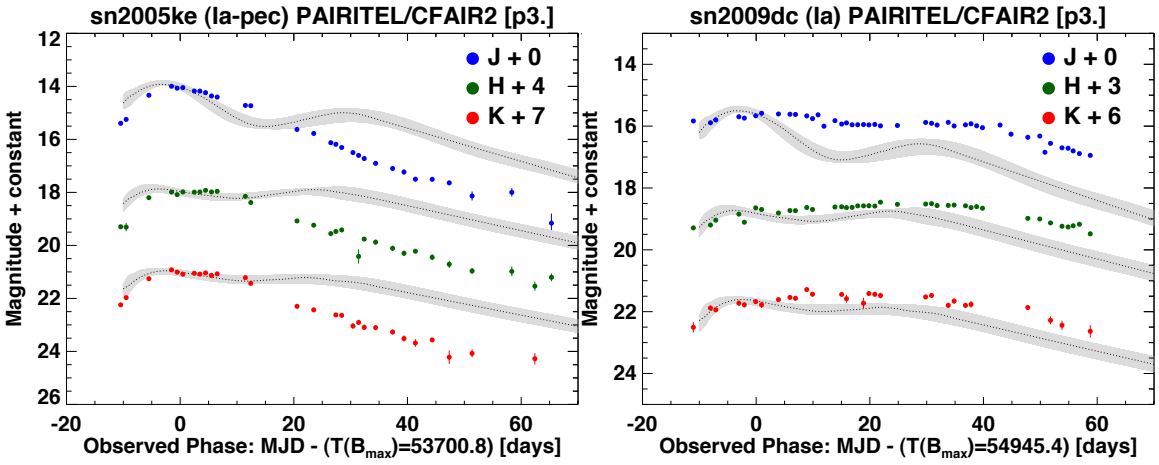

Figure 5.4.— PAIRITEL JHK_s LCs of peculiar SN Ia SN 2005ke and SN 2009dc

Well-sampled PAIRITEL CfAIR2 JHK_s LCs of SN 2005ke (**Left**) and SN 2009dc (**Right**). SN 2005ke is a fast-declining, intrinsically underluminous SN 1991bg-like SN Ia with possible circumstellar interaction (Patat 2005; Immler et al. 2006) which shows only a single NIR peak in JHK_s unlike the double peaked structure for normal SN Ia represented by the overplotted fiducial LC template (dashed lines with gray uncertainty regions). SN 2009dc is an intrinsically overluminous, slowly declining SN Ia (Taubenberger et al. 2011) which displays a flatter set of JHK_s LCs with suppressed NIR peaks. For comparison to both peculiar SN Ia, we overplot the fiducial WV08 NIR LC template for normal SN Ia as dashed lines with template uncertainties marked as gray regions. The NIR LCs of SN 2005ke and SN 2009dc have been normalized to so that their brightness at $t_{B\mathrm{max}}$ (observed phase = 0) matches the template, demonstrating that these NIR LCs are clearly not consistent with the mean NIR LC template for normal SN Ia. We exclude SN Ia like SN 2005ke an SN 2009dc from the construction of our SN Ia NIR LC templates (see §5.1) and they should also be excluded from distance fitting for the Hubble diagram.

Because we have excluded these peculiar objects, our newest template does not extend to SN 1991bg-like, SN 1991T-like SN Ia or other unusual SN Ia. This seems a reasonable approach while the sample still contains only ~ 200 objects and until NIR LC fitting tools are available that can handle the full spectrum of SN Ia decline rates and LC morphologies. Until then, unusual supernovae can be identified from a NIR light curve alone, or they can be identified from their optical spectra and light curves which we obtain as a matter of course at the CfA (e.g. Matheson et al. 2008; Hicken et al. 2009a,b, Hicken et al. 2012 *in preparation*). Phillips 2011 provide an extensive description of the photometric and spectroscopic properties of the peculiar SN Ia observed at NIR wavelengths which are not appropriate to include in a NIR template constructed for spectroscopically normal SN Ia, including mysterious objects like the extremely peculiar SN Ia SN 2006mr observed by the CSP (Contreras et al. 2010). In any case, we defer incorporating these unusual objects until the database is more fully populated or until SN LC fitters are extended to include them.

5.1.2 F12 NIR Template Construction

The IR light curves for all SN Ia used to construct the template were registered to a common rest-frame phase $t_{\rm rest}$ by subtracting $t_{B\rm max}$ from the observed phase $t_{\rm obs}$ (both in MJD [days]) and accounting for time dilation based on the heliocentric redshift, $z_{\rm helio}$ (Leibundgut et al. 1996; Goldhaber et al. 2001) given by

$$t_{\rm rest} = \frac{t_{\rm obs} - t_{B\rm max}}{(1 + z_{\rm helio})} \tag{5.1}$$

We determined $t_{B\rm max}$ for the CfAIR2 data set using MLCS2k2.v007 (Jha et al. 2007) fits to our own CfA optical CCD observations (Hicken 2009; Hicken et al.

2009a,b, Hicken et al. 2012 *in preparation*) combined with other optical data from the literature where available (e.g. Ganeshalingam et al. 2010; Contreras et al. 2010; Stritzinger et al. 2011). To transform the data from the observer-frame to the rest-frame, we applied the K-corrections of Krisciunas et al. 2004b to the NIR light curves based on the heliocentric redshift, which are shown in Figure 5.5. Future work will include more refined K-corrections for the NIR photometry based on the available NIR spectral sample (e.g Hsiao et al. 2007; Marion et al. 2009) currently being analyzed by Boldt et al. 2012 *in preparation* (G.H. Marion, L. Boldt, and M. Stritzinger — private communication).

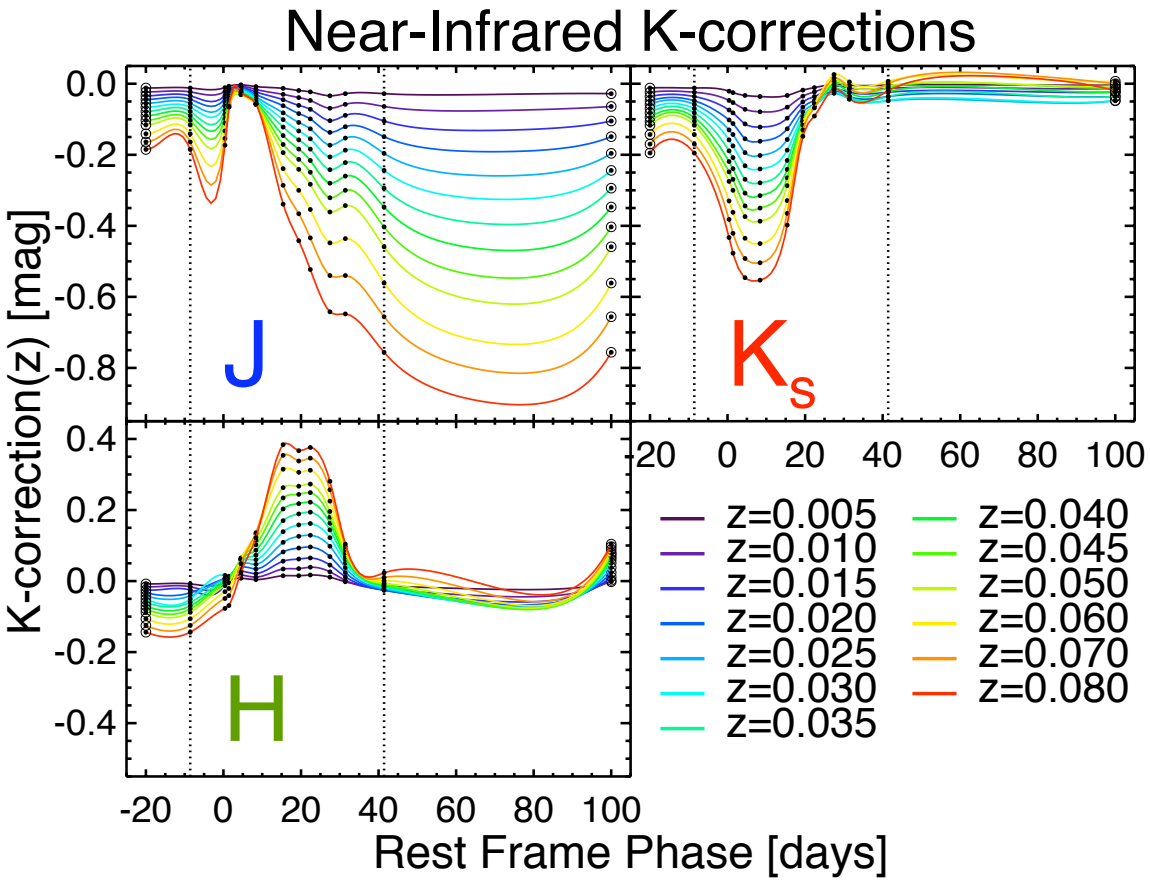

Figure 5.5.— Near-Infrared JHK_s SN Ia K-corrections, in magnitudes, plotted as a function of the rest frame phase=$(MJD - t_{B\max})/(1+z)$, where $t_{B\max}$ is the MJD of B-band maximum light and z is the heliocentric redshift. Plotted K-corrections are subtracted from the observed photometric data to correct them to the SN Ia rest frame (See *** below). Colored curves correspond to redshifts in the range $0.005 < z < 0.080$, covering all SN Ia considered in this paper. Plotted JHK_s Y-axes span $\Delta = 1$ mag for each band, revealing NIR K-corrections up to several tenths of a magnitude even for low-z SN Ia. K-corrections (solid black circles) are derived from 11 spectra for SN 1999ee presented in Table 11 of Krisciunas et al. 2004b (hereafter K04b). We linearly interpolate missing phases from Table 11 of K04b (J: 0.39 days; K_s: 19.42 days) and manually extrapolate to phases of -20 and 100 days (black circle-dots) to constrain the spline fits (solid colored curves) and estimate K-corrections outside the K04b phase range of ∼-9 to 42 days. Future work will use JHK_s SN Ia spectral templates (e.g. Hsiao et al. 2007) fit from a database of NIR spectra (e.g. Hsiao et al. 2007; Marion et al. 2009) to derive more accurate K-corrections for a wider range of phase and diversity of spectral features beyond SN 1999ee (Boldt et al. 2012 *in preparation*).

***: The caption of K04b Table 11 mistakenly reads: "The following corrections are *subtracted* from the photometric data to correct them to the **Observer's** frame (redshift z=0.00)", where it should say "...**rest** frame". See K04b Appendix B and Hamuy et al. 1993 for clarification of their convention for K-corrections.

To construct the new F12 template, we used the mean NIR LC template from WV08 to derive an initial guess for the magnitude at maximum light in the JHK_s bands for each normal SN Ia LC. Between $[-10, +40]$ days, where we have excellent sampling, we constructed our light curve templates by an unweighted averaging of the points from this initial set of standardized light curves into 1-day bins, and we used 2-day bins for phases > 40 days. Due to the large sample of data, no outlier rejection was used (or was necessary) in this process. The SN Ia light curves were then registered to a common magnitude scale by fitting each to this zeroth-iteration template and determining the maximum magnitude at $t_{B\max}$ ($JHK_s(t_{B\max})$). The fitting process is insensitive to the determination of the initial JHK_s magnitude at $t_{B\max}$ because this process is repeated with each iteration and the memory of the first guess is completely erased after the second iteration. To refine this template, we determined the magnitude value at $t_{B\max}$ that minimized the χ^2 of the template versus the data over the span from $[-10, +20]$ days. These new magnitude offsets were then used to seed the process above where we had previously used zero for the $JHK_s(t_{B\max})$ values. The procedure was iterated twice more to construct final values at $t_{B\max}$ for each SN Ia, and the final template was constructed based on these values. We found that three iterations were sufficient to reach convergence. We derive 1-σ template uncertainties by computing the standard deviation of the residuals of the light-curve data with respect to the mean template in each of the 1 or 2-day phase bins. The complete template and its uncertainties in JHK_s were both smoothed twice with a boxcar of length 4 days. The smoothing has very little effect near maximum light because of our dense sampling at those epochs. Varying the smoothing timescale between 1 and 5 days did not substantially affect the template.

This template construction procedure was performed for each of the JHK_s NIR passbands. Both the WV08 and F12 the H-band templates exhibit small scatter from $[-10, +30]$ days with a particularly tight distribution (narrower uncertainty regions in Figure 5.6) from $[-10, +20]$ days. We also observe similarly small scatter for the F12 K-band template in the phase range of $[-10, +30]$ days. Unlike the WV08 template, where we drew no firm conclusions with regard to K_s-band SN Ia light curves due to increased sky background in K_s, we now have enough K_s-band data that we believe the early time K_s-band template (< 40 days) to be a reasonable representation of the mean SN Ia properties at that wavelength. Like the WV08 template, the F12 J-band aggregate light curve has small scatter about the template from $[-10, +10]$ days but begins to show variations in the time and flux of the secondary maximum for individual supernovae at phases > 30 days. Overall the F12 and WV08 NIR templates are very similar, with the F12 template further refined in the K_s-band and in JHK_s at phase ranges > 35 days where the data analyzed in WV08 was sparse enough that a simple linear fit was assumed.

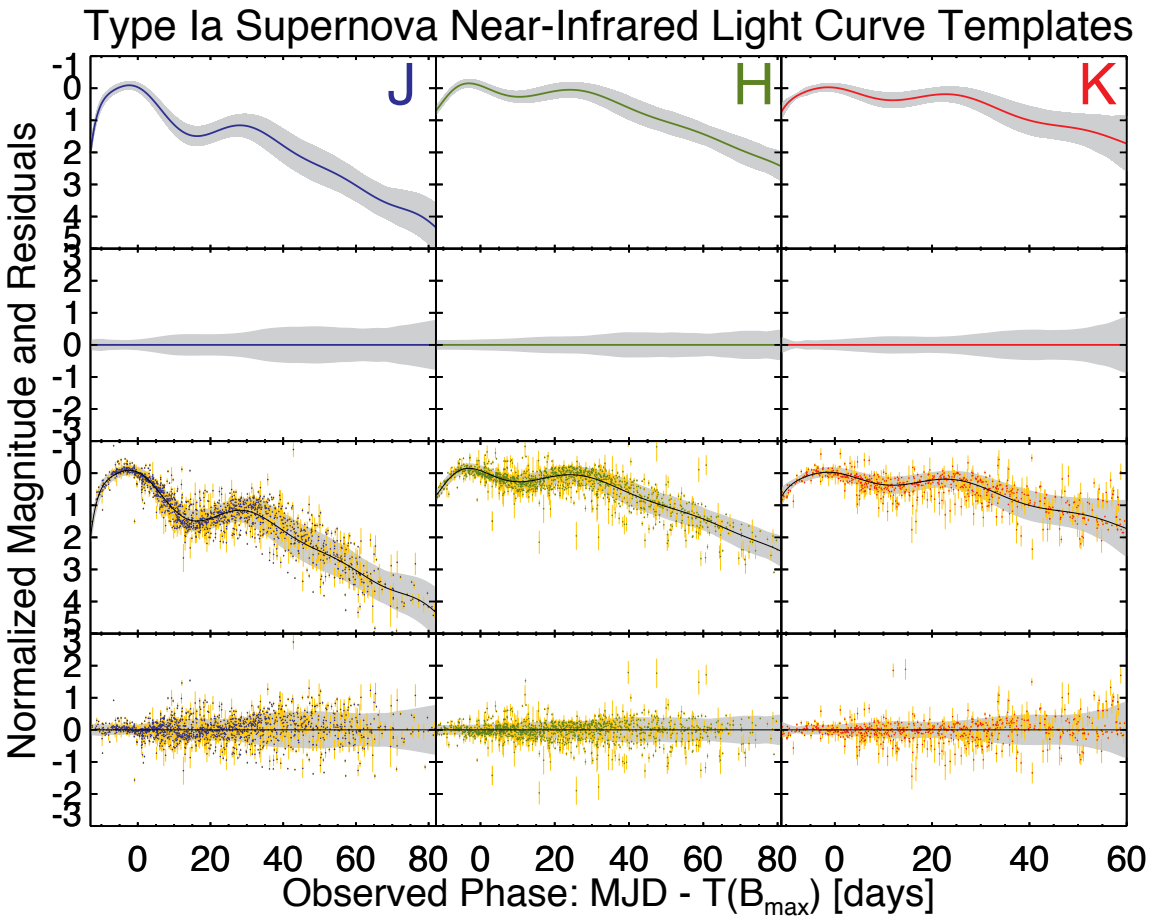

Figure 5.6.— NIR JHK_s LC Templates

Template fits are derived from all spectroscopically normal SN Ia considered in §5.1 including CfAIR2 data and data from the Literature (See Table 5.1). Mean template fits and uncertainties are provided in Table 5.2 while convenient polynomial fit coefficients are provided in Table 5.3.

(**Row 1**) Mean JHK_s templates are shown as blue, green, and red solid lines, normalized to 0 mag at $MJD = t_{B\max}$ (phase = 0). Templates are derived from 11 or 12-Degree polynomial fits to the aggregated SN Ia photometry weighted by the 1-σ photometric errors (See Row 3). Polynomial fits are valid only in the phase ranges $[-13, 82]$, $[-12, 81]$, and $[-11, 60]$ days for JHK_s respectively. The structure in the K_s-band template at late times is likely an artifact of the small sample size at those phases so the K_s-band fits are likely most valid at phases < 40 days.

(**Row 2**) Residuals for the JHK_s templates from Row 1. The 1-σ template uncertainties (gray regions) are computed from the standard deviation of the residuals in 1 day bins at phases < 40 days and 2-day phase bins for phases ≥ 40 days (excluding 3-σ outliers) and boxcar smoothing the resulting error curve twice with a 4-day moving window. The H-band templates exhibit small scatter from $[-10, +30]$ days with a particularly tight distribution (narrower uncertainty regions) from $[-10, +20]$ days. We also observe similarly small scatter for the K-band template in the phase range of $[-10, +30]$ days. The J-band aggregate light curve has small scatter about the template from $[-10, +10]$ days but begins to show variations in the time and flux of the secondary maximum for individual supernovae at phases > 30 days.

(**Row 3**) Same as Row 1, with the aggregated photometry (blue, green, and red) circles for JHK_s respectively, and 1-σ photometric errors (yellow error bars) over-plotted for all SN Ia used in the template fits.

(**Row 4**) Same as Row 2 with the residuals and their 1-σ errors over-plotted with the same color scheme as Row 3. Although 3-σ outliers are not explicitly excluded from the template fit, the few rare examples shown in Rows 3 and 4 to emphasize the insensitivity of the fit to their inclusion or exclusion given the overall size of the sample.

Unlike Krisciunas et al. (2004a), and similar to WV08, we do not further adjust this phase by the optical light-curve width parameter. In WV08, we found that compensating for the light-curve width gave no improvement in the template fits or in the resulting dispersion of absolute magnitudes (see §4.1) determined between −10 and +20 days in phase. However, the position of the second IR maximum is variable. In WV08 we suggested it would be worth exploring whether a width-correction parameter would produce a more effective template for fitting the second maximum and indeed evidence now exists suggesting that the position and magnitude of the second NIR peak is related to intrinsic luminosity (e.g Mandel et al. 2009; Kattner et al. 2012). Whereas Krisciunas et al. (2004a) and Wood-Vasey et al. (2008) both found no correlation between first and second peak NIR absolute magnitudes using the available data, Mandel et al. 2009 find evidence for a correlation between the peak J-band absolute magnitude and the position and phase of the secondary J-band maximum. Kattner et al. 2012 also find suggestive evidence for a non-zero decline rate relation correlating the first peak absolute JH-maxima (and perhaps the Y-band maximum) to the decline rate parameter Δm_{15} (Phillips 1993) from an analysis of 27 well-sampled CSP LCs. These results suggest that while NIR LCs are still intrinsically more standard than optical LCs, they are not perfect standard candles. Rather, NIR SN Ia LCs are *standardizeable* candles, since distance determinations may be improved by incorporating additional information about the intrinsic variability in the NIR. The LC fitting approach of Mandel et al. 2009, 2011 takes into account the entire multi-wavelength NIR and Optical correlation structure between the features of SN Ia LCs at all observed phases in order to make best use of all the available information. However, as shown in WV08, even without

Table 5.2. F12 NIR JHK_s LC Templates

$t_{\rm rest}$[a]	M_J[b]	σ_J[c]	$t_{\rm rest}$[a]	M_H[b]	σ_H[c]	$t_{\rm rest}$[a]	M_K[b]	σ_K[c]
-13	1.43	0.19	...	...	...	...	...	...
-12	1.15	0.20	-12	0.70	0.12	...	...	...
-11	0.84	0.21	-11	0.55	0.12	-11	0.74	0.23
-10	0.57	0.20	-10	0.39	0.12	-10	0.52	0.17
-9	0.35	0.18	-9	0.25	0.12	-9	0.37	0.11
-8	0.18	0.15	-8	0.12	0.12	-8	0.26	0.08
-7	0.07	0.14	-7	0.02	0.12	-7	0.17	0.09
-6	-0.01	0.13	-6	-0.06	0.13	-6	0.11	0.12
-5	-0.06	0.12	-5	-0.12	0.13	-5	0.06	0.12
-4	-0.08	0.12	-4	-0.14	0.13	-4	0.02	0.11
-3	-0.08	0.12	-3	-0.15	0.13	-3	-0.01	0.12
-2	-0.07	0.12	-2	-0.14	0.13	-2	-0.03	0.13
-1	-0.04	0.12	-1	-0.12	0.14	-1	-0.03	0.13
0	0.00	0.13	0	-0.08	0.14	0	-0.02	0.14
1	0.06	0.14	1	-0.03	0.15	1	0.01	0.14
2	0.14	0.16	2	0.01	0.15	2	0.04	0.16
3	0.23	0.17	3	0.06	0.15	3	0.08	0.17
4	0.34	0.19	4	0.11	0.15	4	0.13	0.18
5	0.47	0.21	5	0.15	0.16	5	0.17	0.19
6	0.60	0.23	6	0.19	0.16	6	0.22	0.20
7	0.74	0.24	7	0.22	0.17	7	0.27	0.21
8	0.88	0.26	8	0.24	0.17	8	0.30	0.22
9	1.01	0.27	9	0.26	0.17	9	0.34	0.23
10	1.14	0.28	10	0.27	0.18	10	0.36	0.24
11	1.25	0.29	11	0.27	0.19	11	0.37	0.24
12	1.35	0.29	12	0.26	0.20	12	0.37	0.24
13	1.43	0.30	13	0.25	0.20	13	0.37	0.24
14	1.49	0.30	14	0.23	0.21	14	0.36	0.24
15	1.53	0.30	15	0.21	0.22	15	0.34	0.24
16	1.55	0.30	16	0.18	0.22	16	0.31	0.24
17	1.54	0.30	17	0.16	0.22	17	0.29	0.23
18	1.53	0.30	18	0.14	0.23	18	0.26	0.22
19	1.49	0.30	19	0.11	0.23	19	0.24	0.22
20	1.45	0.30	20	0.09	0.23	20	0.21	0.22
21	1.40	0.30	21	0.07	0.23	21	0.20	0.22
22	1.34	0.30	22	0.06	0.23	22	0.19	0.23
23	1.29	0.31	23	0.05	0.24	23	0.19	0.24
24	1.24	0.31	24	0.05	0.24	24	0.19	0.25
25	1.20	0.32	25	0.05	0.24	25	0.21	0.25
26	1.17	0.33	26	0.06	0.24	26	0.23	0.27
27	1.16	0.34	27	0.07	0.25	27	0.27	0.28
28	1.16	0.35	28	0.09	0.25	28	0.31	0.30
29	1.17	0.37	29	0.12	0.26	29	0.36	0.32
30	1.20	0.39	30	0.15	0.27	30	0.42	0.33
31	1.24	0.41	31	0.18	0.29	31	0.48	0.35
32	1.29	0.43	32	0.22	0.30	32	0.54	0.36
33	1.36	0.46	33	0.27	0.30	33	0.61	0.38
34	1.43	0.48	34	0.31	0.32	34	0.67	0.40
35	1.51	0.50	35	0.36	0.33	35	0.74	0.41
36	1.59	0.52	36	0.41	0.34	36	0.80	0.42
37	1.68	0.54	37	0.46	0.35	37	0.86	0.43
38	1.76	0.55	38	0.51	0.36	38	0.91	0.44
39	1.85	0.57	39	0.56	0.37	39	0.96	0.44
40	1.93	0.57	40	0.61	0.37	40	1.00	0.45
41	2.00	0.58	41	0.66	0.36	41	1.04	0.45
42	2.07	0.59	42	0.71	0.36	42	1.07	0.45
43	2.13	0.59	43	0.76	0.36	43	1.10	0.44
44	2.19	0.58	44	0.80	0.36	44	1.13	0.43
45	2.24	0.59	45	0.85	0.36	45	1.15	0.43
46	2.29	0.59	46	0.89	0.36	46	1.17	0.44
47	2.34	0.59	47	0.93	0.35	47	1.19	0.44
48	2.38	0.59	48	0.97	0.35	48	1.21	0.45
49	2.43	0.58	49	1.00	0.35	49	1.23	0.46
50	2.47	0.58	50	1.04	0.35	50	1.26	0.47
51	2.52	0.57	51	1.08	0.36	51	1.29	0.48
52	2.57	0.56	52	1.11	0.36	52	1.32	0.50
53	2.62	0.55	53	1.15	0.36	53	1.36	0.53
54	2.68	0.54	54	1.18	0.35	54	1.40	0.57
55	2.74	0.53	55	1.22	0.35	55	1.45	0.55
56	2.80	0.52	56	1.26	0.34	56	1.50	0.56
57	2.87	0.51	57	1.30	0.34	57	1.55	0.68
58	2.93	0.51	58	1.34	0.34	58	1.61	0.75
59	3.00	0.50	59	1.38	0.33	59	1.67	0.64
60	3.06	0.49	60	1.43	0.33	60	1.72	0.43
61	3.13	0.48	61	1.47	0.32	...	...	...
62	3.19	0.48	62	1.52	0.32	...	...	...
63	3.24	0.48	63	1.57	0.33	...	...	...
64	3.30	0.48	64	1.62	0.35	...	...	...
65	3.35	0.49	65	1.67	0.36	...	...	...
66	3.40	0.49	66	1.72	0.36	...	...	...
67	3.45	0.49	67	1.77	0.37	...	...	...
68	3.49	0.49	68	1.82	0.38	...	...	...
69	3.54	0.50	69	1.87	0.39	...	...	...
70	3.59	0.53	70	1.92	0.40	...	...	...
71	3.64	0.55	71	1.97	0.41	...	...	...
72	3.70	0.58	72	2.01	0.41	...	...	...
73	3.76	0.59	73	2.06	0.41	...	...	...
74	3.82	0.61	74	2.10	0.41	...	...	...
75	3.89	0.63	75	2.14	0.41	...	...	...
76	3.96	0.65	76	2.19	0.40	...	...	...
77	4.02	0.68	77	2.23	0.39	...	...	...
78	4.08	0.71	78	2.28	0.40	...	...	...
79	4.12	0.72	79	2.33	0.42	...	...	...
80	4.16	0.72	80	2.38	0.44	...	...	...
81	4.19	0.72	81	2.44	0.45	...	...	...
82	4.21	0.74	...	...	...	...	...	...

[a] Rest-frame phase $t_{\rm rest}$ [days] given by Eq. 5.1

[b] $M_X = M_X(t_{\rm rest}) - M_X(t_{B\rm max})$ for $X = JHK_s$ Normalized to 0 mag at $t_{\rm rest} = t_{B\rm max}$

[c] 1-σ template uncertainty [mag] defined in §5.1.2 and the caption of Figure 5.6.

Table 5.3. F12 NIR JHK_s LC Template Polynomial Fit Coefficients

p_i[a]	J[b]	H[c]	K[d]
p_0	0.0010218929	-0.078857464	-0.017378073
p_1	0.052549166	0.041020428	0.017357852
p_2	0.0083870294	0.0036654047	0.0059699801
p_3	9.2788301e-05	-0.00059605667	-0.00023957086
p_4	-1.3403725e-05	1.0474768e-05	-3.0045704e-05
p_5	-4.1337862e-06	1.0791741e-06	8.4945250e-07
p_6	2.3327457e-07	-6.0220362e-08	1.2977093e-07
p_7	4.9650017e-09	1.3579999e-09	-9.4638970e-09
p_8	-7.8624384e-10	-1.5972875e-11	2.8621824e-10
p_9	3.0496642e-11	9.6765063e-14	-4.7591411e-12
p_{10}	-6.3546273e-13	-2.3905661e-16	4.5473655e-14
p_{11}	7.9836308e-15	-2.3480118e-16	$\cdots$

y

[a]Polynomial coefficients p_i for the F12 JHK_s mean LC templates. For a given rest-frame phase $t_{\rm rest}$ (Eq. 5.1) in the phase ranges where the fits are valid (see below), the p_i coefficients can be used to output the normalized mean template magnitude, given by $M(t_{\rm rest}) = \Sigma_{i=0}^{N_{\rm degree}} p_i t_{\rm rest}^i$ [mag], where $N_{\rm degree}$=12, 11, 12 in JHK_s, respectively (Also see Figure 5.6 and Table 5.2).

[b]J-band $N_{\rm degree}$=12-Degree polynomial fit only valid in phase range $[-13, 82]$ days.

[c]H-band $N_{\rm degree}$=11-Degree polynomial fit only valid in phase range $[-12, 81]$ days.

[d]K-band $N_{\rm degree}$=12-Degree polynomial fit only valid in phase range $[-11, 60]$ days.

accounting for NIR LC shape, it is possible to derive NIR-only distance estimates for SN Ia which are comparable in precision to estimates derived with Optical-only data *after* the complex process of LC shape correction. Due to the uncertainties inherent in any LC shape correction process, it becomes useful to establish a baseline with distances derived from NIR data that is intrinsically standard enough over certain phase ranges to allow the determination of accurate and precise distances without any LC shape correction.

5.2 LC Fitting

In this section we describe the simple approach we employed to fit NIR JHK_s LCs to the available NIR data from CfAIR2 and the Literature. Fit results characterizing the observed properties of the nearby SN Ia sample are listed in Table 5.1, focusing on the observed apparent JHK_s magnitudes of the SN Ia at $t_{B\max}$. LC fits for CfAIR2 SN Ia data are shown in Figure 5.1 with a subset of particularly well-sampled LCs shown in Figure 5.2. When LCs are well-sampled, simple $N_{\rm degree}$-degree polynomial fits to the data are sufficient to characterize the LC over a wide phase range. This can be seen in Figure 5.7 where we plot PAIRITEL CfAIR2 JHK_s LCs for the well-sampled SN Ia SN 2006X. When LCs are sparsely-sampled, we use information from the mean NIR LC template (see §5.1) to help inform the fit at phases where data are missing, effectively using the template LC to place a smoothed prior on the LC value at those phases. We do this by simply combining the LC data with the mean template data and adjusting the error weighting of the polynomial fit such that the data are weighted higher in phase ranges where LC points are present and

the template is weighted higher in regions where data are sparse or absent, such as the early and late time portions of the LC. Figures 5.8–5.9 illustrate the LC fitting process for two example SN Ia, the well-sampled SN 2006X and the sparsely-sampled SN 2007cq. These examples illustrate how the fit uses a fiducial, mean JHK_s LC template from WV08 to inform the fit at phases where data are sparse, but ensures that the fit is dominated by the data (and not the template) where data are present, in order to account for real intrinsic deviations from the mean template for individual objects.

For SN Ia well sampled around $t_{B\mathrm{max}}$, linear or cubic spline interpolation is generally sufficient to determine $m(t = 0)$, the observed apparent magnitude at $t_{B\mathrm{max}}$ in JHK_s (fit results are presented in Table 5.1). For SN Ia sparsely sampled around $t_{B\mathrm{max}}$, the vertical offset from the fiducial template is fit with χ^2 minimization using all the LC data in each band to estimate of the apparent magnitude at $t_{B\mathrm{max}}$ and its uncertainty. In phase ranges where data are absent, we estimate the polynomial fit uncertainties as the 1-σ uncertainties in the fiducial mean LC template as given in Table 5.2. This is equivalent to assuming a prior value on the uncertainty given by the population uncertainty, which we estimate as the standard deviation of the LC magnitude values a those phases from the sample used to derive the template. In phase ranges where the data are present, we estimate the fit uncertainties as the 1-σ uncertainties of the polynomial fit itself. For all phase ranges, we add in quadrature the uncertainty in determining the magnitude at $t_{B\mathrm{max}}$ either from linear interpolation to data well-sampled near $t_{B\mathrm{max}}$ or fitting for the y-axis offset via χ^2 minimization to the entire LC when data are sparsely sampled near $t_{B\mathrm{max}}$. In cases where $t_{B\mathrm{max}}$ is determined from fits to well-sampled optical data, the uncertainty

on $t_{B\max} \lesssim 0.5$ days and we ignore this uncertainty in the fit. In cases where optical data currently are not reduced or otherwise unavailable, we must estimate $t_{B\max}$ from the fit times of the NIR LC features (or from optical spectra, where available). When $t_{B\max}$ is estimated from fits to the well-sampled first NIR peak t_1, we ignore the error on $t_{B\max}$ in our polynomial fits because the distribution of $t_1 - t_{B\max}$ has an uncertainty $\lesssim 0.1$ days in JHK_s (See Table 5.4). When $t_{B\max}$ is estimated from fits to the temporal features of late-time NIR data, including only the trough between peaks t_t or the time of the secondary maximum t_2, we do incorporate the uncertainty on $t_{B\max}$ into the polynomial fits since these uncertainties can be $\sim$ 2–5 days, which is comparable to uncertainties in $t_{B\max}$ derived from optical spectra.

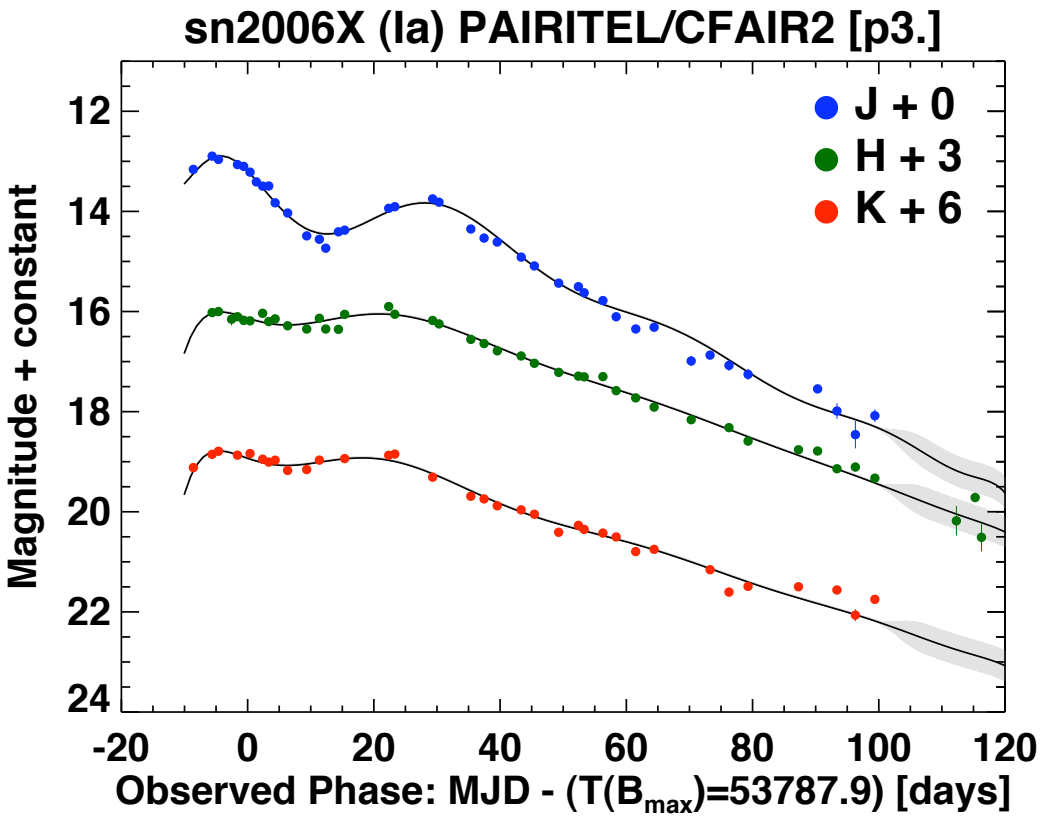

Figure 5.7.— PAIRITEL JHK_s LCs for the well-sampled, spectroscopically normal SN Ia SN 2006X, with polynomial model fits described in §5.2 (also see the caption for Figure 5.8).

While other approaches use cubic splines rather than polynomials (e.g. Burns et al. 2011), we employed polynomials here both for their simplicity compared to cubic splines and for the ease of representing fits to individual LCs or LC templates as a simple $N_{\rm degree}$-parameter model in terms of their polynomial coefficients (see Table 5.3). Polynomial fits also enable easy computation of smoothed error estimates (see gray regions in Figure 5.10). A major disadvantage of polynomials, (but not splines) is that they often do not encode enough information to adequately fit parts of the LC with more detailed structure, for example the J-band trough. Another problem with polynomials is their tendency to exhibit oscillations which deviate from a good fit (in the χ^2 sense) near the endpoints of the region with data[2]. Cubic splines resolve this problem by breaking the data up into several regions which are each fit by separate $N_{\rm degree}$=3 polynomials. A cubic spline with $N_{\rm knots} = 10$ knots, and $N_{\rm knots} + 1$ segments, each fit with a cubic spline ($N_{\rm degree}$=3 $\rightarrow$ 3 parameters) will have $3(N_{\rm knots} + 1)$ parameters. To have the same number of parameters as a $N_{\rm degree} = 12$-degree polynomial, the cubic spline would require $N_{\rm knots} = 3$, giving $3(3 + 1) = 12$ parameters. Adding additional knots runs the risk of over-fitting. However, the cubic spline fit is very sensitive to the placement of the knots and must be guided by prior knowledge of the shape of the LC. An alternative resolution using polynomials, which we employ here, is to apply boundary conditions to the polynomial fit at the lower and upper endpoints where data exist. We effectively do so here by using constraints based on the early and late-time values of the mean JHK_s template (either WV08 or F12) as described above by weighting the early and late time template points higher in the polynomial fit.

---

[2] http://en.wikipedia.org/wiki/Runge\%27s_phenomenon

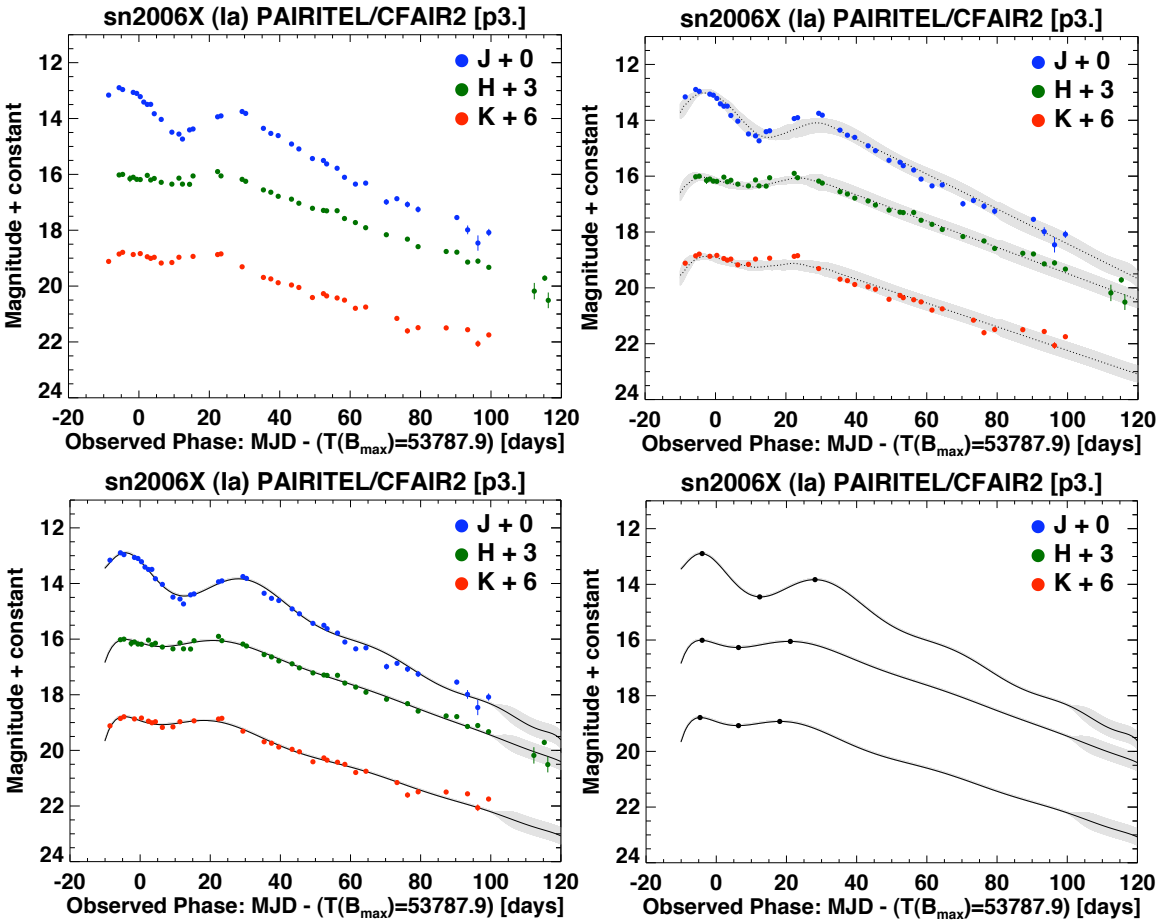

Figure 5.8.— LC fitting process for the well-sampled SN 2006X.

(**Upper Left**) Only the NIR observed-frame LC data are shown, denoted by blue, green, and red filled circles for JHK_s, respectively and offset from each other along the y-axis for clarity. The observer-frame phase t is defined with respect to $t_{B\max}$, the time of maximum light in the B-band such that $t = 0 \equiv t_{B\max}$. We determine $t_{B\max}$ using MLCS2k2 v007 fits (Jha et al. 2007) to the CfA optical data (Hicken et al. 2009b, Hicken et al. 2012 *in preparation*) and/or optical data from the Literature where available. (**Upper Right**) The magnitude data are aligned along the y-axis with respect to a fiducial normal rest-frame SN Ia mean LC template from WV08, over-plotted with a dashed line and uncertainties shown with a gray error snake. The rest-frame template is corrected to the observed-frame by multiplying the rest-frame template phases by $(1 + z)$, where z is the SN Ia heliocentric redshift. The mean LC template is provided in Table 5 of Wood-Vasey et al. 2008**. The WV08 LC template is normalized such that $m(t = 0) \equiv m(t_{B\max}) \equiv 0$ for each of the JHK_s bands. For SN Ia well sampled around $t_{B\max}$, linear or cubic spline interpolation is generally sufficient to determine $m(t = 0)$, the observed apparent magnitude at $t_{B\max}$ in JHK_s. For SN Ia sparsely sampled around $t_{B\max}$, the vertical offset from the fiducial template is fit with χ^2 minimization using all the LC data in each band to estimate of the apparent magnitude at $t_{B\max}$ and its uncertainty. (**Lower Left**) LC fits are over-plotted as black lines with fit uncertainties shown as gray error snakes, which are most uncertain in regions with sparse data. LCs are fit with $N = 11$, 9, and 9 order polynomials in JHK_s, respectively. The mean LC template and its uncertainties are used to inform the fit at phases with missing observed data. To avoid oscillation of the fit near the endpoints, the polynomial fits are constrained by applying early and late-time boundary conditions (where data is usually sparse) to match the fit to LC template. This is done by heavily down-weighting the template uncertainties at those phases. In order to more heavily weight the data in the fit to account for intrinsic deviations for individual SN Ia from the mean template, we also up-weight the template uncertainties at phases where data are present. (**Lower right**) Only the LC fits (black lines) are shown without the data or mean LC template. Major NIR features are over-plotted as black filled circles (error bars not shown) corresponding to the magnitudes of the first peak $m(t_1)$, trough $m(t_t)$, and second peak $m(t_2)$. Table 5.1 lists the fit values of $m(t = 0)$ and its uncertainty (the magnitude at $t_{B\max}$) for all CfAIR2 JHK_s SN Ia.

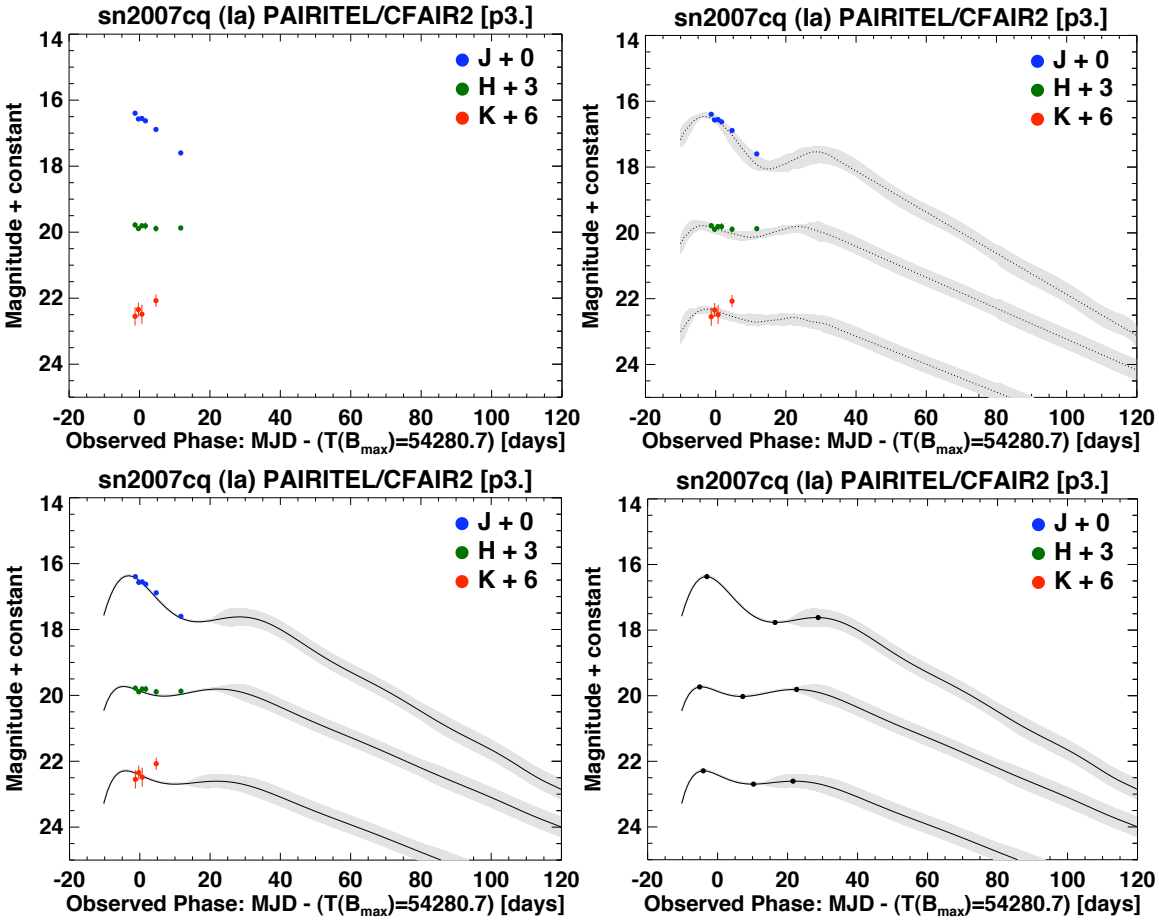

Figure 5.9.— LC fitting process for the sparsely-sampled SN 2007cq

(**Upper Left**) Only the NIR observed-frame LC data are shown, denoted by blue, green, and red filled circles for JHK_s, respectively and offset from each other along the y-axis for clarity. The observer-frame phase t is defined with respect to $t_{B\max}$, the time of maximum light in the B-band such that $t = 0 \equiv t_{B\max}$. We determine $t_{B\max}$ using MLCS2k2 v007 fits (Jha et al. 2007) to the CfA optical data (Hicken et al. 2009b, Hicken et al. 2012 *in preparation*) and/or optical data from the Literature where available. (**Upper Right**) The magnitude data are aligned along the y-axis with respect to a fiducial normal rest-frame SN Ia mean LC template from WV08, over-plotted with a dashed line and uncertainties shown with a gray error snake. The rest-frame template is corrected to the observed-frame by multiplying the rest-frame template phases by $(1 + z)$, where z is the SN Ia heliocentric redshift. The mean LC template is provided in Table 5 of Wood-Vasey et al. 2008**. The WV08 LC template is normalized such that $m(t = 0) \equiv m(t_{B\max}) \equiv 0$ for each of the JHK_s bands. For SN Ia well sampled around $t_{B\max}$, linear or cubic spline interpolation is generally sufficient to determine $m(t = 0)$, the observed apparent magnitude at $t_{B\max}$ in JHK_s. For SN Ia sparsely sampled around $t_{B\max}$, the vertical offset from the fiducial template is fit with χ^2 minimization using all the LC data in each band to estimate of the apparent magnitude at $t_{B\max}$ and its uncertainty. (**Lower Left**) LC fits are over-plotted as black lines with fit uncertainties shown as gray error snakes, which are most uncertain in regions with sparse data. LCs are fit with $N = 11$, 9, and 9 order polynomials in JHK_s, respectively. The mean LC template and its uncertainties are used to inform the fit at phases with missing observed data. To avoid oscillation of the fit near the endpoints, the polynomial fits are constrained by applying early and late-time boundary conditions (where data is usually sparse) to match the fit to LC template. This is done by heavily down-weighting the template uncertainties at those phases. In order to more heavily weight the data in the fit to account for intrinsic deviations for individual SN Ia from the mean template, we also up-weight the template uncertainties at phases where data are present. (**Lower right**) Only the LC fits (black lines) are shown without the data or mean LC template. Major NIR features are over-plotted as black filled circles (error bars not shown) corresponding to the magnitudes of the first peak $m(t_1)$, trough $m(t_t)$, and second peak $m(t_2)$. Table 5.1 lists the fit values of $m(t = 0)$ and its uncertainty (the magnitude at $t_{B\max}$) for all CfAIR2 JHK_s SN Ia.

5.2.1 Estimating $t_{B\max}$ From NIR LC Features

At the time of writing, there exist 35 objects with CfAIR2 NIR data but no optical data yet available. 26 of these SN Ia have CfA optical data to be reduced (Hicken et al. 2012 *in preparation*), while the others may not necessarily have optical data in the Literature. For all of these, we use fits to the NIR features to estimate $t_{B\max}$ using the LC fitting approach described in §5.2. We were motivated to develop a method to used fits to the NIR features to estimate $t_{B\max}$ because LC data must be aligned to a common phase referenced to $t_{B\max}$ in order to be included in the analysis. To estimate the mean properties of the NIR features with respect to $t_{B\max}$, we combined CfAIR2 NIR data with NIR data from CSP and the Literature for spectroscopically normal SN Ia for which we could also find available optical data in the literature. For ~ 210 data sets with both Optical and NIR data (corresponding to 191 unique, normal SN Ia), we fit for $t_{B\max}$ using MLCS2k2 (Jha et al. 2007) fits to the combined optical data sets for each object. We also used our simple polynomial LC fitting process to fit for the phases of the first NIR peak (t_1), the trough between peaks (t_t), and second peak (t_2), excluding fits where actual data points did not exist within ~ 5 days of the specific NIR features. After 3-σ clipping outliers due to bad fits, we find small dispersions in the distributions of these fiducial NIR features with respect to $t_{B\max}$, especially for the first NIR peak t_1, with progressively wider distributions for the trough t_t and second peak t_2. We present the means and standard deviations of the distribution of values of $\bar{t_1} = t_1 - t_{B\max}$, $\bar{t_t} = t_t - t_{B\max}$, and $\bar{t_2} = t_2 - t_{B\max}$ in Table 5.4. These relations allow us to estimate $t_{B\max}$ using NIR data alone, and do so with high precision when well-sampled early-time NIR data exists, allowing a good fit to t_1.

These $t_{B\max}$ estimates allow us to link NIR-only data to the well-measured optical properties of the nearby sample, to referenced LC fits to a standard phase scale, and derive NIR distance estimates even in the absence of optical data, which effects some NIR SN Ia in CfAIR2 and the literature. Figure 5.10 demonstrates the utility of this method with plots of fits to NIR LCs where $t_{B\max}$ is estimated from NIR features in the absence of available optical data. The relations in Table 5.4 are also very useful for standard candle testing from NIR LC shape alone. Krisciunas et al. 2009 derive a bimodal distribution for the timing of the first NIR peak with respect to $t_{B\max}$, confirming the observation that objects with NIR peak after $t_{B\max}$ are subluminous, peculiar SN Ia, whereas those with $t_{B\max}$ before NIR peak (see the relations for normal SN Ia in Table 5.4, where $\bar{t_1} < 0$), are effectively normal SN Ia and essentially standard candles independent of the decline rate.

Table 5.4: Mean Reference Times of NIR LC Features

Observed Phase[a]	J [days]	H [days]	K_s [days]
$\bar{t_1}$	-3.07 ± 0.05	-4.09 ± 0.09	-2.04 ± 0.04
$\bar{t_t}$	16.57 ± 2.42	9.40 ± 2.07	12.55 ± 2.78
$\bar{t_2}$	27.92 ± 4.99	24.44 ± 2.57	22.77 ± 2.68

(*a*) $\bar{t_1}$, $\bar{t_2}$, and $\bar{t_t}$ are the mean observed phases of the first NIR peak, the second NIR peak, and the trough between peaks, each with respect to $t_{B\max}$, the time of maximum light in the B-band, shown for each of the PAIRITEL JHK_s bands. In the J-band, the first NIR peak occurs ~ 3 days before $t_{B\max}$, indicated by $\bar{t_1} = -3.07 \pm 0.05$ days, with a small uncertainty of 0.05 days. The mean phases for each of these LC reference times were derived using 210 JHK_s LC data sets of spectroscopically normal SN Ia from CfAIR2, CSP, and the Literature (191 unique SN Ia), with the means and uncertainties (standard deviations of phases) determined after robust 3-σ clipping to remove contributions from individual LCs with bad model fits. The standard deviations, especially of $\bar{t_1}$, the first NIR peak with respect to $t_{B\max}$ are quite small, allowing $t_{B\max}$ to be inferred with small uncertainty from a well sampled NIR LCs alone, even in the absence of optical data. If the NIR LC is observed after t_1, fits to the trough t_t and the second peak t_2 can also be used to estimate $t_{B\max}$, albeit with larger uncertainty than from the first NIR peak.

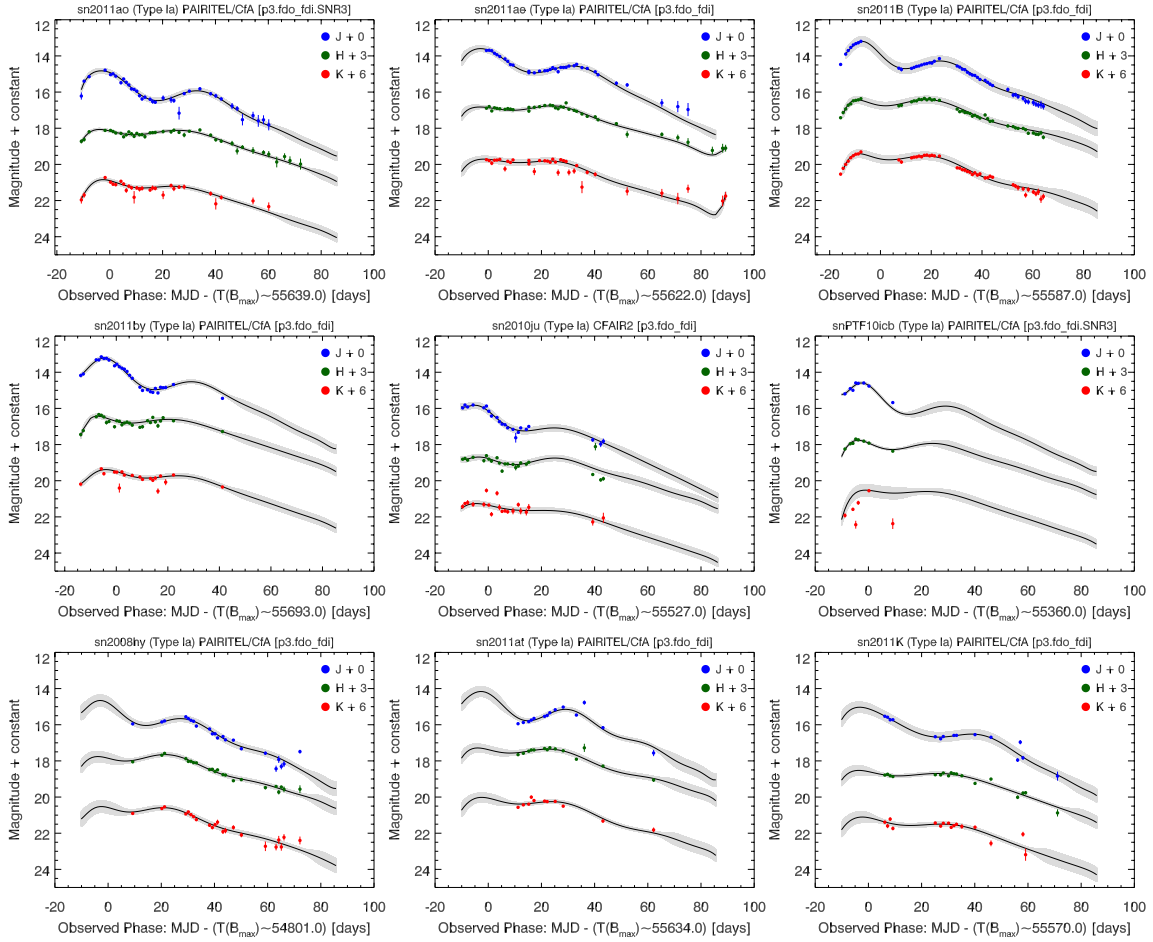

Figure 5.10.— JHK_s LC fits Using NIR Features to Estimate $t_{B\max}$

LC fits for 9 normal SN Ia where $t_{B\max}$ was not available from reduced optical data at the time of this paper. In these case, fits to the time of the NIR first maximum t_1, trough t_t, and secondary maximum t_2 were performed and $t_{B\max}$ was estimated based based on empirically derived relationships (and uncertainties) in the distributions of $\bar{t_1} = t_1 - t_{B\max}$, $\bar{t_t} = t_t - t_{B\max}$, and $\bar{t_2} = t_2 - t_{B\max}$ presented in Table 5.4. No outlier points were removed from these LCs in performing the fit. These $t_{B\max}$ estimates allow LC fits and distances to be derived for NIR data even in the complete absence of optical data.

(First Row) LCs and fits for SN 2011ao, SN 2011ae, and SN 2011B. These SN Ia are all well-sampled covering all 3 NIR features, with the exception of SN 2011B, which has a data gap around $t_{B\max}$, contributing to the larger fit uncertainties (gray regions).

(Second Row) LCs and fits for SN 2011by, SN 2010ju, and SN PTF10icb. These SN Ia are well sampled at early times, near $t_{B\max}$, but more sparsely sampled at late times. Still reasonable fits are possible because the distributions of $\bar{t_1} = t_1 - t_{B\max}$ in JHK_s are very narrow, with uncertainties (given by the standard deviation) of $\lesssim 0.1$ days, allowing us to infer $t_{B\max}$ from fits to the time of the first NIR peak with small uncertainty.

(Third Row) LCs and fits for SN 2008hy, SN 2011at, and SN 2011K. These SN Ia are more sparsely sampled at early times, but reasonably well-sampled at late times. Still it is possible to infer $t_{B\max}$ to within an uncertainty of $\sim$ 2–3 days based on fits to the time of the NIR trough between peaks (See Table 5.4). The additional uncertainty in the estimation of $t_{B\max}$ is reflected in the wider gray error regions near the first NIR maximum in the fit.

5.2.2 SN Ia JHK_s Apparent Magnitudes at $t_{B\max}$

The apparent JHK_s magnitudes at the time of B-band maximum light, $m(t = 0 = t_{B\max})$, are presented in Table 5.1 based on fits to the 93 normal SN Ia LCs in CfAIR2 shown in Figure 5.1. A subset of 31 fits to particularly well-sampled, normal SN Ia from CfAIR2 are also shown in Figure 5.2. The LC fits shown in Figures 5.1–5.2 allow the inferences of the observed properties of the nearby sample (Table 5.1) and for the determination of Infrared and Optical-Infrared colors (§6.3.2) which help us measure extinction and reddening for each SN Ia and estimate distances that are more accurate and more precise than with optical data alone. We do not present fit results for t_1, t_t, t_2, $m(t_1)$, $m(t_t)$, and $m(t_2)$, the times and magnitudes of the major NIR features (peaks and trough) here, since we are still refining the error estimates for the quantities and do not wish to present them without accurate uncertainties. Along with the redshift information for each SN Ia host galaxy in Table 2.3, the data in Table 5.1 will allow us to present a NIR Hubble diagram and quantify the distribution of Absolute magnitudes. This will be presented in Friedman et al. 2012 *in preparation*.

Chapter 6

Conclusions and Future Directions

6.1 Conclusion: Summary of Data and Results

This thesis presents the CfAIR2 data set, which includes 104 Near-Infrared JHK_s-band light curves of SN Ia observed through from 2005–2011 with the PAIRITEL 1.3-m telescope at the Fred Lawrence Whipple Observatory at Mount Hopkins, Arizona. The PAIRITEL NIR JHK_s observations complement the long established optical component of the CfA Supernova Program, a systematic effort at the CfA to obtain high quality, densely sampled, optical supernova spectra and concurrent $UBVRIr'i'$ optical photometry for hundreds of nearby, low-redshift SN of all types in the nearby universe. The dense sampling and rapid follow-up of optically discovered SN Ia has allowed PAIRITEL to obtain a large amount of early-time NIR data. Out of the 122 SN Ia observed by PAIRITEL in JHK_s from 2005-2011, 58 (48%) have NIR observations before $t_{B\max}$, while 34 (28%) have observations at least 5 days before $t_{B\max}$, with fractions comparable to similar SN Ia follow-up work by the CSP (Contreras et al. 2010; Stritzinger et al. 2011), the only complementary existing data set comparable to the extensive CfAIR2 observations. Overall, the 4269 individual data points in the CfAIR2 sample represent the largest homogeneously observed and reduced set of NIR SN Ia observations to date, nearly doubling the number of objects and more than tripling the number of individual JHK_s photometric observations of SN Ia in the literature.

The published subset of my thesis data has already helped confirm and strengthen the claim that SN Ia are more standard in NIR luminosity than at optical wavelengths, less sensitive to dimming by host galaxy dust, and crucial to reducing systematic galaxy distance errors due to the degeneracy between intrinsic supernova

color variation and reddening of light by dust, arguably the most dominant source of systematic error in SN Ia cosmology (Wood-Vasey & Friedman et al. 2008; Mandel, Wood-Vasey, Friedman, & Kirshner 2009; Mandel et al. 2011). Work by Kaisey Mandel using my thesis data combined with optical and other NIR data from the literature has demonstrated that the inclusion of NIR data helps to break the degeneracy between reddening and intrinsic color and ensure that the distance estimates will be less sensitive to the model assumptions of individual LC fitters (Mandel et al. 2011).

6.1.1 Wood-Vasey & Friedman et al. 2008

"TYPE Ia SUPERNOVAE ARE GOOD STANDARD CANDLES IN THE NEAR INFRARED: EVIDENCE FROM PAIRITEL"

ApJ, 689:377-390, 2008 December 10

Our research efforts in NIR observations have helped to confirm that SN Ia are excellent standard candles in the NIR even without correcting for light curve shape or extinction, especially in the rest-frame H-band, where they are ~ 5 times less sensitive to extinction from dust than in the optical V-band. In WV08, we obtained 1087 NIR JHK_s measurements of 21 SN Ia using PAIRITEL, nearly doubling the number of well-sampled NIR SN Ia light curves at the time. We constructed fiducial NIR templates for normal SN Ia from our sample, excluding only three known peculiar SN Ia: SN 2005bl, SN 2005hk, and SN 2005ke. We presented a method to find accurate luminosity distances of SN Ia using the H-band light curve from $[-10, +20]$ days after B-band maximum light. We found that the H-band absolute

magnitudes of this sample of 18 PAIRITEL SN Ia have an *uncorrected* intrinsic RMS of only 0.15 mag. We found a relationship between the H-band extinction and optical color excess of $A_H \sim 0.2E(B-V)$. This variation is as small as the scatter in luminosity distance measurements currently used for cosmology that are based on optical light curves *after* corrections for light-curve shape and for dust absorption. Within the photometric and local-flow uncertainties, the distribution about a best-fit ΛCDM model was consistent with no intrinsic dispersion of our H-band template fit magnitude values. Even without accounting for peculiar velocity uncertainties or making any corrections for extinction or light-curve shape, the RMS scatter of 0.16 mag from these *uncorrected* inferred luminosity distance moduli was found to be smaller than *corrected* distances from optical-based methods (e.g. 0.18 mag; Jha et al. 2007). We also combined the homogeneous PAIRITEL measurements with 23 SN Ia from the literature, showing that these 41 SN Ia have standard H-band magnitudes with an RMS scatter of 0.16 mag (WV08). The good match of our sample with the literature sample suggests that even though we now know there are some systematic problems with the WV08 photometry for individual objects (see §4.3.2), the *mean* NIR absolute magnitudes obtained from the WV08 PAIRITEL measurements are consistent with those found by other studies analyzing independent NIR SN Ia data sets (e.g. Krisciunas et al. 2004b; Mandel et al. 2009, 2011; Folatelli et al. 2010; Burns et al. 2011; Phillips 2011). We also presented a nearby H-band Hubble diagram and found no correlation of the residuals from the Hubble line with respect to optical light-curve properties (WV08).

In the WV08 paper, we measured reddening only from optical data, without using NIR information, and found it unnecessary to apply reddening corrections in

H-band for the objects in our sample. However, work on the highly extinguished SN 2002cv (Elias-Rosa et al. 2008) and work measuring reddening and extinction with optical and NIR data in combination (Mandel et al. 2011) suggests that reddening corrections may be necessary for some SN Ia in the NIR. Reddening uncertainties derived using optical data alone currently represent the most significant systematic error affecting SN Ia luminosity distance measurements. Simulations by Krisciunas et al. (2007) demonstrate major improvements to be gained from the addition of NIR data. Krisciunas et al. (2007) show that simulated distance modulus errors are improved by factors of 2.7 and 3.5 by adding J, and JHK_s to $UBVRI$ data, respectively, a result recently confirmed with a more sophisticated analysis by Mandel et al. 2011 (See §6.1.2). Reducing systematics due to reddening are crucial to future space-based SN surveys which will have data sets large enough to avoid limitations from sample size. In that case, improving the constraints on cosmological parameters with SN Ia will be limited by systematics. We argue that these systematics can be best addressed by the inclusion of NIR SN Ia data, with low-redshift PAIRITEL data forming an important part of the nearby NIR calibration sample for cosmology.

6.1.2 Mandel, Wood-Vasey, Friedman, & Kirshner 2009

"TYPE Ia SUPERNOVA LIGHT-CURVE INFERENCE: HIERARCHICAL BAYESIAN ANALYSIS IN THE NEAR-INFRARED"

ApJ, 704:629-651, 2009 October 10

In addition, Dr. Kaisey Mandel has used a subset of my thesis data (Wood-Vasey & Friedman et al. 2008) along with data from the literature to spearhead the

development of novel sophisticated statistical methods to mathematically model NIR LCs within a Hierarchical Bayesian framework (Mandel et al. 2009) and to combine NIR and optical SN Ia LCs to obtain estimates of extinction by dust and distances to the SN Ia host galaxies that are more precise and more accurate than with optical data alone (Mandel et al. 2011). In WV08, we suggested that using information from the NIR and optical light-curve shapes — especially in the J-band — might result in even smaller scatter and better distance determinations (Wood-Vasey et al. 2008). This suggestion has been confirmed by the work of Mandel et al. 2009, where Mandel and collaborators employ a novel hierarchical Bayesian framework to model NIR only data and explicitly account for variations in the J-band LC shape. With this approach, Mandel et al. 2009 constrain the marginal variances of the NIR SN Ia peak absolute magnitudes to 0.17 ± 0.03, 0.11 ± 0.03, and 0.19 ± 0.04, for the JHK_s bands, respectively (See Fig. 9 of M09). In particular, variance in the peak H-band absolute magnitudes of 0.11 mag is smaller than in any known method using only optical data. Recent work by Kattner et al. 2012 analyzing 27 CSP NIR LCs also finds evidence for a non-zero decline rate relation between the peak absolute JH-maxima (and perhaps the Y-band maximum) to the decline rate parameter Δm_{15} (Phillips 1993). This further confirms the results of Mandel et al. 2009 who also find variation in the intrinsic J-band LC properties.

In WV08, following work by Krisciunas et al. 2004a, 2007 we also suggested that accounting for dust absorption as fit from the optical to the infrared, might provide additional information for correcting NIR LCs and improving distance determinations. To investigate this with modern data sets, Mandel et al. 2011 (hereafter M11) present a sophisticated hierarchical Bayesian model and implement

the novel BayeSN Markov Chain Monte Carlo computational method to estimate distances (see Fig. 16 of M11) and dust properties (see Fig. 3 of M11) of SN Ia using optical and NIR light curve data, further improving reddening estimates and distance errors (see Figs 17-18 of M11). After correcting for NIR LC shape and reddening, M11 also find a minuscule RMS dispersion of ~ 0.11 mag ($\sim 5\%$ in distance) in the combined NIR and optical SN Ia low-z Hubble diagram, compared to ~ 0.15 mag ($\sim 7\%$ in distance) with optical data alone using BayeSN, equivalent to a $\sim 60\%$ improvement in the predictive precision (the inverse variance)[1] of individual distance estimates by including JHK_s NIR data compared to optical $BVRI$ data alone using BayeSN. Unlike previous approaches, the BayeSN method of M11 models the full covariance structure of the observed data set, exploiting multiple informative correlations between light curve properties across all available bandpasses and phases to standardize SN Ia distances. For example, the MLCS2k2 method of Jha et al. 2007 found an intrinsic RMS Hubble diagram dispersion of ~ 0.18 mag ($\sim 8\%$ in distance) from optical SN Ia data alone, considerably worse than the 0.15 mag found with BayeSN by M11 using only optical data. In other words, BayeSN provides distances estimates with a predictive precision a factor of ~ 1.4 times better $[(0.18/0.15)^2]$ than MLCS using comparable optical only data sets, whereas BayeSN provides distance estimates with a predictive precision a factor of ~ 2.7 times better $[(0.18/0.11)^2]$ than MLCS by also including NIR data.

In summary, Mandel et al. 2011 demonstrates a factor of 1.8 improvement in the predictive precision of individual distance estimates with BayeSN by including

[1]The inverse variance of 0.11 mag and 0.15 mag is given by $(0.11/0.15)^2 = 0.55 \sim 60\%$, or a factor of $(0.15/0.11)^2 = 1.85$.

JHK_s NIR data compared to optical $BVRI$ data alone. BayeSN fares even better when compared to MLCS, which can only deal with optical $UBVRI$ data. Compared to MLCS with only optical data BayeSN yields a factor of 1.4 improvement in the precision of distance estimates when BayeSN uses only optical data, and a factor of 2.7 when BayeSN also includes JHK_s data.

6.2 Thesis Results

The major scientific product of this thesis at the time of writing is the CfAIR2 data set itself. Revised photometry for 20 of the 21 previously published SN Ia (with the exception of SN 2005cf; see §4.3.1) also significantly reduces the systematic photometric uncertainties in the WV08 data by implementing a greatly improved data reduction and photometry pipeline (See §3–§4) and applying it in a homogeneous way to all 104 SN Ia in the CfAIR2 data set (Friedman et al. 2012 *in preparation*). These pipeline improvements have resulted in increased agreement with the CfAIR2 data for the set of overlap objects also observed by the CSP (§4.3.2), which provide a crucial external consistency check of our photometry. The most important improvements to our pipeline since WV08 include better noise maps (§ 3.2), rejection of bad images (§ 3.3), a method to correct underestimates of the uncertainty of DoPHOT photometry on the un-subtracted images (§ 4.1.2), and especially improvements to our host galaxy subtraction process where we employ the NNT method, which fares better for PAIRITEL data than the NN2 method used in WV08 (§3.4, §4.2.2). We have also applied great effort toward improving the computational implementation of our mosaicking pipeline (§3.1) and photometry

pipelines (§3.5.1). Photometry for all SN Ia can effectively be run overnight using the computational power of the Harvard FAS Odyssey Cluster, a process which would have taken several weeks using the computational infrastructure we had in place as of the writing of Wood-Vasey et al. 2008.

The limited analysis presented in this thesis — which we review here — will be augmented by future work, to be presented in Friedman et al. 2012 *in preparation*. In §5.1, we constructed fiducial NIR templates of normal SN Ia from our sample, excluding 11 known peculiar SN Ia from CfAIR2 that exhibit a suppressed or absent second NIR LC peak, including, SN 2005bl, SN 2005hk, SN 2005ke, SN 2007if, SN 2008A, SN 2008ae, SN 2008ha, SN 2009dc, SN 2011aa, SN 2011ay, and SN 2011de. By constructing these rest-frame JHK_s templates from the available sample of ~ 200 NIR SN Ia LCs — nearly half of which come from the CfAIR2 data set — we considerably augment the sampling of the template presented in WV08, especially at rest-frame phases > 30 days. The WV08 template itself was constructed using only 41 SN Ia, nearly half of which were also published in WV08. The new NIR SN Ia photometric observations presented in CfAIR2 have the potential to confirm and strengthen the statistical power of our previous results (Wood-Vasey & Friedman et al. 2008,Mandel, Wood-Vasey, Friedman, & Kirshner 2009) using the WV08 data set, and allow us to extend our NIR LC templates to a greater phase range with denser sampling on shorter timescales (See §5.1).

In §5.2 we present a simple method to fit NIR LCs with polynomials, which can account for the double peaked structure of NIR LCs that exceed the complexity of the optical $UBVR$ LCs, which typically show only a single peak, which begins to present a double peaked structure in the I band, becoming most prominent in J

and significant in YHK. We use these LC fits to derive parameters to characterize the properties of the nearby sample of NIR SN Ia, presenting the observed apparent magnitudes in JHK_s at $t_{B\max}$, the time of B-band maximum light in Table 5.1. In §5.2.1 we use these LC fits to constrain the typical phases of the prominent NIR features with respect to $t_{B\max}$, including the time of the first NIR peak ($\bar{t_1}$), the trough between peaks ($\bar{t_t}$), and second peak ($\bar{t_2}$). Confirming previous studies (e.g. Krisciunas et al. 2009), we find very narrow distributions between the first NIR peaks in JHK_s and $t_{B\max}$ of $\bar{t_1} = t_1 - t_{B\max} = -3.07 \pm 0.05$, -4.09 ± 0.09, and 2.04 ± 0.04, in JHK_s respectively with larger uncertainties for the relations between $t_{B\max}$ and the NIR trough and second peak (see Table 5.4). These relations allow us to include SN Ia with only NIR data in the analysis, and provides a tool to distinguish peculiar SN Ia from normal SN Ia from LC properties alone even in the absence of spectroscopy. These results will be useful for future space based and ground based studies where it may not be possible to obtain spectroscopy for all SN Ia, especially space based work at $z > 1.7$ where low signal to noise spectra make it difficult to spectroscopically classify SN Ia even with space telescopes like HST (Aldering 2004; Lauer 2005).

6.3 Future Work

We briefly discuss future work planned for Friedman et al. 2012 *in preparation*, the journal paper which will publish the data presented in this thesis and include more extensive analysis of the data.

"CfAIR2: 104 Type Ia Supernova Near-Infrared Light Curves from PAIRITEL"

To be submitted to the Astrophysical Journal

6.3.1 MLCS2k2 Parameters from Optical SN Ia Data

We have run MLCS2k2.v007 fits (Jha et al. 2007) for the optical data corresponding to the CfAIR2 objects along with other nearby SN Ia that have both optical and NIR data available. We thus limit our analysis to the set of nearby SN Ia with NIR data and potentially some optical data, excluding SN Ia for which there only exist optical data. These data will be included in the analysis in future work (Mandel et al. 2012 *in preparation*). We first use MLCS2k2.v007 fits (MLCS; Jha et al. 2007) to estimate $t_{B\mathrm{max}}$ for all SN Ia with available optical data. See §5.2.1 for a discussion of how we estimate $t_{B\mathrm{max}}$ for cases where we have only NIR data. We first fix $R_V = 3.1$ and used MLCS to estimate $t_{B\mathrm{max}}$. We then set this $t_{B\mathrm{max}}$ as the initial guess for another round where we additionally use MLCS to fit for R_V. This process is computationally intensive because optical data does not constrain R_V very well and some fits do not converge. Nevertheless the purpose of fitting for R_V using optical data alone is to eventually establish the improvement in the accuracy and

precision of R_V estimates when NIR data is also incorporated. Mandel et al. 2011 have already used the BayeSN method to demonstrate the improvement in estimates of A_V, R_V and distance modulus μ when including NIR SN Ia data compared to optical data alone. Following M11, Friedman et al. 2012 *in preparation* will present a method for estimating extinction and dust properties for SN Ia with optical and NIR data, including the additional 104 new NIR SN Ia LCs in CfAIR2. Our aim in Friedman et al. 2012 *in preparation* is to use a less sophisticated approach than MLCS or BayeSN to estimate A_V, R_V, μ (σ_{Av}, σ_{Rv}, σ_μ) with NIR and optical data and compare it to both MLCS fits with optical only data and BayeSN with NIR and optical data. We plan to compare our method for determining distances by combining optical and NIR data to the distances derived from MLCS2k2 using optical data alone (Jha et al. 2007). We restrict our attention to the MLCS2k2 LC fitter for simplicity, although it would also be reasonable to compare our method to SALT (Guy et al. 2005; Astier et al. 2006; Guy et al. 2007). Our hope is that this approach, which we discuss in §6.3.2 will be conceptually simpler than either MLCS or BayeSN, while producing approximately similar results, which can serve as a useful independent check of the more advanced methods.

We plan to fit for the peak absolute JHK_s magnitudes for every SN Ia in our sample and plot these versus the standard optical light-curve shape parameters (e.g. MLCS Δ: Jha et al. 2007; $\Delta m_{15}(B)$: Phillips 1993). This will complement recent work by Kattner et al. 2012, who perform a similar analysis for 27 SN Ia observed by the CSP, finding suggestive evidence for a correlation between NIR peak absolute magnitudes and optical LC shape, contrary to previous earlier analyses with smaller data sets (Krisciunas et al. 2004a; Wood-Vasey et al. 2008). With distance estimates

for each SN, in Friedman et al. 2012 *in preparation*, we plan to produce Hubble diagrams using NIR only, optical only, and optical plus NIR data, to examine the variation of the dispersion in the Hubble diagram. Future work will also include more refined K-corrections for the NIR photometry based on the available NIR spectral sample (e.g Hsiao et al. 2007; Marion et al. 2009) currently being analyzed by Boldt et al. 2012 *in preparation* (G.H. Marion, L. Boldt, and M. Stritzinger — private communication).

6.3.2 Optical - NIR Colors and Extinction Estimates

Combining optical and NIR data can be used to generate optical-NIR colors (see Figures 6.1–6.2) to estimate extinction and host galaxy dust properties (e.g. Mandel et al. 2011). In astronomy, objects that are "reddened" by dust appear redder because shorter wavelength bluer light has been absorbed or scattered away by dust along the line of sight.[2] For SN Ia, we estimate the actual amount of dust dimming by measuring how much the SN color has been reddened by dust relative to the typical un-reddened SN Ia color in the absence of dust. There is additional uncertainty because SN Ia do have some intrinsic color variation. As such, when we observe a SN Ia light curve that is reddened, we do not know how much of its reddening is because of dust in the host galaxy or because it is intrinsically redder. Since both reddening and dimming of light systematically affect our ability to measure accurate distances to SN Ia, resolving this degeneracy between reddening

[2]For example, the sun appears redder at sunset than at noon because its light must pass through a larger column of "dusty" atmosphere at sunset. Astronomers use the word "color" to denote the difference in brightness at two different wavelengths, for example, the optical V-band and the NIR J-band.

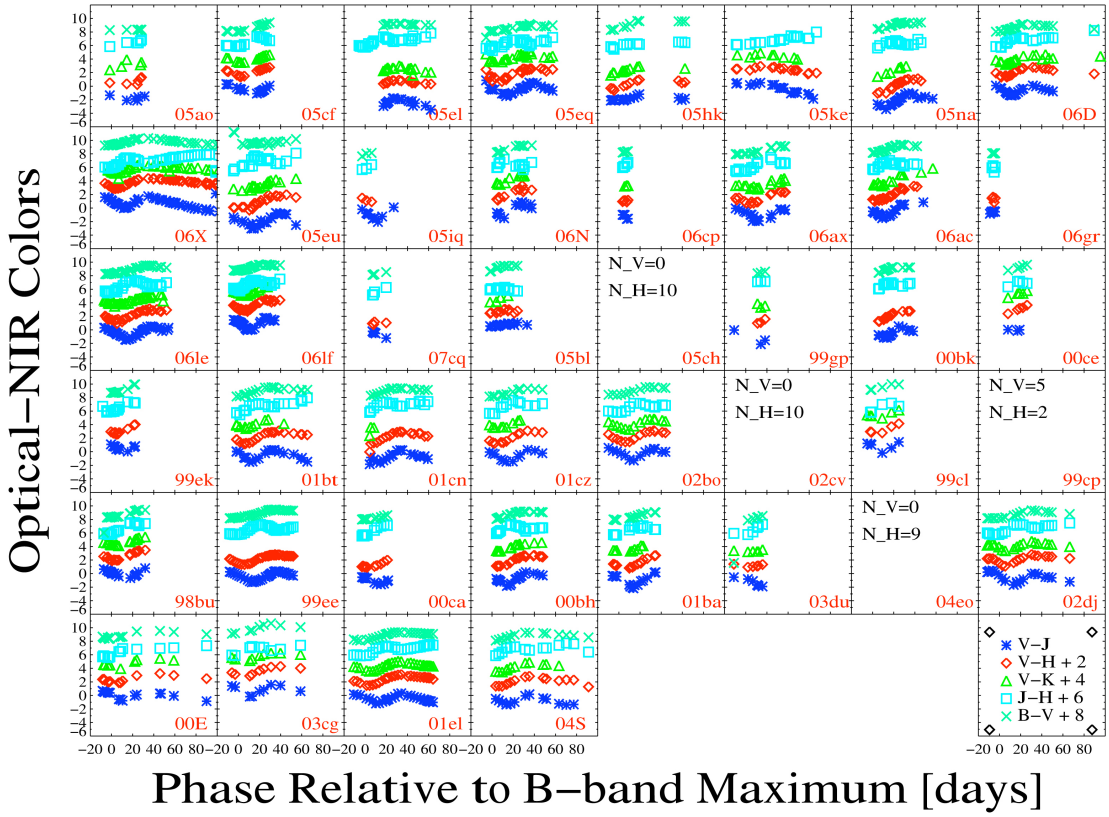

Figure 6.1.— V-JHK Colors for 40 NIR SN Ia

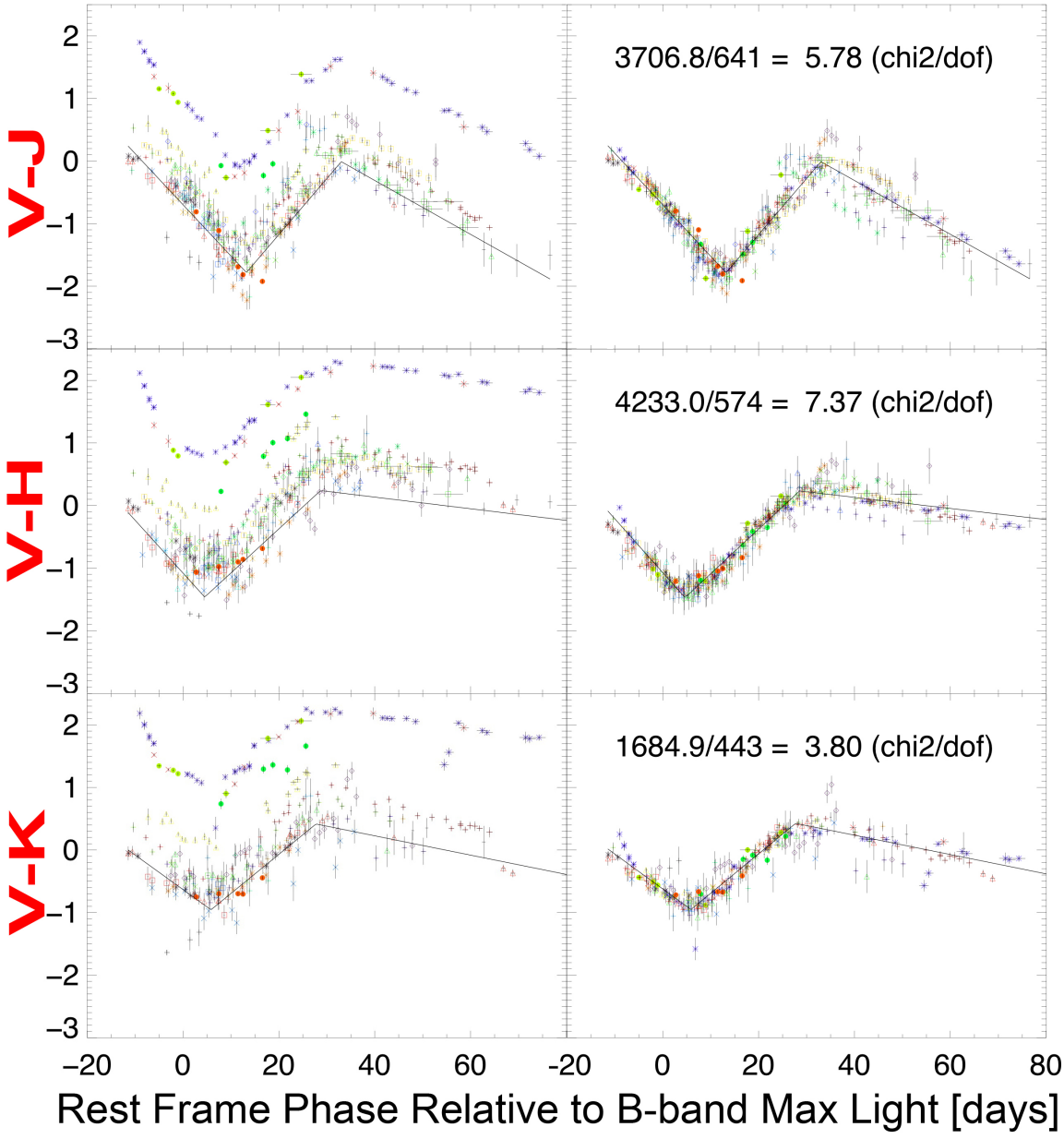

Figure 6.2.— V-JHK Colors for 39 NIR SN Ia Corrected For Extinction.

The color curves plot color versus time for 39 SN Ia with available optical and NIR data. In the left panels, highly reddened objects are displaced more vertically from the black line, which represents the assumed fiducial color curve of a typical SN Ia in the absence of reddening by dust. The right panels show SN Ia color curves after preliminary correction for dimming by dust.

due to dimming by host galaxy dust and intrinsic color variation is crucial to improving our cosmological inferences with SN Ia. The goal is to estimate the mean un-reddened intrinsic color and intrinsic color variance of the SN population as a function of time and then estimate the dust dimming and host galaxy dust properties separately for each SN. This is what is meant by disentangling dust dimming and intrinsic color variation.

Following Mandel et al. 2009, 2011, in Friedman et al. 2012 *in preparation* (or in future papers beyond that), I plan to develop a color curve model using the observed optical and NIR color data for the CfAIR2 set of SN Ia. Mandel et al. 2011 have already identified a subset of SN Ia from WV08 and the literature that appear to have suffered from little to no reddening. This subset consists of $\sim$ 20–40 SN Ia, depending on assumptions regarding the uncertainties of the Mandel et al. 2011 A_V estimates. Using this subset, in Friedman et al. 2012 *in preparation*, we plan to construct an un-reddened NIR intrinsic color template using the same template generation method employed in §5.1 (See Figure 5.6). Given this intrinsic color template, and uncertainties which quantify the intrinsic color variation at each epoch, one can use fits to the NIR LCs described in §5.2 along with optical LC fits using this method (or optical fits from MLCs) to estimate optical-NIR color excesses for each SN Ia. These color excesses, combined with a standard redding law (e.g. CCM Cardelli et al. 1989) allows one to estimate the extinction A_V and the host galaxy dust parameter R_V simultaneously using color excess estimates and uncertainties derived for all available optical and NIR data. Mandel et al. 2011 use all data simultaneously to estimate the extinction for each object without assuming a specific subset of apparently un-reddened objects to estimate the intrinsic NIR

SN Ia colors as is done in standard methods employed in previous work (Phillips et al. 1999; Krisciunas et al. 2007; Folatelli et al. 2010). While the Mandel et al. 2011 BayeSN framework likely leads to the best possible estimates of extinction and dust, it comes at the cost of considerable conceptual and computational complexity. This motivates the deployment of an approximate method which may yield comparable results after incorporating the information about the intrinsic populations of SN Ia and host galaxy dust and extinction already estimated with considerable skill and effort by Mandel et al. 2011.

Given the population parameters of the distributions of extinction values A_V and dust properties R_V already derived by Mandel et al. 2011 using BayeSN, and the intrinsic colors estimated with the method described here, we will have estimates of the population parameters (or hyperparameters) describing the intrinsic SN Ia population. Given these population parameters, we can place informed priors on the values of extinction and dust for individual SN Ia in order to help constrain the estimates of those parameters, even in cases where data in certain bandpasses and phase ranges are absent. Overall, given the observed light curves, a mean LC template, and a LC fitting model procedure, we can estimate colors from optical and NIR data. Given a mean un-reddened intrinsic color template, we can further estimate color excesses in each color for each SN Ia. Given the color excess estimates and uncertainties, along with the population parameters for dust and extinction, we finally can estimate A_V and R_V for individual SN Ia. These are the most important steps toward obtaining distance estimates for individual SN Ia

We have already provided a subset of the CfAIR2 data set to K. Mandel to combine with available optical and NIR data to fit with BayeSN. Eventually, we will

provide K. Mandel with the entire CfAIR2 data set which can be used to derive dust estimates and distance estimates with the combined low-redshift OIR sample (Mandel et al. 2012 *in preparation*). Eventually, we hope to use BayeSN to combine the existing low-redshift and high-redshift SN Ia samples with Optical and NIR data in order to obtain cosmological inferences and dark energy constraints that for the first time take full advantage of the existing NIR data set, a large portion of which is presented in this thesis as the CfAIR2 data set.

6.3.3 Future Directions for NIR SN Ia Observations

With our ongoing PAIRITEL SN program at the CfA adding 10–15 SN Ia per year, the NIR low-z SN Ia training set of CfAIR2 and future CfA data will continue to provide an excellent, homogeneous set to study the NIR properties of nearby SN Ia. Combining the CfAIR2 and future CfA PAIRITEL data with a comparable NIR data set of ~ 75 SN Ia observed by the Carnegie Supernova Project (CSP) and other data including $\sim$ 20–30 objects from the literature (e.g. Krisciunas et al. 2004a and references therein), will provide a growing low-z NIR SN Ia sample (See §2.2)

This growing NIR SN Ia data set will help improve the utility of SN Ia as standard candles and cosmological distance indicators. It will help us better constrain the parent populations of host galaxy dust and extinction, revealing a fuller understanding of the properties of dust in external galaxies, and allowing us to disentangle SN Ia reddening from dust and intrinsic color variation (Mandel et al. 2011). Improved distance measurements using NIR data will also allow us to map the local velocity flow independent of cosmic expansion to understand how peculiar

velocities in the nearby universe affect our cosmological inferences from SN Ia data (Turnbull et al. 2011; Davis et al. 2011). NIR data should also provide the best SN Ia set with which to augment existing optical measurements of the Hubble Constant (Riess et al. 2011). Future samples might also achieve improved distance estimates by accounting for correlations between NIR photometric properties and spectroscopic variation, similar to what has been attempted at optical wavelengths (Bailey et al. 2009; Blondin et al. 2011). Future work might also look for evidence for correlations between NIR LC features and host-galaxy properties, which have been shown to correlate with Hubble diagram residuals for SN Ia observed at optical wavelengths (Kelly et al. 2010). Other non-cosmological applications of NIR SN Ia data include testing physical models of exploding white dwarf stars (e.g Kasen 2006). We hope to continue expanding the sample of SN in the NIR to study their NIR emission properties, construct bolometric LCs, and compare optical, UV, and NIR LCs. Early time photometry will reveal insights into explosion mechanisms, progenitor properties, the circumstellar medium, and companion interaction.

Our work emphasizing the intrinsically standard and relatively dust insensitive nature of NIR SN Ia has further promoted the rest-frame NIR as a promising wavelength range for future space based cosmological studies of SN Ia and dark energy, where reducing the systematic uncertainties from dust extinction and intrinsic color variation becomes more important than simply increasing the statistical power of the sample by observing additional SN Ia (e.g. Gehrels 2010; Beaulieu et al. 2010; Astier et al. 2011). Although ground-based NIR data can be obtained for low redshift objects, limited atmospheric transmission windows effectively require that rest-frame NIR observations of high-z SN Ia be done from space (see Figure 6.3). Currently,

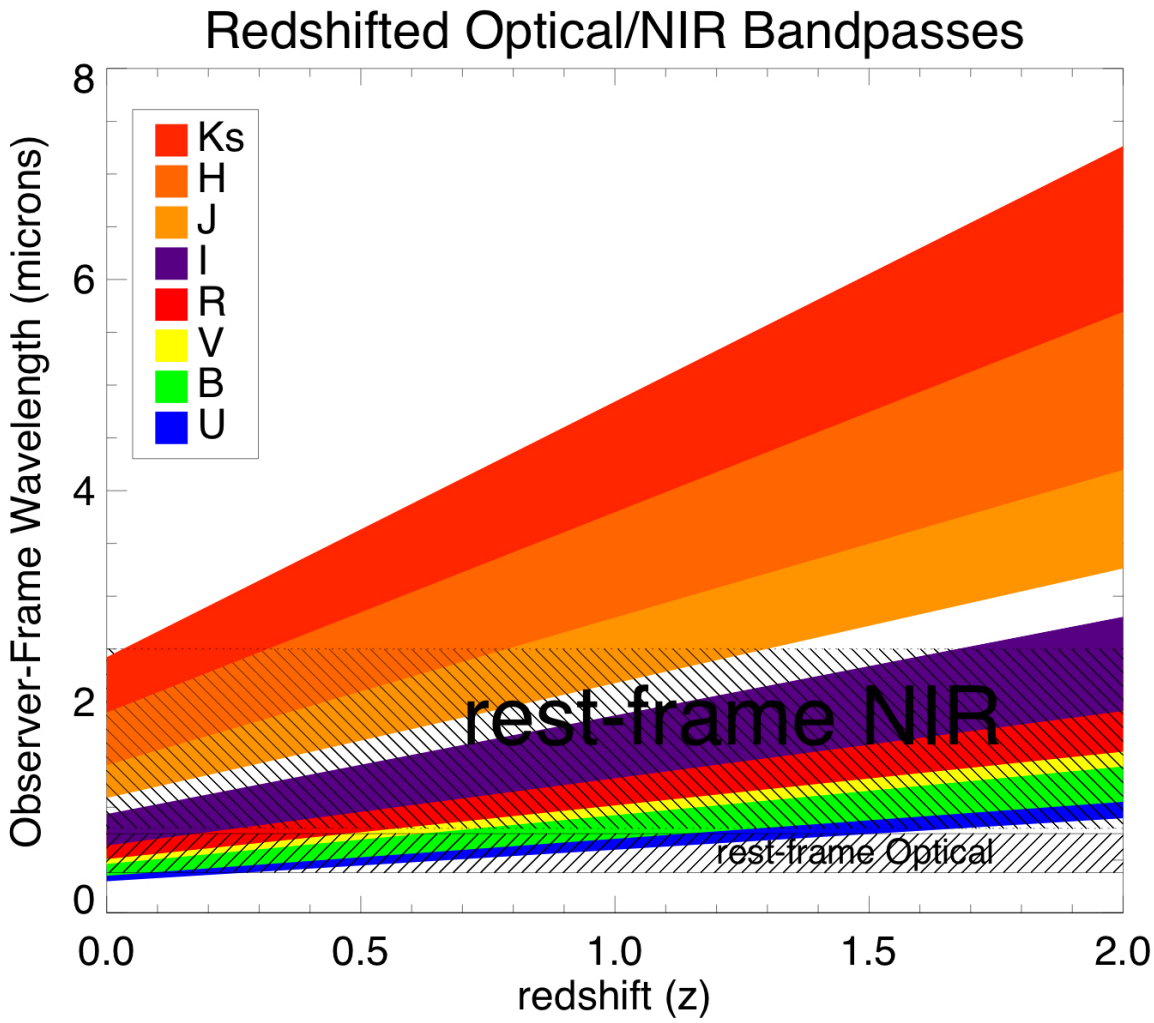

Figure 6.3.— Redshifted Optical and NIR Bandpasses

Space-based detectors designed to detect rest-frame NIR JHK_s light will require wavelength coverage out 2.4–5.0 μm, for example, in order to detect rest-frame H-band at $z \sim 0.5$–2 . Detectors sensitive out to 1.7 μm, such as some of the original WFIRST JDEM mission concepts (e.g. SNAP Aldering 2004, DESTINY: Lauer 2005) would only detect rest-frame H-band light (1.6 μm) out to $z \sim 0.1$. Detectors need to extend further into the infrared in order to maximize the utility of rest-frame NIR data. Measuring w to 1% precision with SN Ia may require building such a detector, which would almost certainly require cryogenics beyond 2 microns (D. Benford — private communication). However, the science gains from such an approach will need to be balanced against increased, potentially cost prohibitive, mission expenses incurred, for example, if cryogenics or advanced detector technology that does not currently exist would be required.

rest-frame SN Ia Hubble diagrams of high-z SN Ia have yet to be constructed beyond the I band (Freedman 2005; Nobili et al. 2005; Freedman et al. 2009), with limited studies of SN Ia and their host galaxies conducted in the mid-infrared with Spitzer (Chary et al. 2005; Gerardy et al. 2007).

Along with current and future NIR SN Ia data, the nearby CfAIR2 data set presented in this thesis will provide a crucial low-z anchor for future space missions capable of high-z SN Ia cosmology in the NIR, including WFIRST (Wide-Field Infrared Survey Telescope; a candidate for which includes the NASA/DOE Joint Dark Energy Mission; JDEM Gehrels 2010), The European Space Agency's EUCLID mission (Beaulieu et al. 2010), and the NASA James Webb Space Telescope (JWST; Clampin 2011). We specifically hope to influence the design of the WFIRST detector to include the rest-frame NIR towards as long a wavelength as possible (ideally 2–5 microns), to ensure that we measure the most precise and accurate galactic distances utilizing the standard nature of rest-frame SN Ia in the JHK_s bands. For example, the SNAP (Aldering 2004) and DESTINY satellites (Lauer 2005) — early candidates for the NASA/DOE Joint Dark Energy Mission (JDEM) mission, before it was changed by NASA to WFIRST (Wide-Field Infrared Survey Telescope) — were designed with detectors sensitive out to 1.7 μm, which would only detect rest-frame H-band light (1.6 μm) out to $z \sim 0.1$. Only a detector capable of observing rest-frame H-band at $z \sim 0.5$–2 could take full advantage of Nature's gift to us of a superb standard candle at the rest frame H-band (see Figure 6.3). Such a detector would require sensitivity from 2.4–5.0 μm. In addition to JWST, which will cover the rest-frame NIR, the astronomical community should strongly consider how to optimize WFIRST and other space missions for the rest-frame NIR.

Until space based NIR observations become feasible with next generation instruments beyond HST, continuing to observe SN Ia in the NIR with ground-based observatories like PAIRITEL is one of the best and most straightforward ways to reduce the most troubling fundamental uncertainties in SN Ia cosmology to further improve the utility of SN Ia as standard candles and cosmological distance indicators. Ultimately, my thesis data set of relatively nearby, low-redshift, NIR SN Ia will help lay the groundwork for next generation ground-based cosmology projects and space missions that observe very distant SN Ia at optical and NIR wavelengths to provide increasingly precise and accurate constraints on dark energy, helping to test whether it varies in time and elucidate the nature of one of the most mysterious discoveries in modern astrophysics and cosmology.

Chapter 7

Appendix

7.1 Estimating the Noise in Each Mosaic Pixel

We estimate the Noise per pixel (in e^-) corresponding to each mosaic pixel with:

$$\text{Noise/pixel} = C \times \sqrt{\frac{1}{N}\left[G \times S + n_{\rm pix}(1 + \frac{n_{\rm pix}}{n_B})\left(G \times B + R^2 + G^2\sigma_f^2\right)\right]} \qquad (7.1)$$

where N is the number of raw images used to construct the mosaic, G is the mosaic GAIN in units of e^-/ADU, S is the number of source counts per pixel in the mosaic (in ADU), B is the number of sky and dark current background counts per pixel in the skark mosaic (in ADU), R is the readnoise (of 40 e^{-2}), $n_{\rm pix} \equiv 1$ is the number of pixels under consideration for the noise estimate, n_B is the number of pixels used to estimate the skark background for each mosaic pixel (typically $\sim 7 - 15$), and $\sigma_f = 0.289$ is a factor that accounts for the errors from analog to digital conversion for our detector. Equation 7.1 is adapted from the Merline & Howell 1995 version of the CCD Equation as presented in section 4.4 of the Handbook of CCD photometry (Howell 2006). Equation 7.1 is an estimate which does not explicitly model noise from other know sources, including confusion noise, fringing, detector non-linearity, and systematic over or underestimation of the sky brightness, especially in the presence of large host galaxies. As such, the quantity inside the square root in Equation 7.1 underestimates the true noise by some factor C. We determine this correction factor C ∼2.9–3.2 empirically for each bandpass using the error normalized residuals of selected standard star photometry (see §4.1.2). Photometric errors for the SN LCs are multiplied by C to account for the underestimate of the noise which would result from setting $C = 1$ in Equation 7.1. The signal-to-noise ratio SNR per pixel is given by $G \times S$ divided by Equation 7.1. PAIRITEL mosaics are median combined by SWarp, so the mosaic GAIN G is not the same as the 2MASS camera gain (which

varies by bandpass), but is scaled by a factor proportional to N — the number of raw images coadded into the mosaic — to keep the product $G \times S$ (the total number of signal photons/e^- detected per pixel) invariant.

7.2 Coordinates for Forced DoPHOT photometry

Photometry is extracted from either the un-subtracted or the subtracted images by forcing DoPHOT to measure the PSF-weighted flux of the object at a fixed position in pixel coordinates. This position was determined by several methods depending on the quantity and quality of the images and difference images available (see §3.3, §3.4), each of which dramatically improved the quality of the SN LC compared to performing forced DoPHOT photometry the approximate position from the IAUC/CBET discovery coordinates (See Figure 7.1). Each of these SN centroid estimation methods typically yields better than $\sim 0.2''$ SN astrometry. We found no systematic bias from errors in PAIRITEL forced DoPHOT photometry as long as the estimated SN centroid is within $\lesssim 0.5''$ of the true SN centroid (see §4.2.5).

Method 1

For well isolated SN, for which forced DoPHOT photometry on the un-subtracted images is sufficient, computing the centroided pixel coordinates of the SN using the average centroid from the PAIRITEL JHK_s-band SWarped images was also sufficient. In some cases, we used only the J-band images, due to poorer image quality resulting from greater sky variance in the H or K images.

Method 2

For some SN, the NIR image quality or quantity was insufficient to compute an accurate centroid, so we used the CfA optical images for the same SN where available (Hicken et al. 2012 *in preparation*) to compute the celestial coordinates of the SN centroid, averaged over all optical images of the same SN. The optical WCS was used to convert the SN pixel centroid to celestial coordinates (RA, DEC). These celestial coordinates are then converted to pixel coordinates in the NIR mosaics using the WCS information in the NIR mosaic header. CfA optical images using the FLWO 1.2-m telescope have higher SNR than the NIR images, have a smaller plate scale than the PAIRITEL NIR images ($0.694''$/pixel vs. $2''$/pixel), and are single images rather than mosaics. which results in more accurate centroids of the celestial coordinates than Method 1. Provided that the optical and NIR WCS information is accurate, coordinates determined with Method 2 are comparable to or more accurate than those determined with Method 2. Both methods give comparable results for bright, well isolated SN.

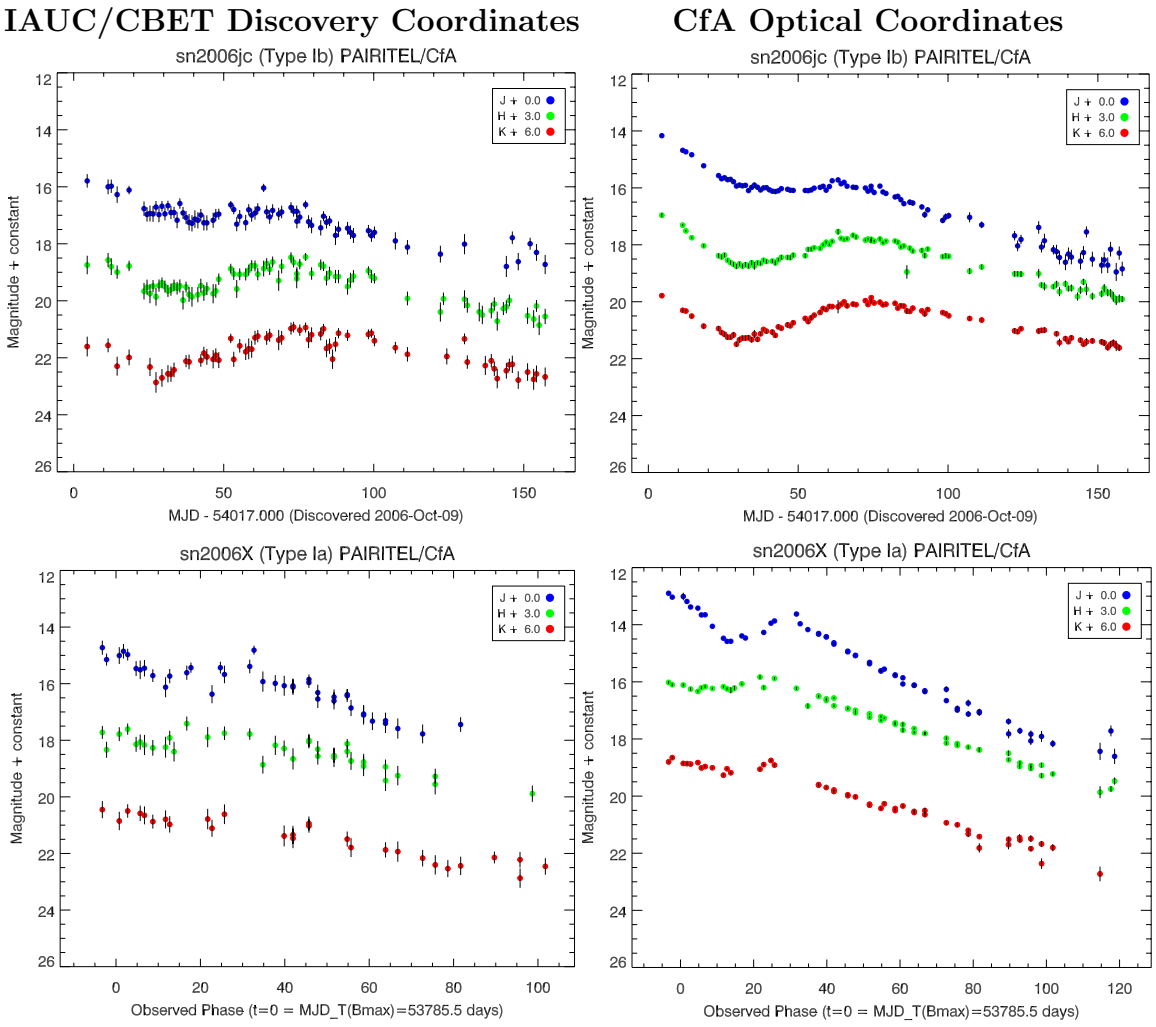

Figure 7.1.— Astrometry Improves Photometry

Example PAIRITEL LCs for SN Ib SN 2006jc and SN Ia SN 2006X, where DoPHOT photometry was performed at forced pixel coordinates in the un-subtracted images.

(**Left**) The forced pixel coordinates for DoPHOT were determined from the optical discovery images as reported in the relevant IAUC/CBET discovery notices. Since these coordinates are approximate, accurate only to within several arcseconds, they can lead to excess scatter in the LCs if the forced DoPHOT pixel position is not perfectly centered on the SN. We quantify this in §4.2.5.

(**Right**) The forced pixel coordinates for DoPHOT were determined by computing average centroids using CfA optical images, using Method 2 described in §7.2. These more accurate coordinates give LCs with smaller scatter because we are no longer cutting off the DoPHOT PSF of the SN or including nearby galaxy light unnecessarily due to inaccurate forced photometry coordinates.

Method 3

For SN near or embedded in the host galaxy, computing centroids using the un-subtracted SWarped NIR or optical images would lead to a centroid biased in the direction of the increasing galaxy flux gradient. This bias is worse for fainter SN with brightness comparable to or less than the host galaxy flux at their position. For these cases, the SN coordinates position was determined by taking the photometric detections of the object in the J-band difference images that had a signal-to-noise ratio > 5. In principle, computing the forced SN coordinates with Method 3 makes the most sense and is simplest, so we use method 3 for every SN where the subtractions are of sufficient quality. In practice, the poor quality of some subtractions often made methods 1 or 2 preferable to method 3, but method 3 is the default SN centroid method we use for over $\sim 95\%$ of the CfAIR2 data set.

7.3 Testing PAIRITEL Photometric Precision

For each 2MASS standard star, we compute the weighted mean PAIRITEL magnitude for all N SN Ia LC images containing that star as

$$\tilde{m_{\rm P}} = \frac{\Sigma m_{{\rm P}i} w_i}{\Sigma w_i} \tag{7.2}$$

with weights $w_i = 1/\sigma^2_{{\rm do},i}$, where $\sigma_{{\rm do},i}$ are the nightly DoPHOT magnitude uncertainties and $i = \{1, 2, \ldots, N\}$ indexes the N nights of the standard star LC that are implicitly summed over for every summation Σ. We interpret the error on the weighted mean of the N PAIRITEL photometric measurements to be the uncertainty in the measurement of the mean PAIRITEL magnitude for that 2MASS

star, computed as:

$$\sigma_{\tilde{m_{\rm P}}} = \sqrt{\frac{1}{\Sigma w_i}} \tag{7.3}$$

Note that in the case where all the DoPHOT uncertainties are the same for each night ($\sigma_{{\rm do},i}$ = constant), the uncertainty reduces to $\sigma_{\tilde{m_{\rm P}}} \rightarrow \bar{\sigma_{\rm P}}/\sqrt{N}$, where $\bar{\sigma_{\rm P}}$ is the sample standard deviation of the magnitude measurements given by $\bar{\sigma_{\rm P}} = \sqrt{(\Sigma(m_{{\rm P}i} - \bar{m_{\rm P}})^2)/(N)}$, and $\bar{m_{\rm P}} = (\Sigma m_{{\rm P}i})/N$ is the unweighted sample mean of the magnitude measurements,

The residuals are given by $r_{\rm P} = m_{\rm do} - \tilde{m_{\rm P}}$, where $m_{\rm do}$ is the PAIRITEL DoPHOT magnitude of that standard star for each night and $\tilde{m_{\rm P}}$ is the mean PAIRITEL magnitude for each standard star computed for N DoPHOT measurements of that star over N nights of the SN Ia LC (see Table 4.2)[1]. The uncertainties on the residuals are given by $\sigma_{r_{\rm P}} = \sqrt{\sigma_{\rm do}^2 + \sigma_{\tilde{m_{\rm P}}}^2} = \sqrt{\sigma_{\rm do}^2 + \tilde{\sigma_{\rm P}}^2/N}$, where $\sigma_{\rm do}$ is the photometric uncertainty for each nightly standard star measurement as estimated by DoPHOT using our input noise mosaics and $\sigma_{\tilde{m_{\rm P}}} = \tilde{\sigma_{\rm P}}/\sqrt{N}$ is the uncertainty of the mean PAIRITEL magnitude for that 2MASS star (see Table 4.2)[2].

We then compute error normalized residuals as $\hat{r_{\rm P}} = r_{\rm P}/\sigma_{r_{\rm P}}$. If $\sigma_{r_{\rm P}}$ were estimated correctly, we would expect the standard deviation of the error normalized residuals to be $\sigma_{\hat{r_{\rm P}}} \approx 1$, which is equivalent to the statement that the data is well

[1]While the 2MASS catalog is used to estimate the photometric zero point for each image, rather than using the residuals of PAIRITEL photometry from the mean 2MASS catalog magnitude, for this internal consistency check we use the mean PAIRITEL magnitude as the reference because we are testing the photometric uncertainties for PAIRITEL, not 2MASS. Defining the residuals with respect to the 2MASS catalog magnitude will be done in §4.1.3, where we test for any systematic offset between PAIRITEL and 2MASS.

[2]We assume no covariance between $\sigma_{\rm do}$ and $\sigma_{\tilde{m_{\rm P}}}$ since the latter is the standard deviation of the N PAIRITEL magnitude measurements, which does not depend on $\sigma_{\rm do}$.

fit by a model of constant standard star brightness (a mean residual of zero) with reduced $\chi^2/\mathrm{doF} = \chi^2/(N-1) \sim 1$ (See Chapter 15 of Press 2002). If $\sigma_{\hat{r_{\mathrm{P}}}} > 1$, then we have underestimated the uncertainties of the residuals. We assume here that the uncertainty on the *mean* PAIRITEL measurement of each 2MASS star is correctly estimated and that any uncertainty underestimate comes from the nightly DoPHOT point source uncertainties σ_{do}. If we have underestimated our uncertainties on the residuals by a factor of F, we expect to measure $\sigma_{\hat{r_{\mathrm{P}}}} \approx F > 1$. Assuming $\sigma_{\tilde{m_{\mathrm{P}}}}$ is estimated correctly, the true DoPHOT point source uncertainties should be $\tilde{\sigma_{\mathrm{do}}} \approx C \times \sigma_{\mathrm{do}}$, where the DoPHOT uncertainty correction factor C is given by:

$$C \approx F \times \sqrt{1 + \left[\frac{F^2 - 1}{F^2}\right] \left(\frac{\sigma_{\tilde{m_{\mathrm{P}}}}}{\sigma_{\mathrm{do}}}\right)^2} \tag{7.4}$$

where $\sigma_{\tilde{m_{\mathrm{P}}}}$ is the PAIRITEL uncertainty for that standard star over N nights, σ_{do} is the nightly uncorrected DoPHOT uncertainty, and $F \approx \sigma_{\hat{r_{\mathrm{P}}}}$ is the empirically measured standard deviation of the error normalized residuals. In the limit where $\sigma_{\tilde{m_{\mathrm{P}}}} = \tilde{\sigma_{\mathrm{P}}}/\sqrt{N} << \sigma_{\mathrm{do}}$, the correction factor C reduces to $F \approx \sigma_{\hat{r_{\mathrm{P}}}}$.

7.4 Testing PAIRITEL Photometric Accuracy

The 2MASS-PAIRITEL residual for each 2MASS star is given by $r_{\mathrm{2MP}} = \bar{m_{\mathrm{2M}}} - \bar{m_{\mathrm{P}}}$, where $\bar{m_{\mathrm{2M}}}$ is the 2MASS catalog magnitude for each star and $\bar{m_{\mathrm{P}}}$ is the median PAIRITEL magnitude for each 2MASS star. The uncertainties on the residuals are given by $\sigma_{r_{\mathrm{2MP}}} = \sqrt{(\sigma_{\mathrm{2M}})^2 + (\sigma_{\tilde{m_{\mathrm{P}}}})^2}$, where σ_{2M} are the photometric errors of stars from the 2MASS point source catalog (Cutri et al. 2003) and $\sigma_{\tilde{m_{\mathrm{P}}}}$ are the PAIRITEL uncertainties on the weighted mean measurement of each 2MASS star given by Equation 7.3 where the DoPHOT uncertainties have already been corrected for noise

underestimates in the mosaic (§4.1.2), giving corrected weights $w_i = 1/\tilde{\sigma_{\mathrm{do},i}}^2$, where $\tilde{\sigma_{\mathrm{do},i}}$ are the nightly *corrected* DoPHOT magnitude uncertainties $\tilde{\sigma_{\mathrm{do}}} \approx C \times \sigma_{\mathrm{do}}$ (σ_{do} are the uncorrected DoPHOT uncertainties), with C given by Equation 7.4 and $i = \{1, 2, \ldots, N\}$ indexes the N nights of the standard star LC.

The key question is whether $\bar{r_{2\mathrm{MP}}}$, the global weighted mean of the 2MASS - PAIRITEL residuals for all observed 2MASS stars in SN Ia fields is consistent with zero given the uncertainties. This is equivalent to asking whether the following equation is true: $|\bar{r_{2\mathrm{MP}}}| < N_\sigma \times \sigma_{\bar{r_{2\mathrm{MP}}}}$, where $\sigma_{\bar{r_{2\mathrm{MP}}}}$ is the N_σ-σ uncertainty on $\bar{r_{2\mathrm{MP}}}$ given by N_σ times the standard error on the weighted mean over all residuals. In §4.1.3, we show that $|\bar{r_{2\mathrm{MP}}}| < N_\sigma \times \sigma_{\bar{r_{2\mathrm{MP}}}}$ for JHK_s, and quantitatively rule out any major global systematic differences between PAIRITEL and 2MASS photometry, demonstrating in Figure 4.7 that the weighted mean global PAIRITEL-2MASS magnitude residuals are 0.0014 ± 0.0006, 0.0014 ± 0.0007, and -0.0055 ± 0.0007 in JHK_s, respectively, where the uncertainties are the standard errors of the mean. This shows that, when averaging over thousands of stars, PAIRITEL and 2MASS agree to within a few thousandths of a magnitude in JHK_s, with evidence for a small, but statistically significant PAIRITEL-2MASS offsets of ~ 0.001, 0.001, and -0.006 mag in JHK_s, respectively, at the $N_\sigma \sim 2$–3σ level. After correcting for an additional $\sim 10\%$–20% of underestimated uncertainty on the 2MASS-PAIRITEL residuals, in §4.1.3, we show that the number of individual standard star measurements consistent within the 1-σ, 2-σ, and > 3-σ levels are described by Gaussian errors. For example, if $\sim 99\%$ of 2MASS stars have PAIRITEL and 2MASS photometry consistent at the 3-σ or better level, we can be confident that the photometric errors are Gaussian and not systematically over or underestimated.

References

Alard, C. 2000, A&AS, 144, 363

Alard, C., & Lupton, R. H. 1998, ApJ, 503, 325

Albrecht, A., et al. 2006, ArXiv Astrophysics e-prints

Aldering, G. 2004, in Wide-Field Imaging From Space

Allen, S. W., Rapetti, D. A., Schmidt, R. W., Ebeling, H., Morris, R. G., & Fabian, A. C. 2008, MNRAS, 383, 879

Amanullah, R., et al. 2010, ApJ, 716, 712

Astier, P., Guy, J., Pain, R., & Balland, C. 2011, A&A, 525, A7

Astier, P., et al. 2006, A&A, 447, 31

Bailey, S., et al. 2009, A&A, 500, L17

Barris, B. J., Tonry, J. L., Novicki, M. C., & Wood-Vasey, W. M. 2005, AJ, 130, 2272

Barris, B. J., et al. 2004, ApJ, 602, 571

Beaulieu, J. P., et al. 2010, in Astronomical Society of the Pacific Conference Series, Vol. 430, Pathways Towards Habitable Planets, ed. V. Coudé Du Foresto, D. M. Gelino, & I. Ribas, 266

Becker, A. C., Rest, A., Miknaitis, G., Smith, R. C., & Stubbs, C. 2004, in Bulletin of the American Astronomical Society, Vol. 36, American Astronomical Society Meeting Abstracts, 108.12

Becker, A. C., Silvestri, N. M., Owen, R. E., Ivezić, Ž., & Lupton, R. H. 2007, PASP, 119, 1462

Bertin, E., Mellier, Y., Radovich, M., Missonnier, G., Didelon, P., & Morin, B. 2002, in Astronomical Society of the Pacific Conference Series, Vol. 281, Astronomical Data Analysis Software and Systems XI, ed. D. A. Bohlender, D. Durand, & T. H. Handley, 228–+

Blondin, S., Mandel, K. S., & Kirshner, R. P. 2011, A&A, 526, A81

Blondin, S., & Tonry, J. L. 2007, ApJ, 666, 1024

Blondin, S., et al. 2006, AJ, 131, 1648

Bloom, J. S., Caldwell, N., Pahre, M., & Falco, E. E. 2003, Proposal, 1

Bloom, J. S., Starr, D. L., Blake, C. H., Skrutskie, M. F., & Falco, E. E. 2006, in Astronomical Society of the Pacific Conference Series, Vol. 351, Astronomical Data Analysis Software and Systems XV, ed. C. Gabriel, C. Arviset, D. Ponz, & S. Enrique, 751–+

Bronder, T. J., et al. 2007, in American Institute of Physics Conference Series, Vol. 924, The Multicolored Landscape of Compact Objects and Their Explosive Origins, ed. T. di Salvo, G. L. Israel, L. Piersant, L. Burderi, G. Matt, A. Tornambe, & M. T. Menna, 415–420

Burns, C. R., et al. 2011, AJ, 141, 19

Candia, P., et al. 2003, PASP, 115, 277

Cardelli, J. A., Clayton, G. C., & Mathis, J. S. 1989, ApJ, 345, 245

Carpenter, J. M. 2001, AJ, 121, 2851

Chary, R., Dickinson, M. E., Teplitz, H. I., Pope, A., & Ravindranath, S. 2005, ApJ, 635, 1022

Clampin, M. 2011, in Society of Photo-Optical Instrumentation Engineers (SPIE) Conference Series, Vol. 8146, Society of Photo-Optical Instrumentation Engineers (SPIE) Conference Series

Cohen, M., Wheaton, W. A., & Megeath, S. T. 2003, AJ, 126, 1090

Conley, A., Carlberg, R. G., Guy, J., Howell, D. A., Jha, S., Riess, A. G., & Sullivan, M. 2007, ApJ, 664, L13

Conley, A., et al. 2006, ApJ, 644, 1

—. 2008, ApJ, 681, 482

—. 2011, ApJS, 192, 1

Contreras, C., et al. 2010, AJ, 139, 519

Cutri, R. M., et al. 2003, 2MASS All Sky Catalog of point sources. (The IRSA 2MASS All-Sky Point Source Catalog, NASA/IPAC Infrared Science Archive. http://irsa.ipac.caltech.edu/applications/Gator/)

Davis, T. M., & Lineweaver, C. H. 2004, , 21, 97

Davis, T. M., et al. 2007, ApJ, 666, 716

—. 2011, ApJ, 741, 67

Dunkley, J., et al. 2009, ApJS, 180, 306

Eisenstein, D. J., et al. 2005, ApJ, 633, 560

Elias, J. H., Frogel, J. A., Hackwell, J. A., & Persson, S. E. 1981, ApJ, 251, L13

Elias, J. H., Matthews, K., Neugebauer, G., & Persson, S. E. 1985, ApJ, 296, 379

Elias-Rosa, N., et al. 2006, MNRAS, 369, 1880

—. 2008, MNRAS, 384, 107

Ellis, R. S., et al. 2008, ApJ, 674, 51

Filippenko, A. V. 2005, in Astronomical Society of the Pacific Conference Series, Vol. 332, The Fate of the Most Massive Stars, ed. R. Humphreys & K. Stanek, 33

Filippenko, A. V., Li, W. D., Treffers, R. R., & Modjaz, M. 2001, in Astronomical Society of the Pacific Conference Series, Vol. 246, IAU Colloq. 183: Small Telescope Astronomy on Global Scales, ed. B. Paczynski, W.-P. Chen, & C. Lemme, 121

Filippenko, A. V., et al. 1992a, ApJ, 384, L15

—. 1992b, AJ, 104, 1543

Folatelli, G., et al. 2010, AJ, 139, 120

Foley, R. J., et al. 2008, ApJ, 684, 68

—. 2009a, AJ, 138, 376

—. 2009b, AJ, 137, 3731

Freedman, W. L., et al. 2001, ApJ, 553, 47

—. 2009, ApJ, 704, 1036

Freedman, W. L. . T. C. S. P. 2005, in ASP Conf. Ser. 339: Observing Dark Energy, 50–+

Friedman, A., King, J. Y., Li, W. D., & Lick Observatory Supernova Search. 1999a, IAU Circ., 7286, 1

Friedman, A., & Li, W. 1999, IAU Circ., 7154, 1

Friedman, A., Li, W. D., & Chornock, R. 2001a, IAU Circ., 7566, 1

Friedman, A., Li, W. D., & Puckett, T. 1999b, IAU Circ., 7316, 2

Friedman, A., Li, W. D., & Schwartz, M. 2000, IAU Circ., 7533, 2

—. 2001b, IAU Circ., 7597, 1

Frieman, J. A., Turner, M. S., & Huterer, D. 2008a, ARA&A, 46, 385

Frieman, J. A., et al. 2008b, AJ, 135, 338

Frogel, J. A., Gregory, B., Kawara, K., Laney, D., Phillips, M. M., Terndrup, D., Vrba, F., & Whitford, A. E. 1987, ApJ, 315, L129

Fruchter, A. S., & Hook, R. N. 2002, PASP, 114, 144

Ganeshalingam, M., et al. 2010, ApJS, 190, 418

Garavini, G., et al. 2007, A&A, 470, 411

Garg, A., et al. 2007, AJ, 133, 403

Gehrels, N. 2010, ArXiv e-prints

Gerardy, C. L., et al. 2007, ApJ, 661, 995

Giannantonio, T., Scranton, R., Crittenden, R. G., Nichol, R. C., Boughn, S. P., Myers, A. D., & Richards, G. T. 2008, Phys. Rev. D, 77, 123520

Goldhaber, G., et al. 2001, ApJ, 558, 359

Goobar, A. 2008, ApJ, 686, L103

Goobar, A., & Leibundgut, B. 2011, Annual Review of Nuclear and Particle Science, 61, 251

Gopal Vishwakarma, R., & Narlikar, J. V. 2010, Research in Astronomy and Astrophysics, 10, 1195

Guy, J., Astier, P., Nobili, S., Regnault, N., & Pain, R. 2005, A&A, 443, 781

Guy, J., et al. 2007, A&A, 466, 11

—. 2010, A&A, 523, A7

Hamuy, M., Phillips, M. M., Suntzeff, N. B., Schommer, R. A., Maza, J., Smith, R. C., Lira, P., & Aviles, R. 1996, AJ, 112, 2438

Hamuy, M., Phillips, M. M., Wells, L. A., & Maza, J. 1993, PASP, 105, 787

Hamuy, M., et al. 2006, PASP, 118, 2

Hernandez, M., et al. 2000, MNRAS, 319, 223

Hicken, M., Garnavich, P. M., Prieto, J. L., Blondin, S., DePoy, D. L., Kirshner, R. P., & Parrent, J. 2007, ApJ, 669, L17

Hicken, M., Wood-Vasey, W. M., Blondin, S., Challis, P., Jha, S., Kelly, P. L., Rest, A., & Kirshner, R. P. 2009a, ApJ, 700, 1097

Hicken, M., et al. 2009b, ApJ, 700, 331

Hicken, M. S. 2009, PhD thesis, Harvard University

Hook, I. M., et al. 2005, AJ, 130, 2788

Howell, S. B. 2006, Handbook of CCD astronomy (Cambridge University Press)

Hsiao, E. Y., Conley, A., Howell, D. A., Sullivan, M., Pritchet, C. J., Carlberg, R. G., Nugent, P. E., & Phillips, M. M. 2007, ApJ, 663, 1187

Immler, S., et al. 2006, ApJ, 648, L119

Jha, S., Riess, A. G., & Kirshner, R. P. 2007, ApJ, 659, 122

Jha, S., et al. 1999, ApJS, 125, 73

—. 2006, AJ, 131, 527

Kasen, D. 2006, ApJ, 649, 939

Kattner, S., et al. 2012, ArXiv e-prints

Kelly, P. L., Hicken, M., Burke, D. L., Mandel, K. S., & Kirshner, R. P. 2010, ApJ, 715, 743

Kessler, R., et al. 2009, ApJS, 185, 32

Kilbinger, M., et al. 2009, A&A, 497, 677

Kirshner, R. P. 2004, The Extravagant Universe (Princeton University Press)

—. 2010, Foundations of supernova cosmology (Cambridge University Press), 151

Kirshner, R. P., Willner, S. P., Becklin, E. E., Neugebauer, G., & Oke, J. B. 1973, ApJ, 180, L97+

Knop, R. A., et al. 2003, ApJ, 598, 102

Kocevski, D., et al. 2007, ApJ, 663, 1180

Kowalski, M., et al. 2008, ApJ, 686, 749

Krisciunas, K., Hastings, N. C., Loomis, K., McMillan, R., Rest, A., Riess, A. G., & Stubbs, C. 2000, ApJ, 539, 658

Krisciunas, K., Phillips, M. M., & Suntzeff, N. B. 2004a, ApJ, 602, L81

Krisciunas, K., Prieto, J. L., Garnavich, P. M., Riley, J.-L. G., Rest, A., Stubbs, C., & McMillan, R. 2006, AJ, 131, 1639

Krisciunas, K., et al. 2001, AJ, 122, 1616

—. 2003, AJ, 125, 166

—. 2004b, AJ, 127, 1664

—. 2004c, AJ, 128, 3034

—. 2005a, AJ, 130, 350

—. 2005b, AJ, 130, 2453

—. 2007, AJ, 133, 58

—. 2009, AJ, 138, 1584

—. 2011, AJ, 142, 74

Lampeitl, H., et al. 2010, MNRAS, 401, 2331

Larson, D., et al. 2011, ApJS, 192, 16

Lauer, T. R. 1999, PASP, 111, 227

—. 2005, New Astronomy Review, 49, 354

Leaman, J., Li, W., Chornock, R., & Filippenko, A. V. 2011, MNRAS, 412, 1419

Leggett, S. K., et al. 2006, MNRAS, 373, 781

Leibundgut, B., et al. 1993, AJ, 105, 301

—. 1996, ApJ, 466, L21

Li, W., Chornock, R., Leaman, J., Filippenko, A. V., Poznanski, D., Wang, X., Ganeshalingam, M., & Mannucci, F. 2011a, MNRAS, 412, 1473

Li, W., et al. 2003, PASP, 115, 453

—. 2011b, MNRAS, 412, 1441

Li, W. D., et al. 2000, in American Institute of Physics Conference Series, Vol. 522, American Institute of Physics Conference Series, ed. S. S. Holt & W. W. Zhang, 103–106

Mandel, K. S., Narayan, G., & Kirshner, R. P. 2011, ApJ, 731, 120

Mandel, K. S., Wood-Vasey, W. M., Friedman, A. S., & Kirshner, R. P. 2009, ApJ, 704, 629

Maoz, D., & Mannucci, F. 2011, ArXiv e-prints

March, M. C., Trotta, R., Berkes, P., Starkman, G. D., & Vaudrevange, P. M. 2011, MNRAS, 418, 2308

Marion, G. H., Höflich, P., Gerardy, C. L., Vacca, W. D., Wheeler, J. C., & Robinson, E. L. 2009, AJ, 138, 727

Marion, G. H. H., & collaborators. 2011, in prep.

Matheson, T., et al. 2008, AJ, 135, 1598

Meikle, W. P. S. 2000, MNRAS, 314, 782

Miknaitis, G., et al. 2007, ApJ, 666, 674

Modjaz, M. 2007, PhD thesis, Harvard University

Modjaz, M., et al. 2006, ApJ, 645, L21

—. 2009, ApJ, 702, 226

Nobili, S., et al. 2005, A&A, 437, 789

Pastorello, A., et al. 2007a, MNRAS, 377, 1531

—. 2007b, MNRAS, 376, 1301

Patat, F. 2005, MNRAS, 357, 1161

Patat, F., et al. 2007, Science, 317, 924

Perlmutter, S., et al. 1997, ApJ, 483, 565

—. 1999, ApJ, 517, 565

Phillips, M. M. 1993, ApJ, 413, L105

—. 2011, ArXiv e-prints

Phillips, M. M., Lira, P., Suntzeff, N. B., Schommer, R. A., Hamuy, M., & Maza, J. 1999, AJ, 118, 1766

Phillips, M. M., Wells, L. A., Suntzeff, N. B., Hamuy, M., Leibundgut, B., Kirshner, R. P., & Foltz, C. B. 1992, AJ, 103, 1632

Phillips, M. M., et al. 2006, AJ, 131, 2615

—. 2007, PASP, 119, 360

Press, W. H. 2002, Numerical recipes in C++ : the art of scientific computing (Cambridge University Press)

Prieto, J. L., Rest, A., & Suntzeff, N. B. 2006, ApJ, 647, 501

Quimby, R. M. 2006, PhD thesis, The University of Texas at Austin

Rest, A., et al. 2005, ApJ, 634, 1103

Riess, A. G., Press, W. H., & Kirshner, R. P. 1996, ApJ, 473, 88

Riess, A. G., et al. 1998, AJ, 116, 1009

—. 1999, AJ, 117, 707

—. 2005, ApJ, 627, 579

—. 2007, ApJ, 659, 98

—. 2011, ApJ, 730, 119

Rowe, B., Hirata, C., & Rhodes, J. 2011, ApJ, 741, 46

Scalzo, R. A., et al. 2010, ApJ, 713, 1073

Schechter, P. L., Mateo, M., & Saha, A. 1993, PASP, 105, 1342

Schmidt, B. P., et al. 1998, ApJ, 507, 46

Schweizer, F., et al. 2008, AJ, 136, 1482

Skrutskie, M. F., et al. 2006, AJ, 131, 1163

Sollerman, J., et al. 2009, ApJ, 703, 1374

Spergel, D. N., et al. 2007, ApJS, 170, 377

Stritzinger, M., & Sollerman, J. 2007, A&A, 470, L1

Stritzinger, M., et al. 2002, AJ, 124, 2100

—. 2010, AJ, 140, 2036

Stritzinger, M. D., et al. 2011, AJ, 142, 156

Taubenberger, S., et al. 2008, MNRAS, 385, 75

—. 2011, MNRAS, 412, 2735

Tegmark, M., et al. 2004, Phys. Rev. D, 69, 103501

Tominaga, N., et al. 2005, ApJ, 633, L97

Tonry, J. L., et al. 2003, ApJ, 594, 1

Turnbull, S. J., Hudson, M. J., Feldman, H. A., Hicken, M., Kirshner, R. P., & Watkins, R. 2011, MNRAS, 2088

Valentini, G., et al. 2003, ApJ, 595, 779

Wang, L. 2005, ApJ, 635, L33

Wang, L., Goldhaber, G., Aldering, G., & Perlmutter, S. 2003, ApJ, 590, 944

Wang, X., et al. 2008, ApJ, 675, 626

—. 2009a, ApJ, 699, L139

—. 2009b, ApJ, 697, 380

Weinberg, S. 1989, Reviews of Modern Physics, 61, 1

Weinberg, S. 2008, Cosmology (Oxford University Press)

Williams, A. J. 1997, , 14, 208

Wood-Vasey, W. M. 2010, The future of supernova cosmology (Cambridge University Press), 202

Wood-Vasey, W. M., et al. 2007, ArXiv Astrophysics e-prints

—. 2008, ApJ, 689, 377